Micro-scale Processing of Diamond Structures and Devices

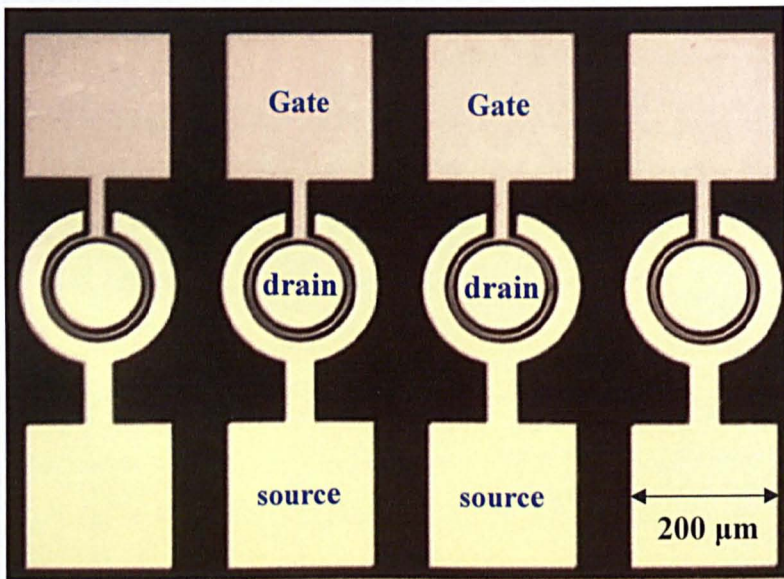**University of**
Strathclyde
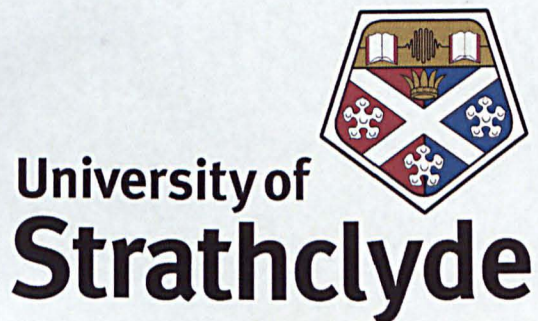
Chee-Leong Lee

A thesis presented in fulfilment
of the requirements for the degree of
Doctor of Philosophy
to the University of Strathclyde, Department of Physics

2008
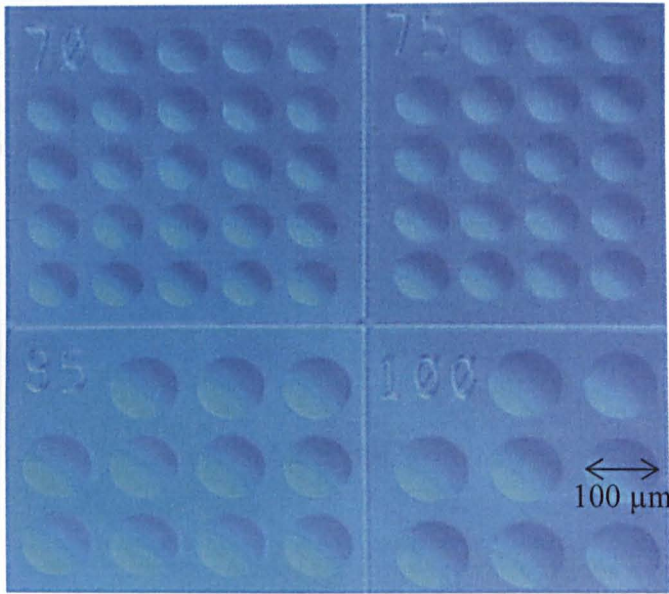
An optical image of arrays of Type IIa natural diamond micro-lenses with different diameters.

An optical image of the four fabricated MOSFET devices.

Declaration of Author's Rights

ABSTRACT

In this project, Inductively Coupled Plasma (ICP) etching of natural and synthetic diamond using oxygen-based (Ar/O$_2$) and chlorine-based (Ar/Cl$_2$) plasmas was investigated. The effects of ICP platen and coil powers and gas pressures on the diamond etching were also studied. It was demonstrated that the diamond etch rate and etch selectivity using Ar/Cl$_2$ plasma etching, with high etch controllability (on the nanometre scale) and capabilities of removing the sub-surface damage and improving the surface smoothness, is only half of those by using Ar/O$_2$ plasma.

Based on these studies, various diamond micro-optics including diamond micro-spherical positive and negative lenses, micro-cylindrical and micro-ring lenses, complex micro-lenses and optical gratings were designed and successfully fabricated. Structural and optical characterisations revealed the high optical quality and functionality of the fabricated diamond micro-optics. Applications of diamond micro-optics, such as micro-lensed micro-VECSEL photonic devices were also demonstrated.

Utilising ICP Ar/Cl$_2$ plasma etching and other processes, prototype diamond electronic devices such as diamond MISFETs and MOSFETs have been fabricated. To realize such diamond FET devices, ohmic contacts with low specific contact resistances, which can be achieved by applying aqua regia surface treatment and laser ablation techniques on the p-doped diamond, are imperative. However, it was found that the gate leakage currents of the diamond MISFET devices were quite large due to leakage through the diamond intrinsic layer under the gate. To overcome this problem, diamond MOSFET devices employing SiO$_2$ as gate insulation material were developed, which were able to sustain large gate biases with very low leakage currents. However, these diamond MOSFET devices could not be fully pinched-off which may be due to the high boron concentration and relatively thick delta layer, which leads to excessive charge in the channel of the device. By fabricating a recess gate diamond p-MOSFET, gate field control was much enhanced.

Acknowledgements

Table of Contents

Chapter 4 Experimental Techniques for Characterising Diamond Micro-optical and Micro-electronic Devices

Chapter 5 Diamond Micro-optics: Fabrication and Characterisation of Spherical Diamond Micro-lenses

Chapter 6 Special Diamond Micro-optics: Micro-cylindrical, Micro-ring, Complex micro-lenses and Optical Gratings

Chapter 7 Process Development for Fabricating Diamond Micro-electronic Devices

Chapter 8 Diamond Micro-electronic Devices: Metal Insulator Semiconductor Field Effect Transistor and Metal Oxide Semiconductor Field Effect Transistor

Chapter 1

Introduction

1.1   Introduction

It is well known that natural diamond is precious gems. Due to its superior physical, chemical, optical and electrical properties, today diamond is used much wide rather than just for making jewellery. Optically, diamond is unmatched in being transparent from deep ultraviolet to beyond a wavelength of 100 μm, making it a particularly attractive material for optics applications. In addition, diamond has low coefficient of thermal expansion (1×10^{-6} °C^{-1}) [1-2] and high thermal conductivity of 20 $Wcm^{-1}K^{-1}$ at room temperature [1-2], making it the best thermal conductor of any material. Thus heat dissipation is much of less concern for diamond-based optical and electronic devices. Furthermore, diamond is the hardest known material, chemically inert and possesses the properties of high wear resistance and low friction. Diamond is therefore also a perfect material to be used for making grinding and cutting tools.

Diamond extreme properties derive from its strong, covalent carbon-carbon bonds called sp^3 bond [3]. Within the crystal, each carbon atom is symmetrically bonded to four neighbouring carbon atoms situated at the corners of a surrounding tetrahedron. A unit cell of diamond crystal structure is shown in Figure 1.1. The carbon atoms are represented by the small spheres on the corners and face centre of a cube, and at four sides inside. The thick lines joining them represent the covalent bonds [3] with the cubic length, a_0, of 0.357 nm at room temperature [4].

It can be observed in Figure 1.1 that diamond has a cubic crystal structure in which all carbon atoms have four covalent (sp^3) bonds. The bonds between the carbon atoms are far stronger than those in silicon and germanium. It is the strong bonding that makes diamond hard. This arrangement of atoms, and its spatial repetition through the crystal, is the prototype crystalline structure found for the mono-elemental, intrinsic semiconductors such as silicon and germanium. From this perspective, diamond should be a semiconductor. However, diamond has a large

electronic band gap of about 5.45 eV (Si: 1.1 eV; Ge: 0.7 eV). At room temperature, very few valence electrons can break loose from diamond bonds to take part in electrical conduction. For this reason, intrinsic diamond is practically an insulator [5-6]. Nevertheless, the diamond conductive property can be altered by doping [5-6]. Additionally, with a very high breakdown voltage (10 $MVcm^{-1}$) and high hole mobility (3800 $cm^2V^{-1}s^{-1}$) [7], p-doped diamond is a promising semiconductor material for developing high power electronic and optoelectronic devices.
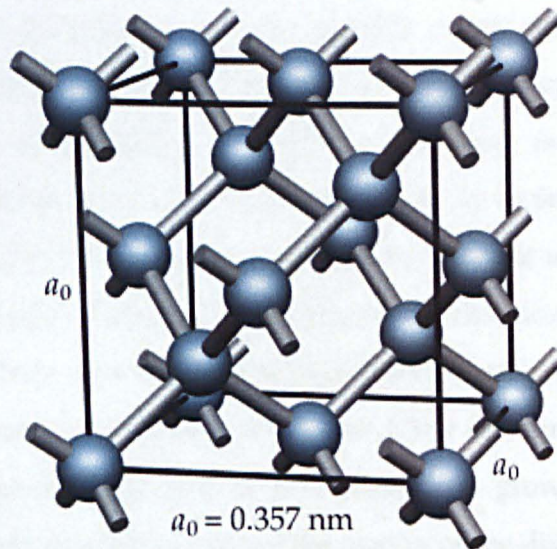
Figure 1.1   One cubic unit cell of the diamond structure [4].

In this chapter, a brief history of diamond will be first reviewed. Then, the type of diamond as well as diamond machining techniques (i.e. mechanical cutting, polishing and dry etching) will be described. A literature review on diamond micro-optics (e.g. micro-lenses and gratings) and micro-electronics (e.g. Field Effect Transistors) will be presented. Diamond micro-optics and micro-electronics are main diamond devices developed and studied in the project.

1.2   History of Diamond [3]

Up to the 1950s, only natural diamonds were available. These natural diamonds are coveted as gems and therefore are extremely expensive. The high cost created a large barrier for diamond use in optoelectronic applications besides a gem stone. Hence, the race began to synthesise diamond in the laboratory. Since 1953, synthetic

diamonds under high-pressure, high-temperature (HPHT) have been manufactured. In this method, diamond is crystallised from metal solvated carbon at pressures above 50 kbar and temperatures exceeding 1500 K. The HPHT diamonds are now used widely in the cutting, grinding and sawing of other hard materials. It is also possible to grow larger diamond by means of the HPHT method, but the process is costly.

At about the same time that HPHT growth was achieved, experiments started to indicate that diamond growth may even be possible at low pressure by deposition from carbon-containing gases such as methane. Great excitement ensued when it was convincingly proven in the early 1980s that sustainable, metastable growth of diamond can be achieved when such a gas is diluted by hydrogen and excited to become plasma. Suitable plasma can be generated by different means such as by gas flow over a hot tungsten filament, by microwave activation or by plasma jet. Polycrystalline diamonds grown by plasma-assisted chemical vapour deposition (PACVD) are now commercially available. The CVD diamond technology opens great opportunities for diamond as it is now possible to grow diamond films and coatings. It is also made possible to control the quality of the diamond grown and the ability to dope the materials in order to engineer its properties. Therefore, diamond is now moving into many other applications for which its unique properties make it an ideal material. For this reason, various types of diamond are introduced in the following sections to gain a better understanding of this material.

1.3   Type of Diamond [1]

In general, diamond can be classified into two categories: natural diamond and synthetic diamond. Both of the natural and synthetic diamonds have been categorised into four main types:

a) Type Ia

Most of the natural diamonds (about 98 %) fall into this type [8]. Type Ia diamond contains around 0.3 % of nitrogen which is substituted in small aggregates. The presence of these nitrogen impurities produces infrared absorption since nitrogen

itself gives rise to strong absorption in the infrared [9]. The concentration of the incorporated nitrogen impurity can be as high as 5.28×10^{20} atoms/cm^3 with the carbon density of 1.76×10^{23} atoms/cm^3 [4].

b) Type Ib

Almost all synthetic diamonds are of this type. The nitrogen atoms are primarily singly dispersed such that each atom occupies a lattice site. This occurs when the diamond is doped with nitrogen. The concentration of the substitutional nitrogen atoms in the lattice sites can be up to 500 ppm [10]. In contrast, natural diamond of this type is very rare, which accounts for about 0.1 % of natural diamonds.

c) Type IIa

Type IIa diamonds are of high purity and are insulators. These diamonds contain extremely low levels of nitrogen (less than 5 ppm [10]). The nitrogen levels are so low that the nitrogen is hardly detectable by infrared absorption measurements. The single-crystalline type IIa diamonds contains no dislocations and other defects such as interstitial atoms and vacant lattice sites (vacancies) and thus, are an ideal material for developing diamond optical devices. Type IIa diamonds are even rare in nature compared to type Ib and Type IIa diamonds can now be synthesised by CVD method.

d) Type IIb

Diamonds of this type are extremely rare in nature. Type IIb diamonds contain very low concentration of nitrogen (less than 1 ppm [11]) but contain single substitutional boron atom resulting in absorption in the red to infra-red region. Hence, these types of diamonds are normally used to make *p*-type semiconductor diamond. Type IIb diamond can be synthesised by deliberately incorporating boron atoms into the material and excluding nitrogen.

1.3.1 Natural Diamond

Although diamond consists of carbon, at least 58 other elements have been found as impurities in type I natural diamond (for example, aluminium, 10 parts per million (ppm); hydrogen, 1000 ppm; silicon, 80 ppm) [8]. However, among these impurities

only two elements, boron and nitrogen, may replace carbon atoms in the diamond lattice. Nitrogen is the major impurity and may substitute for carbon atoms individually or in pair [1]. The presence of nitrogen and the manner of its substitution influence diamond physical properties including thermal conductivity and electrical resistivity.

1.3.2 Synthetic Diamond

Synthetic diamond is the diamond synthesised in the laboratory and is produced commercially in large amounts for industrial uses. There are two main types of synthetic diamonds: High-Pressure and High-Temperature (HPHT) diamond and Chemical Vapour Deposition (CVD) diamond.

1.3.2.1 High-Pressure and High-Temperature (HPHT) Diamond

HPHT diamond is synthesised in the diamond stable region of the carbon phase diagram where high pressure and high temperature are required. Two types of diamond can be produced via the HPHT method, mono-crystalline diamond (MCD) and poly-crystalline diamond (PCD). It should be noticed that the nomenclature "MCD" is sometimes also used to refer to single crystal diamond. The diamond formed by sintering HPHT technique is referred as PCD. These diamonds generally contain Cobalt and should not be confused with the polycrystalline diamond grown by CVD technique known as PCVD.

1.3.2.2 Chemical Vapour Deposition (CVD) Diamond

Chemical Vapour Deposition (CVD) is a technique in which a gas–phase chemical reaction occurs above a substrate surface causing deposition onto that surface [1,12]. In order to deposit diamond by this method, a carbon-containing gas must be "activated" to provide the gas phase species required for growth. This activation can be thermal (hot filament) or plasma (DC or RF microwave). In addition, in order to form diamond rather than other carbonaceous materials, the substrate onto which growth occurs must be maintained at a sufficiently high temperature.

For CVD diamond growth, methane (CH_4) diluted in an excess of hydrogen is used. The nature of resulting diamond films is strongly dependent upon growth conditions. Measures of the ratio of diamond-like bonding to graphite-like bonding and the amounts of C-H incorporation and the crystallinity are used to assess the growth quality. In general, there are two main types of CVD diamonds:

a) Polycrystalline CVD diamond

Polycrystalline diamond grown by using CVD technique is referred as PCVD. Even though the quality of the PCVD diamond is lower than the single crystal CVD diamond, the commercial price of the PCVD diamond is much cheaper than the single crystal CVD diamond.

b) Single Crystal CVD diamond

Single crystal CVD diamond normally contains nitrogen. However, rapid advances of this technology have enabled high purity diamond to be grown. The nitrogen level for the high purity diamond can be lower than 1 part per billion (ppb). Hence, the synthetic single crystal CVD diamond is suitable for fabricating high quality diamond electronic devices.

1.4 Diamond Processing

The extreme properties of diamond make it a highly desirable material for many applications. Nevertheless, due to its outstanding mechanical properties such as the extreme hardness, processing and micromachining of diamond is a technique challenge. To date, several techniques have been developed to process diamond including mechanical methods or plasma dry etching techniques. These techniques will be briefly reviewed in the following sections.

1.4.1 Mechanical Processing

Important mechanical processing of diamond required for fabricating diamond optical and electronic components is diamond cutting and polishing. These processes are required so as to cut diamond into the desired size or to polish the diamond to achieve a highly smooth surface.

1.4.1.1 Diamond Cutting

Diamond cutting begins with examining and marking the diamond. The diamond can be cut by cleaving, mechanically sawing, laser cutting and electrical discharge machining (EDM) techniques:

a) Cleaving [13]

Diamond cleavage occurs predominantly along a set of crystalline planes. For diamond the easiest cleavage planes are {111} planes. When cleaving, a diamond is set at a holder called a "dop". A scratch groove is made first by using another diamond. A steel knife is then set into the groove and is tapped with a wooden mallet. If the scratch groove was made accurately along the crystalline planes, the diamond will cleave easily. However, if the scratch is misaligned, the mallet tap may shatter the diamond.

b) Mechanical Sawing

For sawing a diamond, the diamond sample is set into "dop" like cleaving and is then clamped into an arm above a saw which revolves at a high speed. Traditionally, a special diamond saw is used for cutting the diamond. However, if the diamond must be cut in a direction that is not along a cleavage plane, a thin phosphor-bronze saw blade (< 0.1 mm) is used.

c) Laser-Cutting

Diamond can be cut by using a pulsed laser beam. Diamond is prone to cracking during laser processing. In order to achieve successful cutting, the pulse duration of the laser beam should be adjusted carefully according to the type of diamond. The cutting surfaces are normally poor and further polishing process is required in order to improve the surface quality.

d) Electrical Discharge Machining (EDM)

If the diamond is conductive, EDM technique can be used for cutting. Conductive polycrystalline diamond (PCD) and boron-doped PCVD diamond are normally cut

using EDM method. The cut surface with EDM technique is rougher than those achieved with laser cutting [14].

1.4.2 Diamond Polishing [15]

Diamond polishing is an important process to obtain a highly smooth surface. There are mainly two types of polishing: Scaife polishing and resin-bonded polishing. In this work, the highly smooth diamond samples (with a root-mean-square surface (RMS) roughness of less than 0.5 nm over a 5 x 5 μm^2) used for Field Effect Transistor (FET) fabrication were either Scaife polished or resin-bonded polished.

a) Scaife Polishing

This method has been used in the gem trade for diamond faceting and polishing for centuries. A scaife is a metal wheel. The wheel can be made of different materials such as cast iron or bronze and is typically "dressed" prior to polishing by impregnating the surface of the wheel with diamond grit or powder. The diamond is normally polished by hand. The diamond sample is clamped in a hand-held metal holder known as a "dop". Scaife polishing is considered to be a chemo-mechanical process. Abrasive forces from the diamond-impregnated scaife wheel remove material by mechanical fracture. It is also thought that the high temperature due to friction along with the wheel chemistry leads to a chemical component in the process. The removal rates achieved in scaife polishing are highly dependent on the face you are polishing and the polishing direction. In this project, diamond samples with {100} surface have been used and a scaife polishing process has been developed by Element Six Ltd. to achieve surfaces with the lowest surface RMS roughness of less than 0.1 nm over a 1 x 1 μm^2.

b) Resin-bonded Polishing

This method involves polishing diamond with a wheel which contains diamond grit. The wheel is typically made of organic resin on which diamond grit was pre-embedded. Resin-bonded polishing is often used in a more productionised setting. Unlike Scaife polishing, the diamond is not polished in one fixed direction and there is no chemical aspect to the polishing.

1.4.3 Dry Etching

Due to the absence of a reliable wet etching approach on diamond materials, attention has been shifted to dry etching techniques such as Reactive Ion Etching (RIE) [16], Inductively Coupled Plasma (ICP) [17-22], Electron Cyclotron Resonance (ECR) [23] or Focused ion Beam Etching (FIB) [24].

The use of high density plasma (10^{11} ions/cm^3) plasma etch systems such as ICP and ECR has resulted in improved etch characteristics as compared to the conventional RIE [25]. The improved performance can be attributed to high plasma densities which are 2 to 4 orders of magnitude higher than RIE and thus improving the bond breaking efficiency and the sputter desorption of etch products [25]. Additionally, plasma induced etching is more readily controlled due to the effective decoupling of both ion energy and ion density [25]. ICP plasma has advantage such as uniform density and energy distribution while keeping the ion and electron energy low [25]. Thus, ICP produces low surface damage while maintaining a fast etch rate [25]. A highest etch rate of about 0.2 µm/min on diamond by ICP Ar/O_2 plasma etching was reported by Choi [26]. In this work, novel diamond micro-optics (e.g. micro-lenses) and micro-electronics (e.g. FET) were successfully fabricated by using ICP dry etching method.

1.5 Literature Review: Diamond Micro-optics and Micro-electronics

1.5.1 Diamond Micro-optics (Micro-lenses and Grating)

In this work, novel diamond micro-optics such as high quality diamond micro-lenses in different formats and diamond gratings were developed. Previous works on the diamond micro-optics and the techniques of fabricating micro-lenses and gratings are reviewed in the following sections.

1.5.1.1 Micro-lenses

A large number of very different methods have been attempted to make either individual micro-lenses or micro-lens arrays with varied success. One of the earliest forms of micro-lens was developed by Robert Hooke in 1664 [27]. He melted the ends of thin strands of Venetian glass in a flame, which became a hemispherical form

under the action of surface tension. He then mounted these lenses in pitch and polished the back flat. This thermal reflow technique has been widely applied to polymer materials with a low melting temperature such as photoresist. By combining the thermal reflow with etching process, it is possible to produce micro-lens arrays in hard materials. In this way, micro-lens pattern is first formed in the polymer material by thermal reflow, and then the lens pattern is transferred into the hard material by dry etching. The fabrication of micro-lenses using the combined thermal reflow and etching techniques has been proposed by Popovic *et al.* [28] and Daly *et al.* [29].

Since then, micro-lenses have been fabricated in different materials. Park *et al.* [30] has fabricated plano-convex refractive micro-lenses in sapphire using chlorine-based ICP plasma etching. The thermal reflow and ICP etch techniques have also been adopted by Choi *et al.* [31]. In their work, plano-convex micro-lenses on natural diamond have been successfully fabricated using ICP oxygen plasma etching [26]. In addition, bifocal and negative micro-lenses on gallium nitride (GaN) have also been fabricated by the same group [31]. In that work, GaN bifocal micro-lenses were fabricated by using ICP etching with two different plasmas (Cl_2/BCl_3 and Cl_2/Ar) in order to achieve different etch selectivities. The difference in etch selectivity between the two etch processes enabled the fabrication of the dual-power micro-lens. On the other hand, the negative GaN micro-lenses were realised by using hot-embossing method. To fabricate such negative micro-lenses, sapphire plano-convex micro-lenses were first made. These lenses were then coated with silica and were pressed onto the photoresist layer coated on the GaN substrate [31]. Then, silica was etched away using a chemical solution to separate the assembly. The resulted negative micro-lens pattern left in the photoresist layer on the GaN substrate was then etched to transfer the negative micro-lenses on GaN.

Micro-lenses can also be formed using the inkjet printing technology [32-33]. In this method, drops of UV curable optical adhesive were dispensed from the printer and form micro-lenses in a similar fashion to those formed by the reflow method [20-22,26]. Then the lenses are cured by UV light. Under computer control, the lens array can be printed in a predefined pattern. Several parameters such as print head

temperature, drive waveform parameters and substrate temperature can be altered to optimise the micro-lens structures.

To date, only diamond spherical convex micro-lenses have been fabricated. Diamond micro-lenses in other formats such as, negative, cylindrical and ring micro-lenses, have not yet been reported. Due to the unique optical properties of diamond, the abovementioned diamond micro-lenses have been fabricated in this work.

1.5.1.2   Gratings

Sub-wavelength gratings on CVD diamond have been successfully fabricated by Karlsson *et al.* [34] in order to reduce the Fresnel reflection. These antireflection (AR) diamond gratings were optically evaluated with a spectrophotometer. It was found that the transmission through an AR diamond grating was increased from 71 % to 97 %. The fabrication of the diamond grating was performed with e-beam lithography and ICP plasma etching. The diamond gratings with the shortest period were fabricated by Lister *et al.* [35]. In his work, the grating with a period of 23 nm has been fabricated onto the CVD diamond using the e-beam lithography and RIE oxygen plasma etching.

1.5.2   Diamond Micro-electronics (Field Effect Transistors)

Various diamond micro-electronic devices have been demonstrated. This review mainly focuses on the diamond field effect transistors (FETs) and the key technique to achieve the diamond FETs-ohmic contact formation on the p-doped diamond.

1.5.2.1 Ohmic Contact on p-doped Diamond

In general, a potential barrier is developed at metal-semiconductor interfaces due to either the difference in the work functions of the two materials (Schottky-Mott Model) or to the presence of interface states which pin the Fermi level (Bardeen Model). The fundamental physics of these two models is elucidated in **Section 2.3.1**. The barrier height of different metal contacts on single crystal diamond has been measured using various techniques, including capacitance-voltage (C-V) [36], photoemission spectroscopy [37], photoelectron spectroscopy [38]. The

reported values of barrier height are found to be independent of the metal [36-38]. Hence, it can be concluded that the Fermi level is strongly pinned at the diamond surface, presumably due to the covalent nature of diamond which tends to offer a high density of surface states. Thus, Schottky contacts have been obtained via less reactive materials such as Au on lightly to moderately doped, undamaged diamond surface [36, 39-42]. On the other hand, reasonably good ohmic contacts can be formed by choosing or intentionally creating damaged surfaces, i.e. graphitisation [43-47].

Several methods for achieving good ohmic contacts on diamond have been reported. These research results showed that to obtain ohmic contacts on diamond with a low contact resistance, it is important to form a very high conductive layer at the interface between the metal contact and diamond. A transformation from diamond to high conductive non-diamond carbon (graphitisation) via laser ablation was observed by several researchers. Geis *et al.* reported an interesting study on modification (i.e. graphitisation) of diamond surface using a pulsed 190 nm ArF laser [43]. After laser ablation and etching using either a solution of H_2SO_4 and CrO_3 or a He-O_2 plasma, a brownish surface layer with a mixture of diamond and graphite (unidentified graphite-like carbon phases) was formed [43]. Since the damaged diamond (i.e. graphitisation) enables diamond surface to be remarkably conductive, ohmic contacts can formed on the surface. In order to achieve surface graphitisation, various experiments have been performed by using laser ablations. For example, a diamond sample was irradiated with a 193 nm laser [44]. It was found that the heating and the laser power determines the local graphitisation and carbide forming and consequently affecting the contact properties. Depending on the temperature and type of diamond, the non-diamond carbon formed after ion implantation can be completely graphitised [45-46]. The ohmic contact formed by graphitisation is also shown by Chen *et al.* [47].

A most common method of realising ohmic contacts on semiconductor materials is by heavily doping the region (e.g. ion implantation) under the contact and utilising the tunnelling current through the narrow depletion region. Ion implantation is very

promising technique to dope the diamond surface in order to achieve good ohmic contact. Prins *et al.* [48-49], Kalish *et al.* [46, 50] and Sandhu *et al.* [51] have studied ion implantation into diamond. Kalish *et al.* has used B, Li and P ion beams with energies from 40 to 170 keV for implantation and a contact resistance of 0.01 $\Omega.cm^2$ has been achieved by using B ion implantation. However, in his work, the contact metals were not specified. The lowest value of the specific contact resistance (1.4 x 10^{-7} $\Omega.cm^2$) was achieved by using Si implantation (or Si and B dual implantation) [52]. In that work, Ti was used as the contact metal layer.

The carburisation reaction of a carbide-forming refractory metals such as Ti, Mo and Ta [39-40, 42, 53-57] on diamond is also a widely used method to form good ohmic contacts. The ohmic behaviour of these metal contacts was attributed to the formation of carbide at the interface during annealing. Carbides are reliable contacts as well as good diffusion barriers especially for high-temperature devices. For the case of Ti contact, the Ti metal is carburised by an annealing typically at about 450 °C in argon and nitrogen ambient. A very thin TiC layer is formed at the diamond/Ti interface which allows tunnelling of the carriers through the contact and thus reducing the contact resistance. This process has been studied extensively by Moazed *et al.* [53] and Tachibana *et al.* [58-59]. For such Ti contacts, a Pt layer is normally used as a diffusion-blocking layer deposited on the top of Ti layer and a Au cap is finally deposited which acts as an anti-oxidation highly-conductive layer and can be directly wire bonded.

Another approach of achieving a good ohmic contact on diamond is to use Si-based contacts [60]. By this method, the diamond surface is heavily doped with B (doping concentration above 1 x 10^{20} cm^{-3}) in a very thin surface layer and the contact resistance measured is 10^{-2} $\Omega.cm^2$. Unique formation of graded junctions of Si/SiC/diamond may be considered as a combination of carbide formation and damaging of the diamond lattice by Kr^+ ion implantation [61]. The specific contact resistance obtained by this method was about 10^{-3} $\Omega.cm^2$ on relatively highly doped diamond.

Ohmic contacts on boron-doped diamond achieved in this work were realised by chemical etching and UV laser graphitisation utilising Ti metal contact.

1.5.2.2 Diamond Field Effect Transistors (FETs)

Due to its high breakdown field, high hole mobility and large band gap [3, 62], diamond is a promising material for developing high power and high frequency electronic devices, such as Field Effect Transistors (FETs), There are several different types of FET device including Metal Semiconductor Field Effect Transistors (MESFETs), Metal Insulator Semiconductor Field Effect Transistors (MISFETs) and Metal Oxide Semiconductor Field Effect Transistors (MOSFETs). The insulator material used in MOSFET device is SiO_2. Hence, the FET device with the oxide layer as insulator is referred as MOSFET. The FET device with insulator excluding SiO_2 (i.e. intrinsic diamond) is expressed as MISFET. On the other hand, the FET device without insulator is called MESFET. In this case, the metal layers are in contact with the semiconductor.

Table 1.1 shows the comparisons of figures of merit and other properties of diamond with the conventional semiconductor materials such as Si, SiC and GaN [62]. It can be seen in Table 1.1 that there are three different figures of merit [63-65]. Johnson's figure of merit defines the power-frequency for a low voltage transistor. Keyes's figure of merit provides a thermal limitation to the switching behaviour of transistors used in integrated circuit while Baliga's figure of merit defines the material parameters to minimise the conduction losses in power FETs.

Table 1.1   Comparisons of figures of merit and other properties of diamond with the conventional semiconductor materials such as Si and GaN.

Properties	Si	SiC	GaN	CVD Diamond
Band gap (eV)	1.1	3.2	3.44	5.45
Breakdown Field (MVcm^{-1})	0.3	3	5	10
Electron Mobility (cm^{2}V^{-1}s^{-1})	1450	900	440	4500
Hole Mobility (cm^{2}V^{-1}s^{-1})	480	120	200	3800
Thermal conductivity (Wcm^{-1}K^{-1})	1.5	5	1.3	20
Johnson's Figure of Merit [63]	1	410	280	8200
Keyes's Figure of Merit [64]	1	5.1	1.8	32
Baliga's Figure of Merit [65]	1	290	910	17200

Due to these excellent properties of diamond, diamond FETs have been studied intensively and these researches are reviewed here chronologically. The early diamond MESFETs were fabricated and reported by Shiomi *et al.* [66] and Gildenblat *et al.* [67] on boron-doped diamond films grown by the plasma-assisted chemical vapour deposition method. No pinch-off characteristics were observed for their MESFETs. Later on, many attempts have been made to improve the device performance by incorporating a gate insulator so as to reduce the gate leakage current [68-69]. This leads to the fabrication of diamond MISFETs. For example, Shiomi *et al.* [68] inserted a 0.23 μm thick intrinsic diamond layer between the gate electrode and the boron-doped diamond layer. It was reported that the inserted intrinsic diamond layer could withstand 70 V between gate and drain. To fabricate diamond MOSFETs, Grot *et al.* [69] used 0.1 μm thick SiO$_2$ layer as a gate insulator and deposited Au(1250 nm)/Ti(50nm) as metal contacts. Their devices showed field control characteristics but did not exhibit complete pinch-off of the channel.

Tsai *et al.* [70] reported on the fabrication of a diamond MESFET with the channel formed by solid state diffusion in 1990. Boron was diffused into type IIa diamond and simultaneously electrically activated by a rapid thermal annealing technique. Electrical contacts of Ti/Au were made on diamond via evaporation, followed by

annealing at 800 °C for 30 minutes. A low reverse-bias leakage current (below 10^{-12} A at 5 V) was observed.

Zeisse *et al.* [71] introduced the ion-implantation process to fabricate diamond MOSFETs. In their devices, a boron implanted surface layer on the natural diamond serves as a conducting layer and the gate insulator is a 100 nm-thick SiO_2 layer which was deposited by plasma-enhanced chemical vapour deposition (PECVD). This was the first reported diamond FET device fabricated by using ion-implantation technique.

Nishimura *et al.* [72], Grot *et al.* [73] and Tessmer *et al.* [74] have fabricated MOSFETs on polycrystalline diamond. However, all the devices did not show the current pinch-off. The first diamond MESFETs with pinch-off characteristics were fabricated by Shiomi *et al.* [75], in which a self-aligned recessed structure was fabricated.

Dreifus *et al.* [76] demonstrated diamond MOSFETs that exhibited complete current pinch-off in the active channel. The current pinch-off was observed up to 500 °C. The first diamond MESFET with an ultra-thin boron doped layer (delta layer) was fabricated by Shiomi *et al.* [77]. In their devices, an un-doped 150 nm thick diamond buffer layer was grown on type Ib diamond substrate, followed by a 11 nm thick boron-doped diamond layer (with doping concentration larger than 10^{19} cm^{-3}) and a 75 nm-thick undoped diamond cap layer. The gate length and width used are 4 μm and 39 μm, respectively. Again, complete pinch-off characteristic was observed in these devices.

In 1997, Looi *et al.* [78] reported the first normally off enhancement mode diamond MESFET device. For these devices, the drain-to-source current was less than 1 nA at no gate bias, corresponding to an off-state. By applying negative gate voltage, an on-state was established. With a gate voltage of -1.8 V, the drain-to-source current magnitude was 4.7 μA.

Hokazono *et al.* [79] successfully fabricated surface *p*-channel diamond MOSFET. They used SiO_x as gate insulator with a gate length of 6 μm. The I_{DS}-V_{DS} characteristics of the MOSFETs were improved by reducing gate leakage current in the MOS structure and current saturation was observed in their devices. By employing a stacked gate of CaF_2 and Cu, Saito *et al.* [80] demonstrated a MISFET device with complete current saturation. With a gate length of 1.1 μm and a width of 50 μm, the measured maximum drain current density for their devices was 240 mA/mm at -3 V of gate voltage.

Surface channel diamond MESFET has been fabricated by Kueck *et al.* [81]. In his work, ohmic contact was deposited onto an oxygen terminated highly boron-doped layer with a thickness of 2 nm and a high peak concentration ($N_A > 10^{20}$ cm^{-3}). The gate metal was deposited onto the H-induced surface in the channel area of the MESFET devices. A drain current density of 75 mA/mm and a threshold voltage (V_T) of -1.5 V was obtained for a 1 μm gate length. The historical development of diamond FETs is summarised in Table 1.2.

In this work, MISFET and MOSFET have been successfully fabricated by employing highly boron delta (δ)-doped diamond layers (< 20 nm) with doping concentrations from 0.5 to 1 x 10^{21} cm^{-3}. The insulator materials used are intrinsic diamond and SiO_2. In addition, gate-recessed MOSFETs have also been fabricated in order to enhance the field effect control on the gate channel.

Table 1.2   Historical development of diamond field effect transistors.

Year	Diamond FET	Researchers	References
1989	MESFET on CVD diamond	Shiomi *et al.*	[66]
1989	MESFET on CVD diamond	Gildenblat *et al.*	[67]
1990	MISFET with CVD intrinsic diamond	Shiomi *et al.*	[68]
1990	MOSFET with SiO_2	Grot *et al.*	[69]
1990	MESFET by rapid thermal annealing	Tsai *et al.*	[70]
1991	MOSFET with ion implanted channel	Zeisse *et al.*	[71]
1991	MISFET on polycrystalline diamond	Nishimura *et al.*	[72]
1992	Recessed gate MOSFET	Grot *et al.*	[73]
1992	MOSFET on polycrystalline diamond	Tessmer *et al.*	[74]
1994	Self-aligned gate-recessed MESFET	Shiomi *et al.*	[75]
1994	MOSFET on improved diamond films	Dreifus *et al.*	[76]
1995	δ-doped MISFET	Shiomi *et al.*	[77]
1997	Normally-off diamond MESFET	Looi *et al.*	[78]
1999	Surface Channel MOSFET	Hokazono *et al.*	[79]
2005	Diamond MISFET with stacked gate	Saito *et al.*	[80]
2007	Surface Channel MISFET	Kueck *et al.*	[81]

1.6   Work Objective and Achievements

The main objective of this project is to develop new diamond micro-optics and micro-electronics for various applications. To achieve these targets, novel fabrication processes such as ICP Ar/Cl_2 plasma etching have been exploited and developed. In diamond micro-optics, we have designed and fabricated special diamond negative micro-lenses, micro-ring and cylindrical lenses, complex lenses and optical gratings. The functionalities of such diamond micro-optics are characterised by using Atomic Force Microscopy (AFM) and confocal microscopy. In diamond micro-electronics, the objective is to develop diamond based FET devices. For making such diamond FET devices, realising good metal ohmic contacts on the boron doped diamond surface is a key requirement. In this work, we have employed Au/Ti metal contacts as Ti is a carbide forming metal and Ti carbide is readily formed by annealing. We have also developed various diamond surface treatment methods including aqua

regia etching and laser ablation so as to achieve metal ohmic contacts on diamond with a low contact resistance. By using these processes, diamond MISFET and MOSFET devices are successfully fabricated. Current-voltage (*I-V*) characteristics of these FET devices were measured so as to evaluate their electrical properties. These measured results confirmed the functionalities of the diamond FET devices.

1.7   Outline of Thesis

In this thesis, the studies and research results on diamond micro-optics (micro-lenses and grating) and micro-electronics (Field Effect Transistors) are presented. The thesis is organised in such a way that the theoretical backgrounds of diamond micro-optics and electronics are first described, while the experimental results of the project are presented in the following chapters.

In **Chapter 1**, the literature review, motivation and objective of this research project are presented. In **Chapter 2**, the physics backgrounds of micro-optics, metal semiconductor contacts, Circular Transmission Line Model (CTLM) and Field Effect Transistor are described. All the experimental procedures involved in the fabrication of both micro-optics and micro-electronic devices will be described in **Chapter 3**. In **Chapter 4**, the electrical, chemical and surface characterisation techniques will be presented. Investigations and results on diamond micro-optics such as micro-lenses and optical grating will be discussed in **Chapter 5** and **Chapter 6**. The extensive investigations on the process developments such as surface treatment for fabricating diamond MISFET and MOSFET devices and results on diamond MISFET and MOSFET field effect transistors are reported in **Chapter 7** and **Chapter 8**. Finally, conclusions of this research project and suggested future work are presented in **Chapter 9**.

1.8 References

[1] J.E. Field, *The Properties of Natural and Synthetic Diamond*, Academic Press (1992).

[2] M.H. Nazere, A.J. Neves, *Properties, Growth and Applications of Diamond*, INSPEC Publication (2001).

[3] K.H.J. Buschow, R. Cahn, M.C. Flemings, B. Ilschner, E.J. Kramer, S. Mahajan, P. Veyssiere, *The Encyclopedia of Materials: Science and Technology*, Pergamon Press (2001).

[4] F. Fizzotti, A.L. Giudice, Ch. Manfredotti, C. Manfredotti, M. Castellino, E. Vittone, *Dia. Rel. Mat.*, **16**, 836 (2007).

[5] L.S. Pan, D.R. Kania, *Diamond: Electronic Properties and Applications*, Springer (1994).

[6] E. Wilks and J. Wilks, *Properties and Applications of Diamond*, Butterworth-Heinemann Ltd. (1991).

[7] J. Isberg, J. Hammersberg, E. Johansson, T. Wilkstrom, D.J. Twitchen, A.J. Whitehead, S.E. Coe, G.A. Scarsbrook, *Science*, **297**, 1670 (2002).

[8] R. Abbaschian, H; Zhu, C. Clarke, *Dia. Rel. Mat.*, **14**, 1916 (2005).

[9] H. Lim, S. Park, H. Cheong, *J. Korean Phys. Soc.*, **48**, 1556 (2006).

[10] M.A. Prelas, G. Popovici, L.K. Bigelow, *Handbook of Industrial Diamonds and Diamond Films*, Marcel Dekker (1997).

[11] A. T. Collins, *Phil. Trans. :Phys Sci. Eng.*, **342**, 233(1993).

[12] R.S. Sussmann, J.R. Brandon, G.A. Scarsbrook, C.G. Sweenery, T.J. Valentine, A.J. Whitehead, C.J.H. Wort, *Dia. Rel. Mat.*, **3**, 303 (1994).

[13] R.H. Telling, C.J. Pickard, M.C. Payne, J.E. Field, *Phy. Rev. Lett.*, **84**, 5160 (2000).

[14] F. Dousinger, F. Lichtner, H. Lubatschowshi, *Femtosecond Technology for Technical and Medical Applications*, Springer (2004).

[15] J.R. Hird, J.E. Field, *Proc. R. Soc. Lond. A*, **460**, 3547 (2004).

[16] G.M.R. Sirineni, H.A. Naseem, *Dia. Rel. Mat.*, **6**, 952 (1997).

[17] M. Karlsson, K. Hjort and F. Nikolajeff, *Opt. Lett.*, **26**, 1752 (2001).

[18] E. Gu, H.W. Choi, C. Liu, C. Griffin, J.M. Girkin, I.M. Watson, and M.D. Dawson, *Appl. Phys. Lett.*, **84**, 2754 (2004).

[19] D.S. Hwang, T. Saito, N. Fujimori, *Dia. Rel. Mat.*, **13**, 2207 (2004).

[20] C.L. Lee, H.W. Choi, E. Gu, H. Murphy, M.D. Dawson, *Dia. Rel. Mat.*, **15**, 725 (2006).

[21] C.L. Lee, E. Gu, M.D. Dawson, *Dia. Rel. Mat.*, **16**, 944 (2007).

[22] C.L. Lee, E. Gu, I. Friel, G. Scarsbrook, M. Dawson, *Dia. Rel. Mat.*, **17**, 1292 (2008).

[23] S.J. Pearton, C.R. Abernathy, F. Ren, *Appl. Phys. Lett.*, **64**, 3643 (1994).

[24] Y. Fu, B.N.K. Ann, *J. Vac. Sci. Tehnol. B.*, **19**, 1259 (2001).

[25] T. Kim, Phd Thesis, University of Strathclyde (2001).

[26] H.W. Choi, E. Gu, C. Liu, C. Griffin, J.M. Girkin, I.M. Watson, M.D. Dawson, *J. Vac. Sci. & Technol. B*, **23**, 130 (2005).

[27] H.P. Herzig, *Micro-optics*, Taylor and Francis (1997).

[28] Z.D. Popovic, R.A. Sprague, G.A. Neville-Connell, *Appl. Opt.*, **27**, 1281 (1988).

[29] D. Daly, R.F. Stevens, M.C. Hutley, N. Davies, *Meas. Sci. Technol.*, **1**, 759 (1990).

[30] S-H. Park, H. Jeon, Y-J. Sung, G-Y. Yeom, *Appl. Opt.*, **40**, 3698 (2001).

[31] H.W. Choi, E. Gu, C. Liu, J.M. Girkin, M. Dawson, *J. Appl. Phys.*, **97**, 63101 (2005).

[32] B.P. Keyworth, D.J. Corazza, J.N. McMullin, L. Mabbott, *Appl. Opt.*, **36**, 2198 (1997).

[33] B.T. Teipan, D.L. MacFarlane, *Appl. Opt.*, **38**, 2040 (1999).

[34] M. Karlsson, F. Nikolajeff, *Opt. Exp.*, **11**, 502 (2003).

[35] K.A. Lister, B.G. Casey, P.S. Dobson, S. Thoms, D.S. Macintyre, C.D.W. Wilkinson, J.M.R. Weaver, *Microelect. Engr.*, **73-74**, 319 (2004).

[36] G.H. Glover, *Sol. Stat. Elect.*, **16**, 973 (1973).

[37] C.A. Mead and T.C. McGill, *Phys Lett.*, **58A**, 249 (1976).

[38] F.J. Himpsel, P. Heimann, D.E. Eastman, *Sol. Stat. Commun.*, **36**, 631, (1980).

[39] H. Shiomi, Y. Nishibayashi, N. Fujimori, *Jpn. J. Appl. Phys.*, **28**, 758 (1989).

[40] G.S. Gildenblat, S.A. Grot, C.W. Hatfield, A.R. Badzian, T. Badzian, *IEEE Elec. Dev. Lett.*, **11**, 371 (1990).

[41] G.S. Gildenblat, S.A. Grot, C.R. Wronski, A.R. Badzian, T. Badzian, *Appl. Phys. Lett.*, **53**, 586 (1988).

[42] S.A. Grot, G.S. Gildenblat, C.W. Hatfield, C.R. Wronski, A.R. Badzian, T. Badzian, R. Messier, *IEEE Elect. Dev. Lett.*, **11**, 100 (1990).

[43] M.W. Geis, M. Rothschild, R.R. Kunz, R.L. Aggarwal, K.F. Wall, C.D. Parker, K.A. Mcintosh, N.N. Efremow, J.J. Zayhowski, D.J. Ehrlich, J.E. Butler, *Appl. Phys. Lett.*, **55**, 2295 (1989).

[44] S. Deshmukh, L.M. Hitchcock, E.W. Rothe, G.P. Reck, *Dia. Rel. Mat.*, **3**, 195, (1994).

[45] R. Kalish, *Dia. Rel. Mat.*, **2**, 621 (1993).

[46] R. Kalish, C-U. Saguy, B. Ran, H. Ferber, H. Guettler, R. Zachai, *Dia. Rel. Mat.*, **8**, 877 (1999).

[47] Y.G. Chen, M. Hasegawa, H. Okushi, S. Koizumi, H. Yoshida, T. Sakai, N. Kobayshi, *Dia. Rel. Mat.*, **11**, 451 (2002).

[48] J.F. Prins, *J. Phys. D*, **22**, 1562 (1989).

[49] J.F. Prins, *Phys. Rev. B*, **31**, 2472 (1985).

[50] R. Kalish, A. Reznik, S. Prawer, D. Saada, J. Adler, *Phys. Stat. Sol. (a)*, **174**, 83 (1999).

[51] G.S. Sandhu, M.L. Swanson, W.K. Chu, *Appl. Phys. Lett.*, **55**, 1397 (1989).

[52] G.R. Brandes, C.P. Beetz, C.F. Feger, R.W. Wright, J.L. Davidson, *Dia. Rel. Mat.*, **8**, 1936, (1999).

[53] K.L. Moazed, J.R. Zeidler, M.J. Taylor, *J. Appl. Phys.*, **68**, 2246 (1990).

[54] A.T. Collins, E.C. Lightowiers, A.W.S. Williams, *Dia. Res. (Suppl. Indust. Dia. Rev.)*, 19 (1970).

[55] K.L. Moazed, R. Nguyen, J.R. Zeidler, *IEEE Elect. Dev. Lett.*, **9**, 350 (1988).

[56] D. Narducci, J.J. Cuomo, C.R. Guarnieri, S.J. Whitehair, in Diamond, Silicon Carbide and Related Wide Bandgap Semiconductors, (MRS Symposium Proceedings **162**), *Materials Research Society*, Pittsburgh, Pennsylvania, 333 (1990).

[57] Y. Chen, M. Ogura, S. Yamasaki, H. Okushi, *Semicond. Sci. Technol.*, **20**, 860 (2005).

[58] T. Tachibana, B.E. Williams, J.T. Glass, *Phys. Rev. B*, **45**, 11968 (1992).

[59] T. Tachibana, B.E. Williams, J.T. Glass, *Phys. Rev. B*, **45**, 11975 (1992).

[60] A. Aleksov, A. Denisenko, M. Kunze, A. Vescan, A. Bergmaier, G. Dollinger, W. Ebert, E. Kohn, *Semicon. Sci. & Tech.*, **18**, S59 (2003).

[61] F. Fang, C.A. Hewett, M.G. Fernandes, S.S. Lau, *IEEE Trans. Elect. Dev.*, **36**, 1783 (1989).

[62] C.J.H. Wort, R.S. Balmer, *Materials Today*, **11**, 22 (2008).

[63] E.O. Johnson, *RCA Rev.*, **26**, 163 (1963).

[64] R.W. Keyes, *Proc. IEEE*, **63**, 740 (1975).

[65] B.J. Baliga, *IEEE Elect. Dev. Lett.*, **10**, 455 (1989).

[66] H. Shiomi, Y. Nishibayashi, N. Fujimore, *Jpn. J. Appl Phys*, **28**, L2153 (1989).

[67] G.S. Gildenblat, S.A. Grot, C.W. Hartfield, C.R. Wronski, A.R. Badzian, T. Badzian, R. Messier, Proceedings of Fall 1989 *Material Research Symposium* Meeting, Boston, **162**, 23 (1989).

[68] H. Shiomi, Y. Nishibayashi, N. Fujumore, Second International Conference of New Diamond Science and Technology, *Material Research Symposium*, Washington, DC, 975 (1990).

[69] S.A. Grot, C.W. Hartfield, G.S. Gildenblat, A.R. Badzian, T. Badzian, Second International Conference of New Diamond Science and Technology, *Material Research Symposium*, Washington, DC, 949 (1990).

[70] W. Tsai, M. Delfino, L.Y. Ching, G. Reynolds, D. Hodul, C.B. Cooper, Second International Conference of New Diamond Science and Technology, *Material Research Symposium*, Washington, DC, 937 (1990).

[71] C.R. Zeisse, C.A. Hewett, R. Nguyen, J.R. Zeidler, R.G. Wilson, *IEEE Elect. Dev. Lett.*, **13**, 462 (1992).

[72] K. Nishimura, R. Kato, S.Miyaushi, K. Kobashi, Japan New Diamond Forum, *Fifth Diamond Symposium*, Tsukuba, Japan, 34 (1991).

[73] S.A. Grot, G.S. Gildenblat, A.R. Badzian, *IEEE Elect. Dev. Lett.*, **13**, 462 (1992).

[74] A.J. Tessmer, K. Das, D.L. Dreifus, *Dia. Rel. Mat.*, **1**, 89 (1992).

[75] H. Shiomi, Y. Nishibayashi, N. Toda, S. Shikata, N. Fujimore, *Fourth International Conference on New Diamond Science and Technology*, MY, Kobe, Japan, 661 (1994).

[76] D.L. Dreifus, A.J. Tessmer, J.S. Holmes, C-T. Kao, D.M. Malta, L.S. Piano, B.R. Stoner, *Material Research Symposium*, Spring Meeting, San Fransisco (1994).

[77] H. Shiomi, . Nishibayashi, N. Toda, S. Shikata, *IEEE Elect. Dev. Lett.*, **16**, 36 (1995).

[78] H.J. Looi, L.Y.S. Pang, Y. Wang, M.D. Whitfield, R.B. Jackman, *Dia. Rel. Mat.*, **8**, 927 (1999).

[79] A. Hokazono, K. Tsugawa, H. Umezana, K. Kitatani, H. Kawarada, *Sol. Stat. Elect.*, **43**, 1465 (1999).

[80] T. Saito, K-H. Park, K. Hirama, H. Umezawa, M. Satoh, H. Kawarada, H. Okushi, *Dia. Rel. Mat.*, **14**, 2043 (2005).

[81] D. Kueck, H. El-Hajj, A. Kaiser, E. Kohn, *Dia. Rel. Mat.*, **17**, 732 (2008).

Chapter 2

Physics Background of Diamond Micro-optics and Micro-electronics

2.1 Introduction

Diamond is a promising material for many applications due to its superior optical and electrical characteristics. These properties have enabled diamond to be employed to develop novel micro-electronic and micro-optical devices with high performances. For this reason, this project concentrates on the two major research areas, namely diamond micro-optics and micro-electronics. In micro-optics, optical grating and various types of diamond micro-lenses have been successfully fabricated. In micro-electronics, diamond Field Effect Transistors (FETs) such as diamond MISFETs and MOSFETs, have been fabricated. Physics background on micro-lenses, optical gating, metal-semiconductor contact and field effect transistor will be reviewed in this chapter in order to gain a better understanding of the principles of these components and devices.

2.2 Micro-optics

Lately, there has been an upsurge of interest in micro-optics, such as micro-lenses, as the benefits of photonics are realised. Development in this area has been helped by the fabrication technologies originally devised for silicon. In this work, diamond micro-lenses and optical gratings have been developed. To achieve such diamond micro-optics, we have also developed the fabrication processes and techniques. These fabrication techniques are introduced in **Chapter 3**.

In this section, the theoretical background of the micro-optics is presented in five subsections. **Subsections 2.2.1** to **2.2.3** elucidate the fundamental physics and calculations of the micro-lenses whereas **subsections 2.2.4** and **2.2.5** describe the basic physics for optical gratings and Gaussian laser beam which was employed for pumping the diamond micro-lensed μ-vertical-external cavity of surface emitting laser (diamond micro-lensed μ-VECSEL), respectively. As most of the diamond

micro-lenses were fabricated by photoresist reflow technique, the calculation of the height variation of the photoresist during the reflow process is introduced in **subsection 2.2.1**. The derivation of the focal length of a micro-lens is given in **subsection 2.2.2**. **Subsection 2.2.3** shows the derivation of a circle equation which relates to the height and surface radius of a spherical lens and can be used to fit the lens profile and estimate its deviation from a ideal circle. **Subsection 2.2.4** describes the principle of an optical grating. Finally, **subsection 2.2.5** shows the derivation of the fundamental mode size of Gaussian laser beam.

2.2.1 Calculation of Height of Photoresist After Reflow Process

Photoresist reflow method is one of the important techniques to fabricate micro-spherical lenses. The reflow process is explained in detail in **Chapter 3**. In this process, the patterned photoresist cylindrical microstructures are heated to the melting point. To minimise the surface energy, the cylindrical disks reflow into spherical microstructures as shown in Figure 2.1.
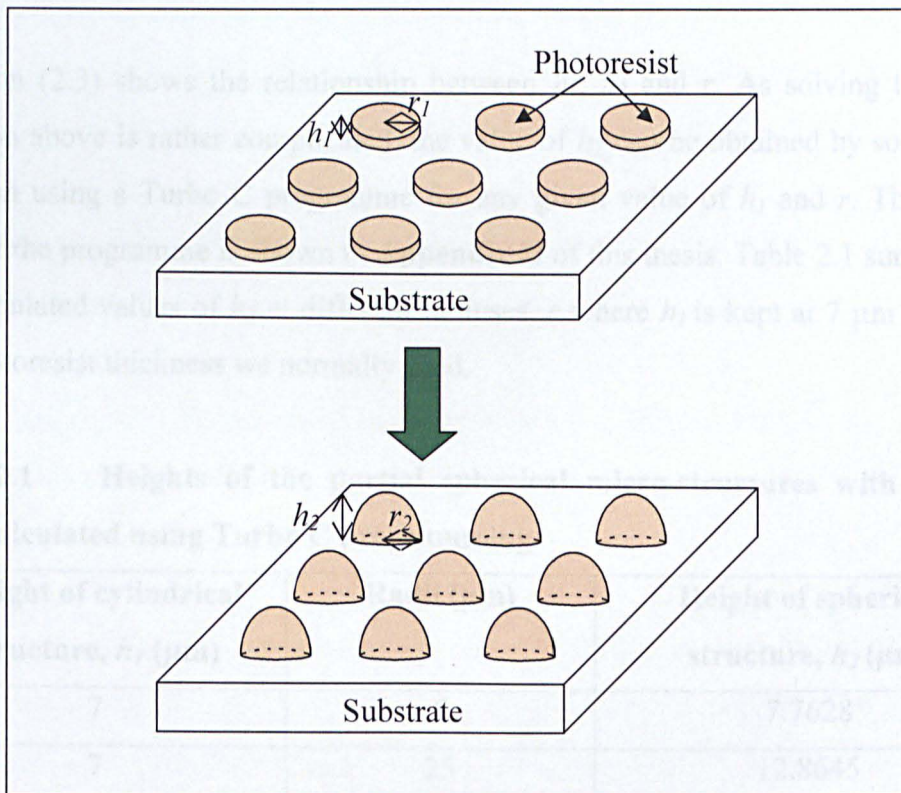
Figure 2.1   Photoresist reflow process.

During the reflow process, the height of the micro-cylindrical disks, h_1 changes to the height, h_2 of the spherical microstructures. The reflow process will not change the volume and the surface radius of the micro-structure, i.e. $r_1 = r_2$.

The volume of a spherical micro-structure is given by:

$$\frac{1}{6}\pi h_2 \left[3r_2^2 + h_2^2\right]$$ (2.1)

and the volume of the cylindrical micro-structure can be written as:

$$\pi r_1^2 h_1$$ (2.2)

As the volumes of both micro-structures are the same, thus:

$$\pi r_1^2 h_1 = \frac{1}{6}\pi h_2 \left[3r_2^2 + h_2^2\right]$$

Since $r_1 = r_2 = r$,

$$\pi r^2 h_1 = \frac{1}{2}\pi h_2 r^2 + \frac{1}{6}\pi h_2^3$$

$$h_2^3 + 3h_2 r^2 - 6r^2 h_1 = 0$$ (2.3)

Equation (2.3) shows the relationship between h_1, h_2 and r. As solving the cubic equation above is rather complicated, the value of h_2 can be obtained by solving the equation using a Turbo C programme for any given value of h_1 and r. The source code of the programme is shown in **Appendix D** of this thesis. Table 2.1 summarises the calculated values of h_2 at different radiuses, r where h_1 is kept at 7 µm which is the photoresist thickness we normally used.

Table 2.1   Heights of the partial spherical micro-structures with various radii calculated using Turbo C programming.

Height of cylindrical structure, h_1 (µm)	Radii (µm)	Height of spherical structure, h_2 (µm)
7	5	7.7628
7	25	12.8645
7	50	13.6601

It is observed that the height of the spherical micro-structure, h_2, is larger than the cylindrical micro-structure, h_1. It is noted that the variation of height of the partial spherical structure is relatively large for r from 5 to 50 μm. In this range, the percentage in height difference is about 43 %. However, the variation of height when r is 25 and 50 μm for the partial spherical structure is very small, which is only about 6 % in difference.

By using the photoresist reflow method to fabricate micro-lenses in substrate such as diamond, the photoresist micro-spherical structure (lens structure) is transferred into the substrate by dry etching. By using Equation (2.3) and measuring the etch selectivity between the photoresist and the substrate, the height of the micro-lenses in the substrate can be estimated. From the lens height and radius, the focal length of the micro-lenses can be easily calculated. The detailed calculation is described in the following section.

2.2.2 Derivation of Focal Length for a Micro-lens [1-4]

All the micro-lenses fabricated in this work can be treated as a thin lens as the lens height is quite small compared to the surface diameter. In fact, the ratio of the height to the diameter of the diamond lenses fabricated in this work is from 0.01 to 0.03.

Gaussian formula for refraction at a single spherical surface is given by [1-4]:

$$\frac{n_1}{p} + \frac{n_2}{q} = \frac{n_2 - n_1}{R} \qquad (2.4)$$

where n_1 and n_2 are the refractive index at medium 1 and 2, respectively. R is the radius of curvature for the refraction spherical surface. p and q are the object and image distances of the ray, respectively.

Figure 2.2(a) shows the relationship between the height, h, surface radius, r, and radius of curvature, R, of a thin lens with a single spherical surface. The letter "c" denotes the centre of the spherical surface which is called optical centre below.
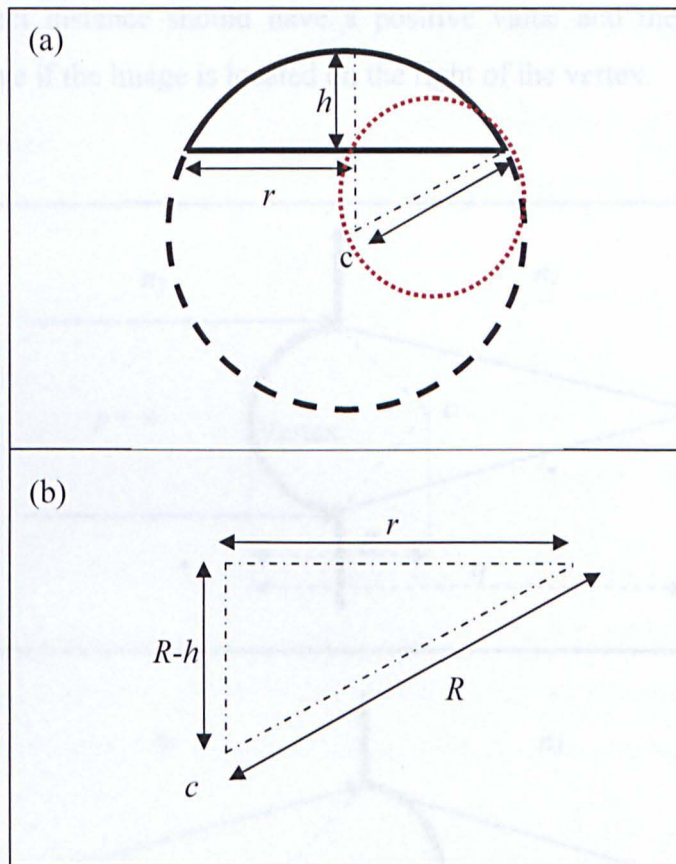
Figure 2.2 **(a) Schematic diagram of a lens with a single spherical surface (upper section of the circle with solid line) with height, *h*, and surface radius, *r*. (b) A magnified part of the red circled area.**

The relationship between these parameters can be established by using Pythagoras Theorem, as shown in Figure 2.2(b),

$$(R - h)^2 = R^2 - r^2$$

$$R = \frac{r^2 + h^2}{2h}$$

(2.5)

Figure 2.3 shows a ray passing from medium 1 to medium 2 and at the interface, there is a spherical surface (lens). The sign convention for a spherical refracting surface is given in Table 2.2 where the ray is entering from the left of the spherical surface lens. The relationship between the lens' focal length, object and image distances can only be established when the sign convention is followed. Based on this sigh convention, if the ray emits from an object is incident from the left of the

vertex, the object distance should have a positive value and the image distance should be positive if the image is located on the right of the vertex.
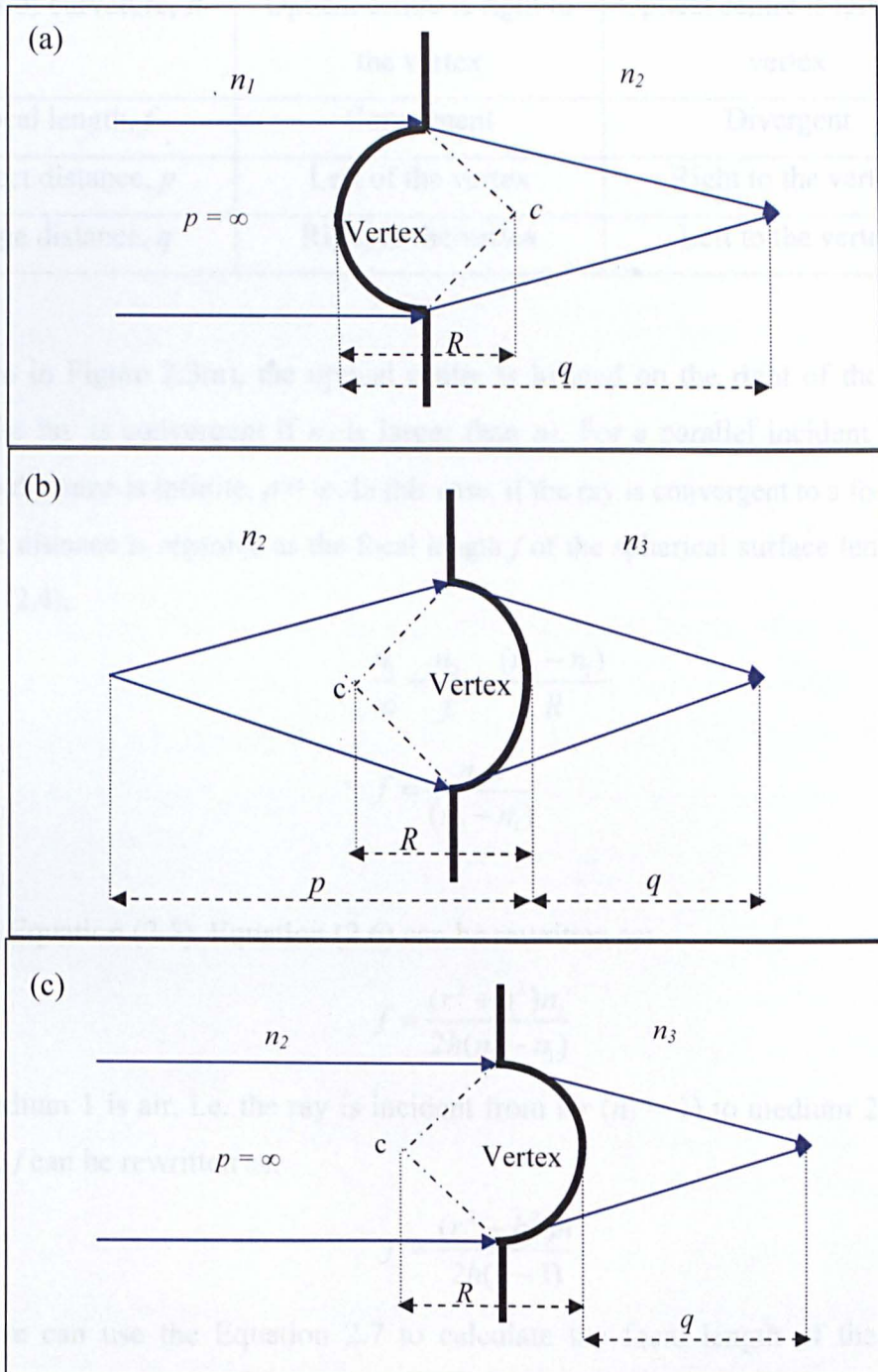
Figure 2.3 **(a) A parallel ray passes through a convex lens from medium 1 to medium 2; (b) A ray that that has been focused in the medium 2 diverged and refocused into medium 3 and (c) a parallel ray passes from medium 2 to medium 3.**

Table 2.2   Sign convention for a spherical refracting surface [1]. The ray is incident from the left of the surface lens.

Parameters	Sign of "+"	Sign of "-"
Radius of curvature, R	Optical centre is right to the vertex	Optical centre is left to the vertex
Focal length, f	Convergent	Divergent
Object distance, p	Left of the vertex	Right to the vertex
Image distance, q	Right to the vertex	Left to the vertex

As shown in Figure 2.3(a), the optical centre is located on the right of the vertex. Hence, the ray is convergent if n_2 is larger than n_1. For a parallel incident ray, the objective distance is infinite, $p = \infty$. In this case, if the ray is convergent to a focal point, the image distance is regarded as the focal length f of the spherical surface lens. Using Equation (2.4),

$$\frac{n_1}{\infty} + \frac{n_2}{f} = \frac{(n_2 - n_1)}{R}$$

$$f = \frac{n_2 R}{(n_2 - n_1)} \tag{2.6}$$

By using Equation (2.5), Equation (2.6) can be rewritten as:

$$f = \frac{(r^2 + h^2)n_2}{2h(n_2 - n_1)}$$

If the medium 1 is air, i.e. the ray is incident from air ($n_1 = 1$) to medium 2 such as diamond, f can be rewritten as:

$$f = \frac{(r^2 + h^2)n}{2h(n - 1)} \tag{2.7}$$

Hence, we can use the Equation 2.7 to calculate the focal length of the surface spherical lens made on medium 2 from air.

In this project, we have fabricated diamond complex lenses which consist of two surface spherical lenses made on both sides of a diamond substrate. In this case, the image formed inside the substrate (medium 2) by the first surface lens can be

considered as an object for the second surface lens and re-imaged by the second surface lens as shown in Figure 2.3(b). For an object with a finite object distance, the second image distance can be calculated by applying Equation (2.4) and (2.5) as follows:

$$\frac{n_2}{p} + \frac{n_3}{q} = \frac{(n_3 - n_2)}{-R}$$

$$q = \frac{(r^2 + h^2)pn_3}{2hp(n_2 - n_3) - (r^2 + h^2)n_2}$$

Normally, this second image is formed in the air, i.e. $n_3 = 1$. Hence, if $n_2 = n$, q can be rewritten as:

$$q = \frac{(r^2 + h^2)p}{2hp(n - 1) - (r^2 + h^2)n} \tag{2.8}$$

Equation (2.4) can also be used to calculate the focal length of a freestanding plano-convex lens. In this case, the first plano-surface does not refract a parallel beam and the object distance p should be ∞ as shown in Figure 2.3(c). By using Equation (2.4), the focal length f of the plano-convex lens can be calculated as:

$$\frac{n_2}{\infty} + \frac{n_3}{f} = \frac{(n_3 - n_2)}{-R}$$

$$f = \frac{n_3 R}{(n_2 - n_3)} \tag{2.9}$$

Again, using Equation (2.5), Equation (2.9) can be rewritten as

$$f = \frac{(r^2 + h^2)n_3}{2h(n_2 - n_3)}$$

Here, the n_2 is the refractive index of the lens material and n_3 is 1 (refractive index of air). Thus the f can be simplified as:

$$f = \frac{(r^2 + h^2)}{2h(n_2 - 1)} \tag{2.10}$$

In this work, various types of diamond micro-lenses have been fabricated. The focal length of these micro-lenses can be estimated by using Equations (2.7) and (2.10).

2.2.3 Circle Equation for Fitting the Profile of a Micro-lens

In this work, Atomic Force Microscopy (AFM) has been employed for extracting the surface profile of the diamond micro-lenses. The measured cross sectional surface profile is fitted by a curvature of a circle. The equation of a circle is given as:

$$(y-a)^2 + (x-b)^2 = R^2 \tag{2.11}$$

where R is the radius of curvature, a and b are the y and x coordinates of the circle centre. Figure 2.4 shows a cross-section of a spherical lens. The surface radius and height of this lens are r and h, respectively. By assuming the left edge of the micro-lens as an origin point with the coordinate of (0, 0), the coordinate of the right edge of the micro-lens is thus (2r, 0). The coordinate of the centre of the circle is (r, h-R) and thus $a = h\text{-}R$ and $b = r$.
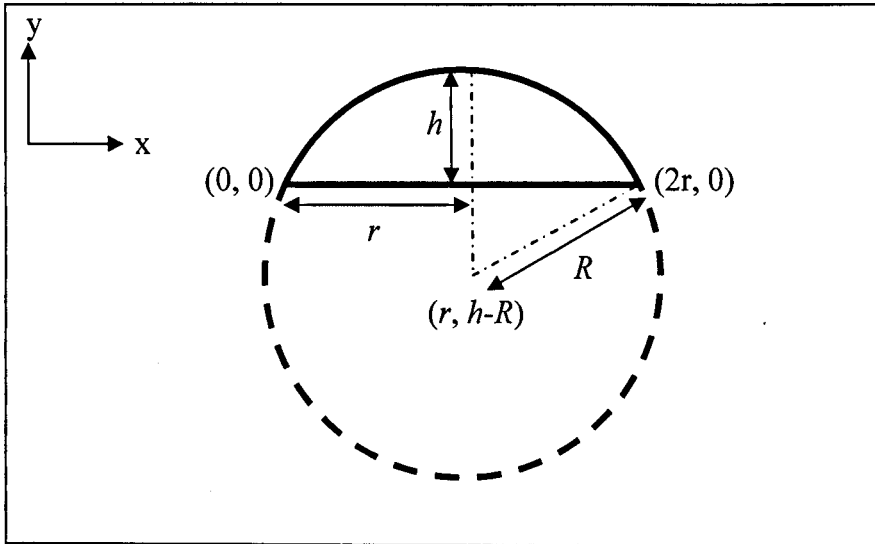
Figure 2.4   A two dimensional micro-lens (upper section of the circle with solid line).

By using Equation (2.5) and Equation (2.11),

$$(y-h+\left[\frac{r^2+h^2}{2h}\right])^2 + (x-r)^2 = \left[\frac{r^2+h^2}{2h}\right]^2$$

$$y = \sqrt{\left[\frac{r^2+h^2}{2h}\right]^2 - (x-r)^2} - \left[\frac{r^2+h^2}{2h} - h\right] \tag{2.12}$$

Hence, Equation (2.12), which contains h and r of a micro-lens, is used to plot a circle with h and r as variables so as to fit with the measured surface profile of a micro-lens.

2.2.4 Optical Reflection Gratings

A repetitive array of diffracting elements, either apertures or obstacles, that has the effect of producing periodic alterations in the phase, amplitude, or both of an emergent wave is said to be a diffraction grating. Reflection and transmission gratings are two well-known optical gratings. In this work, diamond reflection gratings have been successfully fabricated and characterised. The principle of a reflection grating is reviewed briefly in this section and the experimental results of the diamond gratings are shown in **Chapter 6**.

Figure 2.5 is the schematic diagram showing the incident and reflected rays at a reflection grating. In the diagram, a represents the grating period, θ_i and θ_m are the incident and reflected angles, respectively. From this diagram, the difference of the optical path between the two reflected rays separated with a grating period is given by:

$$AB - CD = a(\sin\theta_m - \sin\theta_i)$$

When the difference of the optical path satisfies the condition,

$$m\lambda = a(\sin\theta_m - \sin\theta_i) \qquad (2.13)$$

where m is an integer and λ is the wavelength, the mth order reflection maximum is obtained.
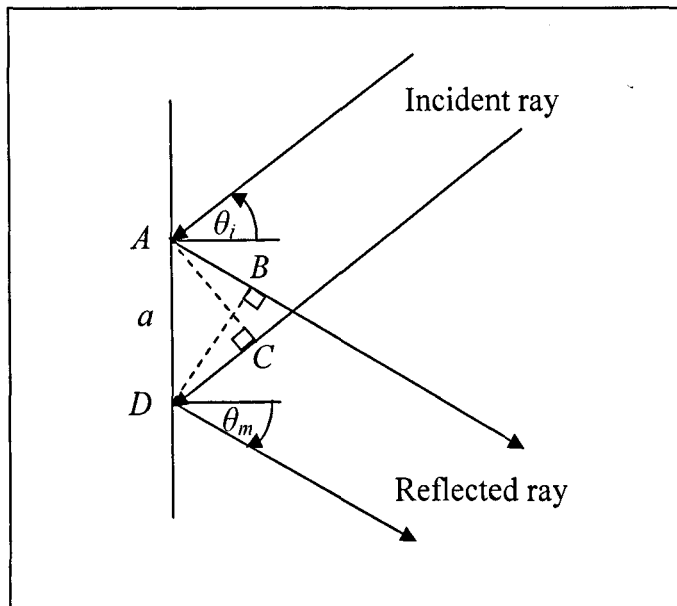
Figure 2.5   Incident and Reflected rays at a reflection grating.

2.2.5   Gaussian Laser Beam (Derivation of Fundamental Mode Size)

VECSEL with diamond heat spreader directly mirror coated on its outer surface to serve as laser cavity has been developed in this work due to the high thermal conductivity of diamond. To ensure stable fundamental mode operation and excellent heat dissipation, diamond micro-lensed μ-VECSEL having a highly compact plano-concave resonator is preferable so that the fundamental mode size is only determined by the physical characteristics of the cold cavity [1-2]. The device was then pumped with laser beam through the heat spreader in order to examine the cavity properties.

In order to obtain a high quality output laser beam, the condition of mode-matching has to be met. Mode matching occurs when the spot size of the pumping beam matches the fundamental mode size in the active region. The calculation of the laser fundamental mode size is therefore an important parameter in the device design. In this section, the physics of the Gaussian beam propagation is presented in order to determine the fundamental mode size, as described in **Chapter 5**.

Gaussian laser beam is a beam of electromagnetic radiation whose transverse electric field and intensity distributions are described by Gaussian function. The Gaussian

beam propagates in the z direction [1]. The fundamental mode is close to a pure Gaussian and its size can be inferred from the rules of Gaussian Optics. On the other hand, the transverse mode of the laser beam can be approximated by Hermite-Gaussian polynomials.

In general, there will be a minimum cross section or beam waist radius, ω_o, between the mirrors of a laser resonator. The characteristics of the propagation of the laser beam in the z direction can be expressed using ω_o and the radius of curvature of the wavefront comprising the beam, $R(z)$, as shown in Figure 2.6.
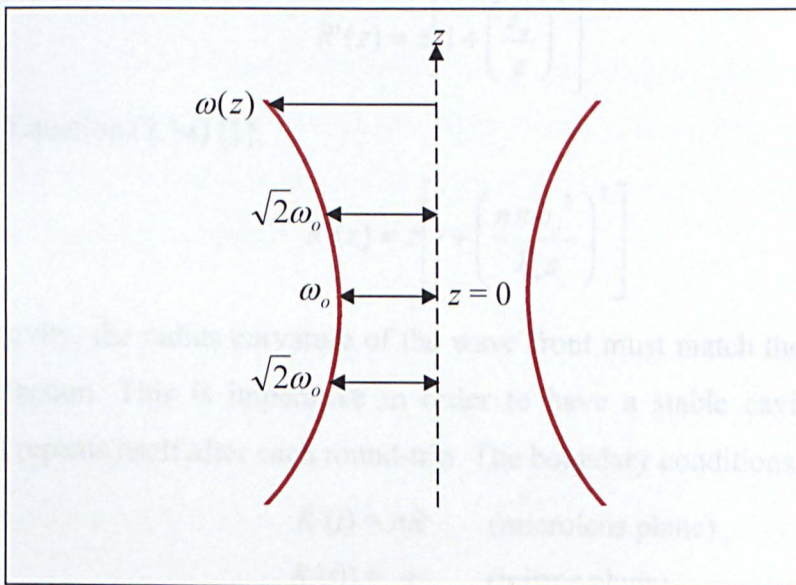
Figure 2.6   A Gaussian beam propagates in the z-axis.

A more complex analysis of electromagnetic waves in the cavity, setting $z = 0$ at the beam waist, yields the beam waist radius (or the half-width) at any location z:

$$\omega(z) = \omega_o \sqrt{1 + \left(\frac{z}{z_o}\right)^2}$$

A practical way to measure the divergence of the beam is the distance over which its cross sectional area doubles. This occurs when the value of z for $\omega(z) = \sqrt{2}\omega_o$. This special distance is called Rayleigh range [1], z_o, where

$$z_o = \frac{n\pi\omega_o^2}{\lambda_o} \tag{2.14}$$

Hence, $\omega(z)$ can be re-written as [1]:

$$\omega(z) = \omega_o \sqrt{1 + \left(\frac{\lambda_o z}{n\pi\omega_o^{\,2}}\right)^2}$$

(2.15)

where λ_o is the wavelength of the laser in vacuum and n is the refractive index. The shape of the beam as specified by Equation (2.15) is a hyperbola of revolution about the z-axis. The smaller the beam waist (or cross section area), the smaller the Rayleigh range and hence the faster the beam diverges.

The radius of curvature of the wavefront comprising the beam can be expressed by:

$$R'(z) = z\left[1 + \left(\frac{z_o}{z}\right)^2\right]$$

By employing Equation (2.14) [1],

$$R'(z) = z\left[1 + \left(\frac{n\pi\omega_o^{\,2}}{\lambda_o z}\right)^2\right]$$

(2.16)

For any laser cavity, the radius curvature of the wave front must match those of the mirrors on reflection. This is imperative in order to have a stable cavity mode, i.e. a mode that repeats itself after each round-trip. The boundary conditions are:

$$R'(t) = nR \qquad \text{(microlens plane)} \qquad (2.17)$$
$$R'(0) = \infty \qquad \text{(mirror plane)}$$

In this case, R is the radius of curvature of the micro-lens. **Section 5.3.2** clearly shows the design of the micro-VECSEL, a semiconductor chip integrated with micro-lens. Using Equation (2.16) and (2.17),

$$nR = t\left[1 + \left(\frac{n\pi\omega_o^{\,2}}{\lambda_o t}\right)^2\right]$$

$$\omega_o = \left[\frac{t\lambda_o}{n\pi}\sqrt{\frac{nR}{t} - 1}\right]^{\frac{1}{2}}$$

(2.18)

Equation (2.18) is the fundamental mode size of the Gaussian beam in the laser cavity of the micro-lensed μ-VECSEL device.

2.3 Diamond Micro-electronics-Metal-Semiconductor Contact and Circular Transmission Line Method (CTLM)

It is imperative that a semiconductor device can be connected to the outside world with no adverse change to its current-voltage characteristics and no additional voltage drop. This can be accomplished only through low-resistance ohmic contacts on the semiconductor. An ideal ohmic contact is the one, when combined with the semiconductor, its carrier flow does not encounter any barrier under positive or negative bias. In principle, this ideal case occurs when the work-functions of the semiconductor and the contact metal are about the same, and there are no appreciable interface states which tend to pin the Fermi Level. In practice, this ideal case is not easily achievable as the work-function of the semiconductor varies with doping concentration. For a wide band gap semiconductor such as p-doped diamond, there is an added difficulty because it is almost impossible to find a metal that has a large enough work-function. Hence, it is not an easy task to achieve a good ohmic contact between p-doped diamond and metal.

In order to provide some understanding on ohmic contacts, basic physics of metal-semiconductor contact is briefly discussed in this section. In addition, the basic principle of contact measurement method based on the circular transmission line method (CTLM) and used to estimate the specific contact resistance ρ_c in this work is introduced.

2.3.1 Metal to p-type Semiconductor Contact

When a metal and a semiconductor with different work-functions are brought into contact at thermal equilibrium, their Fermi levels are forced to align [5-6]. The energy band diagrams for the metal to a p-type semiconductor [5-6] are shown in Figure 2.7. The ohmic or rectifying characteristics of the contact depends upon the work-functions of the metal ($q\varphi_m$) and the semiconductor ($q\varphi_s$). E_c, E_v and E_{Fs} as shown in Figure 2.7 are conduction band, valence band and surface Fermi level of the semiconductor, respectively.

(a) p-type, $q\varphi_m < q\varphi_s$ (rectifying)

(b) p-type, $q\varphi_m > q\varphi_s$ (ohmic)
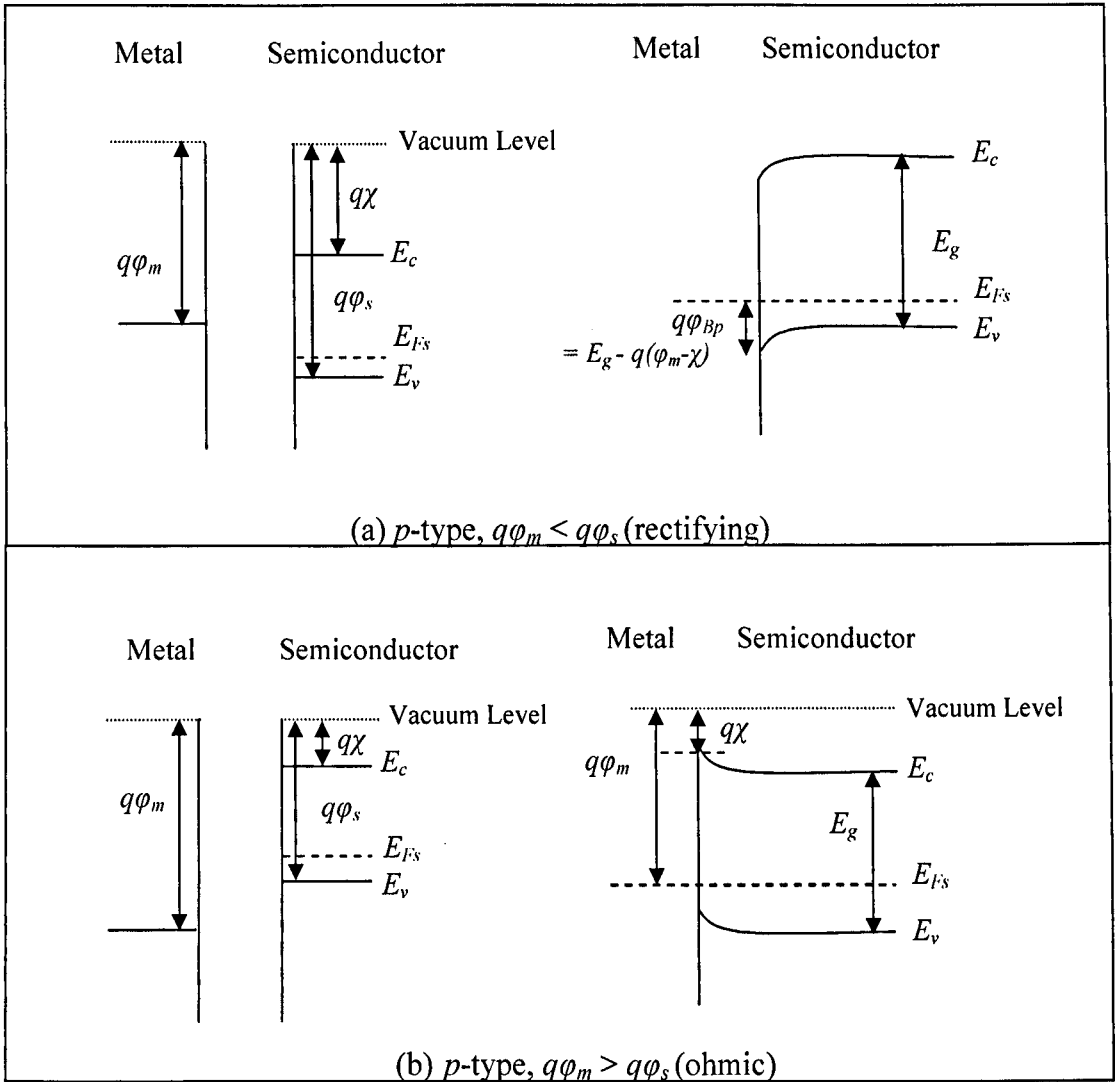
Figure 2.7   Energy band diagrams of metal to p-type semiconductor contacts.

With reference to Figure 2.7, it can be observed in Figure 2.7(a) that the energy band in the p-type semiconductor bends downward and hence causes hole depletion near the surface of the semiconductor while an accumulation layer is formed in Figure 2.7(b) due to the upward energy band bending in the semiconductor which causes hole accumulation. This indicates that for a metal/p-type semiconductor contact, if $q\varphi_m > q\varphi_s$, the contact is ohmic and the contact becomes rectifying when $q\varphi_m < q\varphi_s$. According to the Schottky-Mott model [5-6], there is a Schottky barrier in the rectifying contact. On the other hand, Schottky barrier cannot be seen in the energy band diagram if the metal-semiconductor contact is in ohmic contact.

The height ($q\varphi_{Bp}$) of the Schottky barrier for a p-type semiconductor which is an energy level relatived to the Fermi level, as indicated in Figure 2.7 (a), is given by [6]:

$$q\varphi_{Bp} = E_g - q(\varphi_m - \chi) \qquad (2.19)$$

where $q\chi$ is electron affinity of the semiconductor, E_g is the semiconductor band gap and $q\varphi_{Bp}$ is the Schottky barrier height of the rectifying contact.

Several other interfacial phenomena also affect contact resistance including surface states present at the semiconductor surface, causing the barrier height to be less sensitive of the metal work function ($q\varphi_m$). An explanation of this weak dependence on $q\varphi_m$ was described by Bardeen [7].

As shown in Figure 2.8, the Fermi level is 'pinned' by the high density of surface states, and is given by:

$$q\varphi_{Bp} = q\varphi_o \quad (p\text{-type semiconductor}) \qquad (2.20)$$

where $q\varphi_o$ = Neutral energy level and $q\varphi_{Bp}$ = barrier height.

The meaning of $q\varphi_o$ is explained with reference to Figure 2.8. Native oxide usually appears on semiconductor materials. Assuming a continuous distribution of surface states at the interface between the semiconductor and the metal, a series of energy levels are formed on the surface. Among these, the energy level which coincides with the Fermi level when forming the metal-semiconductor is called the neutral energy level $q\varphi_o$. This neutral energy $q\varphi_o$ specifies the energy level below which all surface states are filled for charge neutrality at the surface [7].

The higher the density of surface states is, the lesser is the deviation of $q\varphi_o$ from E_{FS}. As a result, the barrier height, $q\varphi_{Bp}$, is given by Equation (2.20). It is seen that it is determined by the property of the semiconductor surface and is independent of the work-function of the metal.
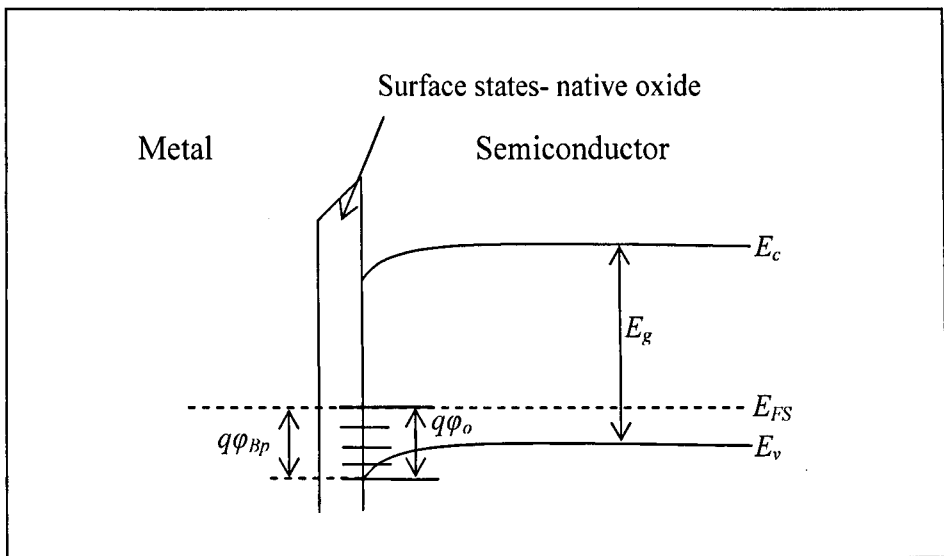
Figure 2.8   Metal to *p*-type semiconductor contacts with surface states.

From the above mentioned two models, the Schottky-Mott model and the Bardeen model, the Schottky-Mott model is not suitable for metal/*p*-doped diamond (oxygen-terminated surface) contact as the Fermi level is strongly pinned at the diamond surface [8], presumably due to the covalent nature of the diamond which tends to offer a high density of surface states [8]. Nevertheless, Schottky-Mott model may provide some useful guide on the choice of the metal system for the *p*-type semiconductors including diamond. On the other hand, Bardeen model may be suitable for the metal/*p*-doped diamond contacts. In this case, to form ohmic contacts on oxygen-terminated diamond surface, metals with higher work function are not necessary Consequently, Ti with a work function of 4.33 eV [9-10] has been chosen in this work. Although the work function of Ti is not very high, by high temperature annealing, a carbide compound known as TiC can be formed on the Ti/diamond interface which can lower the specific contact resistance by either reducing the depletion width or lower the barrier height, and thus enhancing the tunnelling process [10]. In this work, Ti based contacts on *p*-type diamond were investigated and used for developing diamond FET devices.

It is also important to note that the current conduction across a metal/semiconductor contact can be due to thermionic emission and tunnelling (field emission), depending on the doping concentration of semiconductor.

For metal/semiconductor contact, a useful characteristic energy E_{00} is defined as [6]:

$$E_{00} = 0.5(q\hbar)\sqrt{\frac{N_D}{m^*\varepsilon_s}} \qquad (2.21)$$

where q is electronic charge; $\hbar$ is Planck's constant; N_D is doping level of the semiconductor; m^* is hole tunnelling effective mass (0.81 m_o for diamond [11]); and ε_s is permittivity of semiconductor (5.7 ε_o for diamond [12]).

For $E_{00} >> kT$, field emission is the dominant current transportation mechanism through the metal/semiconductor interface. Therefore, one can infer from Equation (2.21) that, for a constant temperature, a highly doped semiconductor material is essential to form an ohmic contact. The doping levels in all the diamond samples used in this project are high, i.e. $\sim 10^{20}$ cm^{-3}. According to Equation (2.21), the characteristic energy, E_{00} has been calculated to be more than kT. Hence, the field emission should be considered.

2.3.2 Specific Contact Resistance

For a contact between two dissimilar materials, such as metal and semiconductor, there exists a total contact resistance, R_c. The magnitude of R_c is determined by the contact geometry and area. Thus, this total contact resistance, R_c is not a suitable parameter to characterise the contact. The parameter that is independent on the geometry of the contact is known as the specific contact resistance, ρ_c. It is defined as the contact resistance of a unit area of the thin interfacial layer normally between a metal contact and a semiconductor substrate (Figure 2.9), as given by [9],

$$\rho_c = \left[\frac{\partial V}{\partial J}\right]_{V=0} \left[\Omega.cm^2\right] \qquad (2.22)$$

where J = Current density through the interface; and V = Potential drop across the interface.
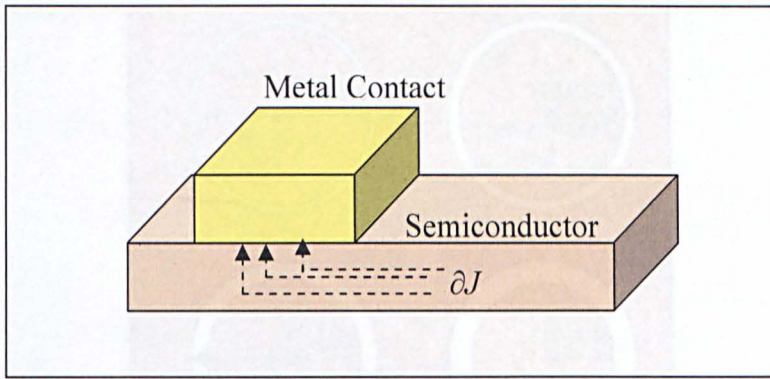
Figure 2.9   Physical layout of a metal/semiconductor contact.

As the specific contact resistance ρ_c cannot be measured directly, several approaches [13-14] have been used to model the current-voltage behaviour of a contact and to extract ρ_c from the measured current (I) and voltage (V) characteristics. One of the approaches is circular transmission line method (CTLM) and the basic principle of CTLM will be presented in the following section.

2.3.3   Circular Transmission Line Method (CTLM)

2.3.3.1   Contact Geometry

The test pattern of either circular (Figure 2.10) or rectangular (Figure 2.11) geometry is commonly used to determine the contact behaviour and specific contact resistance in semiconductor devices [13]. A mesa structure is needed for the rectangular test pattern [13] so as to eliminate the current flow from the edges of the pads as shown in Figure 2.10. For circular test patterns, such complication can be totally avoided as there is no unwanted current flow pattern and hence the specific contact resistance can be measured with high accuracy. Thus, the circular test pattern, as shown in Figure 2.10, has been chosen in this work.
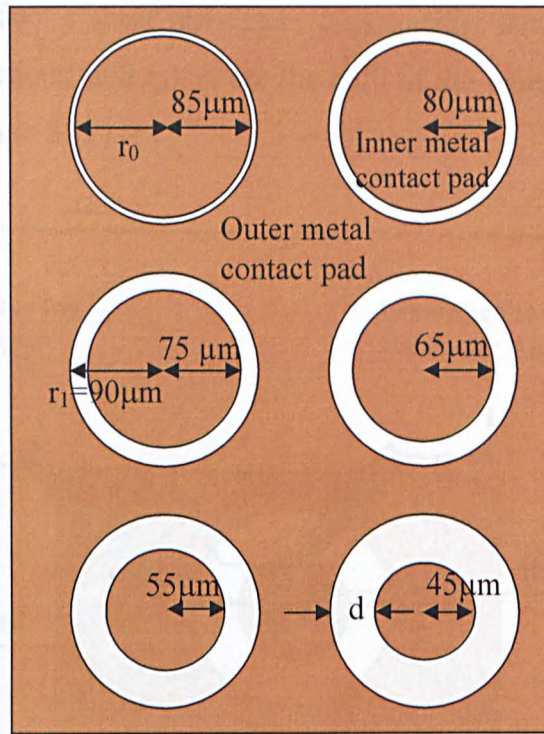
Figure 2.10 A CTLM pattern. r_o and r_1 are the radii of the inner and outer circular contacts; and d is the spacing between r_o and r_1.
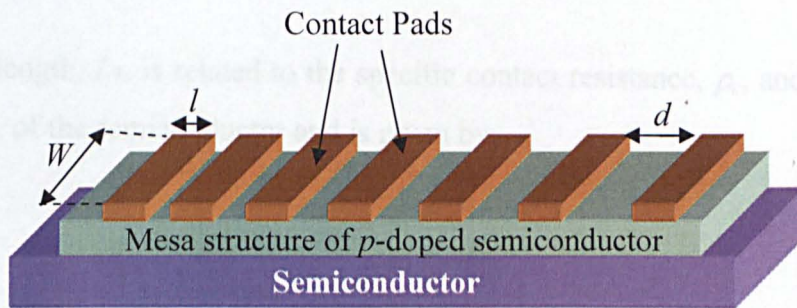
Figure 2.11 Rectangular pattern where W is the width, l is the length of the pads and d is the contact pad separation.

2.3.3.2 Derivation of Specific Contact Resistance

The experimental setup for measuring the specific contact resistance by using the CTLM method is shown in Figure 2.12. By connecting to a Precision Parameter Analyser, a constant current (i_o) flows through the inner and outer circular contact pads. The voltage drop, ΔV, across the two pads is given by [13]:

$$\Delta V = \frac{i_o R_s}{2\pi}[\ln\left(\frac{r_1}{r_o}\right) + \frac{L_T}{r_o}\frac{I_o(r_o/L_T)}{I_1(r_o/L_T)} + \frac{L_T K_o(r_1/L_T)}{r_1 K_1(r_1/L_T)}] \qquad (2.23)$$

where R_s is semiconductor sheet resistance; L_T is transfer length; I_o, I_1, K_o, K_1 are modified Bessel Functions; and r_o, r_1 are the radii of the inner circular contact and the outer contact (Figure 2.12).
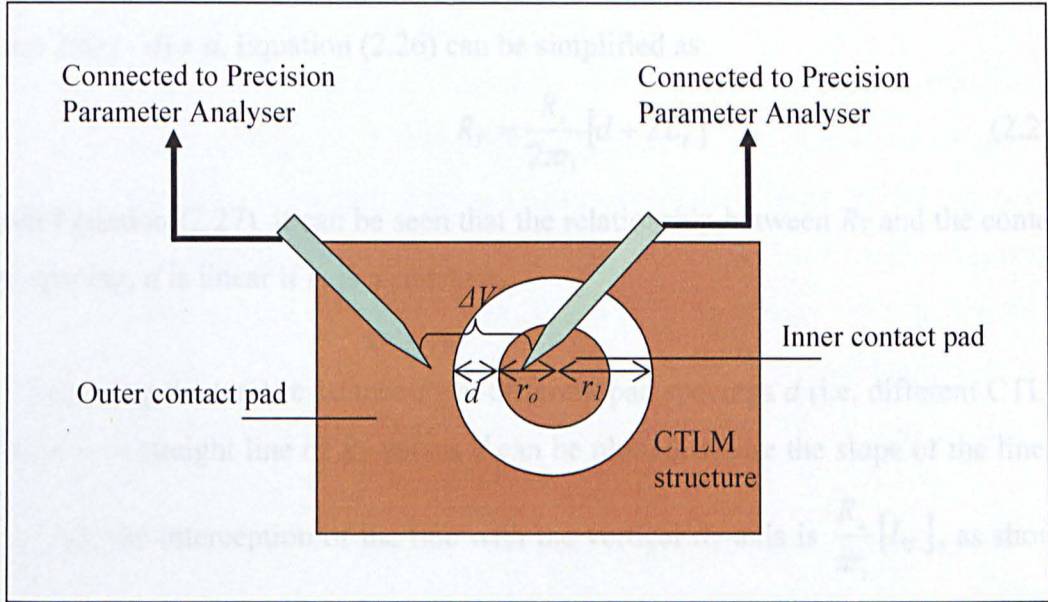
Figure 2.12   Experimental setup for measuring specific contact resistance.

The transfer length, L_T, is related to the specific contact resistance, ρ_c, and the sheet resistance, R_s, of the semiconductor and is given by:

$$L_T = \sqrt{\left(\frac{\rho_c}{R_s}\right)} \qquad (2.24)$$

In the cases where r_o and r_1 are greater than L_T by at least a factor of 4, both I_o/I_1 and K_o/K_1 approximate to unity [13]. Thus, considering the $d = r_1 - r_o$, Equation (2.23) becomes:

$$\Delta V = \frac{i_o R_s}{2\pi}\left[\ln\left(\frac{r_1}{r_1 - d}\right) + L_T\left(\frac{1}{r_1} + \frac{1}{r_1 - d}\right)\right] \qquad (2.25)$$

The total resistance (R_T) between the contacts is defined as the ratio of the voltage (ΔV) and the current (i_o):

$$R_T = \frac{\Delta V}{i_o}$$

Thus

$$R_T = \frac{R_s}{2\pi}\left[\ln\left(\frac{r_1}{r_1-d}\right)+L_T\left(\frac{1}{r_1}+\frac{1}{r_1-d}\right)\right]$$ (2.26)

Since $2\pi(r_1 - d) \gg d$, Equation (2.26) can be simplified as:

$$R_T = \frac{R_s}{2\pi r_1}\left[d+2L_T\right]$$ (2.27)

From Equation (2.27), it can be seen that the relationship between R_T and the contact pad spacing, d is linear if r_1 is a constant.

By measuring the total resistance R_T at different pad spacings d (i.e. different CTLM patterns), a straight line of R_T versus d can be plotted, where the slope of the line is $\frac{R_s}{2\pi r_1}$ and the interception of the line with the vertical R_T-axis is $\frac{R_s}{\pi r_1}[L_T]$, as shown in Figure 2.13. Thus, the values of the transfer length L_T and sheet resistance R_s can be obtained as shown below:

$$L_T = \text{interception}/(2 \text{ x slope})$$ (2.28)

$$R_s = (\text{slope}) \text{ x } 2\pi r_1$$ (2.29)
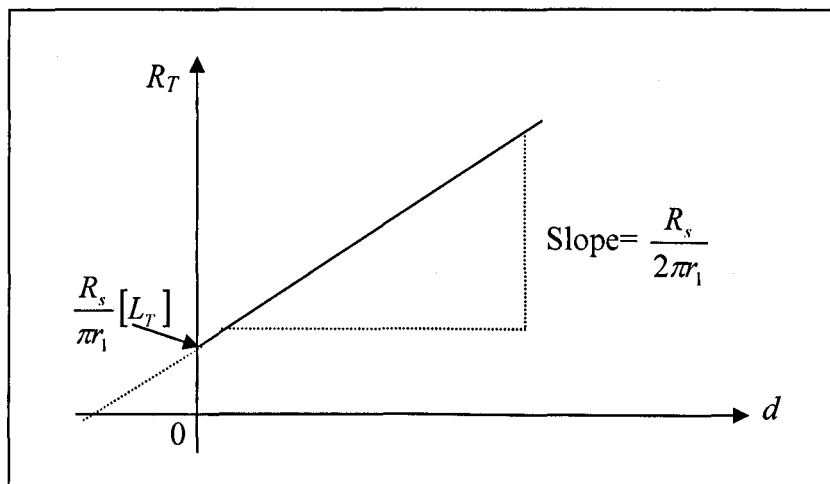
Figure 2.13   The linear relationship of R_T versus d can be used to deduce the specific contact resistance ρ_c.

Using Equation (2.24), Equation (2.28) and Equation (2.29), the value of specific contact resistance, ρ_c, can then be obtained:

$$\rho_c = (L_T)^2 \times R_s \qquad (2.30)$$

2.4   Micro-electronics - Field Effect Transistors

The main function of a Field Effect Transistor (FET) is to act as a digital switch. The FET is used extensively in digital circuit applications and due to its small size, millions of devices can be fabricated in a single integrated circuit. a FET device has three terminals: source, drain and gate. In normal use, the load current flows between source and drain and this current is controlled by the gate voltage which generates an electrical field in the gate area. The name of field effect transistors refers to such current control by the electrical field.

The FET family can be divided into three major groups. There are Junction Field Effect Transistor (JFET), Metal Semiconductor Field Effect Transistor (MESFET) and Metal Insulator Semiconductor Field Effect Transistor (MISFET). Metal Oxide Semiconductor Field Effect Transistor (MOSFET) can be categorised in the family of MISFET. The gate used in MOSFET is normally silicon dioxide (SiO_2). However, the insulator used in MISFET may not necessarily be silicon dioxide. In this work, diamond MISFET and MOSFET with gate materials of intrinsic diamond and SiO_2, respectively, have been successfully fabricated. The physics principles are basically the same for both MISFET and MOSFET devices. We describe the operation principle of MOSFET devices in the following section.

2.4.1   MOSFET-Basic Principle and Operation

As the diamond MISFET or MOSFET devices fabricated in this work are based on p-doped diamond, only p-MOSFET will be discussed in this section. A simplified structure of a p-channel MOSFET is shown in Figure 2.14. In such devices, the current is created by the flow of holes in the channel. The device is thus called the p-channel MOSFET. It can be seen From Figure 2.14, that two p-type regions called the drain and source areas are located on either side of the gate oxide. The region under the gate oxide is referred to as the channel region. The channel length and

channel width of this device are labelled as L and W, respectively, as shown in Figure 2.14. Normally, a channel length greater than approximately 2 μm is considered to be a long channel device [15].
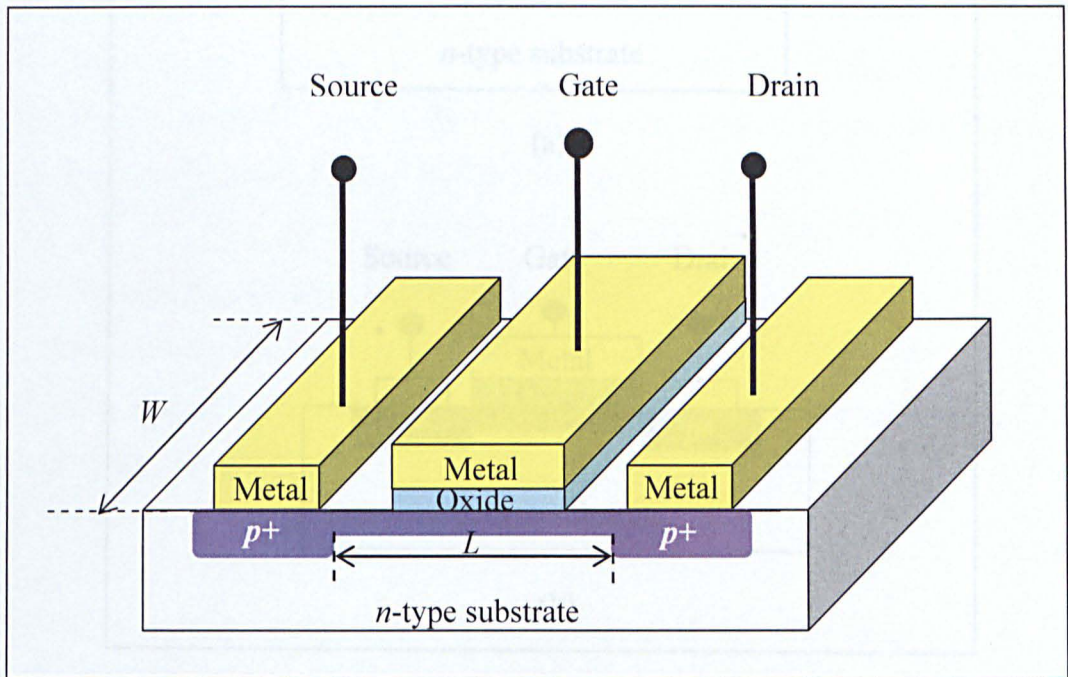
Figure 2.14   Basic structure of a *p*-channel MOSFET (*p*-MOS).

In MOSFET, there are two operation modes, namely enhancement mode and depletion mode. Figure 2.15(a) and 2.15(b) show a *p*-channel enhancement mode MOSFET and a *p*-channel depletion mode MOSFET, respectively. In a *p*-channel enhancement mode device, a negative gate voltage must be applied so as to create an inversion layer of holes under the gate which will "connect" the *p*-type source and drain regions. The inversion layer is actually a layer of holes which is normally referred to as the channel region. This inversion layer is induced by the strong vertical electric field due to the negative voltage applied.

Source   Gate   Drain

Metal
Oxide

$p+$ $p+$

n-type substrate

(a)

Source   Gate   Drain

Metal
Oxide

$p+$ $p+$

n-type substrate

(b)
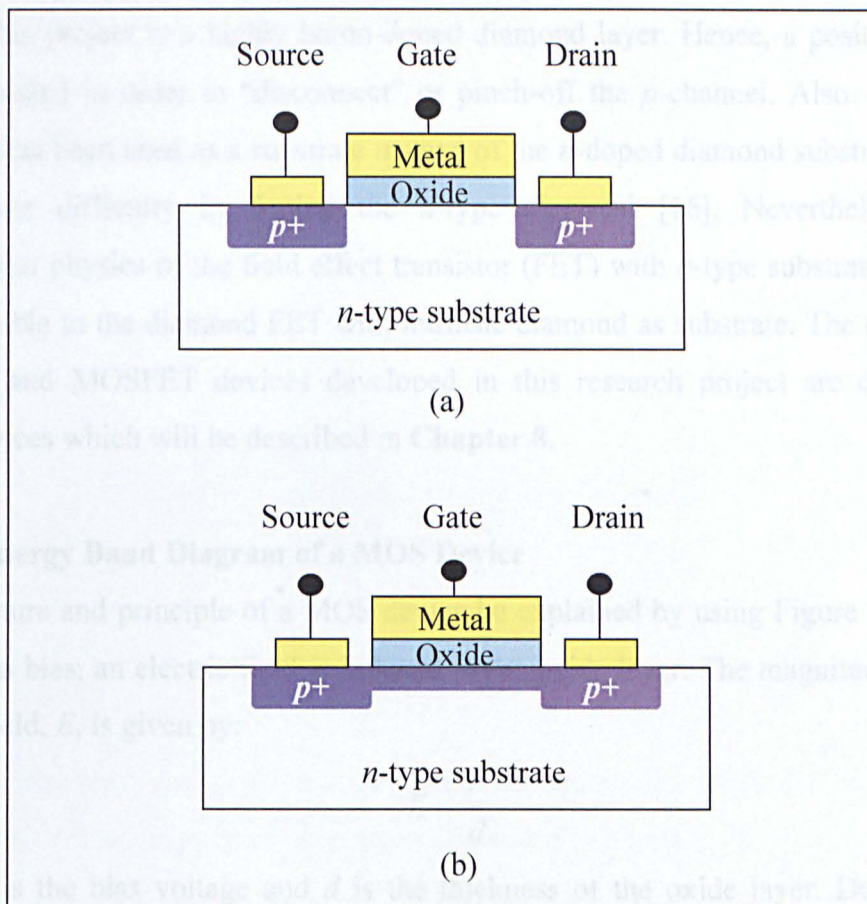
Figure 2.15   Cross section for a *p*-channel (a) enhancement-mode MOSFET and (b) depletion mode MOSFET.

When the source-to-drain voltage, V_{SD}, is applied, holes flow from the source through the channel to the drain terminal. The polarity of V_{SD} is always opposite to V_{DS}. The same case is applied to V_{SG} and V_{GS}. Hence, the drain current, I_D, is generated. Under the same V_{DS}, the strength of this I_D current depends on the amount of carriers (holes) in the channel region and thus in turn, I_D is a function of the vertical electric field in the channel region. Due to this reason, the term *field effect* is used for a *field effect* transistor in which the current is controlled by an electric field perpendicular to the flow of charges.

On the other hand, a *p*-channel region exists in a depletion mode MOSFET device even with zero gate voltage. This is due to the presence of a *p*-doped layer under the gate terminal which is normally created via ion implantation process. In this work, depletion mode MOSFET and MISFET devices have been developed. The *p*-channel

used in this project is a highly boron-doped diamond layer. Hence, a positive gate bias is needed in order to "disconnect" or pinch-off the p-channel. Also, intrinsic diamond has been used as a substrate instead of the n-doped diamond substrate. It is due to the difficulty in doping the n-type diamond [16]. Nevertheless, the fundamental physics of the field effect transistor (FET) with n-type substrate should be applicable to the diamond FET with intrinsic diamond as substrate. The diamond MISFET and MOSFET devices developed in this research project are depletion mode devices which will be described in **Chapter 8**.

2.4.2   Energy Band Diagram of a MOS Device

The structure and principle of a MOS device be explained by using Figure 2.16. By applying a bias, an electric field is induced in the oxide layer. The magnitude of the electric field, E, is given by:

$$E = \frac{V}{d} \tag{2.31}$$

where V is the bias voltage and d is the thickness of the oxide layer. Due to the applied bias, the negative charges are distributed at the metal-oxide interface, which attracts the opposite sign charges-holes in the p-type semiconductor. As a result, holes accumulate at the oxide-semiconductor junction.
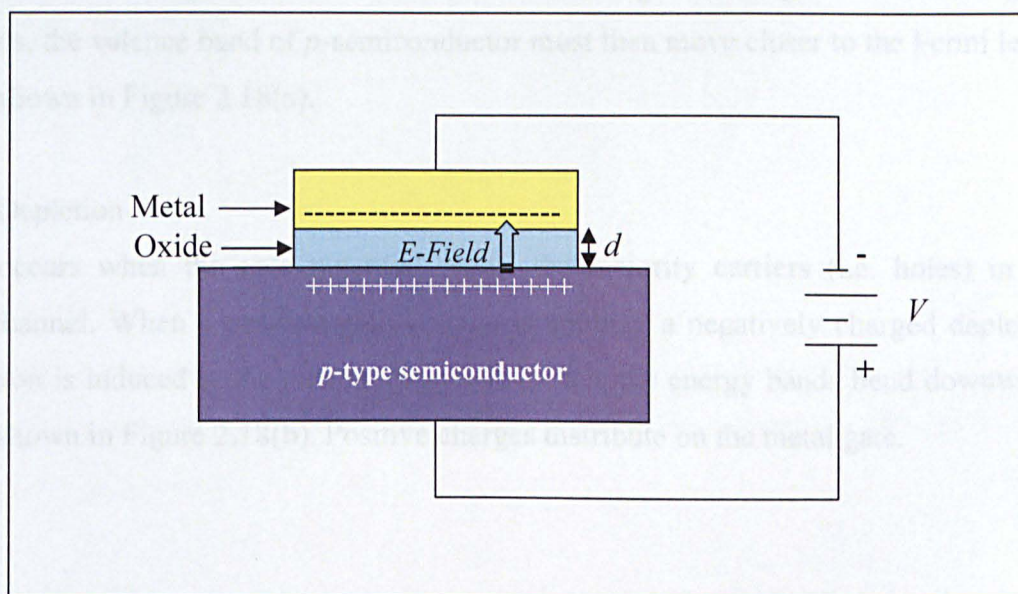
Figure 2.16   A MOS structure with steady-state accumulation layers of holes adjacent to the semiconductor-oxide interface with negative bias.

When a p-MOSFET is connected to the ground, $V_G = 0$, there is no net charge in the semiconductor. All energy bands are flat, as shown in Figure 2.17.

Oxide p-type semiconductor

E_c

E_{Fi}

E_{FM} ——— $V_G = 0$ E_{FS}

E_v
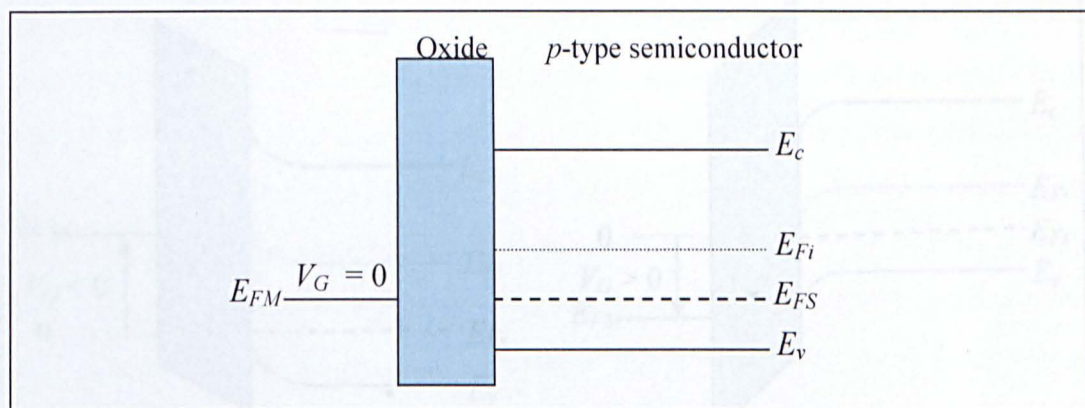
Figure 2.17   Energy band diagram with zero gate voltage applied.

There are four bias conditions in a p-channel depletion mode MOSFET that lead to the changes of the energy band diagram as illustrated in Figure 2.18.

a) Accumulation

This occurs when the gate potential attracts the majority carriers (i.e. holes) in the p-channel. When a negative gate bias is applied, there will be an accumulation layer of holes forms adjacent to the oxide surface and negative charges on the metal gate. Thus, the valence band of p-semiconductor must then move closer to the Fermi level, as shown in Figure 2.18(a).

b) Depletion

It occurs when the gate potential repels the majority carriers (i.e. holes) in the p-channel. When a positive gate voltage is applied, a negatively charged depletion region is induced in the p-semiconductor. Hence, the energy bands bend downward, as shown in Figure 2.18(b). Positive charges distribute on the metal gate.

oxide   p-semiconductor

oxide   p-semiconductor

E_c

E_{Fi}
E_{Fs}
E_v

E_{FM}

$V_G < 0$

0

E_c

E_{Fi}

E_{Fs}

E_v

0
$V_G > 0$
E_{FM}

(a)

(b)

oxide   p-semiconductor

oxide   p-semiconductor

negative
charges

E_c

E_{Fi}
E_{Fs}
E_v

0

$V_G = V_T$
E_{FM}

more
negative
charges

E_c

E_{Fi}
E_{Fs}
E_v

0
$V_G > V_T$
E_{FM}

(c)

(d)
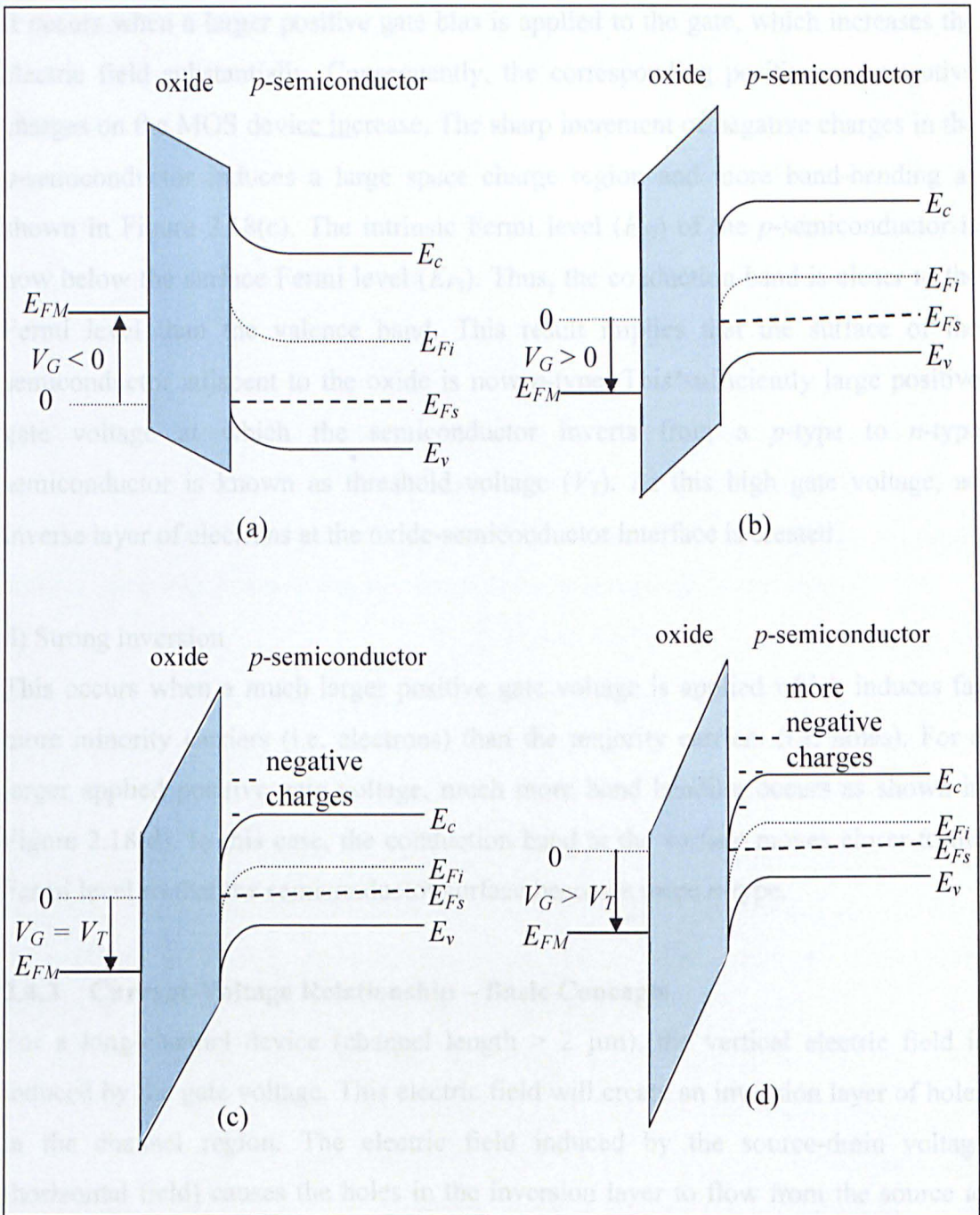
Figure 2.18   Energy band in the *p*-type semiconductor for (a) $V_G < 0$ (accumulation), (b) $V_G > 0$ (depletion), (c) $V_G = V_T$ (inversion) and (d) $V_G > V_T$ (strong inversion).

c) Inversion

It occurs when a larger positive gate bias is applied to the gate, which increases the electric field substantially. Consequently, the corresponding positive and negative charges on the MOS device increase. The sharp increment of negative charges in the p-semiconductor induces a large space charge region and more band-bending as shown in Figure 2.18(c). The intrinsic Fermi level (E_{Fi}) of the p-semiconductor is now below the surface Fermi level (E_{Fs}). Thus, the conduction band is closer to the Fermi level than the valence band. This result implies that the surface of the semiconductor adjacent to the oxide is now n-type. This sufficiently large positive gate voltage at which the semiconductor inverts from a p-type to n-type semiconductor is known as threshold voltage (V_T). At this high gate voltage, an inverse layer of electrons at the oxide-semiconductor interface is created.

d) Strong inversion

This occurs when a much larger positive gate voltage is applied which induces far more minority carriers (i.e. electrons) than the majority carriers (i.e. holes). For a larger applied positive gate voltage, much more band bending occurs as shown in Figure 2.18(d). In this case, the conduction band at the surface moves closer to the Fermi level so that the semiconductor surface becomes more n-type.

2.4.3 Current-Voltage Relationship – Basic Concepts

For a long-channel device (channel length > 2 μm), the vertical electric field is induced by the gate voltage. This electric field will create an inversion layer of holes in the channel region. The electric field induced by the source-drain voltage (horizontal field) causes the holes in the inversion layer to flow from the source to the drain. In a long channel device, both electric fields are independent of the charges in the channel while both of the electric fields become dependent on the charge in a short channel device.

Figure 2.19(a) shows a basic p-MOSFET structure for the case when $V_{GS} < V_T$ and the applied V_{SD} voltage is small. The thickness of the inversion channel layer in Figure 2.19(b) quantitatively represents the relative charge density, which is

essentially constant along the entire channel length. The corresponding I_D versus V_{DS} curve is shown in the figure as well.

When V_{SD} increases, there is a voltage drop across the channel near the drain terminal as illustrated in Figure 2.19(b). Hence, the induced inversion charge density near the drain terminal decreases, as illustrated in Figure 2.19(b). So, the conductance of the channel decreases, resulting in a decrease of the slope of the I_D versus V_{DS} curve.

When V_{SD} increases to the point $V_{SD}(sat)$ where the voltage drop at the drain terminal is equal to V_T, the induced inversion charge density is zero at the drain terminal. This effect is schematically shown in Figure 2.19(c). At this point, the conductance at the drain is zero, which means that the slope of the I_D versus V_{DS} is zero. Hence,

$$V_{SD}(sat) = V_{SG} + V_T \qquad (2.32)$$

Thus, $V_{SD}(sat)$ is the source-to-drain voltage which produces a zero inversion charge density at the drain terminal.

When V_{SD} becomes larger than the $V_{SD}(sat)$, the point of zero inversion charge density in the channel moves toward the source terminal. In this case, holes enter the channel from the source, travelling through the channel toward the drain. At the point where the induced inversion charge density goes to zero, the holes are injected into the space charge region where they are swept by the electric field to the drain terminal. If the change in the channel length (ΔL) is small compared to the original length, L, then the drain current will be constant for $V_{SD} > V_{SD}(sat)$. When this occurs, the region of the I_D versus V_{DS} characteristics is referred to as the saturation or pinch-off region, as shown in Figure 2.19(d).
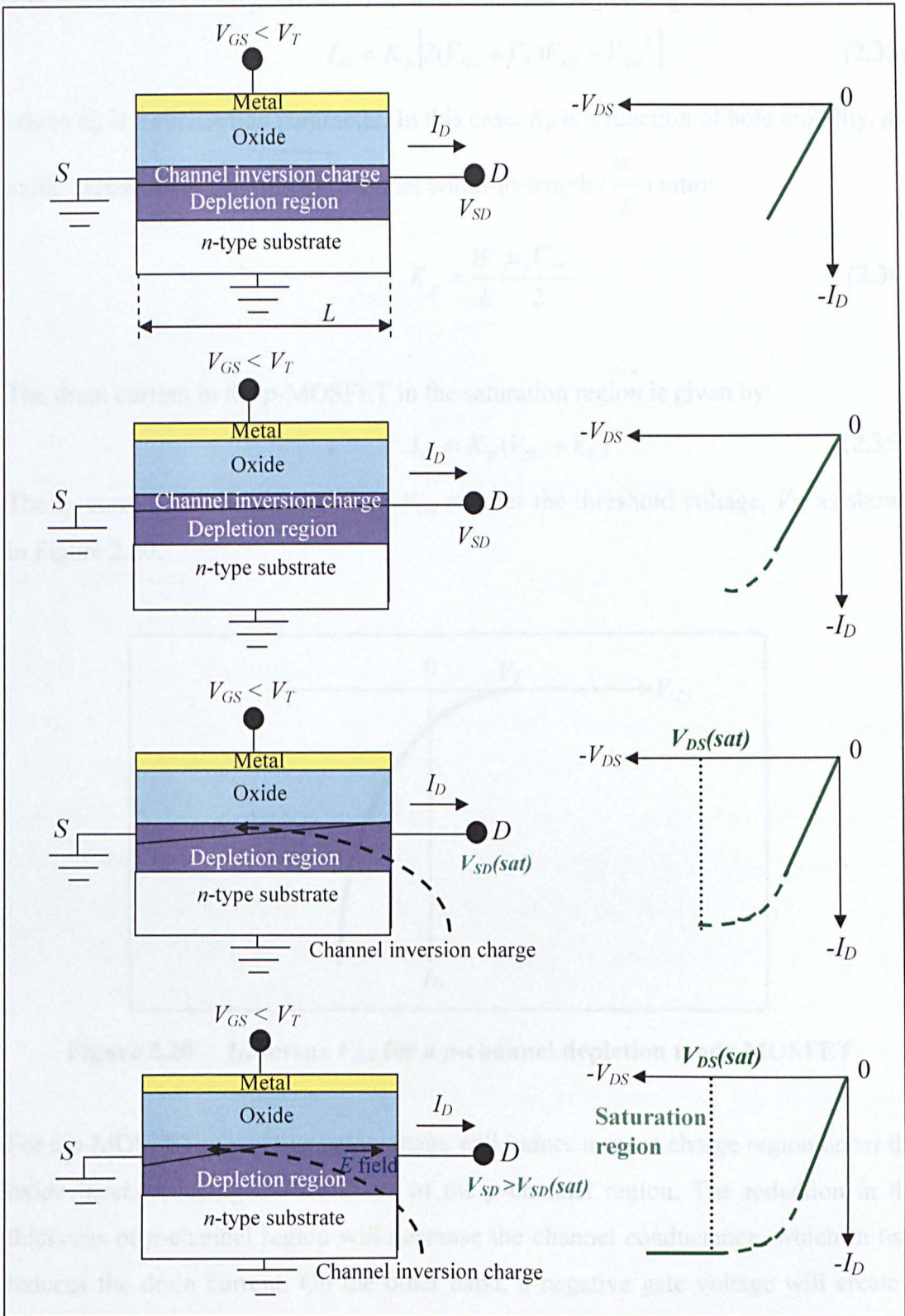
Figure 2.19 *p*-MOSFET structure and I_D versus V_{DS} for (a) a small V_{SD} value, (b) a larger V_{SD} and (c) $V_{SD} = V_{SD}(sat)$ and (d) $V_{SD} > V_{SD}(sat)$.

The drain current for a p-MOSFET in non-saturation region is given by:

$$I_D = K_p \left[2(V_{SG} + V_T)V_{SD} - V_{SD}^2 \right]$$ (2.33)

where K_p is a conduction parameter. In this case, K_p is a function of hole mobility, μ_p, oxide capacitance, C_{ox}, and the channel width-to-length ($\frac{W}{L}$) ratio:

$$K_p = \frac{W}{L} \frac{\mu_p C_{ox}}{2}$$ (2.34)

The drain current in the p-MOSFET in the saturation region is given by:

$$I_D = K_p (V_{SG} + V_T)^2$$ (2.35)

The I_D current will be cut off when V_{GS} reaches the threshold voltage, V_T, as shown in Figure 2.20.
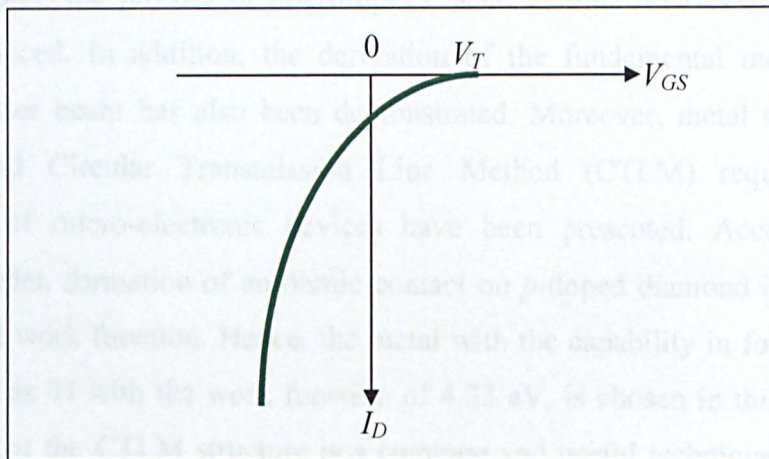
Figure 2.20 I_D versus V_{GS} for a p-channel depletion mode MOSFET.

For a p-MOSFET, a positive gate voltage will induce a space charge region under the oxide layer, reducing the thickness of the p-channel region. The reduction in the thickness of p-channel region will decrease the channel conductance, which in turn reduces the drain current. On the other hand, a negative gate voltage will create a hole accumulation layer, which increases the drain current. Typical current-voltage curves for a p-MOSFET with different gate voltages are shown in Figure 2.21. It can be seen that the I_D is higher when the gate bias is more negative.
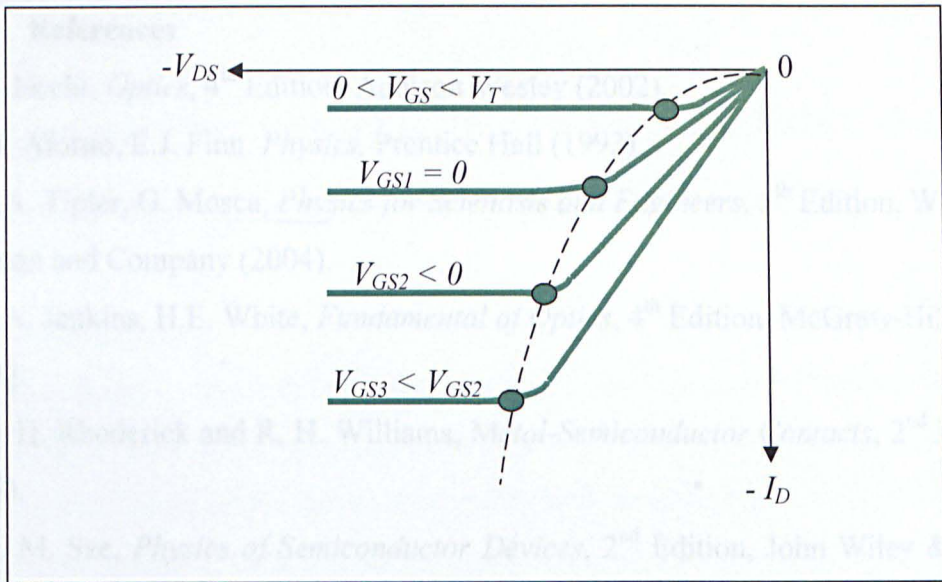
Figure 2.21 I_D versus V_{DS} curve for a *p*-channel depletion mode MOSFET.

2.5   Summary

In this chapter, the physics of micro-optics, such as micro-lenses and grating has been introduced. In addition, the derivation of the fundamental mode size of a Gaussian laser beam has also been demonstrated. Moreover, metal semiconductor contacts and Circular Transmission Line Method (CTLM) required for the fabrication of micro-electronic devices have been presented. According to the Bardeen model, formation of an ohmic contact on *p*-doped diamond is independent of the metal work function. Hence, the metal with the capability in forming carbide easily, such as Ti with the work function of 4.33 eV, is chosen in this work. It has been seen that the CTLM structure is a common and useful technique to determine the specific contact resistance, ρ_c, as it is simple and easy to use. Finally, the fundamental physics of the MOSFET such as the basic operation, the energy band diagram of a MOS structure and the current-voltage relationship of a *p*-type MOSFET have been shown.

2.6 References

[1] E. Hecht, *Optics*, 4th Edition, Addison Wesley (2002).

[2] M. Alonso, E.J. Finn, *Physics,* Prentice Hall (1992).

[3] P.A. Tipler, G. Mosca, *Physics for Scientists and Engineers*, 5th Edition, W.H. Freeman and Company (2004).

[4] F.A. Jenkins, H.E. White, *Fundamental of Optics*, 4th Edition, McGraw-Hill (1976).

[5] E. H. Rhoderick and R. H. Williams, *Metal-Semiconductor Contacts*, 2nd Edition (1988).

[6] S. M. Sze, *Physics of Semiconductor Devices*, 2nd Edition, John Wiley & Sons, (1981).

[7] J. Bardeen, *Phys. Rev.*, **71**, 717 (1947).

[8] L.S. Pan, D.R. Kania, *Diamond: Electronic Properties and Applications*, Springer (1994).

[9] J. Singh, *Semiconductor Devices: An Introduction*, McGraw-Hill (1994).

[10] T. Tachibana, B.E. Williams, J.T. Glass, *Phys. Rev. B*, **45**, 11968 (1992).

[11] S.H. Gamal, T.S. Al-Harbi, *Microelectron. J.*, **32**, 327 (2001).

[12] G. Davies, *Properties and Growth of Diamond*, IEEE INSPEC (1994).

[13] G. S. Marlow, M. B. Das, *Sol. State Electronics*, **25** (2) 91-94 (1982).

[14] C. J. Bernard, Ph.D. Thesis, Auburn University (1992).

[15] D. Neamen, *An Introduction to Semiconductor Devices*, McGraw-Hill (2006).

[16] R. Kalish, *J. Phys. D: Appl. Phys.*, **40**, 6467 (2007).

Chapter 3

General Photolithographic Processes for Fabricating Diamond Micro-optics and Micro-electronics

3.1   Introduction

In this chapter, the fabrication techniques developed for making diamond micro-optics and micro-electronic devices are described. In this work, various types of diamond micro-optics have been fabricated including positive (or convex), negative (or concave) spherical micro-lenses, micro-cylindrical and micro-ring lenses, complex positive micro-lenses and gratings. Except for the negative micro-lenses and diamond gratings, the procedures for fabricating the above-mentioned micro-optics are relatively similar. The negative micro-lenses were fabricated by adopting a hot-embossing method and a hard mask (e.g. SiO_2) technique was used to fabricate the diamond gratings. The fabrication of diamond micro-electronic devices, such as Metal Oxide Semiconductor Field Effect Transistor (MOSFET), involves the ohmic contact formation in addition to the device structure fabrication. The common processes used in each fabrication step will be described in **Sections 3.2-3.10**, so as to provide a clear picture of the fabrication procedure.

3.2   Surface Cleaning

Prior to photoresist application, the diamond surface should be cleaned with acetone to remove the organic contaminants, followed by methanol to remove the residue of acetone, as acetone is not dissolvable in water. The sample is then rinsed with DI water and subsequently dried. Cleaning steps are required because of the inevitable contamination which occurs during storage and handling between processing steps. Contaminants may consist of atomic, ionic, or polymer layers, which are sometimes very difficult to detect. Such films can cause gross resist adhesion failure during development or etching processes. Thorough cleaning method using piranha solution (a combination of sulphuric acid (H_2SO_4) and hydrogen peroxide (H_2O_2) with H_2SO_4: $H_2O_2 = 4:1$) to remove any organic contaminant on diamond has also been adopted following the acetone and methanol cleaning. A combination of H_2SO_4 with a strong

oxidising agent such as potassium nitrate (KNO_3) or H_2O_2 can lead to a change in the termination of the diamond surface, in this case, to oxygen-terminated surface [1].

3.3 Silicon dioxide (SiO_2) Deposition

A layer of SiO_2 was deposited using Plasma Enhanced Chemical Vapour Deposition (PECVD) on the diamond substrate. This layer served as an insulator for MOSFET fabrication. The recipe used is given as follows. The flow rate of silane and nitrous oxide was set as 170 and 710 sccm, respectively. The RF power and temperature used are 70 W and 300 °C, respectively. The deposition rate is about 0.45 nm/s.

3.4 Photolithography [2-3]

In microelectronics, the word "lithography" is commonly used to describe a process in which a pattern is delineated in a layer of material sensitive to photons, electrons or ions. In this project, optical lithography or photolithography is used. The overall procedure of the photolithography is summarised in Figure 3.1 and will be described in subsequent sections.

```
┌─────────────────────────────────────┐
│        Dehydration of sample         │
└─────────────────────────────────────┘
                  ↓
┌─────────────────────────────────────┐
│     Apply adhesion promoter (HMDS)   │
└─────────────────────────────────────┘
                  ↓
┌─────────────────────────────────────┐
│      Spin (at 4000 rpm for 30 s)     │
└─────────────────────────────────────┘
                  ↓
┌─────────────────────────────────────┐
│   Apply photoresist (SPR 220 or S1818)│
└─────────────────────────────────────┘
                  ↓
┌─────────────────────────────────────┐
│      Spin (at 4000 rpm for 30 s)     │
└─────────────────────────────────────┘
                  ↓
┌─────────────────────────────────────┐
│   Soft-Bake PR (at 90 or 110°C for 1 min)│
└─────────────────────────────────────┘
                  ↓
┌─────────────────────────────────────┐
│  Expose PR to UV (250 mW for 30s or 8s )│
└─────────────────────────────────────┘
                  ↓
┌─────────────────────────────────────┐
│  Develop PR in Microposit Developer (30 s)│
└─────────────────────────────────────┘
                  ↓
┌─────────────────────────────────────┐
│      Hard-Bake (at 125°C for 2 mins) │
└─────────────────────────────────────┘
```
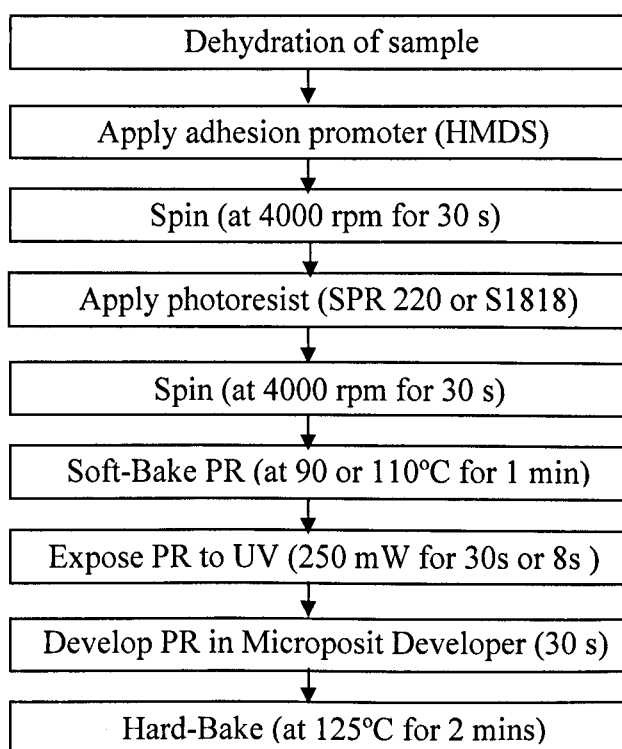
Figure 3.1   Process steps of photolithography.

3.4.1 Photoresist

Photoresists are organic compounds whose solubility changes when exposed to ultraviolet light. The regions in the photoresist that are exposed to light become either more soluble or less soluble in a solvent called developer. When the exposed regions become more soluble, a positive image of the mask is defined in the photoresist, and the compound is called positive resist (PR). Two photoresists were used in this research, i.e. SPR 220 and S1818.

3.4.2 Photoresist Application

Dehydration of the diamond substrate prior to photoresist coating is necessary to ensure a hydrophobic sample surface for good resist adhesion. Dehydration bake is achieved by heating the sample at about 120°C for 15 minutes to evaporate the moisture from the surface and also volatile residual organic contaminants. It is also important that the substrate be coated with resist immediately after surface preparation to avoid re-adsorption of water on the substrate.

Adhesion promoters are used for good adhesion to the substrate. The most common adhesion promoter is hexamethyldisilazane (HMDS). HMDS is coated onto the sample before it is spun at 4000 rpm for 30 s. After a minute, the photoresist is dispensed onto the sample, which is then accelerated up to a constant rotational speed for 30 seconds. In this case, SPR 220 is used and the photoresist thickness is about 7 μm if the spinner is set to 4000 rotational per minute (rpm). SPR 220 photoresist is a thick photoresist and hence it is normally employed in the micro-optics fabrication. However, thin photoresist such as S1818 is used if the metal lift-off process is required. The thickness of this photoresist is about 1.8 μm for the spin speed of 4000 rpm. The S1818 photoresist is therefore being used for micro-electronic fabrication.

3.4.3 Photoresist Soft-Bake

After photoresist coating, the diamond substrate is given a pre-expose bake (known as soft bake) to remove the resist solvent and increase the resist adhesion. This also causes the resist thickness to decrease and its surface to become less

susceptible to particulate contamination. Pre-expose or soft-bake for SPR 220 photoresist is performed at 90 °C for 1.5 minutes but at 110 °C for 1 minute for S1818 photoresist.

3.4.4 Photoresist Exposure

To make a photoresist pattern, the diamond substrate is placed in a Karl Suss MA 6 Mask Aligner and is brought into contact with a photo mask. The mask and substrate are then exposed to the UV light (power 250 mW, wavelength of 365 nm) in the mask aligner with an optimised exposure time for different photoresists. The exposure times used for SPR 220 and S1818 photoresists are 30 seconds and 8 seconds respectively.

3.4.5 Photoresist Development

Development is a critical step in photoresist processing and plays a key role in defining the resist profile and controlling the line-width. In this work, a Microposit developing solution is used. The photoresist developing depends on the exposure time and the power of the lamp. For this experiment, the developing time for both SPR 220 and S1818 are 30 seconds using diluted (dilute ratio of 1:1) Microposit developer.

3.4.6 Photoresist Hard-bake

After development, the sample is put through a hard-bake process. The purpose of hard-bake is to drive out the remaining solvents in the photoresist, strengthen the photoresist, and most importantly to improve the photoresist etching resistance. Hard-bake could also improve the adhesion of photoresist to the diamond substrate due to further thermal dehydration. The hard-bake time and temperature for micro-lenses fabrication were set to 2 minutes and 120°C, respectively. On the other hand, the fabrication of micro-electronic devices which employing the S1818 photoresist requires the hardbake temperature of 115 °C for 1 minute. Both hard-bake time and temperature must be carefully controlled since under-baking may cause high photoresist etch rate and affects its adhesion on the sample whereas over-baking can cause bad resolution.

3.4.7 Photoresist Reflow Process

Photoresist reflow method is a technique to form spherical micro-lenses. The basic principle requires exposing and developing photoresist to leave small pedestals. Once the pedestals have been formed, the photoresist temperature is raised above its glass transition temperature (T_g) [4]. Above this temperature, the photoresist becomes liquid, flows and the final form taken is determined by the surface adhesive forces and surface tension of the photoresist [4]. To form micro-spherical lens in our work, a 7 μm thick layer of Shipley SPR220 photoresist was first spin-coated onto the diamond substrate. After mask patterning, the photoresist pillars were formed. The substrate was then placed on a hotplate at 125°C for 2 minutes to allow the photoresist pillars to re-flow. Due to the surface tension, spherical lens structures were formed. These lens structures were then transferred onto the diamond substrate by ICP etching using Ar/Cl$_2$ plasma.

3.5 ICP Etching

3.5.1 ICP Plasma [2-3]

Plasma processes are widely used in semiconductor processing. Plasma is defined as an ionised gas with equal numbers of positive and negative charges. More precisely, plasma is a quasi-neutral gas of charged and neutral particles that exhibits collective behaviour. The plasma source used in this experiment is an Inductively Coupled Plasma (ICP). Plasma processes could be used for pattern etching or causing etch-induced damage. Pattern etch will selectively remove materials from the designated areas and transfers the pattern from photoresist or hard mask to the substrate films.

3.5.2 Chemical, Physical and Reactive Ion Etches [3]

Basically, there are three types of etch processes: pure chemical etch, pure physical etch, and something in between called reactive ion etch (RIE). For pure chemical etch, there is no physical bombardment. Materials are removed solely by chemical reaction. The etch rate of the pure chemical etch could be very high or very slow, depending on the process. It is usually used for strip processes. In pure physical etch, the material is physically dislodged from the surface by the energetic ions. The etch rate for the pure physical etch is normally slow. Reactive ion etch is also called *ion*

assistance etch, since the ions in this etch process are not necessarily reactive. Reactive species in most etch processes are neutral free radicals, which normally have higher concentrations than the ions in the semiconductor etch processing plasmas. The reason is that the activation energy for ionisation is normally significantly higher than the activation energy for dissociation, and the species concentration is exponentially related to the activation energy.

3.5.3   Etch Process [3]

In the plasma etch process, a STS (Surface Technology Systems) ICP etching tool is used. It consists of two chambers, a load-lock chamber and a process chamber and two RF powers, ICP paten and coil powers. The chuck temperature could be altered by changing the electronic heat controller. The sample is held onto a silicon tray before loading into a load-lock chamber. The silicon tray is transferred into the process chamber after the load-lock chamber has been pumped down to 80 mTorr. The etchants (Ar and Cl_2 or Ar and O_2) are introduced to the vacuum process chamber. After pressure is stabilised, RF power is used to strike a glow discharge plasma. Some of the etch molecules dissociate in the plasma from the impact of collisions with electrons, which generates free radicals. The free radicals then diffuse across the boundary layer to reach the sample surface, and are adsorbed on the surface. With the help of the ion bombardment, these free radicals react with the surface atoms or molecules quickly and form gaseous byproducts. The volatile byproducts desorb from the surface, diffuse across the boundary layer, get into the convection flow, and are pumped out from the chamber.

3.5.4   ICP Platen and Coil Powers [5-6]

The ICP reactor has two major power sources, platen and coil powers. A schematic diagram of ICP is illustrated in Figure 3.2. In ICP etch tool, platen and coil powers are important parameters to control the etch characteristics. The energetic ion bombardment breaks the chemical bonds between the atoms on the diamond surface. The ICP platen power controls the ion energies while ICP coil power controls the ion densities. An increase in ICP platen power will lead to an increase in the DC bias and ion bombardment. Consequently, there will be an increase in the etch rate. An

increase in ICP coil power will lead to an increase in ion density and hence leads to an increase of etch rate. Therefore, variation in the ICP coil power will affect the plasma density and thus affecting the concentration of the reactive species that are responsible for the chemical component of the etching mechanism.
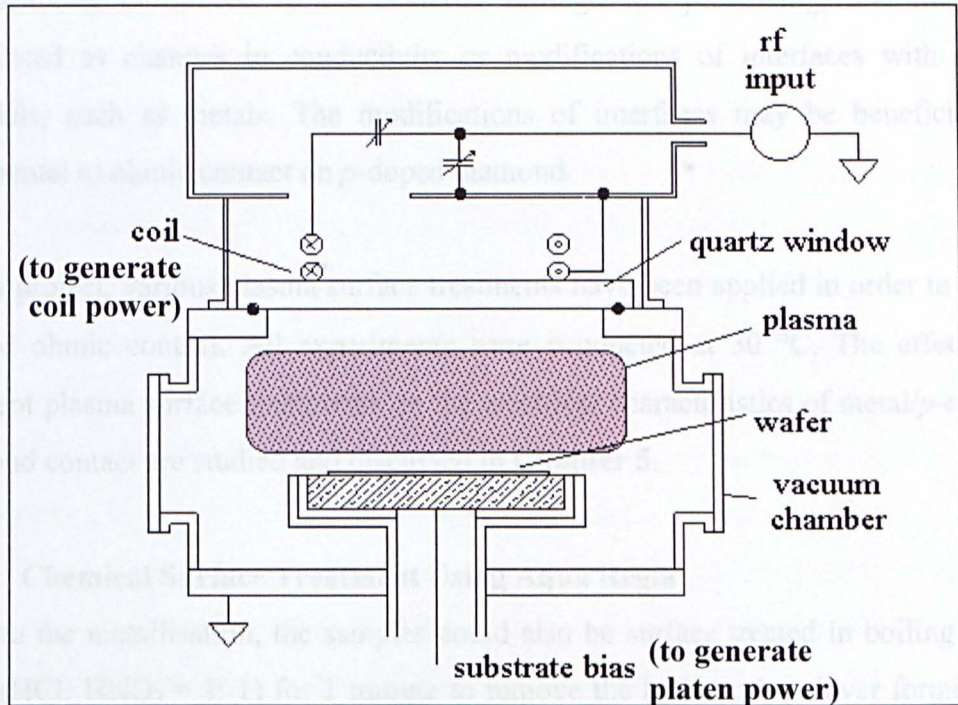
Figure 3.2   A Schematic Diagram of ICP etch tool.

In this work, the ICP etch tool was used for various purposes. For example, the ICP was used to provide surface treatment of the sample prior to metallisation. **Section 3.6** shows the use of ICP tool to provide the plasma surface treatment. In addition, the ICP tool can be adopted as an etching tool to remove the intrinsic diamond layer for MOSFET fabrication or to transfer the photoresist micro-lens pattern onto the diamond substrate.

3.6   Surface Treatments Prior to Metallisation for Micro-electronic Device Fabrication

Surface treatment prior to metallisation is one of the important factors that influence the electrical characteristics of metal/diamond contacts. In this work, prior to

metallisation, diamond surface was treated by either plasma etching or chemical cleaning.

3.6.1 Plasma Surface Treatment

Etch-induced damage in diamond encompasses the range of deleterious modifications introduced to the material through the processing, and may be manifested as changes in conductivity or modifications of interfaces with other materials, such as metals. The modifications of interfaces may be beneficial or detrimental to ohmic contact on p-doped diamond.

In this project, various plasma surface treatments have been applied in order to form a good ohmic contact. All experiments were conducted at 30 °C. The effects of different plasma surface treatments on the electrical characteristics of metal/p-doped diamond contact are studied and discussed in **Chapter 5**.

3.6.2 Chemical Surface Treatment Using Aqua Regia

Prior to the metallisation, the samples could also be surface treated in boiling aqua regia (HCl: HNO_3 = 3: 1) for 1 minute to remove the hydrocarbon layer formed on the diamond surface after the sample growth [7]. It was then blown dried with N_2 and immediately loaded into the metal sputter tool or e-Beam evaporator for metal deposition.

3.7 Reactive Ion Etching (RIE)

RIE is a very useful etching tool employed particularly for vertical etching. In this project, RIE was employed for the vertical etch of SiO_2. The etch recipes for the SiO_2 are described as follows. The flow rate of Ar and CHF_3 was set to 15 and 5 sccm, respectively. The platen power used was 200 W. The pressure was set to 20 mTorr. The etch rate of the SiO_2 is calculated as 0.36 nm/s.

3.8   Buffer Oxide Etch (BOE) Etch

Buffer oxide etch (BOE) is a chemical consisting of HF and NH_4OH in the volume ratio of 7:1. BOE is a chemical widely used for etching SiO_2 in the semiconductor industry. The etch rate of SiO_2 by BOE is about 1 nm/s.

3.9   Metallisation

Metallisation is a process that deposits metal layers on the sample surface. Metal with high work function such as Palladium (5.12 eV) [8] or Platinum (5.65 eV) [8] is required in order to fabricate a good ohmic contact to wide band gap semiconductor such as p-doped diamond. Alternatively, carbide forming metal such Ti is utilised in the ohmic contact formation on p-doped diamond. This metal will serve as the first layer in the metallisation scheme. Metals like Titanium (Ti) and Gold (Au) are used in this work as some phases formed by the interactions of these metal layers and p-doped diamond are found to be instrumental to ohmic contact formation [9], which are explained in details in **Chapter 1**. For thicker metal layers, such Ti (50 nm) and Au (100 nm), metal sputter tool was used. These metal layers are normally employed for the drain and source terminals formation. The chamber of the metal sputter tool needs to be pumped down to 4 x 10^{-6} Torr before the metal layers are deposited. The e-beam evaporator was used to deposit thin metal layers such as Ni (10 nm) and Au (10nm), as shown in Figure 3.3. The metal layers are used for the formation of the gate terminals. It was pumped down to a pressure of 5 x 10^{-6} Torr before metal deposition was carried out. In addition, the temperature of the evaporator chamber must be maintained below 90 °C throughout the evaporation to facilitate the metal lift-off process.
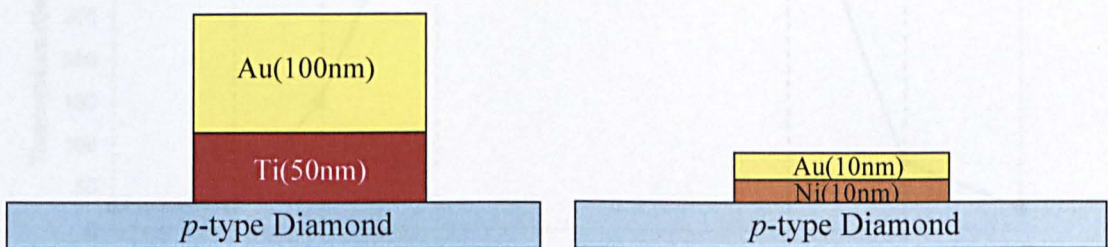
Figure 3.3   **A typical metallisation scheme consisting of Ti(50nm)/Au(100nm) (left) and Ni(10nm)/Au(10nm) (right).**

3.10 Rapid Thermal Annealing (RTA)

After metal lift-off, rapid thermal annealing (RTA) is used to anneal the damage-induced by plasma etching, restore the crystal structure and to achieve certain useful phases formed between metal and p-doped diamond for good ohmic contact formation. A Rapid Thermal Processor (RTP) system can ramp up and cool down sample temperature very quickly. Normally, it takes less than 10 seconds to reach the required annealing temperature. In this project, the preheat temperature was set at 150°C and the RTA temperature range was within 400 to 600°C, typically at 450, 500 and 550 °C. It took about 15 seconds to ramp up to 450 °C. Annealing was carried out for 1 minute under pure nitrogen (N_2) flow. After that, it took about 20 seconds to ramp down and another 20 seconds to cool down. The temperature was measured by a thermocouple which was placed directly under the sample holder. The RTA duration is determined by the length of time during the annealing process or "Ohmic" stage. Figure 3.4 shows the temperature change of the RTP system in an annealing process for this work. A typical RTA process sequence is as follows:

- Purging

- Preheat

- Temperature ramp up

- Annealing (Ohmic)

- Temperature ramp down

- Force Cooling
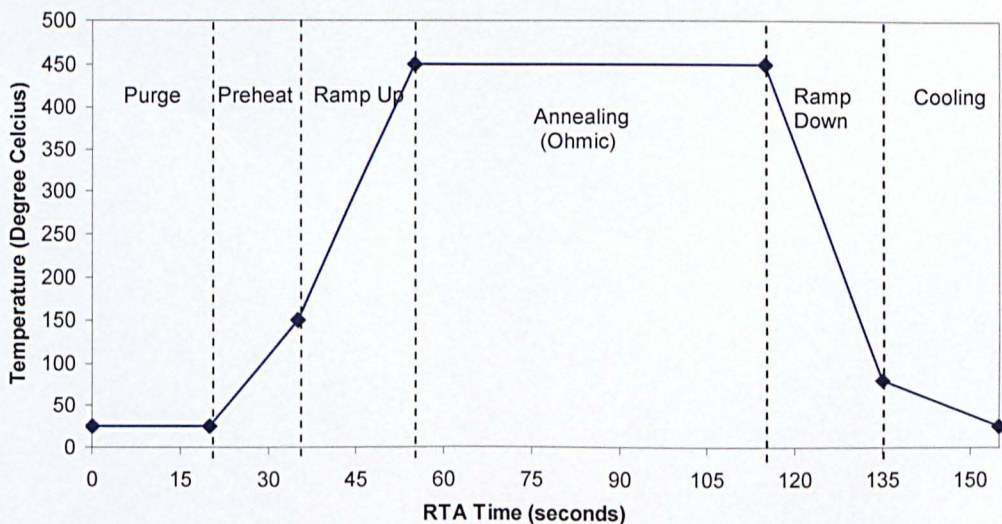
Figure 3.4   **RTA cycle at an annealing temperature of 450°C and for a duration of 60s.**

3.11   Summary

The fabrication steps of the diamond micro-optics (i.e. micro-lenses and grating) such as photolithography and plasma etching are demonstrated in this chapter. Also, the fabrication procedures of micro-electronic devices (i.e. MOSFET) and test structures such as photolithography, metallisation, plasma etching, chemical treatment and annealing using RTA are presented. The electrical, chemical and surface characterisations of these fabricated structures will be analysed using different techniques as described in **Chapter 4**.

3.12   References

[1] Y. Chen, M. Ogura, S. Yamasaki, H. Okushi, *Semicond. Sci. Tehnol.*, **20**, 860 (2005).

[2] H. Xiao, *Introduction to Semiconductor Manufacturing Technology*, Prentice Hall, (2001).

[3] B. El-Kareh, *Fundamentals of Semiconductor Processing Technology*, Kluwer Academic Publishers, (1995).

[4] D. Daly, *Microlens Array*, Taylor and Francis (2001).

[5] J. Ji, F.E.H. Tay, J. Miao, J. Sun, *Journal of Physics: Conference Series*, **34**, 1137 (2006).

[6] F.A. Khan, L. Zhou, V. Kumar, I. Adesida, R. Okojie, *Mat. Sci. & Eng. B*, **95**, 51 (2004).

[7] L.S. Pan, D.R. Kania, *Diamond: Electronic Properties and Applications*, Springer (1994).

[8] H. B. Michaelson, *J. Appl. Phys.*, **48**, 4729 (1977).

[9] T. Tachibana, B.E. Williams, J.T. Glass, *Phys. Rev. B*, **45**, 11968 (1992).

Chapter 4

Experimental Techniques for Characterising Diamond

Micro-optical and Micro-electronic devices

4.1 Introduction

This chapter introduces the experimental techniques used in this work, mainly concentrating on Atomic Force Microscopy (AFM), Confocal Microscopy, Spectroscopic Ellipsometry and Semiconductor Parameter Analysing. Conventional characterisation techniques such as Scanning Electron Microscopy (SEM), X-ray Photoelectron Spectroscopy (XPS) and Secondary Ion Mass Spectroscopy (SIMS) will also be explained briefly.

The study of diamond surface and interface is very important for understanding the diamond electrical characteristics, such as ohmic contact formation in a diamond micro-electronic device. This study is also indispensable for developing diamond micro-optics. In this project, XPS, SIMS, and AFM were employed as tools for surface analysis. XPS measurements were performed so as to obtain the elemental composition on the *p*-doped diamond surface after ICP Ar/Cl_2 plasma etching. SIMS was used to study the boron depth profile of the diamond samples with a boron-doped delta layer. AFM was used to measure the surface morphology of the diamond micro-optics, such as diamond micro-lenses. Laser scanning confocal microscopy is important to characterise the optical properties of the diamond micro-optics. SEM was used to image diamond micro-lenses and gratings with a high resolution. As for electrical characterisations, the metal/*p*-doped diamond contacts are investigated and electrical performances of the diamond MISFET and MOSFET devices were measured by using a Semiconductor Parameter Analyser.

4.2 Optical Characterisation

4.2.1 Spectroscopic Ellipsometry

Spectroscopic Ellipsometry is a contact-less and non-destructive method of measuring the thickness of a transparent thin film. Figure 4.1 shows an experimental

setup for measuring the thickness of a material. In a reflectometer, a white light polarised beam is obtained after passing a polariser. The beam is then incident onto the surface of the sample to be analysed after passing the analyser.
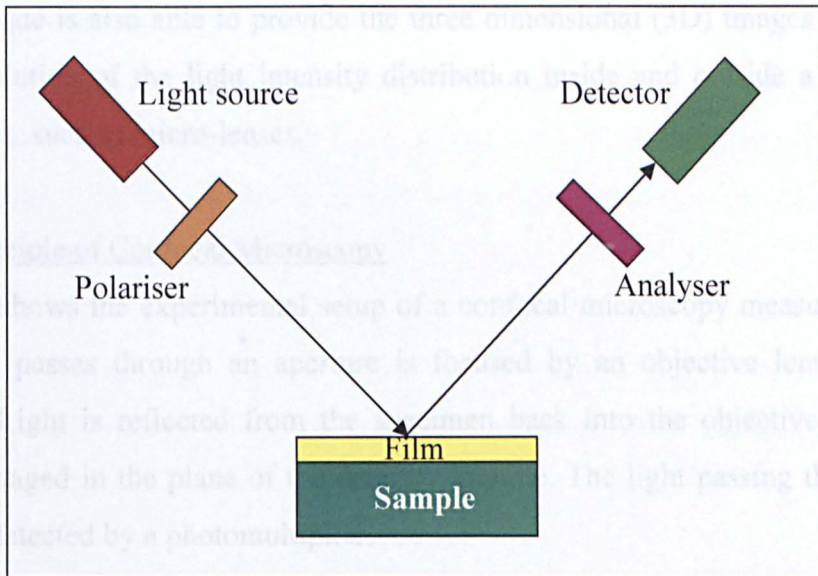

Figure 4.1   Experimental setup to measure film thickness using spectroscopic Ellipsometry technique.

The reflected light intensity is measured over a broadband wavelength range [1]. For a thin film with a known refractive index, the reflected light intensity is determined by light interference of the reflected light beams from the top and bottom surface of the thin film. The phase difference of the two reflected light beam is determined by the thickness of the thin film. Hence, the thickness of the thin film can be obtained by comparing the incident and reflected intensity and the change in polarisation angle at different wavelengths. One of the advantages of using spectroscopic Ellipsometry to measure film thickness is its simplicity and low cost [1].

4.2.2   Confocal Microscopy

Confocal microscopy is a practical and conceptual advance in optical microscopy. It is a planar imaging technique. Confocal microscopy has been used extensively in wide fields, including biology, medicine and material science due to its ability to produce extremely high quality images of optical sections at various depths. The confocal microscopy used in this work is called the reflection-transmission laser

scanning confocal microscopy (LSCM), which is developed by the Institute of Photonics, University of Strathclyde. For diamond micro-lens characterisation, it is extremely beneficial to use such confocal reflected and transmitted light imaging modes, i.e., to collect reflection and transmission optical sections simultaneously. This technique is also able to provide the three dimensional (3D) images with high spatial resolution of the light intensity distribution inside and outside a miniature micro-optics, such as micro-lenses.

4.2.2.1 Principle of Confocal Microscopy

Figure 4.2 shows the experimental setup of a confocal microscopy measurement. A laser beam passes through an aperture is focused by an objective lens onto the specimen. Light is reflected from the specimen back into the objective lens, and object is imaged in the plane of the detector pinhole. The light passing through the pinhole is detected by a photomultiplier.
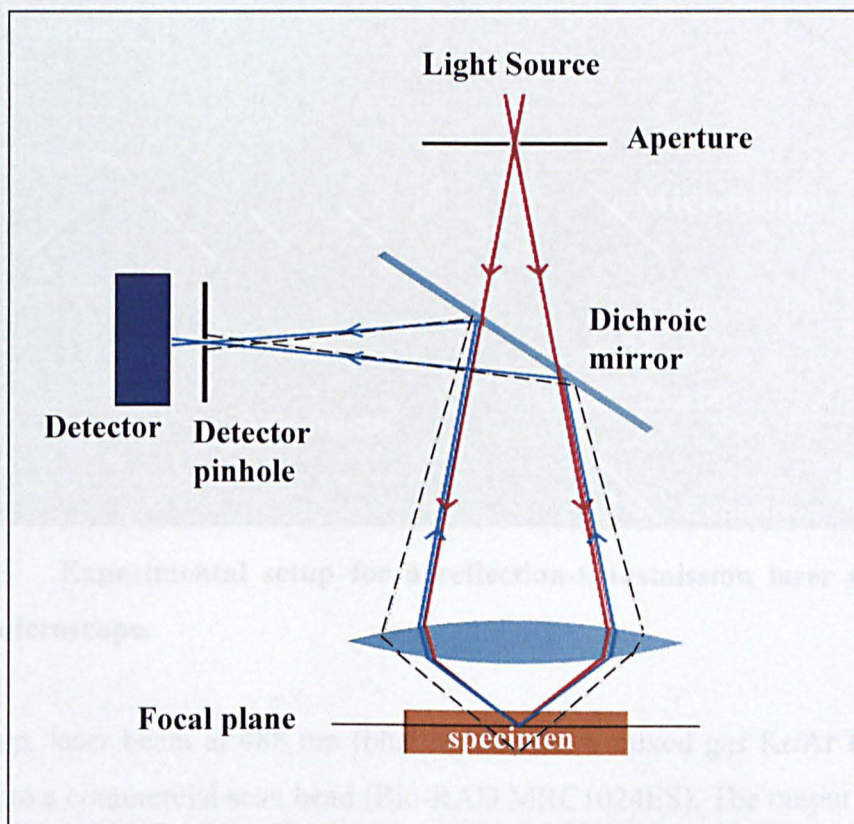

Figure 4.2 Experimental setup of a confocal microscopy measurement.

Some of the incident light, which is represented by the dotted line, can be reflected from the specimen that is located in planes closer or further from the objective lens. The focal point for this light is located before the plane of the detector pinhole. Thus, light is converging in front of the plane of pinhole and very little of light passes through to the photomultiplier. A two-dimensional image is then collected by scanning the specimen. Since light in front of the pinhole plane is rejected from the image, this two dimensional image is an optical section through the specimen. As such, confocal microscopy can be a non-destructive technique to image a three dimensional structure.

4.2.2.2 Experimental Setup

The experimental setup of a reflection-transmission laser scanning confocal microscope is shown in Figure 4.3.
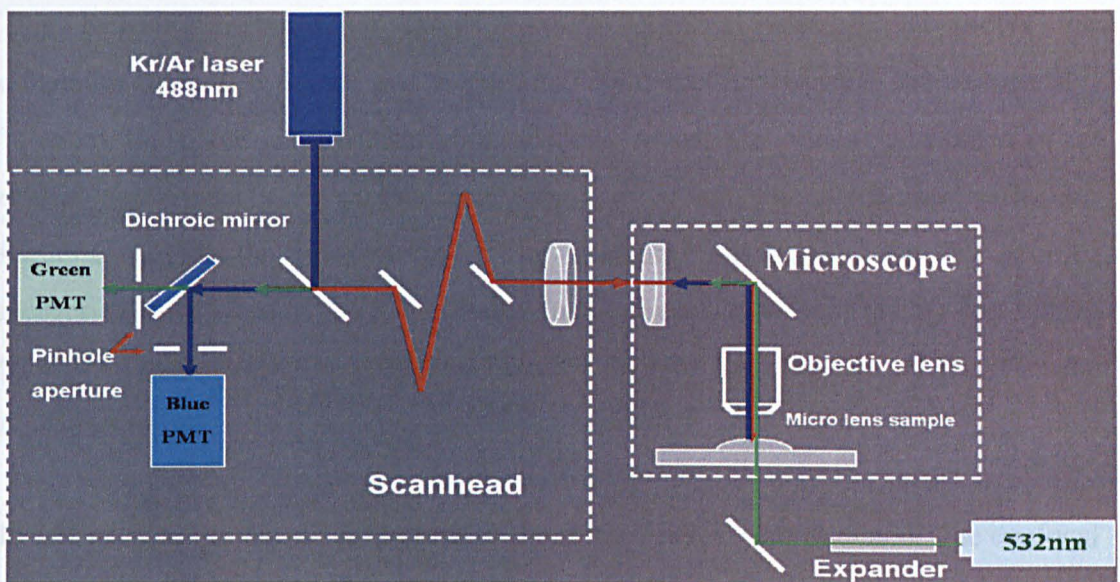
Figure 4.3   Experimental setup for a reflection-transmission laser scanning confocal microscope.

In this setup, laser beam at 488 nm (blue light) from a mixed gas Kr/Ar laser was directed onto a commercial scan head (Bio-RAD MRC1024ES). The output from the scan head was then coupled into an upright microscope (Nikon E600FN) with the objective lens (20X, 0.75 NA). As seen in Figure 4.3, the blue light is then reflected back from an optical sample such as a micro-lens. The transmitted source was

provided by a 10 mW miniature diode-pumped, frequency doubled Nd:YAG laser operating at 532 nm. This green laser beam is expanded 16 times using a Galilean telescope expander, before being sent into the microscope as shown in Figure 4.3. A mirror was placed just below the microscope stage to direct collimated green light into the back surface of the sample. Before passing back the reflected blue and transmitted green light through the scan head, both lights were collected by the microscope. Finally, the beams were detected by two photomultipliers after a dichroic mirror. Narrow passband filters (488 ± 5 and 540 ± 20 nm) were mounted before each detector in order to ensure that there is only one light source entering each detector. Also, the light outside of the focal plane was rejected using pinhole apertures in the scan head. The axial and lateral resolutions which were measured during calibration of the confocal system are 0.8 (± 0.1) µm and 0.25 (± 0.02) µm, respectively [3].

This reflection-transmission laser scanning confocal microscopy allows the collection of both reflected and transmitted light sectional images simultaneously. Whereas the plane-view transmission sections reveal the optical properties of an optical component such as the focal length of a lens, the plane-view reflection sections provide the information of the structural topography. For the case of measuring micro-lenses, the transmission image reveals how light ray are focused by the micro-lenses while the reflection image shows the top view optical image of the micro-lenses.

In this project, the optical properties of the micro-lenses were obtained. The confocal microscopy characterisations were performed by Dr. Erdan Gu from the Institute of Photonics in University of Strathclyde.

4.3   Electrical Characterisation

4.3.1   Current-Voltage (*I-V*) Measurements

The Current-Voltage (*I-V*) characteristics of diamond micro-electronic devices were measured by using a micro-probe station and a Precision Semiconductor Parameter Analyser-HP4155A. The instrument setup is shown in Figure 4.4. It is important that

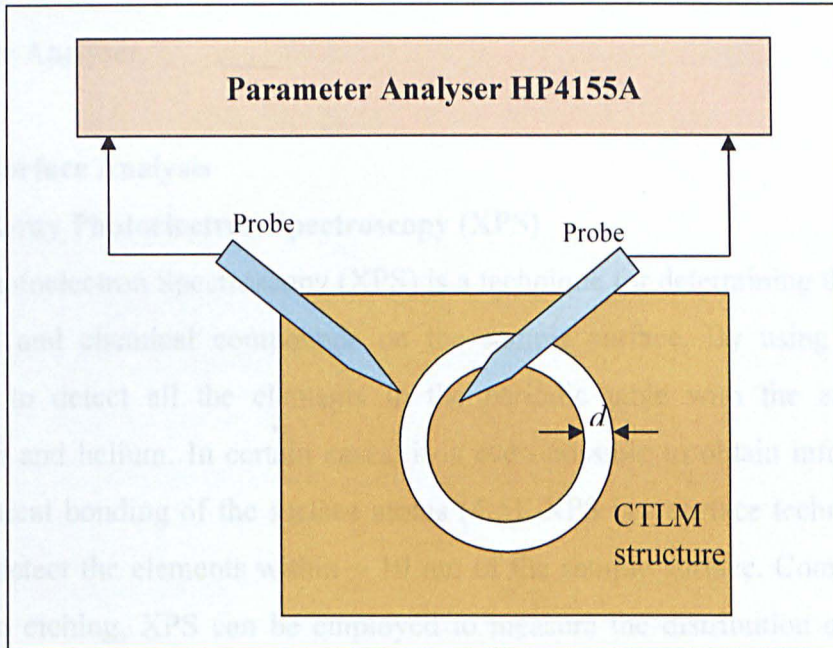during the measurement, the probes should be pressed gently so as to prevent the metal contact damage.

Figure 4.4   Experimental setup for *I-V* measurements.

As an example, typical *I-V* curves measured for ohmic and non-ohmic metal/diamond contacts are shown in Figure 4.5. For an ohmic contact, its *I-V* curve is linear and its inverse gradient is the total resistance (R_T) across the contacts. By using the Circular Transmission Line Method introduced in Chapter 2 and measuring various values of R_T at different circular contact pad separations d, the specific contact resistance, ρ_c, can be calculated.
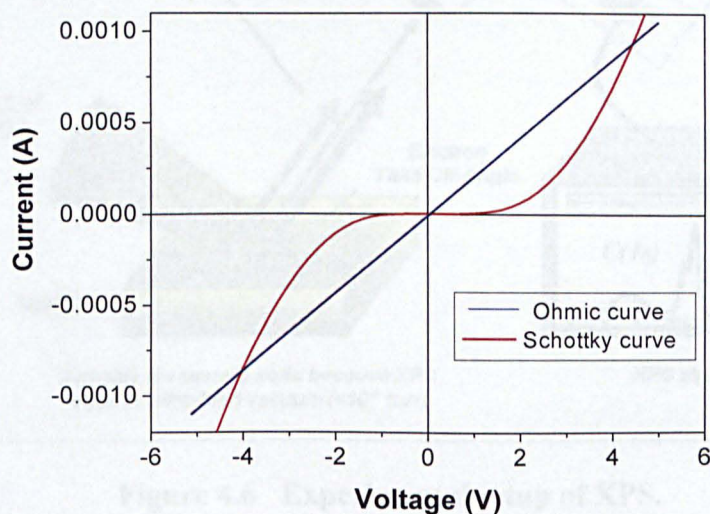

Figure 4.5   Typical *I-V* curves showing Ohmic and Schottky characteristics.

In this project, the *I-V* characteristics of the metal/*p*-doped diamond contacts were investigated in detail. The performances of diamond MISFET and MOSFET micro-electronic devices have also been studied by using the Semiconductor Parameter Analyser.

4.4   Surface Analysis

4.4.1   X-ray Photoelectron Spectroscopy (XPS)

X-ray Photoelectron Spectroscopy (XPS) is a technique for determining the chemical elements and chemical compounds on the sample surface. By using XPS, it is possible to detect all the elements in the periodic table with the exception of hydrogen and helium. In certain cases, it is even possible to obtain information on the chemical bonding of the surface atoms [4-5]. XPS is a surface technique and is used to detect the elements within ~ 10 nm of the sample surface. Combining with ion beam etching, XPS can be employed to measure the distribution of elemental composition as a function of depth (depth profile) in the sample. Such a depth profile can also be obtained by tilting the sample angle with respect to electron detector. Figure 4.6 shows the XPS setup.
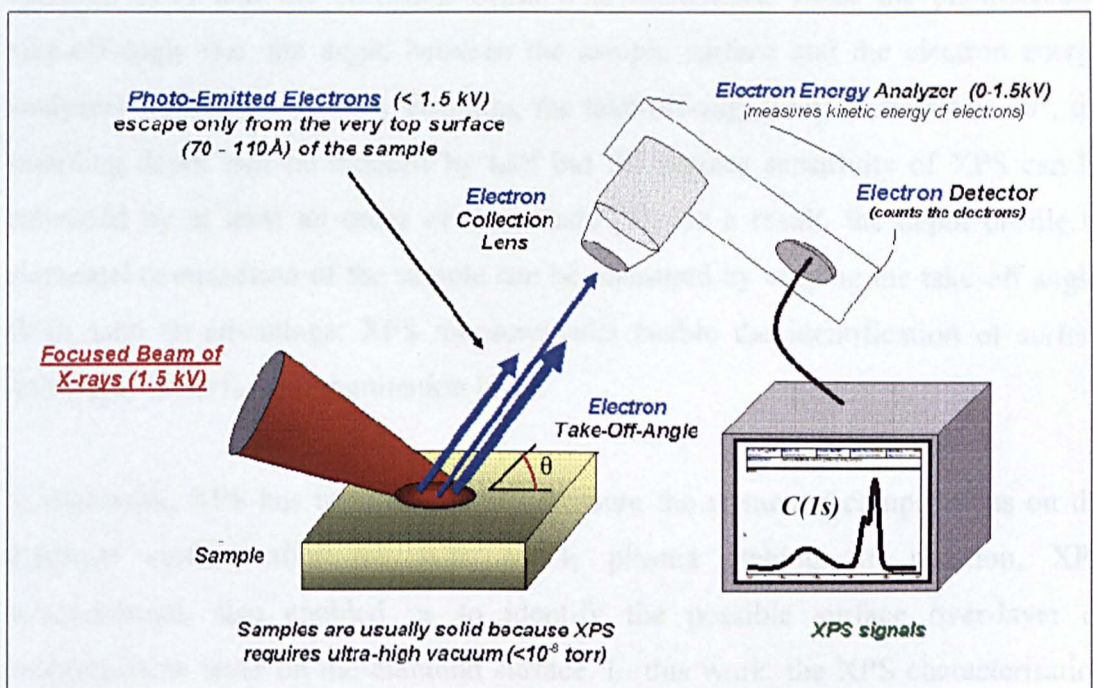

Figure 4.6   Experimental setup of XPS.

4.4.1.1 Principle of XPS

As shown in Figure 4.6, a focused beam of soft x-rays (1-5 keV) illuminates the sample to be studied. A x-ray photon is normally absorbed completely by a single electron in the sample atom, providing enough energy for it to escape from its orbit to form a free photoelectron. The energy of the photoelectron is:

$$E_g = h\nu - b \qquad (4.1)$$

where E_g is the kinetic energy of the escaping electron, $h\nu$ is the x-ray photon energy and b is the binding energy. If the incident x-ray energy is known and the escaping electron energy is measured, the binding energy of the electron can be calculated. Since each element has a unique set of binding energies, the measured binding energies in turn provide information of the element from which the electrons came.

The sampling depth d and XPS take-off-angle is correlated by [5]:

$$d = 3\lambda \sin \theta \qquad (4.1)$$

where λ is the photoelectron mean free path (a distance that a photoelectron can traverse through the solid before experiencing inelastic scattering) and θ is the photoelectron emission (take-off) angle as defined in Figure 4.6. It can be seen from equation (4.1) that the sampling depth d is maximised when the photoelectron take-off-angle (i.e. the angle between the sample surface and the electron energy analyser) approaches 90°. By changing the take-off-angle, say from 90° to 30°, the sampling depth will be reduced by half but the surface sensitivity of XPS can be enhanced by at least an order of magnitude [5]. As a result, the depth profile of elemental composition of the sample can be measured by varying the take-off angle. With such an advantage, XPS measurements enable the identification of surface over-layer or surface contamination layer.

In this work, XPS has been adopted to measure the elemental compositions on the diamond surface after the ICP Ar/Cl_2 plasma etching. In addition, XPS measurements also enabled us to identify the possible surface over-layer or contamination layer on the diamond surface. In this work, the XPS characterisation was performed under the contract for Element Six Ltd.

4.4.2   Secondary Ion Mass Spectroscopy (SIMS)

Secondary Ion Mass Spectroscopy (SIMS) is extremely sensitive to element analysis with excellent depth resolution, making it an ideal tool for the examination of the dopant profile in diamond and other semiconductor materials.

4.4.2.1 Principle of SIMS

In a SIMS instrument, a focused ion beam (1 to 30 keV) is used to bombard a selected area of interest on a sample. As a result of the collisions, the surface atoms from the sample are knocked out. A fraction of these sputtered atoms are ionised (secondary ions) and these ions are analysed with a mass spectrometer to achieve the element identification. Elemental depth profiles are obtained as a direct consequence of the fact that the sample is slowly eroded by the sputtering process itself. Lateral resolution is achieved either by focusing the primary-ion beam on a detail to be analysed (ion micro-probe analysis) or by flooding primary-ions on a somewhat larger area and forming an image based on the distribution of a specific secondary ion (ion microscopy). SIMS is a destructive method because the sample is actually etched during the measurement.

One important function of SIMS is to analyse the elemental depth profile of a sample. This profile analysis provides important information on the distribution of dopants in a semiconductor. In this work, the depth profiles of the boron-doped delta layer of diamond samples were measured under the contract for Element Six Ltd.

4.4.3   Scanning Electron Microscopy (SEM)

Scanning Electron Microscope is a microscope that utilises electrons rather than light to form an image.

4.4.3.1 Principle of SEM

The way a SEM works is as follows: A beam of electrons of kilovolt energy is generated by an electron gun. This electron beam is attracted through an anode, condensed by a condenser lens and focused onto a small point at the sample surface using an objective lens. The electron beam hits the sample and produces secondary

electrons from it. These secondary electrons are collected by a secondary electron detector. As the yield of the secondary electrons is correlated with the surface topography of a sample, by collecting, processing and analysing the secondary electrons generated from the sample, the sample's topographic image can be obtained [6].

There are several advantages of using SEM to image and analyse the samples including:

• SEM may produce images with a high resolution, revealing details about 1 to 5 nm in size. Hence, detailed features can be observed by SEM imaging at a high magnification.

• Comparing with other high resolution imaging techniques such as transmission electron microscopy (TEM), preparation of SEM samples is relatively easy. One main requirement for a SEM sample is that the sample should be conductive.

In this work, the high resolution images of diamond micro-lenses and optical gratings were obtained by using SEM. The SEM measurements were performed by Dr. Paul Edwards in Department of Physics, University of Strathclyde.

4.4.4 Atomic Force Microscopy (AFM)

Atomic Force Microscopy (AFM) is a real-space imaging technique that can produce topographic images of a surface with atomic resolution in all three dimensions. Almost any solid surface can be studied using AFM. AFM has many advantages over other established imaging techniques; it is a non-destructive technique which has the capability of imaging nanoscale topography and to measuring accurate surface roughness.

An AFM consists of four primary components [6], an AFM probe, a laser, a photodetector and a piezoelectric scanner as shown in Figure 4.7(a) [7] and 4.7(b).
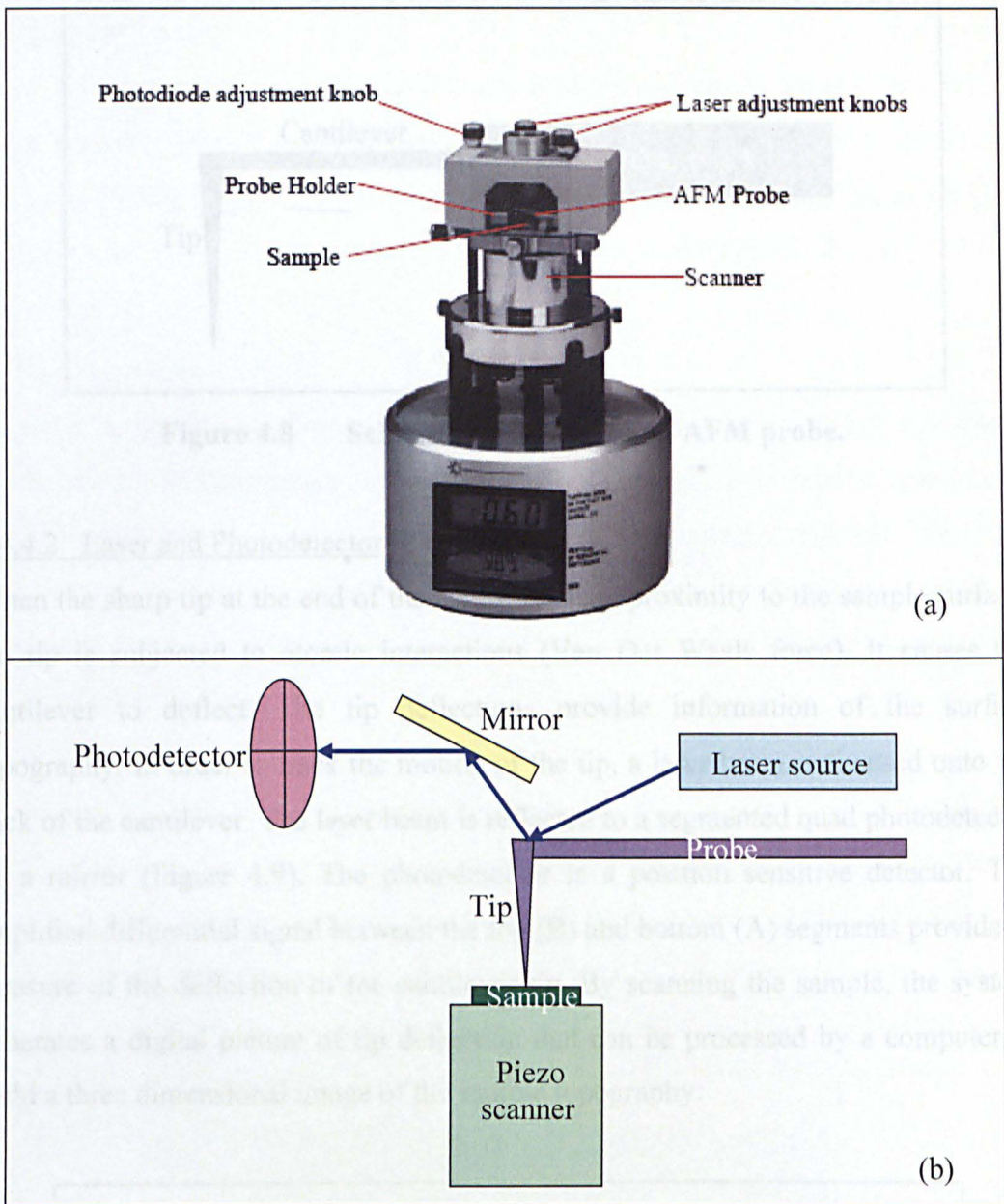
Figure 4.7 **(a) Photograph of a Multimode AFM. (b) Schematic diagram of an AFM.**

4.4.4.1 AFM Probe

The AFM probe as illustrated in Figure 4.8 consists of three parts:

(i) Cantilever block – to support a very fine cantilever which has the delicate tip situated at the end; (ii) Cantilever – to hold the tip; and (iii) Tip – to scan the sample surface. AFM cantilever and tip are normally made of silicon or silicon nitride and are coated by metal e.g. aluminium on the back so as to reflect the laser beam.
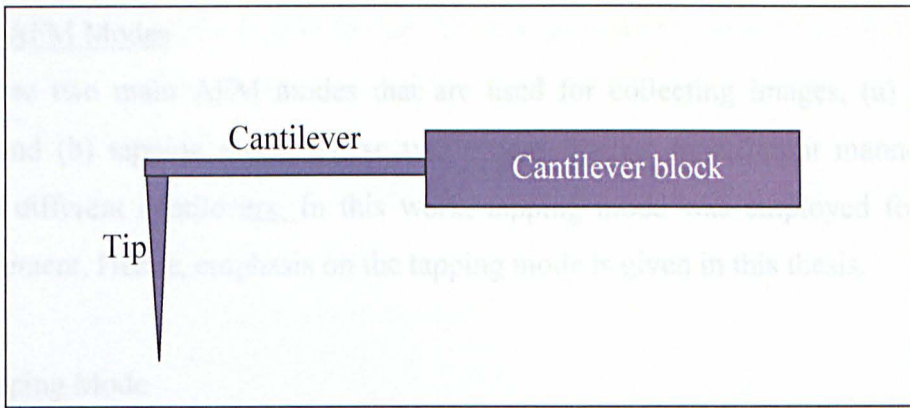
Cantilever

Cantilever block

Tip

Figure 4.8 **Schematic diagram of an AFM probe.**

4.4.4.2   Laser and Photodetector

When the sharp tip at the end of the cantilever is in proximity to the sample surface, the tip is subjected to atomic interactions (Van Der Waals force). It causes the cantilever to deflect. The tip deflections provide information of the surface topography. In order to track the motion of the tip, a laser beam is focused onto the back of the cantilever. The laser beam is reflected to a segmented quad photodetector by a mirror (Figure 4.9). The photodetector is a position sensitive detector. The amplified differential signal between the top (B) and bottom (A) segments provides a measure of the deflection of the cantilever tip. By scanning the sample, the system generates a digital picture of tip deflection that can be processed by a computer to yield a three dimensional image of the sample topography.
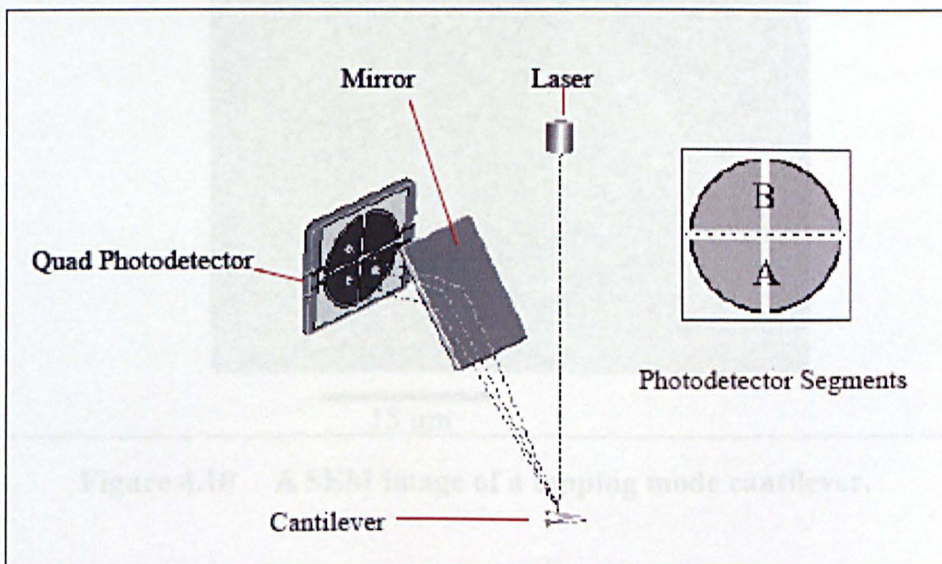
Mirror   Laser

Quad Photodetector

B

A

Photodetector Segments

Cantilever

Figure 4.9   **A schematic diagram of a laser and a photodetector system.**

4.4.4.3 AFM Modes

There are two main AFM modes that are used for collecting images, (a) contact mode and (b) tapping mode. These two modes operate in different manners and require different cantilevers. In this work, tapping mode was employed for AFM measurement. Hence, emphasis on the tapping mode is given in this thesis.

- Tapping Mode

Tapping mode is a technique that was developed to overcome the drawbacks encountered with the contact mode. Tapping mode, as its name implies, operates by the oscillating cantilever intermittently in proximity to the sample surface. The probe will have a maximum oscillation amplitude in the free air but the amplitude is reduced in proximity to the sample surface. Consequently, there will be change in the amplitude that is measured.

Tapping mode probes use rectangular cantilevers and the cantilever tip normally has a radius of curvature less than 10 nm. Such a tip is shown in Figure 4.10 [7]. It can be seen that the tapping tip lies directly beneath the end of the cantilever, which will allow to position the tip precisely.
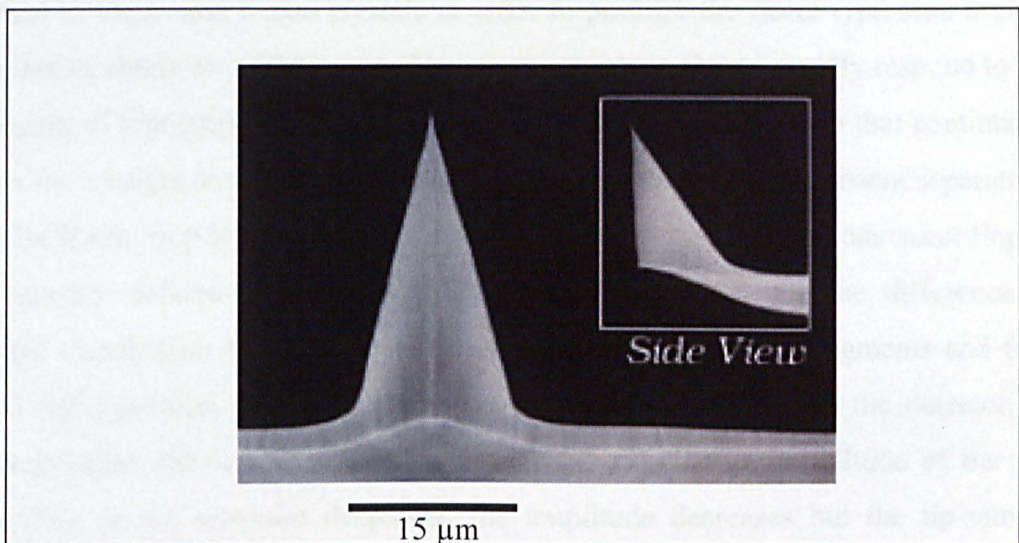

Figure 4.10   A SEM image of a tapping mode cantilever.

Since there is no contact between the tip and the sample, wear of the probe and damage of the surface are reduced, which improves the image quality. In addition, the kinetic energy of the oscillating cantilever enables the tip to penetrate the adsorbed layer to reach the real surface of the sample. Due to the many advantages of the tapping mode, it is rapidly becoming a widely used technique and this mode is chosen for measuring diamond samples in this work.

In tapping mode, a sharp tip mounted on the end of a long flexible cantilever is pressed against the sample surface with a known force (known from the curvature of the cantilever) and tapping across the surface while keeping the force constant. The vertical movements required to maintain the force are the measurements of the surface topography. This will give the 3-D surface morphology of a particular sample. The surface RMS (root mean square) roughness can be obtained by limiting the tip to move around a certain area.

4.4.4.4 Piezo Scanner

In order to scan the sample and to have a precise control on the sample position, a piezoelectric scanner is utilised. A piezo scanner consists of three piezo crystals (x, y and z-axis) that respond separately to an applied voltage. AC voltages are applied to the x- and y-axis crystals in order to produce the raster-type scan motion required to obtain an AFM image. The piezo scanner is able to rapidly respond to the changing of topography of the sample by means of a feedback loop that continually alters the z height to ensure that the sample and probe are at a consistent separation. The feedback loop is a system that controls the tip-sample interactions according to an operator defined set-point. The feedback system measures the difference in voltage distribution between the upper and lower photodetector segments and thus alters the z-position of the scanner to re-centre the laser beam in the detector. In tapping mode, the set-point is determined by the oscillating amplitude of the tip. Therefore as the set-point decreases, the amplitude decreases but the tip-sample forces increase. The laser spot oscillates vertically across the photodetector array as a result of the vibration of the cantilever. The signal obtained from the photodetector is rectified and then is low pass filtered into a DC voltage. In this case, the magnitude

of the voltage is proportional to the cantilever amplitude. The feedback system compares the recorded amplitude to the set-point and adjusts the cantilever position of the z-axis in order to keep them equal. This feedback loop allows the operator to optimise the scan conditions, thus minimising the possibility of tip and sample damage whilst maintaining proximity to surface topography.

AFM provides topographic information that is truly three-dimensional. The data are digitally stored, allowing the computer to manipulate and display the data as a three-dimensional rendition, viewed from an altitude and azimuth.

4.4.4.5 Scanning Errors

An AFM image is the convolution of both the cantilever probe geometry and sample topography. Consequently, scanning errors can occur which cause the AFM image to differ from the real sample surface [7]. Scanning errors of this nature are unavoidable and should be taken into consideration when analysing AFM images.

The geometry of the probe influences the resolution limit that can be achieved. If the probe is of a greater size than the gap between two features on the sample, they will appear as one entity. Also, a false topography will be recorded if the angle of the feature is more acute than that of the probe. As shown in Figure 4.11, the geometry of the sample surface can also be the cause of imaging errors. Figure 4.12 illustrates a sample surface which has an overhanging edge, the cantilever tip cannot image such structure and therefore the recorder topography does not contain this feature.
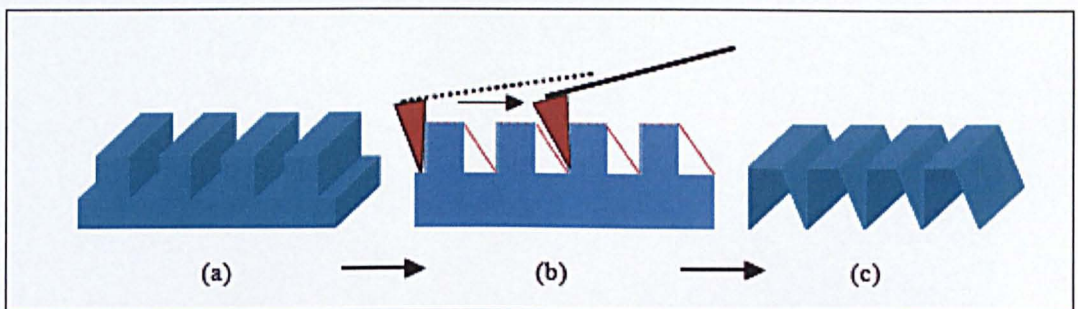

(a)   (b)   (c)

Figure 4.11   Example of artefacts due to probe geometry, where (a) is the actual sample surface, (b) shows the probe path across the surface and (c) is the recorded image.
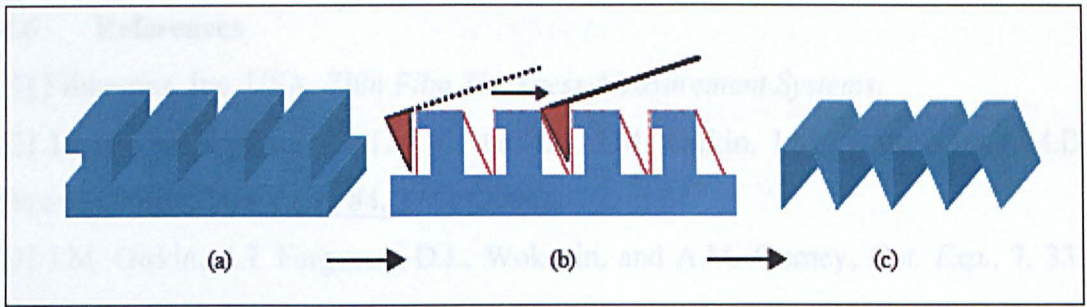
Figure 4.12 **Example of artefacts due to sample geometry, where (a) is the sample surface, (b) shows the probe path across the surface and (c) is the recorded image.**

4.5   Summary

In this chapter, the optical characterisation techniques such as Spectroscopic Ellipsometry and Confocal Microscopy have been discussed. Also, electrical characterisation technique using Current-Voltage (I-V) measurement and the calculation of specific contact resistance, ρ_c have been described. In addition, the surface analysis techniques such as X-ray Photoelectron Spectroscopy (XPS), Secondary Ion Mass Spectroscopy (SIMS), Scanning Electron Microscopy (SEM) and Atomic Force Microscopy (AFM) are presented.

4.6   References

[1] Filmetrics, Inc. USA. *Thin Film Thickness Measurement Systems*.

[2] E. Gu, H.W. Choi, C. Liu, C. Griffin, J.M. Girkin, I.M. Watson, and M.D. Dawson, *Appl. Phys. Lett.*, **84**, 2754 (2004).

[3] J.M. Girkin, A.I. Ferguson, D.L. Wokosin, and A.M. Gurney, *Opt. Exp.*, **7**, 336 (2000).

[4] R.W. Cahn, E. Lifshin, *Concise Encyclopedia of Materials Characterisation*, Pergamon Press (1993).

[5] J.P. Sibilia, *A Guide to Materials Characterisation and Chemical Analysis*, VCH Publishers (1996).

[6] Digital Instruments, Command Module, 442 (1999).

[7] S. Hodgen, Phd Thesis, University of Strathclyde (2005).

Chapter 5

Diamond Micro-Optics: Fabrication and Characterisation of Spherical Diamond Micro-lenses

5.1   Introduction

Diamond has the widest optical transparency band of all known solids, ranging from 220 nm to the far infrared [1]. Being transparent in the ultraviolet, visible and infrared spectral regions, diamond is an ideal material for developing high-quality micro-optics, such as micro-lenses and grating. In addition, the high mechanical hardness and thermal conductivity of diamond greatly support the optical applications making diamond micro-optics very stable and resistant in many aspects. These unique optical properties have made diamond very attractive in developing novel micro-optics.

Nevertheless, due to its hardness and chemically inertness, the processing of diamond to fabricate high performance micro-optics is a technical challenge. To date, micro-machining of diamond is based on dry etching techniques such as Reactive Ion Etching (RIE) [2-3], Inductively Coupled Plasma (ICP) [4-8], Electron-Cyclotron Resonance etching (ECR) [9] or focused-ion beam milling [10]. Dry etching technique on diamond using ICP offers advantages such as high etch rates (i.e. 0.2 μm/min using oxygen-based plasma [6]) and smooth etched surface morphology due to the chemical etching utilising ICP coil power. Fabrication of diamond optical microstructures such as micro-lenses using ICP has been reported by Choi *et al.* [6] and Karlsson *et al.* [7]. Both authors have shown the capabilities of using oxygen-based plasma in spherical micro-lenses fabrication. However, diamond etching using chlorine-based plasma and fabrication of other types of micro-lenses such as micro-cylindrical and micro-ring lenses have not yet been investigated.

In this chapter, detailed investigations on ICP etching of diamond using different plasmas, in this case oxygen-based (Ar/O_2) and chlorine-based (Ar/Cl_2) plasma will be presented. In addition, the fabrication of various micro-structures including

spherical micro-lenses and micro-VESCELs for micro-optic applications will be included.

5.2   Investigation on ICP Etching - Argon and Oxygen Plasma (Ar/O_2)

ICP etching with Ar/O_2 plasma has been used on diamond micro-fabrication. This is due to the high etch rate achievable by using this plasma. Choi *et al.* [6] has reported an etch rate as high as 0.2 μm/min. However, the diamond etching using Ar/O_2 plasma has not yet been fully explored. In this section, the effect and influence of ICP platen power, coil power and gas pressure on diamond etching with Ar/O_2 plasma are investigated in detail.

In general, the etching mechanism of diamond using Ar/O_2 plasma is explained as follows [11].
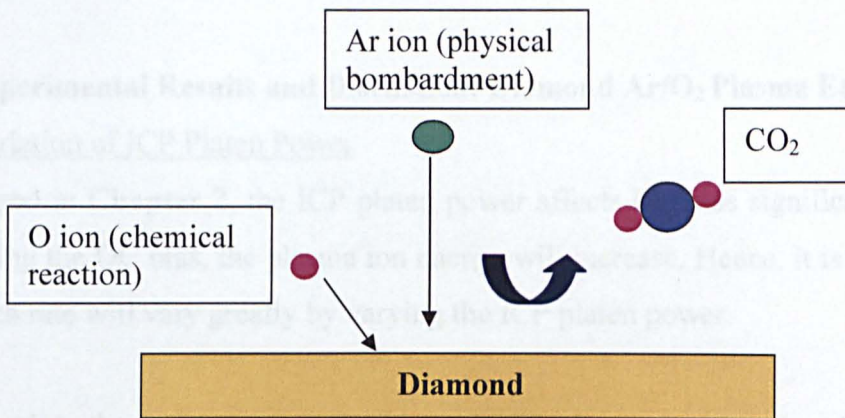

Figure 5.1   Etching mechanism of diamond using Ar/O_2 etchant.

Oxygen (O_2) is the most popular reactive gas in dry etching of diamond [9-10] for its excellent chemical activity in etching carbon-based materials. Ion sputtering also plays an important role in patterning diamond. For this reason, Ar is mixed with O_2 in the etching chamber. During plasma etching, Ar ion is responsible for the physical bombardment to dislodge the carbon atoms from the diamond. The free carbon atoms will then react with oxygen ions to form volatile gaseous products such as CO and CO_2 which are thereby pumped out of the chamber as illustrated in Figure 5.1. Hence, diamond can be etched by oxidation to CO or CO_2 utilising oxygen [11].

Diamond etching by molecular oxygen seems to proceed in two steps [11]. The first step involves formation of graphitic layer:

$$C_{dia} + \frac{1}{2}O_2 \rightarrow CO_{ads}$$

$$CO + CO_{ads} \rightarrow C_{gra} + CO_2$$
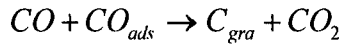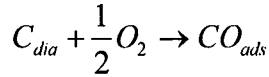
where C_{dia} is the diamond carbon, CO_{ads} is the adsorbed carbon monoxide and C_{gra} is the graphite layer. The second step is related to the subsequent oxygen etching of the graphitic layer. However, at temperature less than 900 °C, the second step proceeds faster than the first step and a clean diamond surface is formed instead of the graphite layer. On the other hand, graphite formation occurs at temperature more than 900 °C [11]. This is due to the increase of the relative rate for the first step compared to the second step.

5.2.1 Experimental Results and Discussion: Diamond Ar/O$_2$ Plasma Etching

5.2.1.1 Variation of ICP Platen Power

As discussed in **Chapter 2**, the ICP platen power affects DC bias significantly and by increasing the DC bias, the plasma ion energy will increase. Hence, it is expected that the etch rate will vary greatly by varying the ICP platen power.

Figure 5.2 plots the etch rate as a function of ICP platen power with a fixed coil power of 400 W and a gas pressure of 5 mTorr. It is observed that the etch rate increases rapidly from 0 to 0.065 µm/min as ICP platen power increases from 0 to 50 W. However, as the platen power further increases, the etch rate does not increase at such a rapid rate. The mechanism of the etching can be explained as follows: The Ar ions created within the plasma bombard carbon atoms in the diamond structure. The increment of ICP platen power will increase the Ar ion energy [12] and therefore enhance the bombardment for removing the carbon atoms on diamond surface. These free carbon atoms will then interact with the oxygen ions to form gaseous CO$_2$ and/or CO. Thus, the diamond etch rate increases with the ICP platen power. However, upon reaching certain ICP platen power, the etch rate approaches saturation owing to the limitation of the Ar ion density. In other words, the number of carbon atoms

being bombarded away will still be the same no matter how high is the ion energy if the Ar ion density remains un-changed.
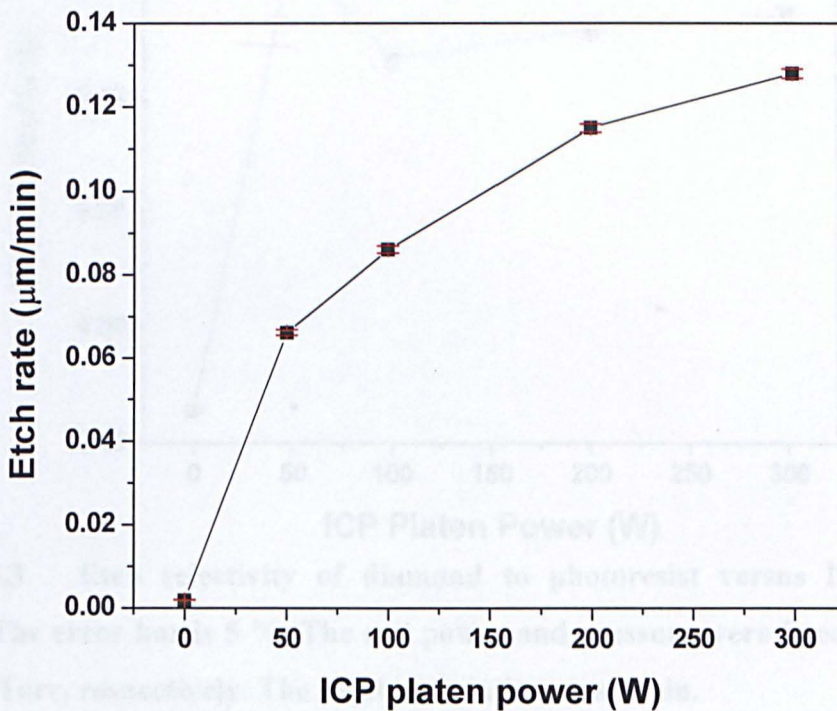

Figure 5.2   Diamond etch rate versus ICP platen power. The error bar is 5 %. The coil power was fixed to 400 W. The pressure was set as 5 mTorr.

The etch selectivity is defined as diamond etch rate divided by photoresist etch rate. The etch selectivity as a function of ICP platen power with a fixed coil power of 400 W is presented in Figure 5.3. It is found that the etch selectivity remains almost constant as the ICP platen power varies except at very low ICP platen power (< 50W). Based on this result, it can be concluded that the etch selectivity of diamond to photoresist is almost independent of the ICP platen power.
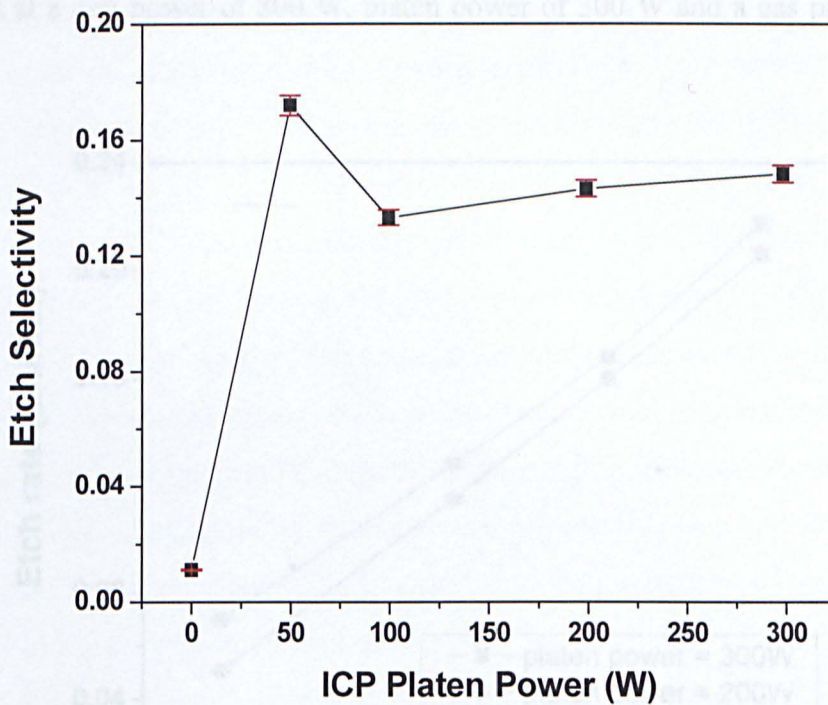
Figure 5.3   **Etch selectivity of diamond to photoresist versus ICP platen power. The error bar is 5 %. The coil power and pressure were fixed as 400 W and 5 mTorr, respectively. The etching duration was 5 min.**

5.2.1.2 Variation of ICP Coil Power

In this section, the effect of ICP coil power varied from 100 to 800 W on the diamond etch rate is investigated. Two platen powers of 200 and 300 W were used so as to study the influence of the platen power on the etch rate at different coil powers. These results are presented in Figure 5.4.

It is observed that the diamond etch rate increases almost linearly with the coil power. This is because an increase in the coil power will lead to an increase of ion density [12]. Therefore when the coil power is increased, more ions are created in the plasma which results in more ion bombardment and etch products and thus a higher etch rate. Another observation is that at the same coil power, the ICP etching with a higher platen power of 300 W has a higher etch rate compared to the etching with a lower platen power of 200 W. This result can be explained as follows: the diamond ICP etching with a higher platen power will generate ions with higher ion energy to bombard carbon atoms in diamond. Thus, at the same coil power (ion density), the etch rate increases with the platen power. A high etch rate of 0.21 µm/min has been

achieved at a coil power of 800 W, platen power of 300 W and a gas pressure of 5 mTorr.
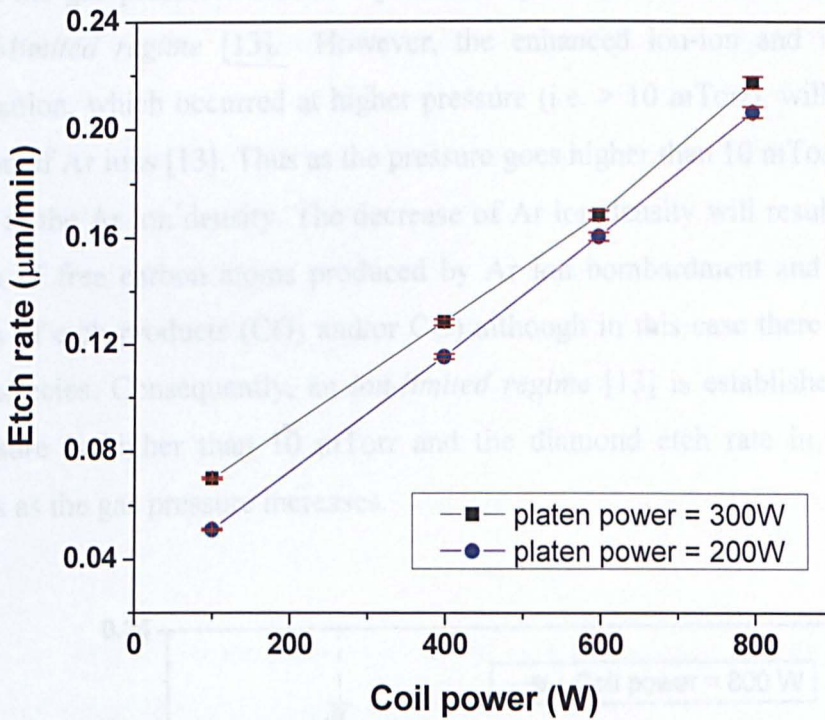

Figure 5.4 **Diamond etch rate versus ICP coil powers with constant ICP platen power of 200W and 300W. The error bar is 5 %. The pressure was fixed to 5 mTorr.**

5.2.1.3 Variation of ICP Gas Pressure

The dependence of diamond etch rate on gas pressure is investigated by varying the pressure from 5 to 30 mTorr. For this experiment, coil power of 800 W was used while the platen power was kept at 300 W. The flow rate of Ar and O_2 were set to 15 sccm and 40 sccm, respectively. The results are shown in Figure 5.5.

It is seen from the figure that initially the etch rate increases as the gas pressure increases from 5 to 10 mTorr then the etch rate decreases as the gas pressure increases further for coil power of 800 W. It is observed that the gas pressure of 10 mTorr gives the maximum etch rate of 0.22 μm/min. The reason for the 'increase-to-decrease' in the etch rate is explained as follows: At the low gas pressure region   (< 10 mTorr), the number of reactive species, such as O ions, increases with the gas pressure in the ICP chamber. Hence, by increasing the gas

pressure, more volatile etch products (CO_2 and/or CO) will form and thereafter be removed from the diamond surface. Consequently, there is an increase in the etch rate with the gas pressure. This low pressure regime (i.e. < 10 mTorr) is called a *chemical-limited regime* [13]. However, the enhanced ion-ion and ion-electron recombination, which occurred at higher pressure (i.e. > 10 mTorr), will reduce the generation of Ar ions [13]. Thus as the pressure goes higher than 10 mTorr, there is a decrease in the Ar ion density. The decrease of Ar ion density will result in a sharp reduction of free carbon atoms produced by Ar ion bombardment and therefore a reduction of etch products (CO_2 and/or CO) although in this case there are enough reactive species. Consequently, an *ion-limited regime* [13] is established when the gas pressure is higher than 10 mTorr and the diamond etch rate in this regime decreases as the gas pressure increases.
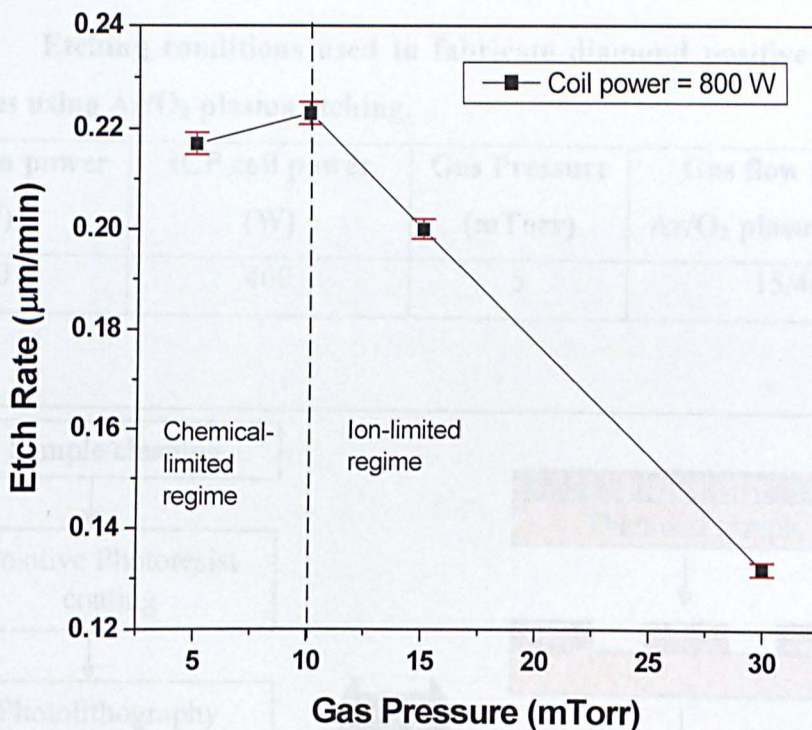

Figure 5.5   Diamond etch rate versus gas pressure with constant ICP platen powers of 300 W. The coil powers were set to 800 W.

5.2.2 Diamond Positive Spherical Micro-lenses

5.2.2.1 Fabrication of Diamond Positive Micro-lenses by Ar/O$_2$ Plasma Etching

Based on the study described in **Section 5.2.1**, diamond positive spherical micro-lenses have been fabricated by Ar/O$_2$ plasma etching. The etch conditions used to fabricate diamond micro-lenses were ICP platen power of 200 W and a coil power of 400 W. It was found that a slightly lower etch rate is desirable to achieve controllable etching. Thus, a gas pressure of 5 mTorr was selected and was sustained by Ar/O$_2$ gas flow rates of 15/40 sccm. Table 5.1 summarises the etching conditions used to fabricate positive spherical micro-lenses using Ar/O$_2$ plasma etching. The positive spherical micro-lenses were fabricated on high-pressure-high-temperature (HPHT) and natural diamond using photoresist "re-flow" and ICP etching technique. The fabrication sequence of the diamond positive micro-lenses is illustrated in Figure 5.6.

Table 5.1 **Etching conditions used to fabricate diamond positive spherical micro-lenses using Ar/O$_2$ plasma etching.**

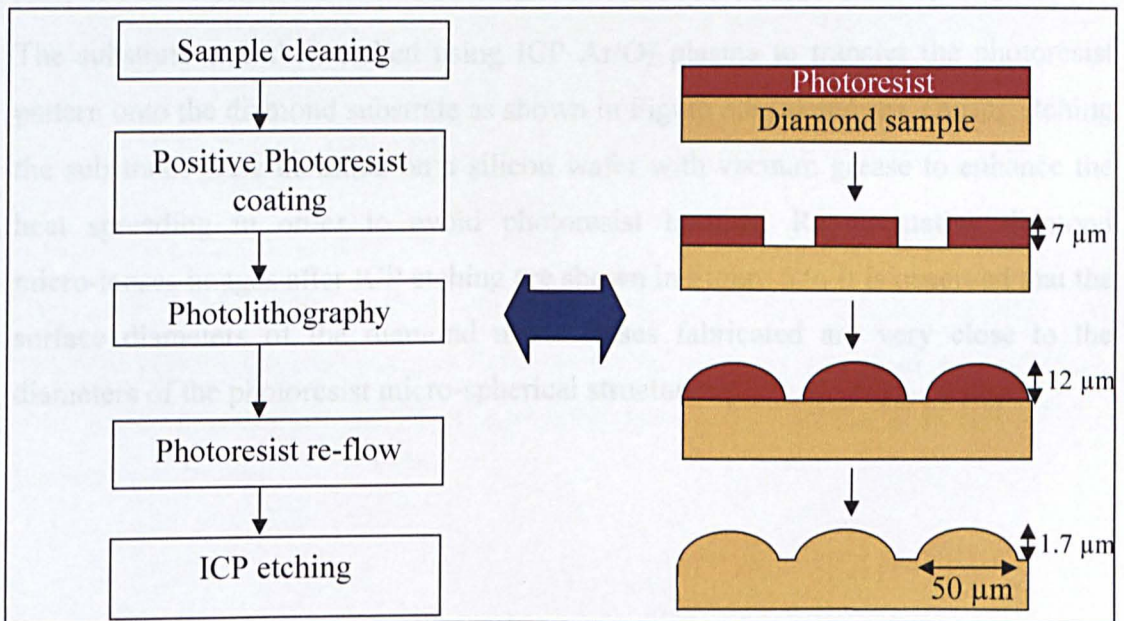| ICP platen power (W)	ICP coil power (W)	Gas Pressure (mTorr)	Gas flow rate of Ar/O$_2$ plasma (sccm)
200	400	5	15/40

Figure 5.6 **Process sequence of positive micro-lens fabrication.**

After sample cleaning (the details of diamond cleaning method are explained in **Chapter 3**), Shipley SPR 220 photoresist was first spin-coated onto the diamond substrates. Cylindrical pillars of photoresist with diameters ranging from 10 μm to 100 μm were then fabricated using standard photolithography method. After the formation of the photoresist pillars, the sample was then placed onto a hotplate at 125 °C for 5 mins. At this temperature, the micro-pillars melted and formed good spherical structures due to the surface tension. An optical image of photoresist micro-structures after re-flow is shown in Figure 5.7.
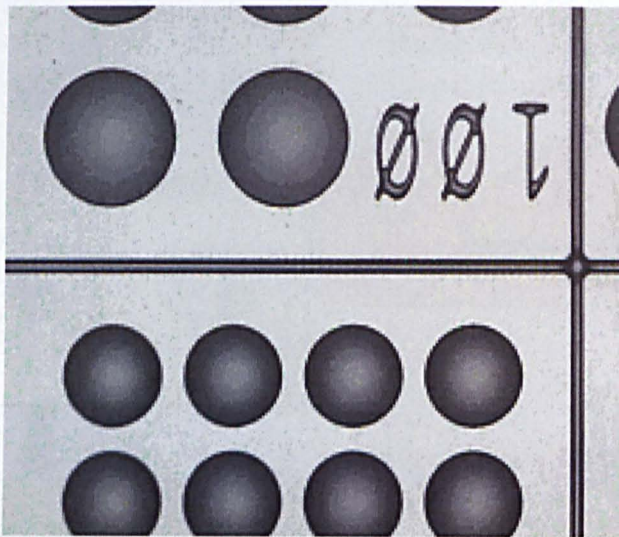

Figure 5.7   Photoresist micro-spherical structures after re-flow process.

The substrate was then etched using ICP Ar/O$_2$ plasma to transfer the photoresist pattern onto the diamond substrate as shown in Figure 5.8 (a) and (b). During etching, the substrates were mounted on a silicon wafer with vacuum grease to enhance the heat spreading in order to avoid photoresist burning. Representative diamond micro-lenses images after ICP etching are shown in Figure 5.9. It is observed that the surface diameters of the diamond micro-lenses fabricated are very close to the diameters of the photoresist micro-spherical structures.

(i)

Photoresist Structures

12 μm

Diamond Substrate

(ii)

Photoresist

Diamond substrate

Partial Photoresist Structures and
Partial Diamond Micro-lenses

50 μm

Diamond Substrate

(iii)

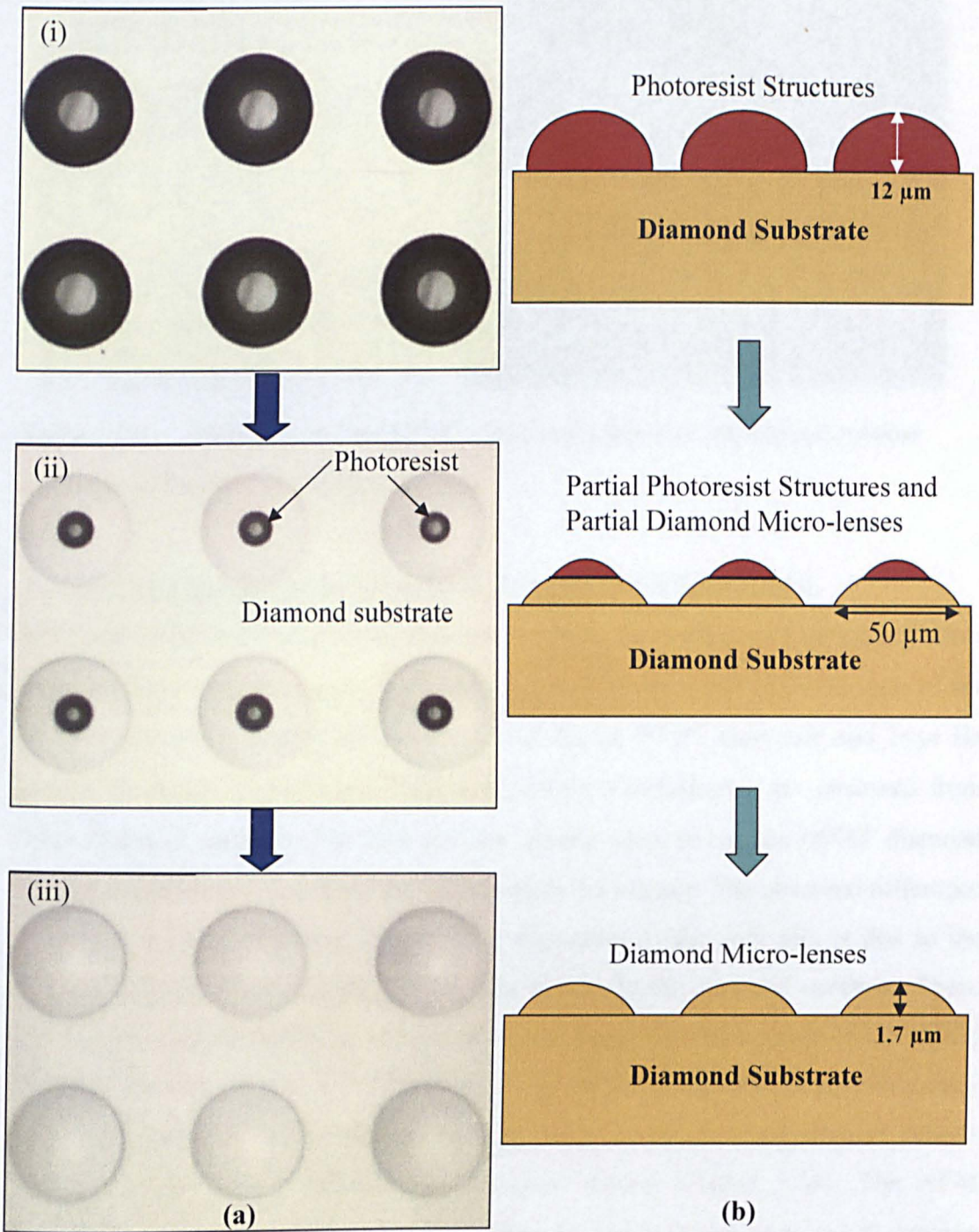Diamond Micro-lenses

1.7 μm

Diamond Substrate

(a)

(b)

Figure 5.8 **(a) ICP etching sequences (i) photoresist micro-structure (ii) partially etched micro-lenses and (iii) complete natural diamond micro-lenses after pattern transfer and (b) the corresponding schematic diagrams of the process flow in (a).**
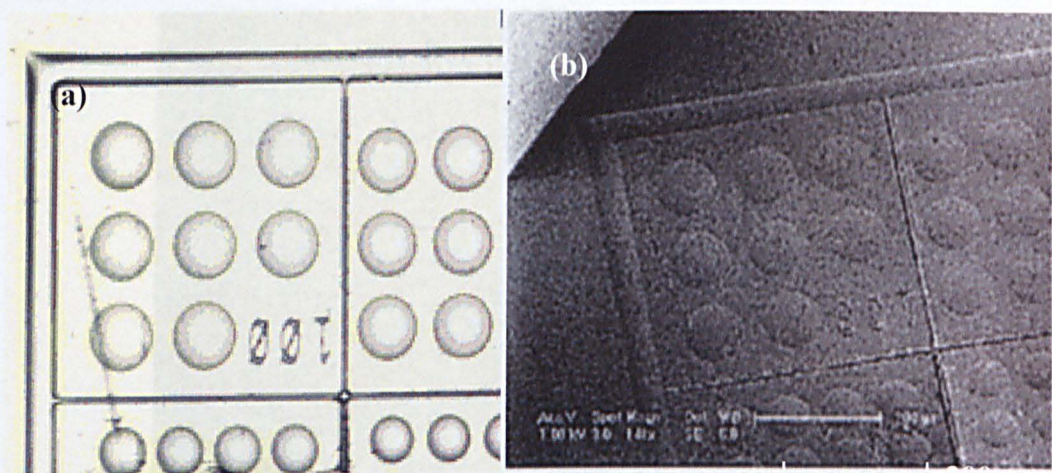
Figure 5.9 **Micro-lenses on HPHT diamond after ICP etching (a) optical microscope image and (b) SEM image.**

5.2.2.2 Characterisations of Diamond Positive Spherical Micro-lenses

SEM and AFM techniques were employed to study the surface morphology of these diamond micro-lenses. Figure 5.10 and Figure 5.11 show the SEM images of the positive micro-lenses after 30 minutes of etching on HPHT diamonds and Type IIa natural diamonds respectively. Different surface morphologies are observed from these diamond samples. The etch pits are clearly seen across the HPHT diamond sample whilst no pit is seen on the natural diamond sample. The observed difference is attributed to the diamond quality. The formation of the etch pits is due to the inherent defects, which caused non-uniform etching in the diamond substrate. These pits become clearly visible as etching proceeds. From the SEM image of the HPHT diamond shown in Figure 5.10, the etch pit density is estimated to be approximately 4.1×10^{10} cm^{-2}. As for the natural diamond, there are much fewer inherent defects and hence the surface remains smooth after etching (Figure 5.11). The AFM measurements show that these natural diamond micro-lenses have a low surface root-mean-square (RMS) roughness of approximately 1.2 nm for a 1 μm x 1 μm area, indicating a high surface quality.
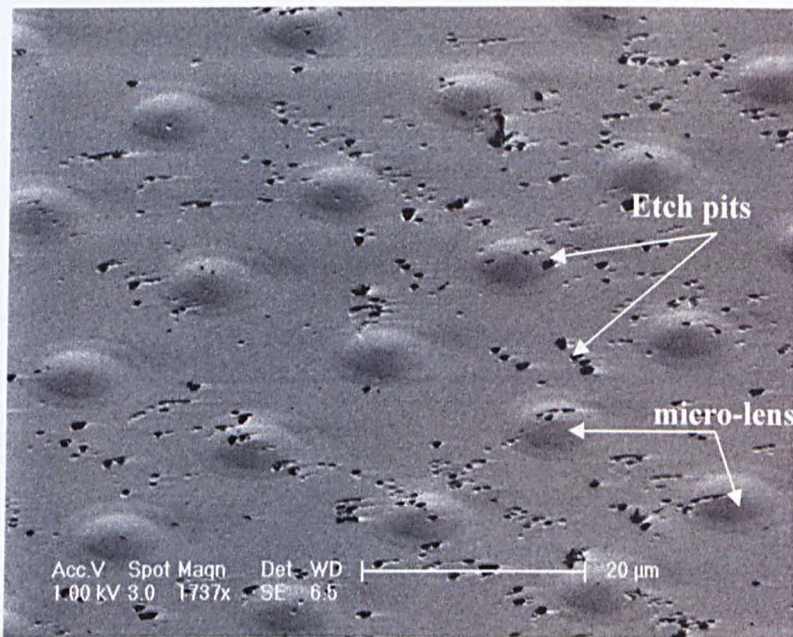
Figure 5.10   SEM image of a HPHT diamond positive micro-lens array.
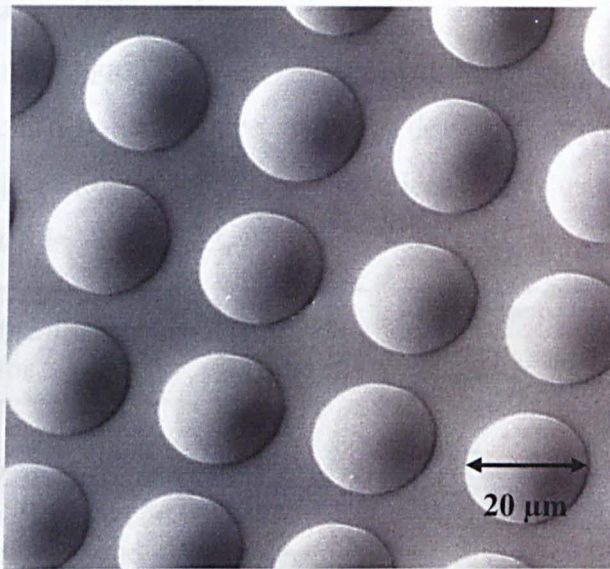
Figure 5.11   SEM image of a Type IIa natural diamond positive micro-lens array.

The optical properties of the positive micro-lenses were characterised using confocal microscopic technique. Cross sectional images, as shown in Figure 5.12, illustrate the focusing capabilities of the 50, 60 and 70 μm diameter micro-lenses. The focal lengths of these micro-lenses determined from the image were found to be very close to the calculated values, indicating the high optical quality of the micro-lenses [5].

microlens

focal point

60 µm

50 µm
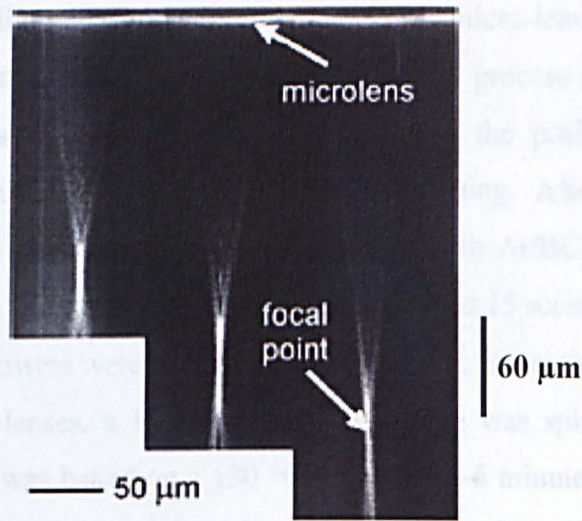
Figure 5.12 Cross-sectional confocal images, illustrating the focusing capabilities of the positive micro-lenses with diameters of 50, 60 and 70 µm with 1.7 µm height [5].

5.2.3 Negative Diamond Micro-lenses

5.2.3.1 Fabrication of Diamond Negative Micro-lenses by Ar/O$_2$ Plasma Etching

Unlike the fabrication of positive micro-lenses, as described in previous subsection, the diamond negative micro-lenses were fabricated by using hot-embossing technique as illustrated in Figure 5.13.

Figure 5.13 Fabrication sequence of diamond negative micro-lenses.

Using this technique, a silicon (Si) substrate with spherical micro-lenses of ~10 μm height was first fabricated as a mould. The photolithograp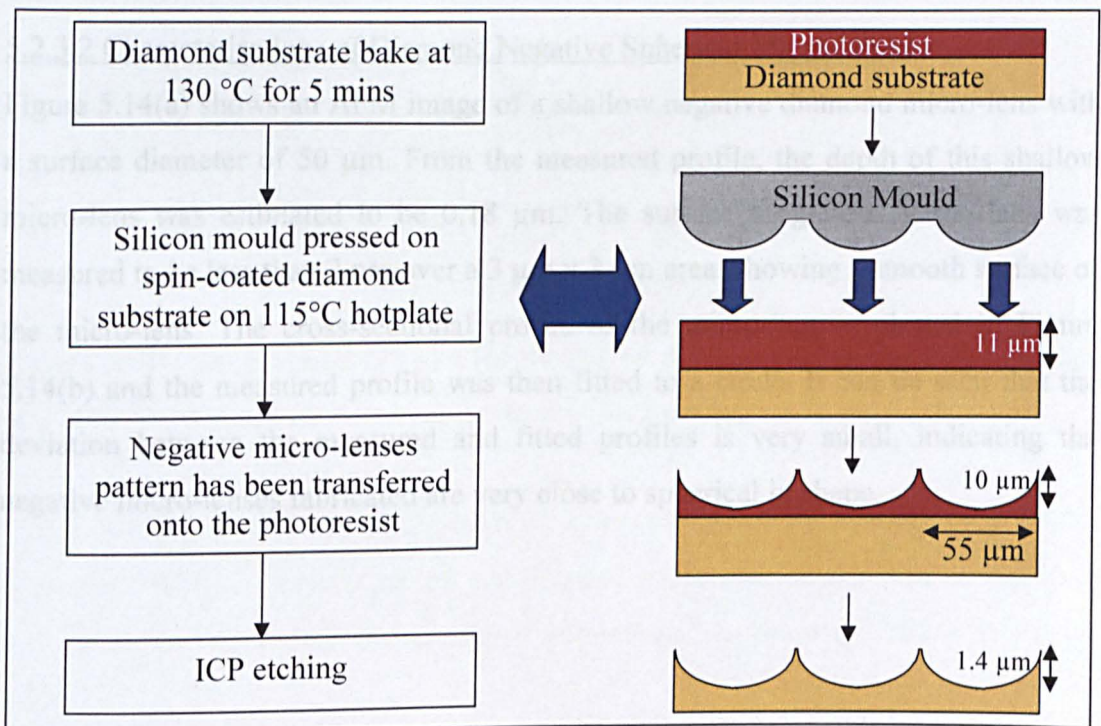hy process of making the silicon micro-lens molds is similar to that of fabricating the positive diamond micro-lenses **(subsection 5.2.2.1)** except ICP silicon etching. After the reflow process, the silicon chips were subjected to ICP etching with $Ar/BCl_3/Cl_2$ plasma. The flow rates of $Ar/BCl_3/Cl_2$ used were 15 sccm, 50 sccm and 15 sccm, respectively, with the platen and coil powers were set to 100 W and 600 W, respectively. To make diamond negative micro-lenses, a HPHT diamond substrate was spin-coated with SPR 220 photoresist and was baked on a 130 °C hotplate for 5 minutes. The silicon micro-lens mould was then pressed against the photoresist layer/diamond on a hotplate, set to 115 °C so as to soften the photoresist, as shown in Figure 5.13.

Subsequently, the diamond substrate and silicon mould were separated gently by using tweezers. The photoresist negative micro-structures were then etched using Ar/O_2 plasma with the same etch conditions of positive micro-lenses so as to transfer the negative micro-lens pattern to the diamond substrate. By this way, negative micro-lenses with diameters of 50 μm and 55 μm are fabricated successfully on HPHT diamonds.

5.2.3.2 Characterisations of Diamond Negative Spherical Micro-lenses

Figure 5.14(a) shows an AFM image of a shallow negative diamond micro-lens with a surface diameter of 50 μm. From the measured profile, the depth of this shallow micro-lens was estimated to be 0.18 μm. The surface roughness of the lens was measured to be less than 2 nm over a 3 μm x 3 μm area, showing a smooth surface of the micro-lens. The cross-sectional profile of the micro-lens is plotted in Figure 5.14(b) and the measured profile was then fitted to a circle. It can be seen that the deviation between the measured and fitted profiles is very small, indicating the negative micro-lenses fabricated are very close to spherical in shape.

(a)

(b)

Figure 5.14 **(a) AFM image and (b) measured surface profile and fitted profile of a HPHT diamond negative micro-lens with diameter of 50 μm.**

Figure 5.15(a) shows an AFM image of a representative deep negative diamond micro-lens with a diameter of 55 μm. Again, evaluation of the lens profile was undertaken by comparing the measured profile with a circle as shown in Figure 5.15(b).
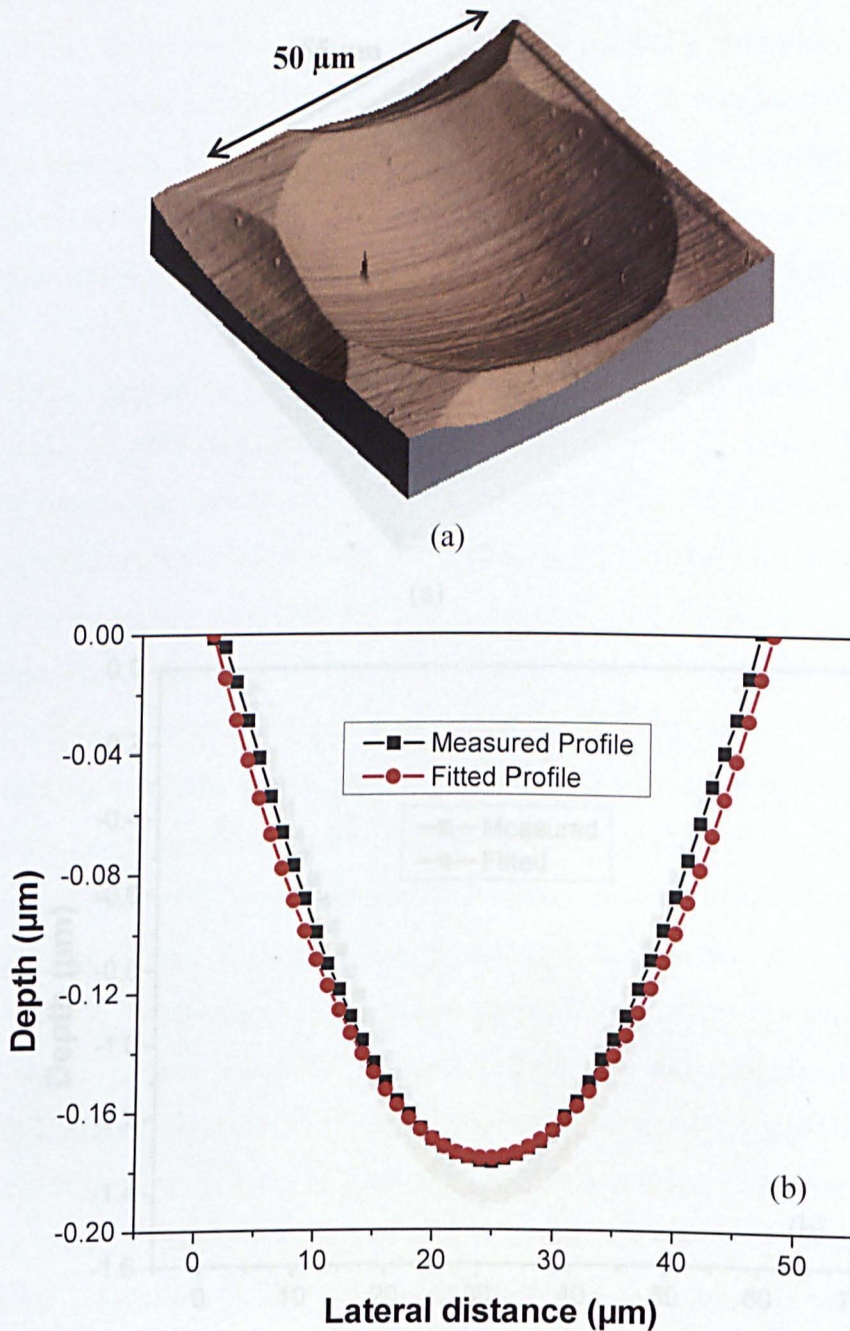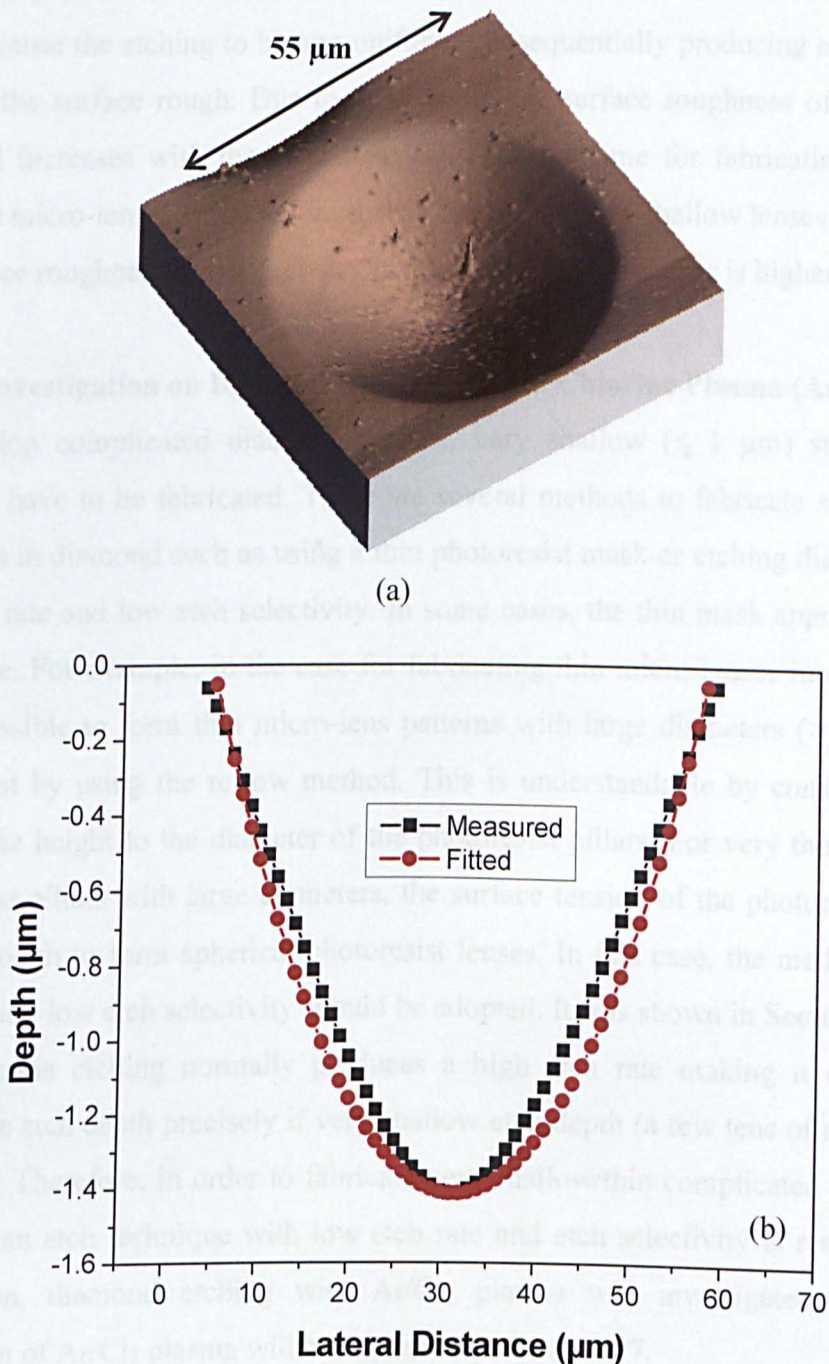
Figure 5.15   **(a) AFM image and (b) measured surface profile and fitted profile of a deep HPHT diamond negative micro-lens with diameter of 55 μm.**

It is evident that the deviation between the measured and fitted profile is very small. Nevertheless, the surface RMS roughness of this lens is rather high, i.e. 15 nm for a 3 μm x 3 μm area. These results show there is a big roughness difference between the shallow and deep negative diamond micro-lenses. As discussed in **subsection**

5.2.2.2, high density intrinsic defects exist in the HPHT diamond. These intrinsic defects cause the etching to be non-uniform, consequentially producing etch pits and making the surface rough. Due to this reason, the surface roughness of the HPHT diamond increases with the etch duration. The etch time for fabricating the deep diamond micro-lenses is much longer than that for etching shallow lenses. Therefore, the surface roughness of the deep negative diamond micro-lenses is higher.

5.3 Investigation on ICP Etching - Argon and Chlorine Plasma (Ar/Cl$_2$)

To develop complicated diamond devices, very shallow (< 1 μm) structures in diamond have to be fabricated. There are several methods to fabricate shallow/thin structures in diamond such as using a thin photoresist mask or etching diamond with low etch rate and low etch selectivity. In some cases, the thin mask approach is not applicable. For example, in the case for fabricating thin micro-lenses in diamond, it is not possible to form thin micro-lens patterns with large diameters (> 50 μm) in photoresist by using the reflow method. This is understandable by considering the ratio of the height to the diameter of the photoresist pillars. For very thin (< 1 μm) photoresist pillars with large diameters, the surface tension of the photoresist is not strong enough to form spherical photoresist lenses. In this case, the method of low etch rate and low etch selectivity should be adopted. It was shown in **Section 5.2** that Ar/O$_2$ plasma etching normally produces a high etch rate making it difficult to control the etch depth precisely if very shallow etch depth (a few tens of nanometre) is desired. Therefore, in order to fabricate very shallow/thin complicated features in diamond, an etch technique with low etch rate and etch selectivity is required. For this reason, diamond etching with Ar/Cl$_2$ plasma was investigated. The etch mechanism of Ar/Cl$_2$ plasma will be explained in **Chapter 7**.

5.3.1 Experimental Results and Discussion: Ar/Cl$_2$ Plasma

Figure 5.16(a) plots the etch rate and etch selectivity of diamond etching with Ar/Cl$_2$ plasma as a function of the ICP coil power at a fixed platen power of 300 W. The gas pressure used was 5 mTorr with the Ar/Cl$_2$ gas flow rates of 25/40 sccm.
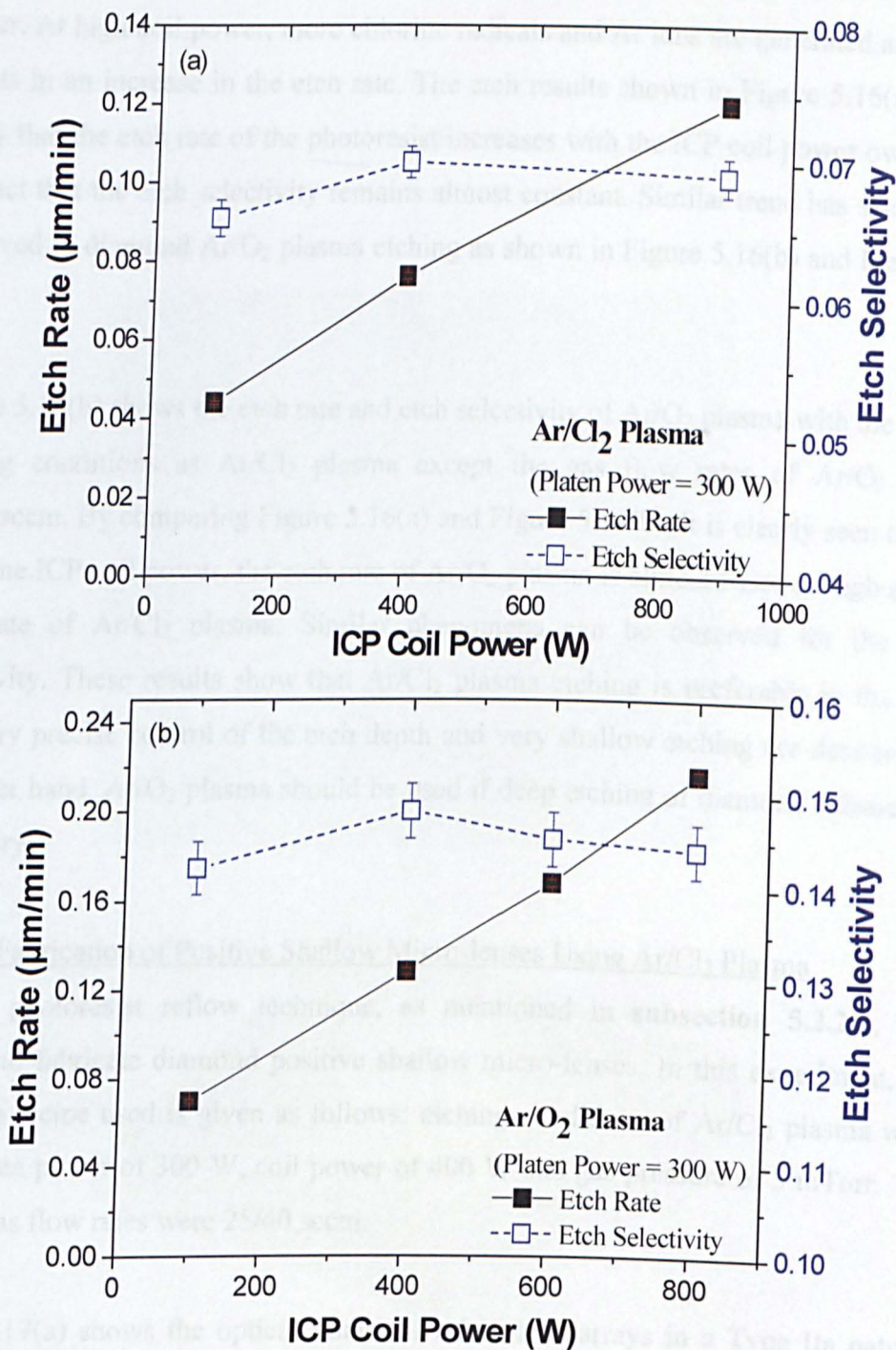
Figure 5.16 Etch rate and selectivity using (a) Ar/Cl$_2$ and (b) Ar/O$_2$ plasmas as a function of ICP coil powers. The ICP platen power and gas pressure were fixed at 300 W and 5 mTorr, respectively.

It is observed that the etch selectivity remains almost constant regardless of the variation of ICP coil power. On the other hand, the etch rate increases linearly with

the ICP coil power which is explainable as the ion density increases with the ICP coil power. At high coil power, more chlorine radicals and Ar ions are generated and this results in an increase in the etch rate. The etch results shown in Figure 5.16(a) also imply that the etch rate of the photoresist increases with the ICP coil power owing to the fact that the etch selectivity remains almost constant. Similar trend has also been observed in diamond Ar/O_2 plasma etching as shown in Figure 5.16(b) and literature [6,8].

Figure 5.16(b) shows the etch rate and etch selectivity of Ar/O_2 plasma with the same etching conditions as Ar/Cl_2 plasma except the gas flow rates of Ar/O_2 were 15/40 sccm. By comparing Figure 5.16(a) and Figure 5.16(b), it is clearly seen that at the same ICP coil power, the etch rate of Ar/O_2 plasma is almost twice as high as the etch rate of Ar/Cl_2 plasma. Similar phenomena can be observed for the etch selectivity. These results show that Ar/Cl_2 plasma etching is preferable in the case that very precise control of the etch depth and very shallow etching are desired. On the other hand, Ar/O_2 plasma should be used if deep etching of diamond substrate is necessary.

5.3.1.1 Fabrication of Positive Shallow Micro-lenses Using Ar/Cl_2 Plasma

Similar photoresist reflow technique, as mentioned in **subsection 5.2.2.1**, was applied to fabricate diamond positive shallow micro-lenses. In this experiment, the ICP etch recipe used is given as follows: etching conditions of Ar/Cl_2 plasma were ICP platen power of 300 W, coil power of 400 W and gas pressure of 5 mTorr. The Ar/Cl_2 gas flow rates were 25/40 sccm.

Figure 5.17(a) shows the optical image of micro-lens arrays in a Type IIa natural diamond fabricated by Ar/Cl_2 plasma etching. A three-dimensional AFM image of such a micro-lens with a diameter of 50 μm is shown in Figure 5.17(b). No etch pit is observed on this natural diamond as reported in **Section 5.2.2.2**. The surface diameter and height of the micro-lens shown in Figure 5.17(b) were measured to be approximately 50 μm and 0.75 μm respectively. The surface RMS roughness of the diamond micro-lenses is less than 1.0 nm for a scanned area of 5 μm x 5 μm. These

results show that the diamond lenses etched by Ar/Cl$_2$ plasma are smooth. Also, it is found that these diamond micro-lenses have a smoother surface than those fabricated by using Ar/O$_2$ plasma etching whose surface RMS roughness is approximately 3 nm with the same AFM scanned area [8]. The effect of the surface smoothing by using Ar/Cl$_2$ plasma etching will be discussed in details in **Chapter 7**.
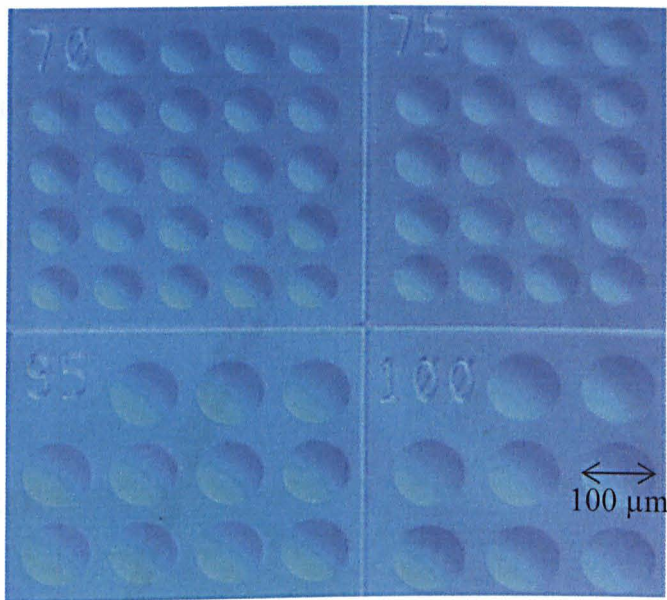
(a)
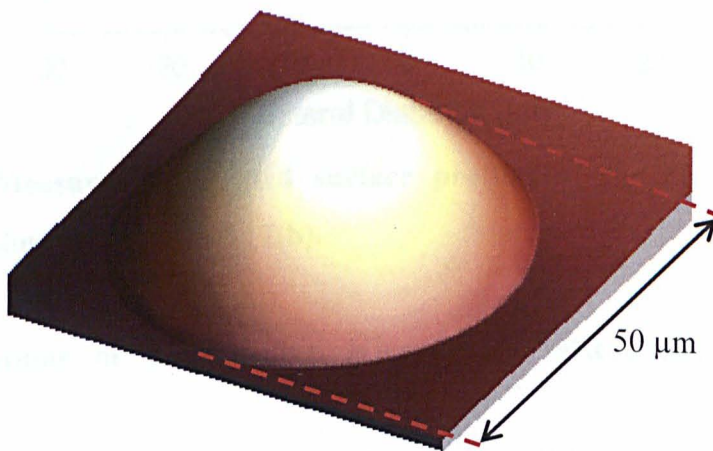
(b)

Figure 5.17 (a) **Optical image of arrays of Type IIa natural diamond micro-lenses with different diameters, and (b) A three-dimensional AFM image of a diamond micro-lens with a diameter of 50 μm.**

The profile of the diamond micro-lenses was reviewed by examining the cross-sectional scan of the AFM images. The measured cross-sectional profile of the diamond micro-lens with a surface diameter of 50 μm and the fitted circle profile are plotted in Figure 5.18. It is observed that the difference between the two profiles is very small. This indicates that the actual profile of the diamond micro-lens is very close to the desired spherical shape.
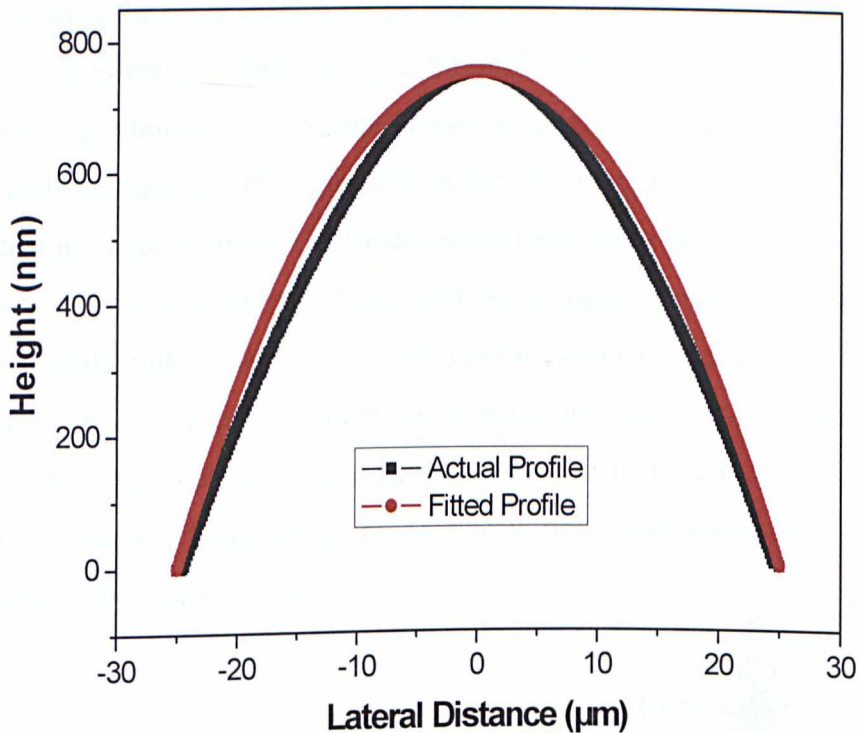
Figure 5.18   Measured and fitted surface profiles of the 50 μm diameter micro-lens as shown in Figure 5.17(b).

5.3.2   Applications of the Positive Micro-lenses: Micro-lensed Microchip VECSEL [14]

Vertical-external cavity surface emitting lasers (VECSELs) have attracted much attention recently because of their attractive attributes including high-power, circularly-symmetric output beams and versatility in operating wavelength [15-16]. The main element constituting a VECSEL is the semiconductor active structure: it is made by a quantum well gain region grown on top of a distributed Bragg reflector (DBR). The laser cavity is usually completed by an external mirror, or mirrors, separated from the semiconductor chip by an air-gap. An example of a conventional

VECSEL is shown in Figure 5.19(a). It can be seen that the laser cavity is separated from the semiconductor chip by an air gap. Heat dissipation from the gain region is important in order to power scale the output of such lasers. One solution to manage the heat effectively is to bond a high thermal conductive material such as diamond, directly on top of the semiconductor structure. Furthermore, this heat spreader approach opens up new applications such as the possibility to realise highly compact quasi-monolithic VECSELs, called μ-VECSEL, which can be accomplished simply by mirror-coating the outer surface of the heat spreader. However, the laser cavity of the μ-VECSEL is mainly stabilised by a thermal lens appearing in the gain region when it is being pumped [17]. As the power is ramped up, the thermal lens effect increases and the fundamental mode size in the active region decreases. Hence, the mode-matching of the pump to the fundamental laser mode is only possible for one given power only and the output of the laser beam quality tends to degrade (due to the presence of the higher transverse modes) as the power is varied. To ensure stable fundamental mode operation in addition to excellent heat removal, micro-lensed μ-VECSEL, having a plano-concave cavity, as shown in Figure 5.19(b), has been fabricated because the fundamental mode size is only determined by the physical characteristic of the cold cavity [14].
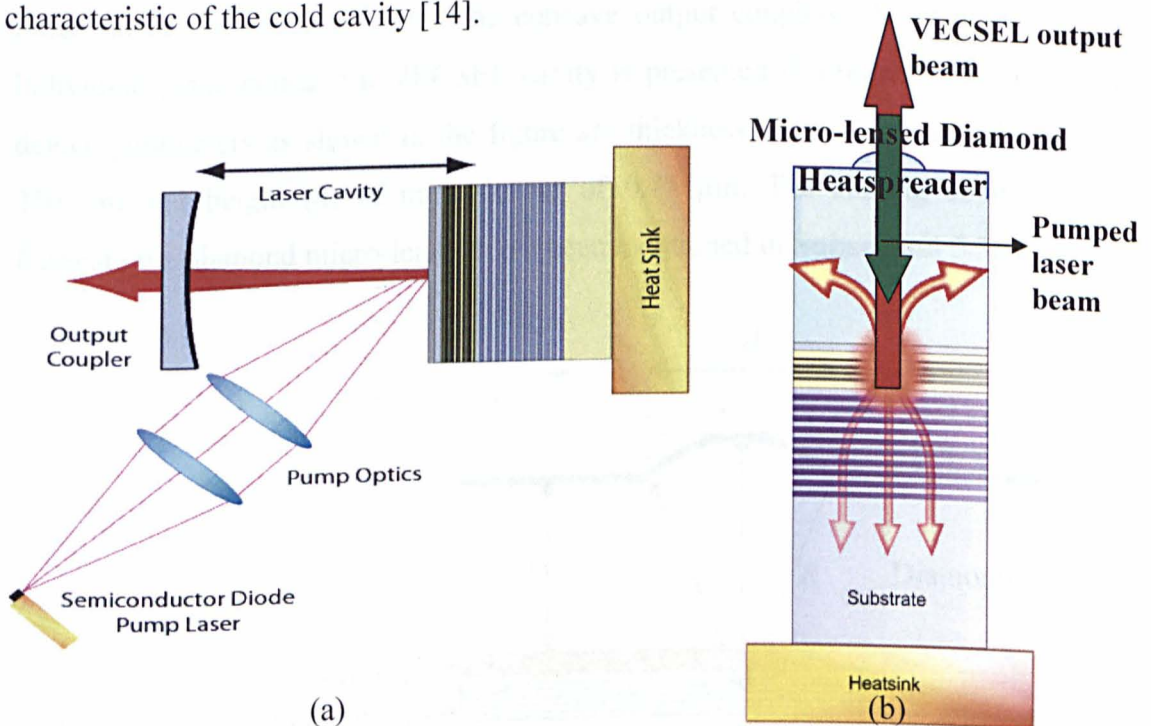

Figure 5.19   (a) A conventional VECSEL pumped by semiconductor diode laser. (b) A μ-VECSEL stabilised by diamond lens.

This section demonstrates the operation and investigates the properties of an array of micro-lensed μ-VECSELs whose plano-concave cavities are achieved by micro-patterning a diamond heat-spreader. This is a collaboration work together with Dr. Nicolas Laurand from the Institute of Photonics, University of Strathclyde where I was responsible in fabricating the good quality micro-lenses with different diameters with the height of 0.75 μm. Meanwhile Dr. Nicolas Laurand was responsible for the integration and deposition of an anti-reflection coating on top of the micro-lenses and finally characterising the integrated structures.

5.3.2.1 Device Design and Fabrication

The 1055-nm-emitting micro-lensed μ-VECSELs under study are constituted of a semiconductor part liquid-capillarity bonded to a single-crystal diamond heat-spreader whose outer surface has been shaped into an array of spherical micro-lenses (μ-lenses) and subsequently mirror-coated. The semiconductor structure consists of 10 InGaAs quantum wells (QWs) grown on top of a 30.5-pair AlAs/Al$_{0.2}$Ga$_{0.8}$As DBR. A SiO$_2$/TiO$_2$ coating, with nominal peak reflectivity of 95 % at 1.055 μm and an anti-reflection at 808 nm, was deposited onto the diamond outer surface in order to create the concave output couplers. A schematic of an individual plano-concave μ-VECSEL cavity is presented in Figure 5.20. The other device parameters as shown in the figure are thickness (*t*) of diamond substrate of 250 μm and height (*h*) of micro-lenses of 0.75 μm. The etching conditions to fabricate the diamond micro-lenses have been mentioned in **Subsection 5.3.1.1.**
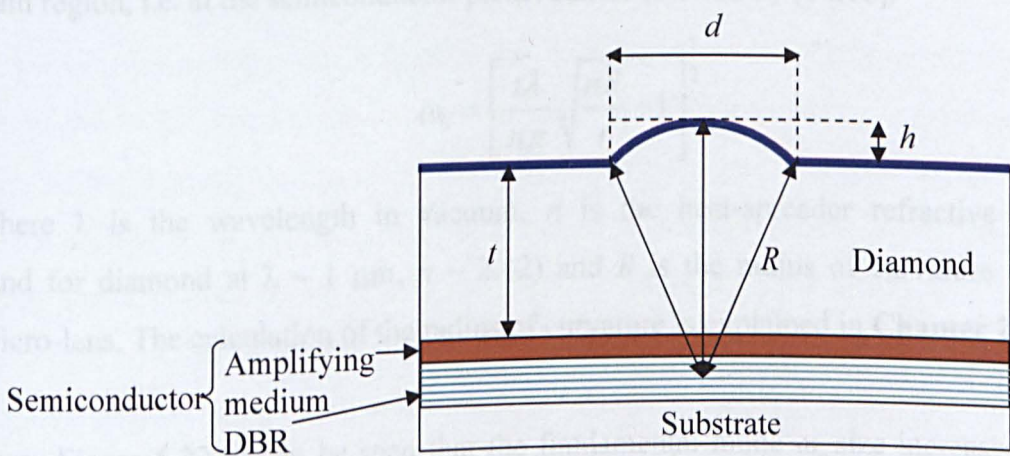

Figure 5.20   Schematic of an individual μ-VECSEL [14].

5.3.2.2 Experimental Setup and Results

A schematic of the experimental set-up is shown in Figure 5.21. The μ-VECSEL array is directly mounted on a copper holder held at a temperature of 10 °C. The holder is fixed on a XYZ translation stage for alignment. The devices are pumped, through the heat-spreader, with polarisation coupled 810-nm diode lasers. The pump beam, with up to an average power of 210 mW, is delivered using a 15-mm focal length lens (NA~ 0.25), yielding pump spot size in the 13-30 μm range. It can be seen in Figure 5.21(a) that the μ-VECSEL signal is separated from the pump by the use of a dichroic mirror followed by a high-pass filter. Figure 5.21(b) shows the schematic diagram of the single μ-VECSEL probing.
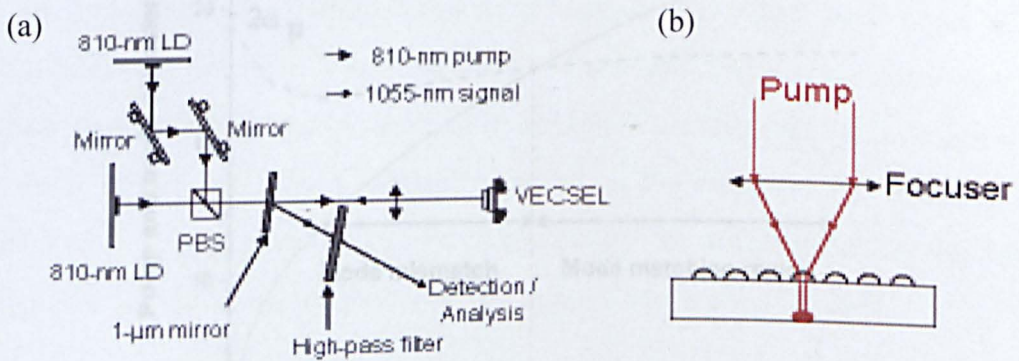
Figure 5.21 (a) Experimental set-up. (b) Schematic of the single μ-VECSEL probing [14].

Given the micro-lensed μ-VECSEL parameters, the fundamental mode size in the gain region, i.e. at the semiconductor plane, can be inferred by [14,16]:

$$\omega_0 = \left[\frac{t\lambda}{n\pi} \sqrt{\frac{nR}{t} - 1} \right]^{\frac{1}{2}} \tag{5.1}$$

where λ is the wavelength in vacuum, n is the heat-spreader refractive index (and for diamond at $\lambda \sim 1$ μm, $n \sim 2.42$) and R is the radius of curvature of the micro-lens. The calculation of the radius of curvature is explained in **Chapter 2.**

From Figure 5.22, it can be seen that the fundamental mode ω_o size increases with the lens diameter d with respect to the radius of curvature R, and a cut-off exists at

$d = 25$ μm ($R \sim 105$ μm). The cavity is therefore stable only for $d > 25$ μm. For d varying from 40 to 100 μm ($R \sim 267$ to 1667 μm) the fundamental mode diameter ranges from 12 to 22.5 μm. The number of modes that can oscillate depends on the mode-matching conditions. If the pump spot size matches the fundamental mode size, the laser operates mainly in the TEM_{00} mode because the higher order modes have a bigger spot size. On the other hand, if the pump spot is big enough to excite higher order modes, then the laser tends to operate in a superposition of modes.
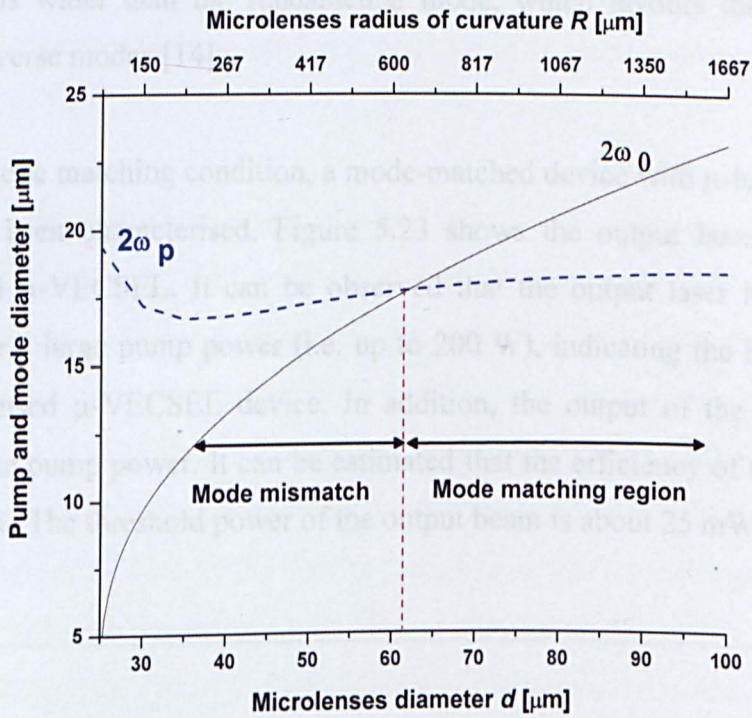
Figure 5.22 **Fundamental mode ($2\omega_0$) and pump diameter ($2\omega_P$) as a function of lens diameter d (bottom axis) and radius of curvature R (top axis) [14].**

In the experiment the pump is focused down onto a single array element through the top of the device. For a given focuser, the pump spot size that can be achieved on the gain region depends on the μ-lens focal length, which itself depends on the μ-lens diameter. The expected pump spot size can be calculated if one knows the pump beam characteristics before the focuser and by considering the μ-lens as a lens of focal light as given by Equation (5.2). Considering that the refractive index of air is 1, the focal length f of this surface lens can be obtained by employing Equation (2.6) as:

$$f(d) = \frac{nR(d)}{(n-1)} \qquad (5.2)$$

The pump beam was measured to have a $1/e^2$ radius of 1.25 mm right before the focuser. Results of the pump spot calculations for a 15-mm focal length of focusing lens are shown in Figure 5.22 along with the fundamental spot size. A minimum pump spot size smaller than the fundamental mode size indicates that mode-matching is possible by simply changing the position of the focus with respect to the μ-VECSEL. In this work, it is found out that the mode-matching is possible for devices with μ-lens diameter above ~ 65 μm ($R > 705$ μm). Below this value the pump spot is wider than the fundamental mode, which favours the excitation of higher transverse modes [14].

To enable mode matching condition, a mode-matched device with μ-lens diameter of 90 μm has been characterised. Figure 5.23 shows the output laser beam of the micro-lensed μ-VECSEL. It can be observed that the output laser beam does not degrade over a large pump power (i.e. up to 200 W), indicating the high quality of the micro-lensed μ-VECSEL device. In addition, the output of the laser beam is limited by the pump power. It can be estimated that the efficiency of the laser beam is about 35 %. The threshold power of the output beam is about 25 mW.
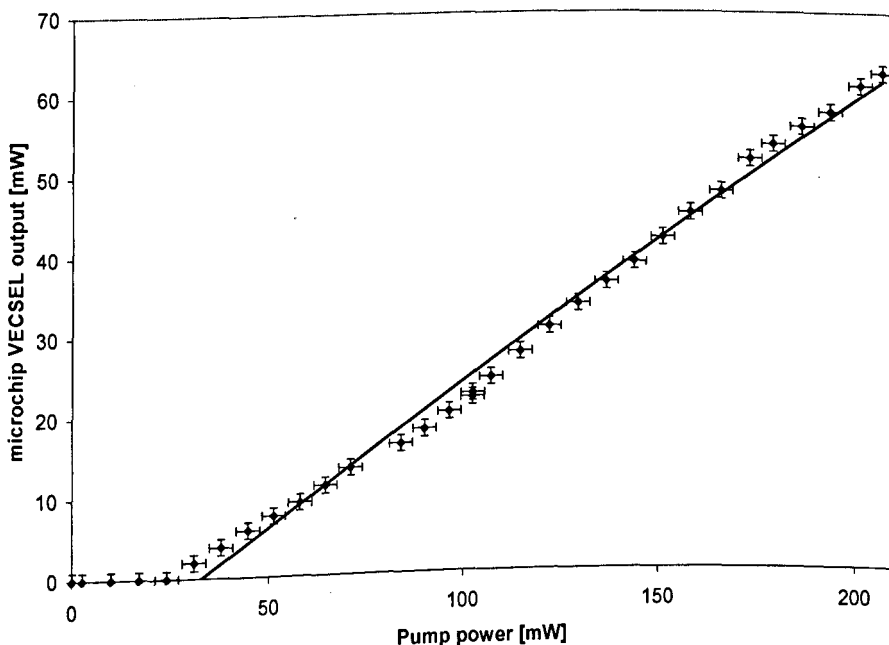

Figure 5.23 **Output laser beam of a micro-lensed μ-VECSEL with lens diameter of 90 μm [14].**

5.4   Summary

In this chapter, detailed investigations on ICP etching of diamond using different plasmas, in this case oxygen-based (Ar/O$_2$) and chlorine-based (Ar/Cl$_2$) plasma, and the effect of the various ICP platen powers, coil powers and gas pressures on the etch rate are presented. Fabrication of various micro-structures including micro-spherical positive and negative lenses is studied. This work also presents an optical application using diamond positive micro-lenses as a laser-cavity-integrated element (micro-lensed μ-VECSEL) to ensure stable fundamental mode operation (reducing thermal lens effect for high power pump laser) in addition to excellent heat removal from the μ-VECSEL.

In this work, the highest etch rate obtained using Ar/O$_2$ plasma (25/40 sccm) is 0.22 μm/min with the etching conditions of ICP platen power of 300 W, coil power of 800 W and gas pressure of 10 mTorr. A comparison between Ar/O$_2$ plasma and Ar/Cl$_2$ plasma has been carried out. It is found that the diamond etch rate and etch selectivity using Ar/Cl$_2$ plasma is only half of those by using Ar/O$_2$ plasma, which enables a good control on the etch depth for fabricating diamond microstructures. In addition, it is observed that Ar/Cl$_2$ plasma gives a smoother surface than the diamond micro-lenses fabricated by using Ar/O$_2$ plasma although studies show that the latter does not damage the surface during etching. Nevertheless, Ar/Cl$_2$ plasma is preferable if precise and very shallow etch depth (i.e. less than 10 nm) is desired, while Ar/O$_2$ plasma is employed for deep etching. Hence, Ar/O$_2$ plasma has been chosen to fabricate deep micro-structures including micro-cylindrical lenses, micro-ring lenses and micro-trenches, as shown in **Chapter 6**.

5.5   References

[1] A.M, Zaitsev, *Optical Properties of Diamond – A Data Handbook*, Springer (2001).

[2] Y. Ando, Y. Nishibayashi, K. Kobashi, *Dia. Rel. Mat.*, **11**, 824 (2002).

[3] G.M.R. Sirineni, H.A. Naseem, *Dia. Rel. Mat.*, **6**, 952 (1997).

[4] F. Silva, R.S. Sussmann, *Dia. Rel. Mat.*, **12**, 369 (2003).

[5] H.W. Choi, E. Gu, C. Liu, C. Griffin, J.M. Girkin, I.M. Watson, M.D. Dawson, *J. Vac. Sci. & Technol. B*, **23**, 130 (2005).

[6] M. Karlsson, F. Nikolajeff, *Opt. Exp.*, **11**, 507 (2003).

[7] C.L. Lee, H.W. Choi, E. Gu, H. Murphy, M.D. Dawson, *Dia. Rel. Mat.*, **15**, 725 (2006).

[8] C.L. Lee, E. Gu, M.D. Dawson, *Dia. Rel. Mat.*, **16**, 944 (2007).

[9] S.J. Pearton, A. Katz, F. Ren and J.R. Lothian, *Elec. Lett.*, **28**, 822 (1992).

[10] E.G. Spencer and P.H. Schmidt, *J. Appl. Phys.*, **43**, 2956 (1972).

[11] M.H. Nazere, A.J. Neves, *Properties, Growth and Applications of Diamond*, INSPEC Publication (2001).

[12] J. K. Sheu, Y.K. Su, G.C. Chi, M. J. Jou, C.C. Liu, C. M. Chang,, *J. Appl. Phys.*, **85**, 1970 (1999).

[13] L. Jiang, N.O.V. Plank, *J. Phys. D.:Appl. Phys.*, **37**, 1809 (2004).

[14] N. Laurand, C.L. Lee, E. Gu, J.E. Hastie, S. Calvez, M.D. Dawson, *Opt. Exp.*, **15**, 9341 (2007).

[15] C.W. Wilmsen, H. Temkin, L.A. Coldren, L. Coldren, *Vertical Cavity Surface Emitting Lasers*, Cambridge University Press (2001).

[16] A.E. Siegman, *Lasers*, University Science Books (1986).

[17] A.J. Kemp, A.J. Maclean, J.E. Hastie, S.A. Smith, J.M. Hopkin, S. Calvez, G.J. Valentine, M.D. Dawson, D. Burns, *Appl. Phys. B-Laser O.*, **83**, 189 (2006).

Chapter 6

Special Diamond Micro-Optics: Micro-cylindrical, Micro-ring, Complex Micro-lenses and Optical Gratings

6.1   Introduction

In chapter 5, spherical diamond micro-lenses such as convex (positive), concave (negative) and micro-lensed microchip VECSEL have been discussed. In this chapter, the fabrication and characterisation of various special diamond micro-optical components including micro-cylindrical and ring lenses, complex micro-lenses and diamond gratings will be presented.

6.2   Diamond Micro-cylindrical and Micro-ring Lenses

Instead of simple spherical micro-lenses, more complex forms of micro-optical components such as micro-cylindrical and micro-ring lenses are required for manipulating light beam and developing new optical filters, micro-cavities and micro-ring resonators.

Micro-cylindrical lenses can be applied to focus collimated light along one axis or to circularise the beam from a laser diode by arranging two cylindrical lenses perpendicularly to each other [1]. Fu *et al.* showed that the integration of a SiO_2 micro-cylindrical lens with a laser diode can lead to the improvement of coupling efficiency [2-3]. It has also been reported that the astigmatism in a diode laser collimator can be corrected by placing a concave micro-cylindrical lens in front of the collimator [2]. However, to our best knowledge, the fabrication of micro-ring lenses has not yet been reported. Nevertheless, micro-ring structures such as micro-resonators and micro-light emitters in ring format have recently attracted much attention [4-7]. Applications of such concepts in areas including deep-ultraviolet LEDs [8] and ultraviolet laser diodes (where the refractive index of diamond is a close match to that of gallium nitride), diamond single-photon sources [9] and biomedical sensors and in-vitro imaging systems would all benefit from the availability of novel optical microstructures formed in diamond. It is expected that

the micro-cylindrical and ring lenses made of diamond will have excellent performances such as high thermal stability and high transparency over a wide range of wavelengths. This section will focuses on fabrication and characterisation of diamond micro-cylindrical and micro-ring lenses.

Similar fabrication process to that of making the positive spherical micro-lenses, as described in **Section 5.2.2**, was applied to fabricate diamond micro-cylindrical and micro-ring lenses. These micro-cylindrical and micro-ring lenses were fabricated in Chemical-vapour-deposition (CVD) diamonds utilising ICP Ar/O_2 plasma etching.

The surface profile and quality of the diamond micro-cylindrical and micro-ring lenses were evaluated by atomic force microscopy (AFM). Laser scanning reflection/transmission confocal microscopy, which is a new technique for measuring micro-optical components [10-12], was used to characterise the optical properties of these diamond lenses. The experimental setup of the confocal microscope has been reported **Chapter 4**.

6.2.1   Micro-cylindrical Lenses

The fabrication of micro-cylindrical lenses involves the standard photolithography and photoresist reflow technique, which has been described in **Section 3.4**. The photolithography process was performed by utilising a special mask which consists of a micro-lens array with a micro-lens width and length of 20 μm and 200 μm, respectively. The micro-structures were then etched using ICP tool. The ICP etching recipe for fabricating the micro-cylindrical lenses is listed in Table 6.1. Under these conditions, the etch rate is 0.065 μm/min. The etching duration was set to 20 minutes.

Table 6.1   ICP parameters for fabricating diamond micro-cylindrical lenses by using Ar/O_2 plasma etching.

Coil Power (W)	Platen Power (W)	Gas Pressure (mTorr)	Gas flow rates of Ar and O_2 (sccm)
400	50	5	15/40

A three-dimensional (3D) AFM image of a portion of a representative diamond micro-cylindrical lens is shown in Figure 6.1(a). The base width of the lens was measured to be 20 μm. In the lens array, all the fabricated micro-cylindrical lenses have the same height of 1.25 μm. The AFM measurements show that the surface RMS roughness of the diamond micro-cylindrical lenses is less than 3 nm for a scanned area of 5 x 5 μm. This is in the same range as the roughness at the non-etched surface. This result indicates that the ICP etching using Ar/O$_2$ plasma does not make the diamond surface rougher. For their optical applications, it is quite important that the diamond lenses have a very smooth surface especially when integrated with photonic and optoelectronic devices to make a micro-optical system.

Evaluation of the profile of the diamond micro-cylindrical lenses was undertaken by examining the cross-sectional profile extracted from AFM images. The measured profiles were then compared to the theoretical curvature of a circle. Such a measured cross-sectional profile of a micro-cylindrical lens and its fitted circular profile are plotted in Figure 6.1(b). There is only a small deviation between the measured and fitted profiles, indicating the cross-sectional profile of the fabricated micro-cylindrical lenses is very close to spherical in shape.
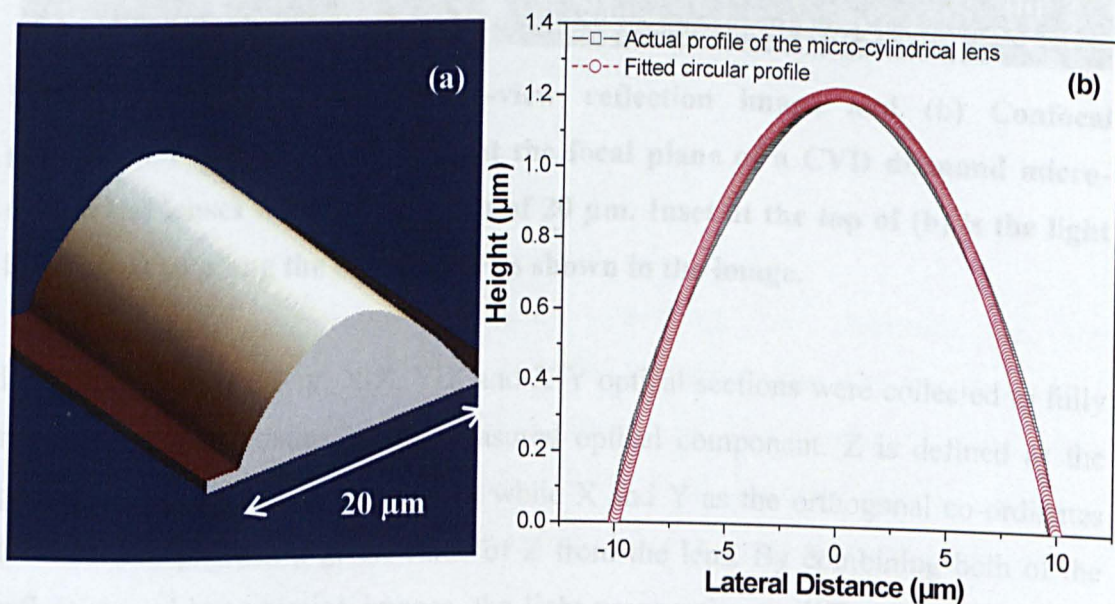

Figure 6.1   (a) AFM image and (b) measured and fitted surface profiles for a CVD diamond micro-cylindrical lens of 20 μm base width.

A confocal plane-view reflection image of the diamond micro-cylindrical lens array with a lens width of 20 μm is presented in Figure 6.2(a). This image shows that the micro-lenses were well defined. A confocal plane-view transmission section at the focal plane of the micro-cylindrical lens array is shown in Figure 6.2(b). The sharp focal lines are clearly observed in this image. The trace at the top of Figure 6.2(b) is an intensity scan at the focal plane of the micro-cylindrical lenses. This section image shows that the light intensity at the focal lines of the micro-cylindrical lenses is quite uniform not only along the lens but also from lens to lens, confirming the high uniformity of the fabricated micro-cylindrical lenses.
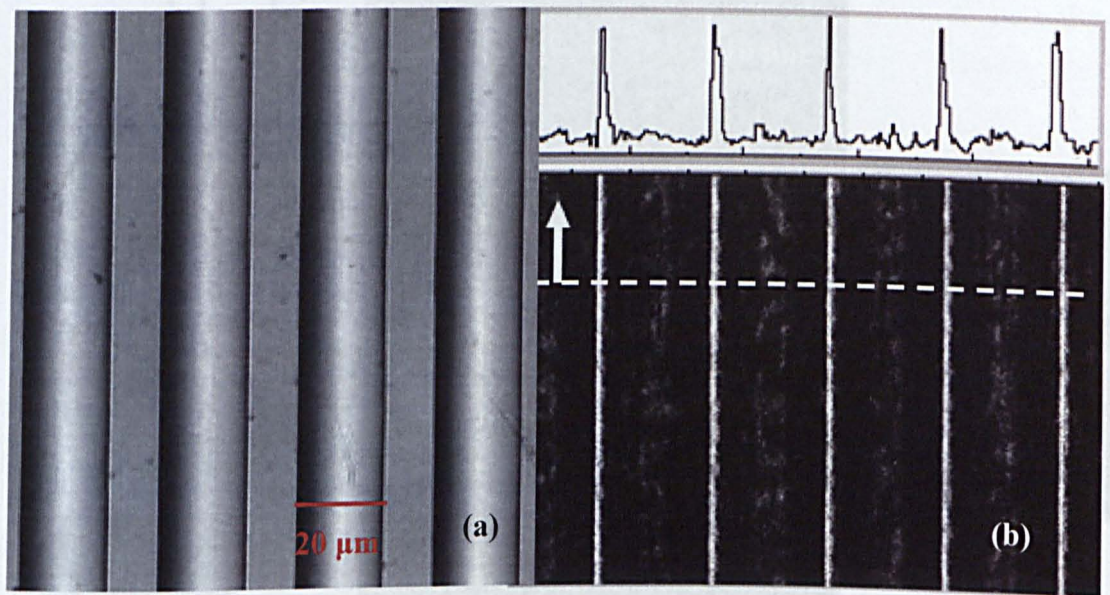

Figure 6.2 **(a) Confocal plane-view reflection image and (b) Confocal plane-view transmission sections at the focal plane of a CVD diamond micro-cylindrical lenses with a lens width of 20 μm. Inset at the top of (b) is the light intensity scan along the dashed line as shown in the image.**

During the measurement, X-Z, Y-Z and X-Y optical sections were collected to fully reveal the characteristics of the measured optical component. Z is defined as the perpendicular distance from the lens while X and Y as the orthogonal co-ordinates for a section plane at a given value of Z from the lens. By combining both of the reflection and transmission images, the light propagation at different planes can be obtained. Figure 6.3(a) is a schematic diagram showing the function of the

micro-cylindrical lenses and the coordinate denotation. A cross-sectional (X-Z section) transmission confocal image of the diamond micro-cylindrical lens array is shown in Figure 6.3(b). It is evident that the collimated light rays, after passing through the lenses, converge to a focal point. Each focal point represents a focal line as shown in Figure 6.2(b). Figure 6.3(c) show the confocal transmission section perpendicular to both focal plane and the X-Z plane of the lenses, i.e. Y-Z section. From this optical section, it can be seen clearly that due to the spherical aberration, the transmission rays do not converge to the same point.
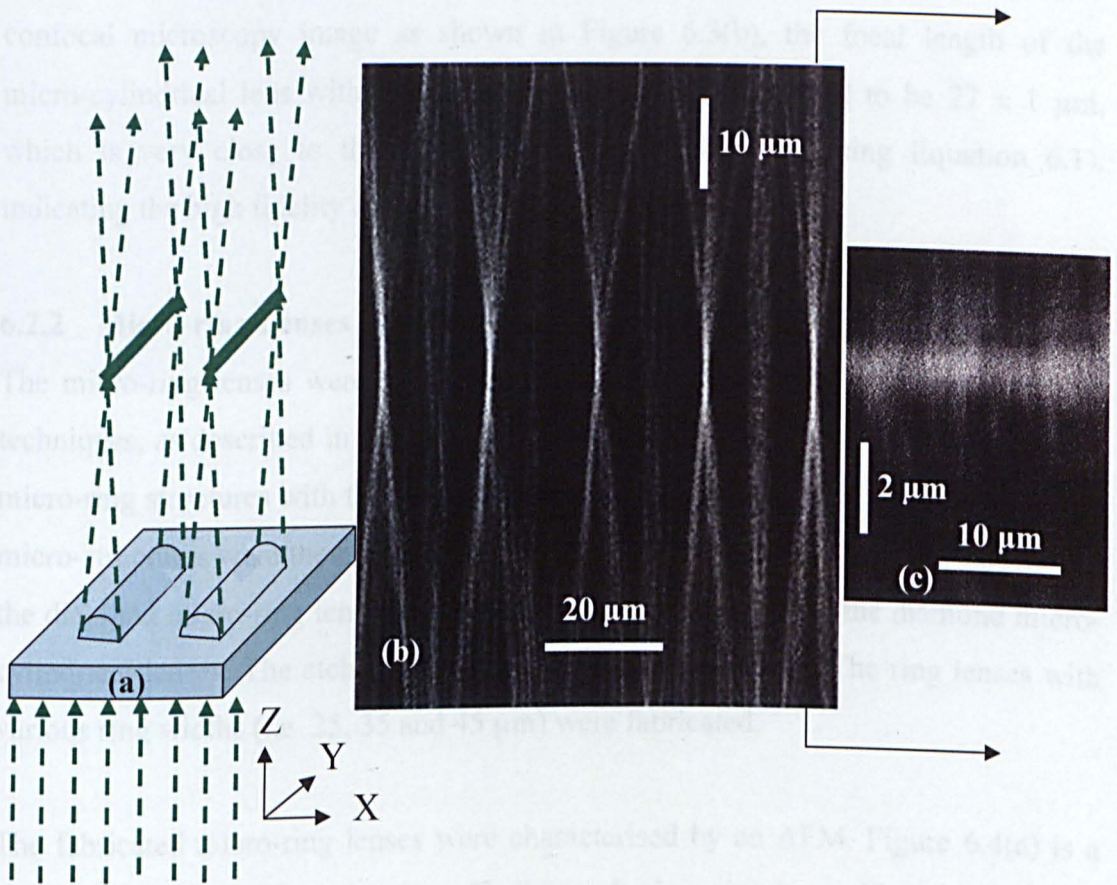

Figure 6.3 (a) Schematic diagram showing the function of the micro-cylindrical lenses and the coordinate denotation. (b) Image of the confocal reflection/transmission X-Z scan and (c) confocal plane view transmission section at the focal plane of a CVD diamond micro-cylindrical lenses with diameter of 20 μm. The scanning has been performed along one of the micro-cylindrical lenses.

In cross-section, the micro-cylindrical lenses can be regarded as plano-convex lenses. For a beam through a diamond convex lens and focused into the air, the paraxial focal length f of a plano-convex lens can be obtained using Equation 2.10 in **Subsection 2.2.2**:

$$f = \frac{(r^2 + h^2)}{2h(n-1)} \tag{6.1}$$

where n is the reflective index of the diamond lens, r and h are the half surface width and the height of the lens, respectively. The value of n for diamond is 2.42 at the wavelength of 532 nm used in the confocal microscopy measurement. From the confocal microscopy image as shown in Figure 6.3(b), the focal length of the micro-cylindrical lens with a lens width of 20 μm is estimated to be 27 ± 1 μm, which is very close to the calculated value of 28.6 μm (using Equation 6.1), indicating the high fidelity of the diamond etch process.

6.2.2 Micro-ring Lenses

The micro-ring lenses were fabricated using standard photolithography and reflow techniques, as described in **Section 3.4**. A special designed photomask consisting of micro-ring structures with the ring widths of 25, 35 μm and 45 μm was adopted. The micro-structures were then etched using ICP tool. The ICP etch recipe for fabricating the diamond micro-ring lenses is the same as that for fabricating the diamond micro-cylindrical lenses. The etching duration was set to 20 minutes. The ring lenses with various ring widths (i.e. 25, 35 and 45 μm) were fabricated.

The fabricated micro-ring lenses were characterised by an AFM. Figure 6.4(a) is a 3D AFM image showing a section of a diamond micro-ring lens with a ring width of 25 μm. This image shows that the micro-ring lenses have the same height with micro-cylindrical lenses of 1.25 μm. The surface RMS roughness has also been measured by AFM and found to be less than 3 nm for a scan area of 5 μm x 5 μm.

The surface profile of the micro-ring lens was obtained by scanning a cross section of the lens. The measured profile was then fitted to a curvature of a circle. Such a measured profile and its fitted circular profile of a micro-ring lens are plotted in

Figure 6.4(b). It can be seen that the variation between measured and fitted profiles is very small, indicating the cross-sectional profile of the micro-ring lens is very close to circle in shape. These results demonstrate that the fabricated diamond micro-ring lenses have good structural and surface qualities and are suitable for optical applications.
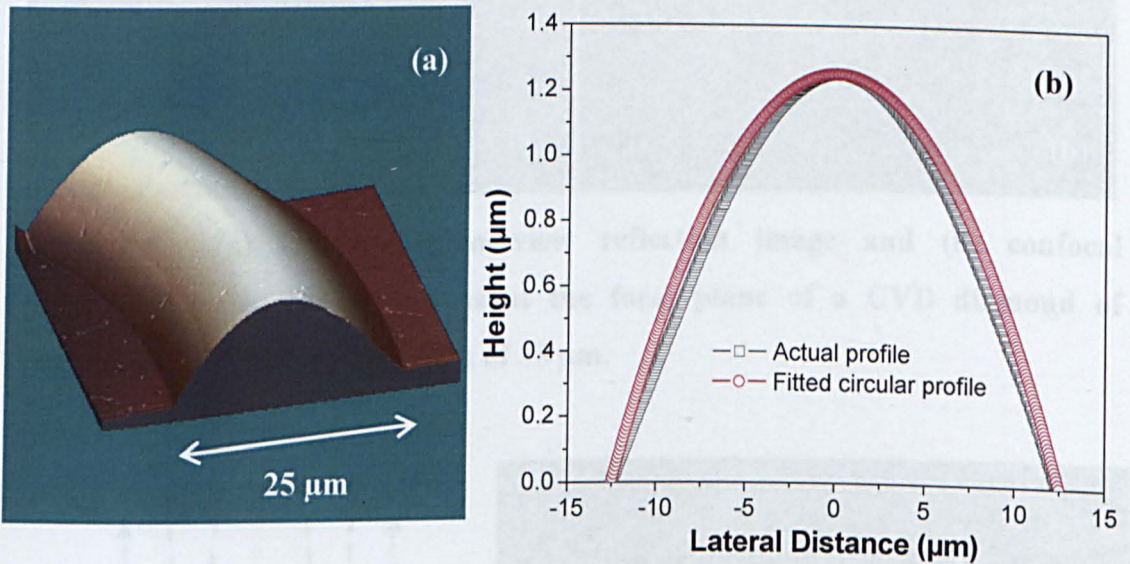

Figure 6.4 **(a) AFM image and (b) measured and fitted surface profiles of a CVD diamond micro-ring lens of 25 μm base width with diameter of 180 μm.**

Figure 6.5(a) shows a confocal plane-view reflection image of a diamond micro-ring lens with a ring width of 35 μm. This image shows that the fabricated micro-lens is well defined. A confocal transmission optical section at the focal plane of the micro-ring lens is shown in Figure 6.5(b). A sharp and uniform focal ring is clearly observed in this image, demonstrating high structural uniformity and high optical quality of the diamond micro-ring lens. Figure 6.6(a) is a schematic diagram showing the function of the micro-ring lenses and the coordinate denotation. A cross-sectional (X-Z section) transmission confocal image of a represented micro-ring lens is shown in Figure 6.6(b).

Figure 6.5 (a) Confocal plane-view reflection image and (b) confocal plane-view transmission sections at the focal plane of a CVD diamond of micro-ring lens with a ring width of 35 μm.

Figure 6.6 (a) Schematic diagram showing the function of a micro-ring lens and the coordinate denotation. (b) Image of the confocal reflection/transmission X-Z scan of the diamond micro-ring lens with ring width of 45 μm.
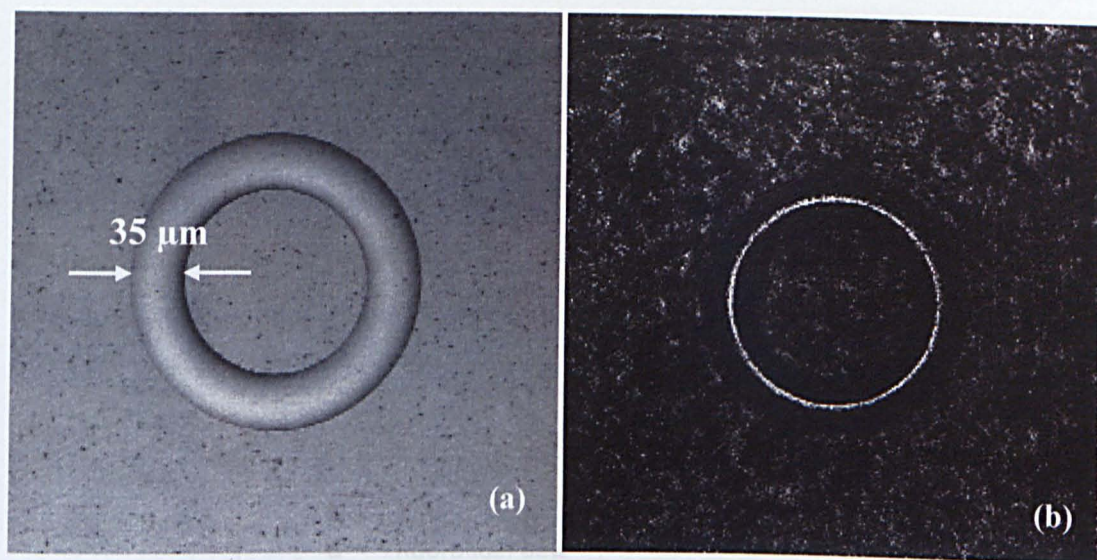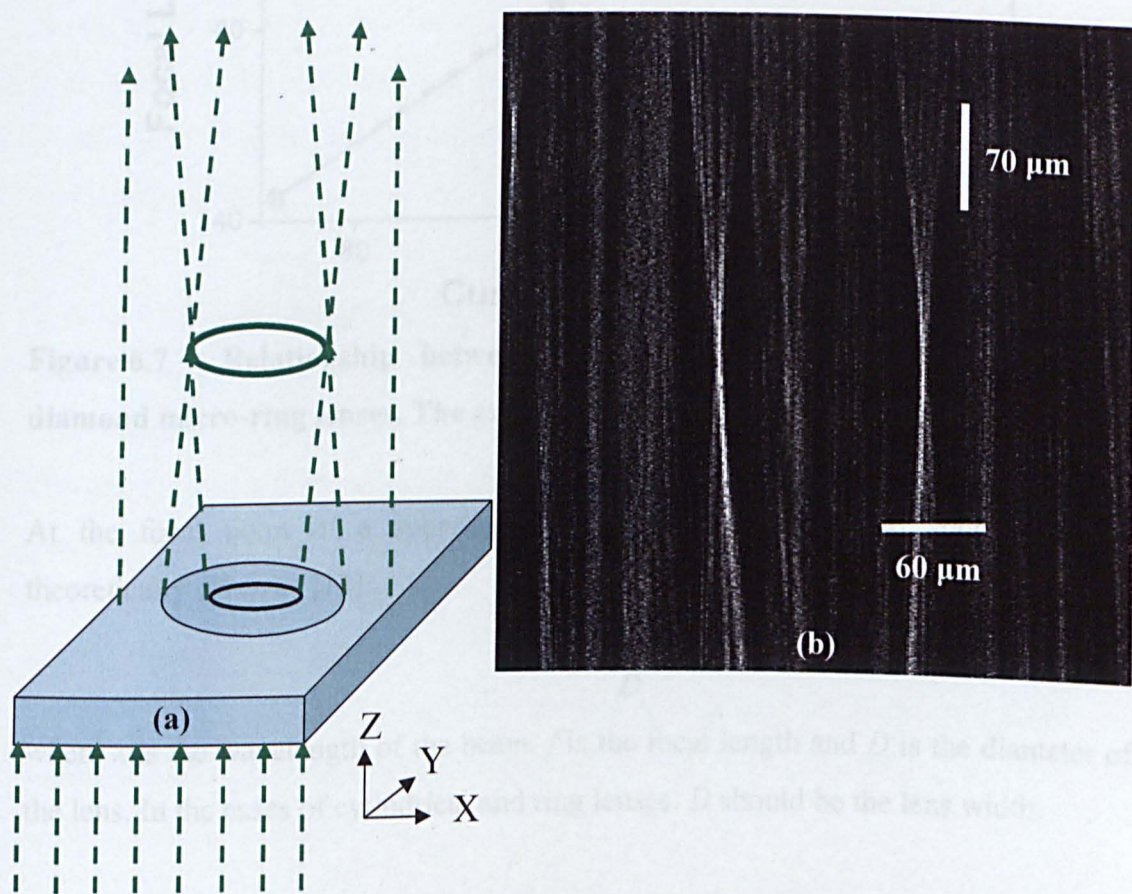
The focal lengths for the micro-rings were measured in the same way by using the confocal microscope. The measured (calculated) values for the micro-ring lenses with ring widths of 25, 35 and 45 μm are 45±1 μm (44.5 μm), 85±1 μm (86.7 μm) and 142±1 μm (143.0 μm) respectively. Figure 6.7 shows the relationship between the focal length and curvature radius of the micro-ring lenses. It can be seen that the measured focal lengths are quite close to those calculated from Equation (6.1).
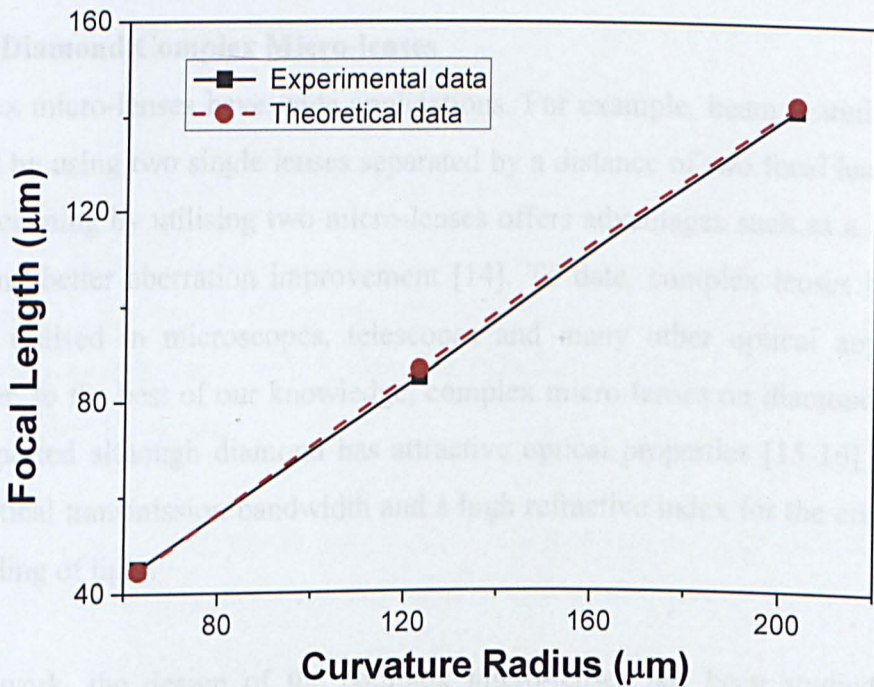
Figure 6.7 **Relationship between focal length and curvature radius of diamond micro-ring lenses. The experimental error is ± 1 μm.**

At the focal point of a spherical lens, the diffraction-limited spot size d is theoretically given as [13]:

$$d = \frac{2.44 f \lambda}{D} \tag{6.2}$$

where λ is the wavelength of the beam, f is the focal length and D is the diameter of the lens. In the cases of cylindrical and ring lenses, D should be the lens width.

The measured spot sizes for the micro-cylindrical lens of 20 μm lens width and the micro-ring lens of 35 μm ring width are 1 μm and 3 μm respectively. They are very close to the theoretical values calculated for both of the micro-cylindrical and ring

lenses, based on Equation (6.2), with spot sizes of 1.86 μm and 3.22 μm, respectively. The *f*-ratio, defined as *f/D* and therefore closely related to the spot size, serves as one of the important lens parameters. For a given lens diameter (width), the diffraction-limited spot size can be reduced by decreasing the focal length of the lens. The lens with a short focal length can be fabricated by decreasing its half surface width as shown by Equation (6.1). However, spherical astigmatism of the lens becomes prominent with decreasing the curvature radius of the lens.

6.3   Diamond Complex Micro-lenses

Complex micro-lenses have wide applications. For example, beam scanning can be realised by using two single lenses separated by a distance of two focal lengths [14]. Beam scanning by utilising two micro-lenses offers advantages such as a large scan angle and better aberration improvement [14]. To date, complex lenses have been heavily utilised in microscopes, telescopes and many other optical applications. However, to the best of our knowledge, complex micro-lenses on diamond have not been reported although diamond has attractive optical properties [15-16] such as a wide optical transmission bandwidth and a high refractive index for the confinement and guiding of light.

In this work, the design of the complex micro-lenses has been studied and the fabrication processes have been developed so as to fabricate diamond complex micro-lenses. The optical functionality of the complex micro-lenses was characterised by a laser scanning transmission/reflection confocal microscope. These investigations are reported in the following sections.

6.3.1   Optical Design

Figure 6.8 is a schematic diagram showing how a parallel beam is focused and re-imaged when passing through a diamond complex lens consisting of two spherical convex surface lenses.
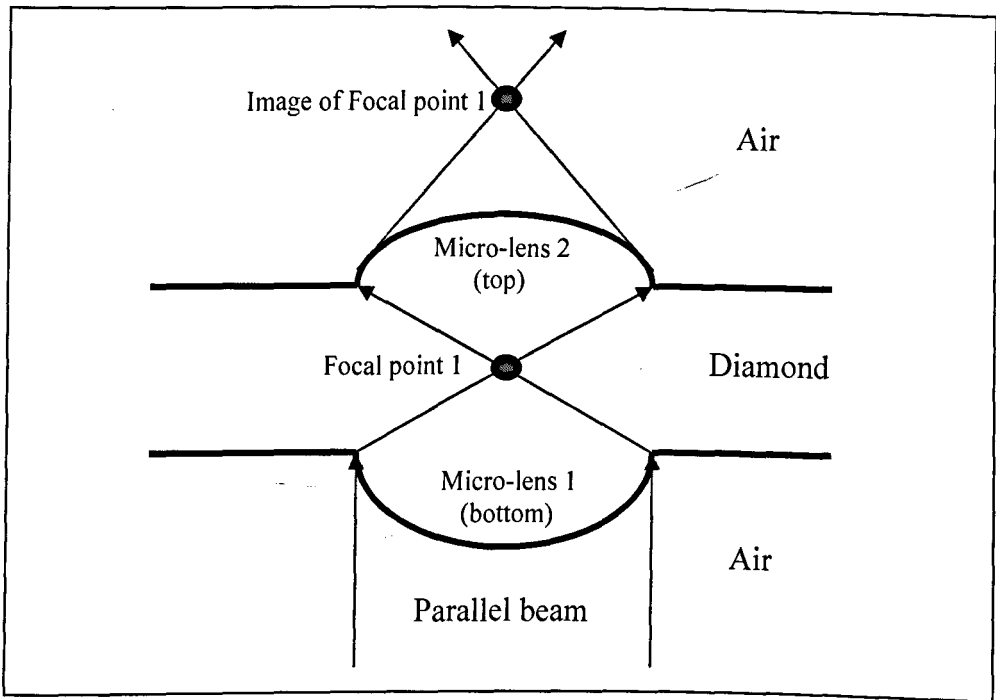
Figure 6.8 **Schematic diagram of the complex micro-lenses with two converging points, one lying inside the substrate and the other is re-imaged outside of the substrate.**

Following the rule of refraction, the incident parallel beam from air into the diamond is first converged to a point by the first surface lens (bottom lens). The focal length, f of this surface lens can be obtained by employing Equation (2.7). Considering that the refractive index of air is 1, the equation can be simplified as:

$$f = \frac{(r^2 + h^2)n}{2h(n-1)} \qquad (6.3)$$

where n is the refractive index of diamond, r is the surface radius of a micro-lens, h is the height of the micro-lens.

This focal point can be re-imaged by the second micro-lens (top lens). The relationship between object and image distances is expressed by Equation (2.8) in **Section 2.2.2.** Again, as the refractive index of air is 1, this relationship is simplified as:

$$q = \frac{(r^2 + h^2)p}{2hp(n-1) - (r^2 + h^2)n} \qquad (6.4)$$

where p and q are the object and image distances of the top micro-lens respectively.

6.3.2 Fabrication of Complex Micro-lenses

The diamond substrate used for complex lens fabrication is a double-side polished circular type IIa natural diamond with a diameter of 4 mm and a thickness of 330 μm. The top micro-lens pattern was first fabricated in photoresist using the standard photolithography and photoresist-reflow method as described in **Section 3.4**. The photoresist lens array pattern was then transferred onto the diamond substrate by ICP Ar/O_2 plasma etching. The ICP etch parameters employed were: a platen power of 40 W, a coil power of 400 W, a chamber pressure of 5 mTorr, and Ar/O_2 flow rates of 15/40 sccm. Under these conditions, the diamond etch rate is 0.05 μm/min. To fabricate the top diamond micro-lenses with a height of 1.56 μm, the total etch time was set to 32 minutes. The etch selectivity is estimated to be 0.14. These top diamond micro-lenses have a surface diameter of 29 μm and based on Equation (6.1), the focal length of these lenses can be calculated to be 48 μm.

The same process steps were applied to fabricate the second lens array at the bottom side of the diamond substrates. During the photolithography, the bottom micro-lenses were aligned carefully so that each micro-lens at the bottom side of the substrates was aligned exactly to that at the top side. Diamond micro-lenses at bottom side with a surface diameter of 27 μm and a height of 1.71 μm were fabricated after the ICP Ar/O_2 plasma etching for 35 minutes.

6.3.3 Experimental Results and Discussion: Natural Diamond Complex Micro-lenses

Figures 6.9(a) and 6.9(b) show the optical images of the top and bottom micro-lens arrays of the diamond complex micro-lenses, respectively. Figure 6.9(c) is the optical image focused at between the top and the bottom micro-lens arrays. This image shows that the top and bottom micro-lens arrays are well aligned.
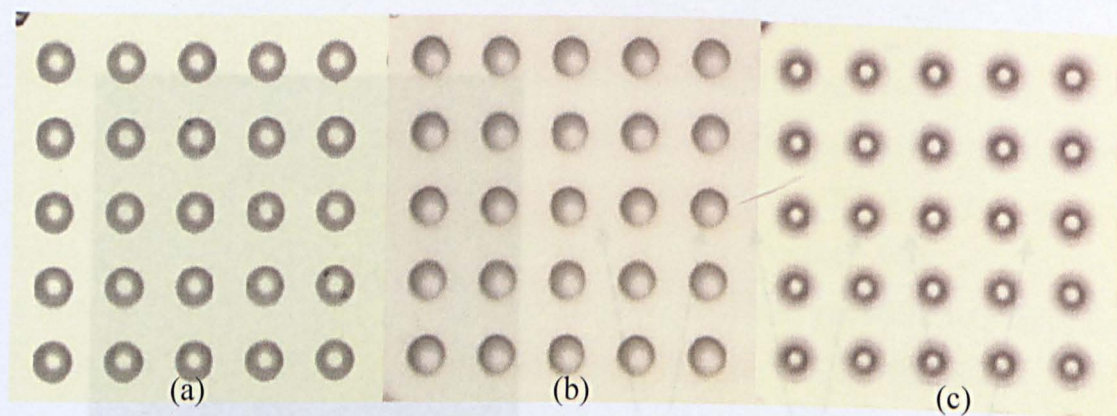
Figure 6.9 **(a) Optical images of the array of the top micro-lenses fabricated on natural diamond, (b) bottom micro-lenses of the complex diamond micro-lenses, and (c) optical images of a microscope with the focal points lie in between the two micro-lenses.**

Confocal microscopy was employed to characterise the functionality of these complex diamond micro-lenses. Figure 6.10(a) shows the confocal transmission optical sections of the three complex diamond micro-lenses. Figure 6.10(b) shows the schematic diagram of the beam passing through the diamond micro-lenses. It is observed in Figure 6.10(a) that the beam has two converging points. The bottom converging point lies inside the diamond while the top one falls into the air. The value of n for diamond is 2.42 at the wavelength of the laser beam of 532 nm used for the confocal microscopy measurement. The focal length of the bottom micro-lenses, f, is calculated to be 92.27 μm using Equation (6.3), which is quite close to the measured value of 94 μm. The object distance, p, for the top micro-lenses is:

$$p = d - f \qquad (6.5)$$

where d is the substrate thickness. p was calculated as 237.73 μm. By using Equations (6.4) and (6.5), the image distance of the top micro-lenses was determined to be 93.89 μm. The positive sign of the image distance indicates that the final image is real. The confocal microscopy measurement gives the image distance of the top micro-lenses as 97 μm. This shows that both theoretical calculations and experimental results are very close indicating the high fidelity of the fabrication process.

6.4   Diamond Optical Gratings

As described in the previous chapters, diamond possessed a very high thermal conductivity, very low thermal expansion coefficient (1.0 ppm/K) and temperature coefficient of refractive index (10 ppm/K). These superb properties make diamond an ideal material for the thermal stable optics such as gratings. Conventional gratings are usually made from optical materials such as Zinc Selenide. However standard coated optics can withstand high power light irradiation, and thus not available for high power laser applications. In addition, the diamond coated optics are not sensitive to the temperature variation. For the development of a temperature-independent optical grating, diamond reflection gratings were fabricated and characterised which are described in the following sections.

6.4.1

A Si diamond layer was first deposited on a 'PHI' diamond substrate by Microwave Chemical Vapour Deposition (MPCVD). It was then coated with a photoresist (SU-8051) layer. The grating pattern with a period of 6 μm was fabricated in photoresist using standard photolithography. A schematic diagram of the fabrication process is shown

The photoresist pattern transferred onto the SiO₂ by RIE etching with ArCHF₃. The gas flow rates of Ar and CHF₃ were set to 15 sccm. The step power of 200 W and a gas pressure of 20 mTorr. Then the photoresist pattern was stripped. The grating mask to transfer the pattern onto the diamond substrate. During the ICP etching, the flow rates of Ar and O₂ used were set to 5 sccm and 45 sccm. The ICP plater and coil powers were

Figure 6.10   (a) Confocal cross section transmission/reflection sections of an array of complex diamond micro-lenses. (b) Schematic diagram of the ray passing through the micro-lenses.

6.4   Diamond Optical Gratings

As described in Chapter 1, diamond possesses a very high thermal conductivity, very low thermal expansion coefficient (1.0 ppm/K) and temperature coefficient of refractive index (dn/dT = 1.0 x 10^{-5} K^{-1}). These superb properties make diamond an ideal material for developing highly thermal stable optics such as gratings. Comparing with the optical components made from optical materials such as Zinc Selenide (ZnSe) and quartz, diamond optics can withstand high power light irradiations and therefore are more suitable for high power laser applications. In addition, the optical properties of diamond optics are not sensitive to the temperature variation, which is imperative for the development of temperature-independent optical devices. In this work, the diamond reflection gratings were fabricated and characterised. These investigations are described in the following sections.

6.4.1   Fabrication of Diamond Gratings

A SiO_2 layer with a thickness of 1μm was first deposited on a HPHT diamond substrate by using Plasma Enhanced Chemical Vapour Deposition (PECVD). It was then spin-coated with a 0.5 μm thick photoresist (S1805) layer. The grating pattern with a width of 4.5 μm and a period of 6 μm was fabricated in photoresist using standard photolithography technique. A schematic diagram of the fabrication process is shown in Figure 6.11.

The grating patterns were then transferred onto the SiO_2 by RIE etching with Ar/CHF_3 plasma. The etch parameters are: flow rates of Ar and CHF_3 were set to 15 sccm and 5 sccm, respectively, platen power of 200 W and a gas pressure of 20 mTorr. After the SiO_2 etching, the photoresist pattern was stripped. The grating pattern in SiO_2 then served as an etch mask to transfer the pattern onto the diamond substrate by ICP Ar/O_2 plasma etching. During the ICP etching, the flow rates of Ar and O_2 used were set to 5 sccm and 45 sccm. The ICP platen and coil powers were 300 W and 50 W, respectively. The pressure was set to 5 mTorr. The high ICP platen power used enable the Ar ions to obtain high energy, resulting in heavy ion bombardments on diamond. Thus the anisotropic vertical etching predominates

during the process. Under the etch conditions, diamond gratings with high vertical side walls have been fabricated.
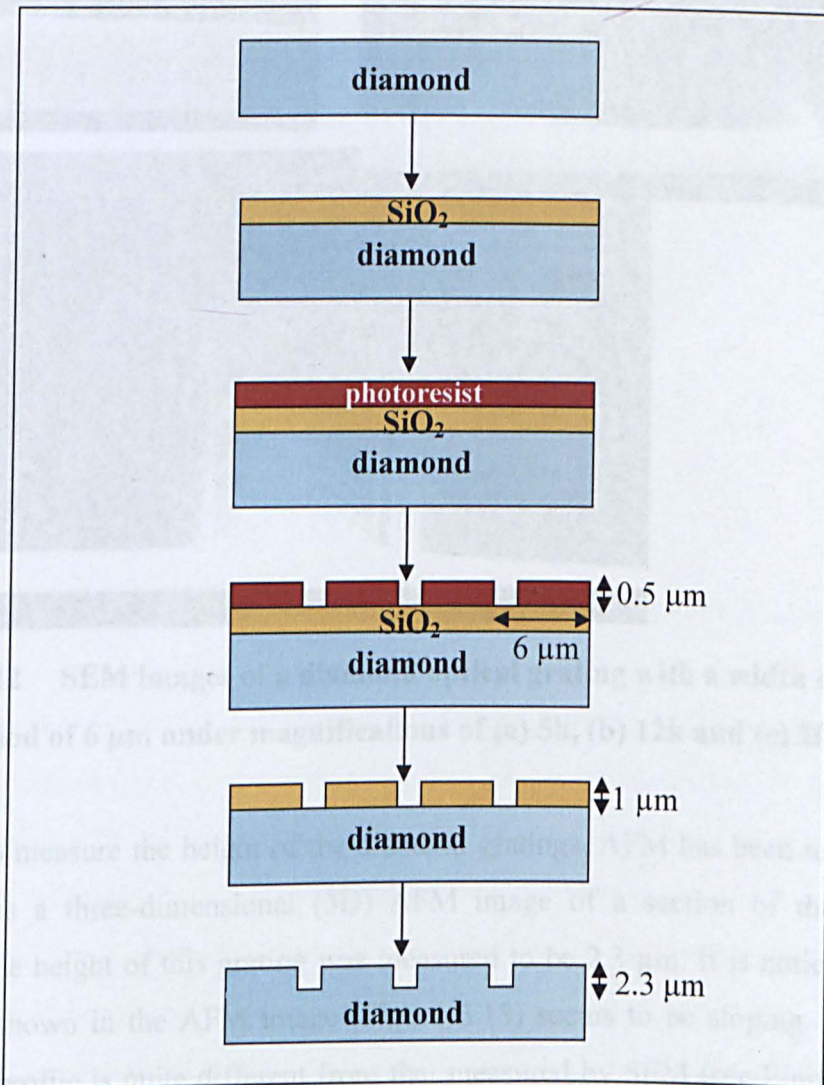

Figure 6.11   Fabrication processes of diamond gratings.

6.4.2   Experimental Results and Discussion: Optical Gratings

The surface profile and quality of the diamond gratings fabricated were evaluated by AFM and SEM techniques. Figures 6.12 (a), (b) and (c) show the SEM images of the diamond grating. The magnified images of the grating were shown in Figure 6.12(b) and Figure 6.12(c). Vertical side walls are observed in these figures. As shown in Figure 6.12, the measured period of the grating is 6 μm which is the same as the designed value.
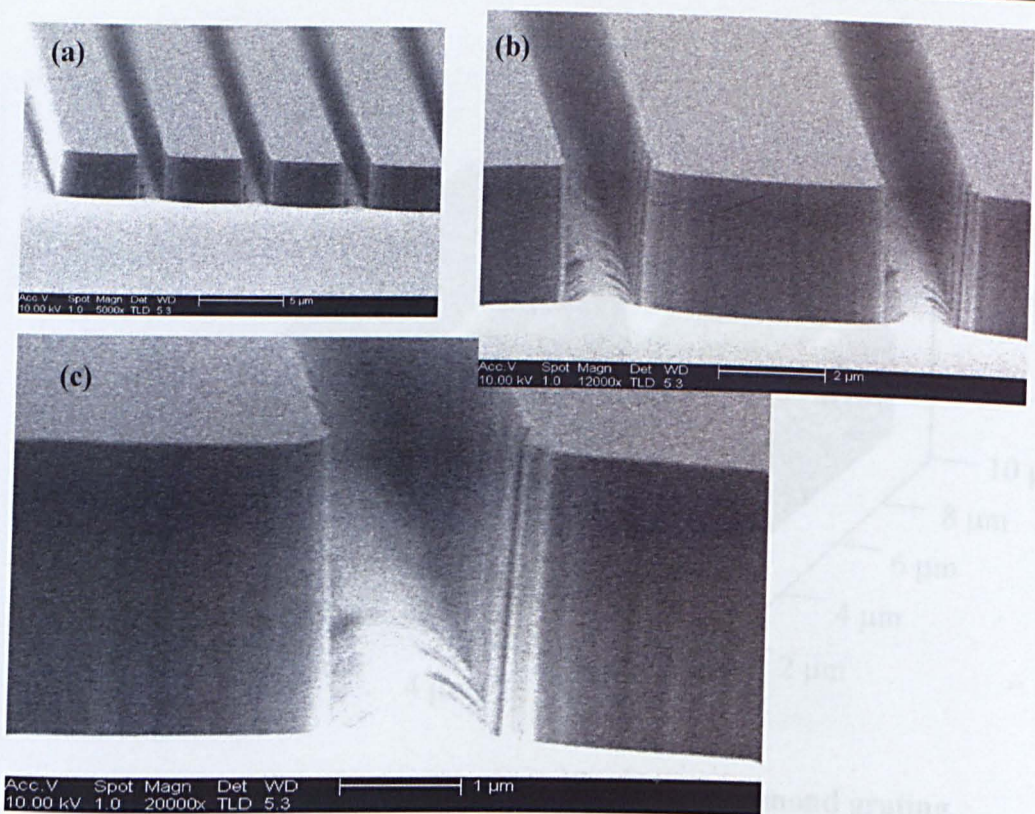
Figure 6.12 **SEM images of a diamond optical grating with a width of 4.5 μm and a period of 6 μm under magnifications of (a) 5k, (b) 12k and (c) 20k.**

In order to measure the height of the diamond gratings, AFM has been used. Figure 6.13 shows a three-dimensional (3D) AFM image of a section of the diamond grating. The height of this grating was measured to be 2.3 μm. It is noticed that the side wall shown in the AFM image (Figure 6.13) seems to be sloping. This AFM measured profile is quite different from that measured by SEM (see Figure 6.12). It is considered that the sloping side wall shown in the AFM image does not represent a real wall profile. Since the AFM tip has a certain size, during scanning it cannot follow the real wall profile exactly especially when a sharp structural change is involved. In this case, SEM is a preferable tool to obtain accurate information on the surface morphology.
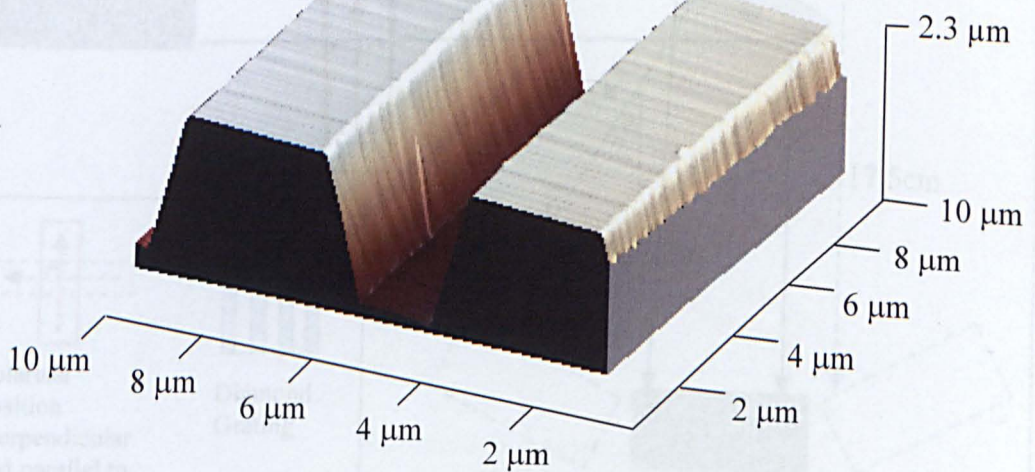
2.3 μm

10 μm

8 μm

6 μm

4 μm

2 μm

10 μm   8 μm   6 μm   4 μm   2 μm

Figure 6.13   AFM image of a section of the diamond grating.

To evaluate the optical functionality of the diamond grating, reflection measurement has been performed. The experimental setup of the measurement is presented is Figure 6.14. A 632 nm laser was employed as a light source for the measurement. During the measurement, diamond grating and incident angle (45°) are fixed. A polariser was placed in front of the laser. We can change the position of the polariser so that the diamond grating is irradiated by only linear polarised light either perpendicular or parallel to the grating as shown in Figure 6.14. A detector was located at a radial position of 17.5 cm from the diamond grating during the measurement. By varying the position of the detector, the intensity of the reflected light (in mV) was collected. For this setup, the maximum reflection angle is limited at 50° by the sample holder. This experiment was performed by Dr. Stephane Calvez from the Institute of Photonics in University of Strathclyde.
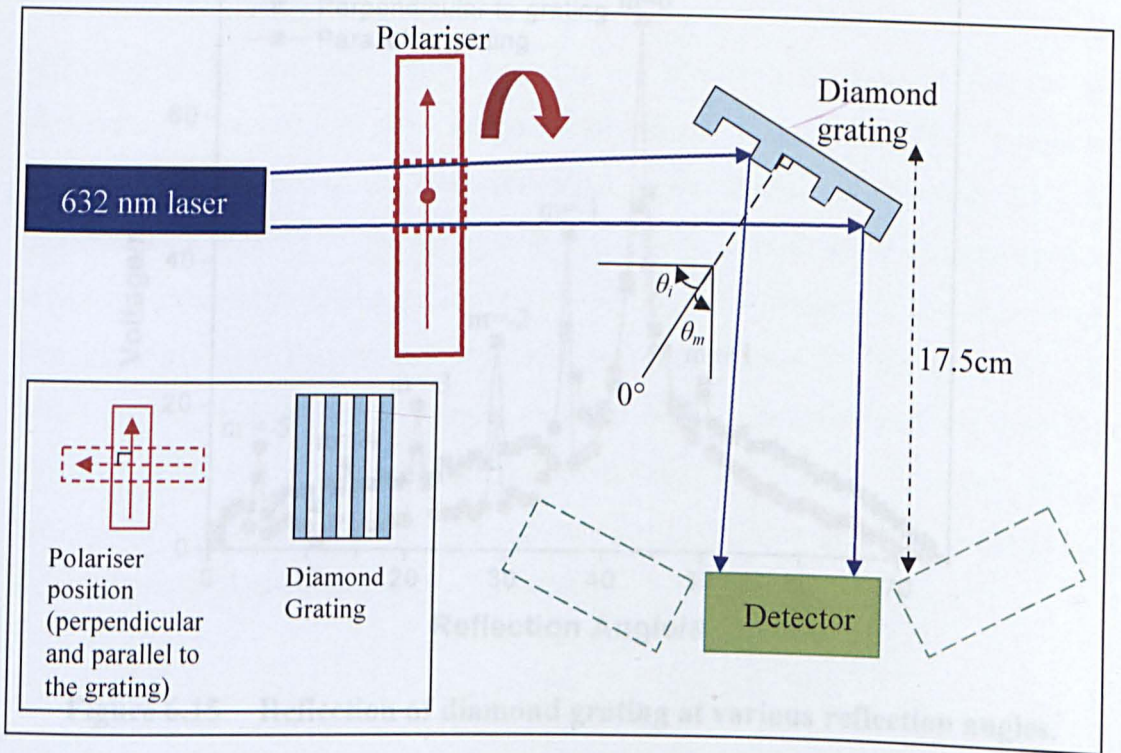
Figure 6.14 **Experimental setup for the diamond reflection grating measurement. Inset is the position of the polariser with respect to the diamond grating (i.e. polarised laser beam either perpendicular or parallel to the diamond grating).**

Figure 6.15 shows how the reflection of the diamond grating varies with the detector angles. The reflection peaks with different orders can be seen clearly in this figure demonstrating the grating functionality. The measurement shows that the first reflection order occurs at the angle of 43°. The second, third, fourth and fifth orders were measured at the angles of 36°, 29°, 21°, 14° and 5°, respectively. It can be observed that there are more negative orders than the positive orders, which might be due to the experimental setup (i.e. the position of the sample).
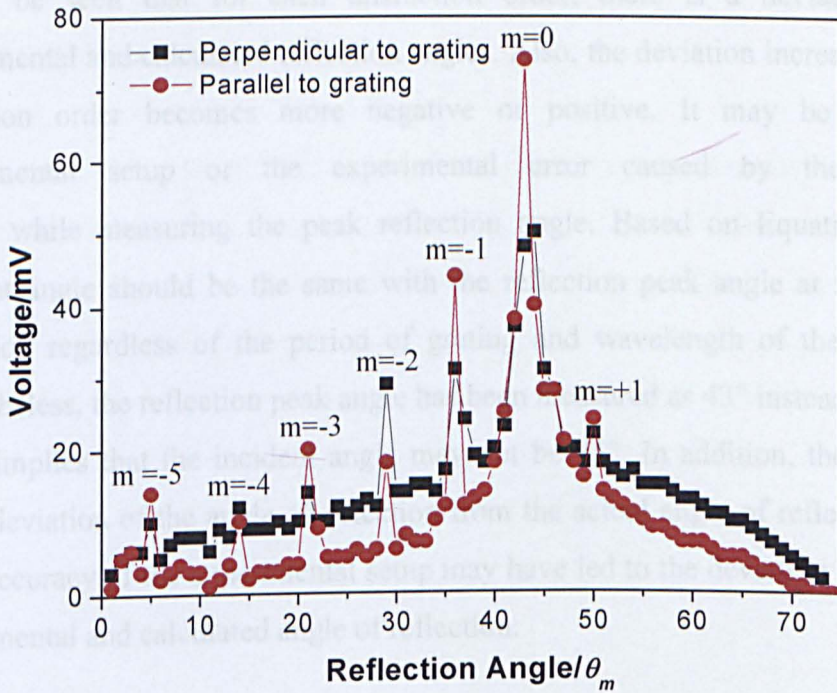
Figure 6.15 **Reflection of diamond grating at various reflection angles.**

The reflection peak angle can be calculated by using Equation (2.13) [17]:

$$m\lambda = a(\sin\theta_m - \sin\theta_i)$$

where m is the order of reflection, a is the grating period, λ is the wavelength of the laser beam (632 nm), θ_m is the reflection peak angle and θ_i is the incident angle (i.e. 45°). Calculated θ_m is shown in Table 6.2.

Table 6.2 **Comparisons of measured and calculated angle of reflection.**

Reflection order (m)	Measured Peak Angle of Reflection (θ_{me}/ ± 2°)	Calculated Peak Angle of Reflection (θ_{mc}/°)	Deviation ($\theta_{me} - \theta_{mc}$)/°
+1	50	54.3	-4.0
0	43	45.0	-2.0
-1	36	37.0	-1.0
-2	29	29.8	-0.7
-3	21	23.0	-2.0
-4	14	16.6	-2.6
-5	5	10.4	-5.4

It can be seen that for each diffraction order, there is a deviation between experimental and calculated reflection angles. Also, the deviation increases when the reflection order becomes more negative or positive. It may be due to the experimental setup or the experimental error caused by the equipment (± 2°) while measuring the peak reflection angle. Based on Equation 2.13, the incident angle should be the same with the reflection peak angle at zero order of reflection regardless of the period of grating and wavelength of the laser beam. Nevertheless, the reflection peak angle has been measured as 43° instead of 45°. This result implies that the incident angle may not be 45°. In addition, there may be a small deviation of the angle of detection from the actual angle of reflection. Hence, the inaccuracy of the experimental setup may have led to the deviation between both experimental and calculated angle of reflection.

6.5   Summary

Diamond micro-cylindrical and micro-ring lenses have been successfully fabricated using photoresist re-flow technique and ICP Ar/O_2 plasma etching. Diamond gratings were fabricated by employing SiO_2 mask. Evaluations of the profiles of these micro-lenses were undertaken by comparing the measured profiles with the theoretical curvature of a circle. It reviews that there is only a small deviation from a perfect spherical surface, indicating the micro-lenses fabricated are very close to the spherical in shape. A laser scanning confocal reflection/transmission microscopy technique has been adopted to evaluate the optical properties of the diamond micro-lenses. Confocal microscopy measurements show that both micro-cylindrical and ring lenses exhibit high optical quality and designed functionality.

Diamond complex micro-lenses were fabricated onto the both sides of the diamond substrate using ICP Ar/O_2 plasma. The focal lengths of the micro-lenses on both sides were carefully designed and calculated based on the refraction formula at the spherical surface by taking into account the light beam direction (into the substrate or out of the substrate). The micro-lenses with designed optical parameters were accomplished by controlling the surface diameter and the height of the micro-lenses during the fabrication process. The laser scanning reflection/transmission confocal

microscopy confirmed that there were two converging points as the laser beam was irradiated through the substrates.

Finally, diamond gratings with depth of 2.3 μm have been successfully fabricated. The period of the grating was measured as 6 μm. The SEM pictures show that the fabricated grating has well-defined sidewall. In addition, the functionality of the diamond grating has been demonstrated by the reflection measurement.

6.6 References

[1] Kuttner, Laser Beam Scanning, *Optical Engineering*, Volume 8, Marcel Dekker, New York (1985).

[2] Y. Fu, B.N.K. Ann, O.N. Shing, IEEE *Phot. Tech. Lett.*, **12**, 1213 (2000).

[3] Y. Fu, B.N.K. Ann, *J. Vac. Sci. Tehnol. B.*, **19**, 1259 (2001).

[4] T. Barwicz, M.A.Popovic, P.T. Rakich, M.R. Watt., H.A. Haus, E.P. Ippen, H.I. Smith, *Opt. Exp.*, **12**, 1437 (2004).

[5] B. Liu, A. Shakouri, J.E. Bowers, *Appl. Phys. Lett.*, **79**, 3561 (2001).

[6] H.W. Choi, C.W. Jeon and M.D. Dawson, *IEEE Phot. Tech. Lett.*, **16**, 33 (2004).

[7] H.W. Choi, P.R. Edwards, R.W. Martin and M.D. Dawson, *Appl. Phys. Lett.*, **83**, 4483 (2003).

[8] V. Adivarahan, S. Wu, W.H. Sun, V. Mandavilli, M.S. Shatalov, G. Simin, J.W. Yang, H.P. Maruska, and M.A. Khan, *Appl. Phys. Lett.*, **85**, 1838 (2004).

[9] B. Lounis and M. Orrit, *Rep. Prog. Phys.*, **68**, 1129 (2005).

[10] H.W. Choi, E. Gu, C. Liu, C. Griffin, J.M. Girkin, I.M. Watson, M.D. Dawson, *J. Vac. Sci. & Technol. B*, **23**, 130 (2005).

[11] E. Gu, H.W. Choi, C. Liu, C. Griffin, J.M. Girkin, I.M. Watson, and M.D. Dawson, *Appl. Phys. Lett.*, **84**, 2754 (2004).

[12] C.J.R. Sheppard and D. M. Shotton, *Confocal Laser Scanning Microscopy*, BIOS Scientific (1997).

[13] S.H. Park, H. Jeon, Y.J. Sung, and G.Y. Yeom, *Appl. Opt.*, **40**, 3698 (2001).

[14] A. Akatay, C. Ataman, H. Urey, *Opt. Lett.*, **31**, 2861 (2006).

[15] R.W. Cahn, P. Haasen, and E.J. Kramer, eds., *Materials Science and Technology*, VCH, Weinheim (1993).

[16] M.A. Prelas, G. Popovici, L.K. Bigelow, eds., *Handbook of Industrial Diamonds and Diamond Films*, Marcel Dekker (1997).

[17] E. Hecht, *Optics*, Pearson Education (2002).

Chapter 7

Process Development for Fabricating Diamond Micro-electronic Devices

7.1   Introduction

Intrinsic diamond is an insulating material with a large resistivity (> 10^{15} Ωcm) [1]. However, diamond can be converted into a semiconducting material once successfully doped. Boron-doped diamond possesses a unique combination of desirable properties such as high breakdown field and high hole mobility [1]. These properties make diamond attractive for a variety of electronic applications. One of the most notable differences of diamond from other semiconductors is its wide energy gap, 5.45 eV at room temperature [1-7] providing a high breakdown field. These features, combined with the surface stability of diamond at high temperatures, make it an ideal candidate for high-temperature electronic applications. Diamond's thermal conductivity, 20 $Wcm^{-1}K^{-1}$ at room temperature, is the highest for any material [3], which facilitates thermal management and heat removal from diamond-based electronic devices. Furthermore, it is well known that device failure is typically caused by the degradation of the device structure as a result of dopant diffusion during high-temperature operation. Hence the low diffusion coefficient of impurities and the low chemical reactivity of diamond are highly demanded properties for achieving device reliability at high-temperature [1,3].

Electron and hole mobilities of 4500 and 3800 cm^2/Vs, respectively have been measured in the single crystal high purity chemical vapour deposited diamond [4]. Thus, diamond is a potential material to develop novel electronic devices for high power, high temperature and harsh-environment applications. In fact, diamond-based Metal Semiconductor Field Effect Transistors (MESFET) [8], Metal Insulator Semiconductor Field Effect Transistors (MISFET) and Metal Oxide Semiconductor Field Effect Transistors (MOSFET) have been reported [9]. A typical MISFET device is illustrated in Figure 7.1. For such MISFET devices, a Schottky contact for field control of the device is normally fabricated on top of the intrinsic diamond or

other dielectrics, such as Al_2O_3 and SiO_2. On the other hand, ohmic contacts are formed directly on the highly-doped (usually boron-doped) thin diamond layer. In order to achieve a strong field control from the gate, the intrinsic or the dielectric layer is usually designed to be very thin (in the nanometer region).
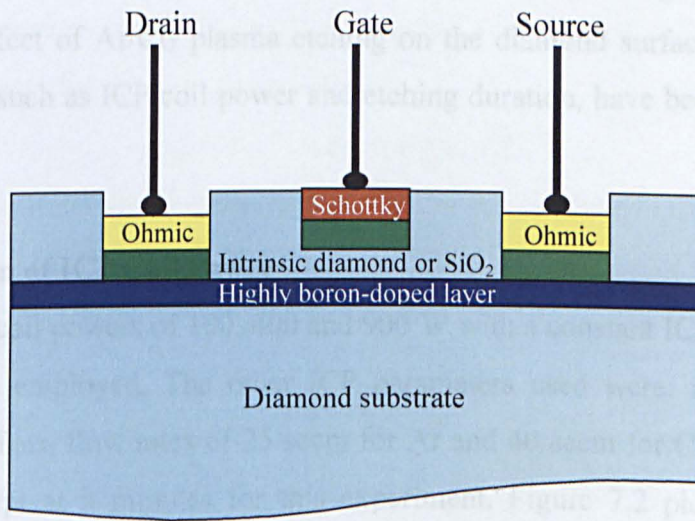

Figure 7.1   A typical diamond MISFET device with boron-doped layer [3].

To fabricate high-quality diamond electronic devices, highly smooth and free-of-damage diamond surface is also a key requirement. This is because the performance of the electrical contacts is greatly influenced by the surface. In this work, a new diamond ICP dry etch technique with Ar/Cl_2 plasma has been developed. It will be shown that the ICP Ar/Cl_2 plasma etching has capabilities of smoothing the diamond surface and hence fulfilling precise etch control.

Although Ar/Cl_2 plasma etching has been employed to etch several hard materials such as Gallium Nitride (GaN) [10], Silicon Carbide (SiC) [11] and sapphire [12], to the best of our knowledge, diamond Ar/Cl_2 plasma etching has not been previously reported. In this chapter, the effect of Ar/Cl_2 plasma etching on the diamond surface smoothing will be studied and the etch rate investigation of using Ar/Cl_2 plasma has been reported earlier in **Section 5.3**. AFM was employed to study the surface morphology of the etched diamond. The diamond materials studied include natural type IIa diamond, high pressure and high temperature (HPHT) diamond and polycrystalline chemical vapour deposition (CVD) diamond. The experimental

results show that Ar/Cl$_2$ plasma etching is capable of smoothing diamond surface. Using the optimised etching conditions, diamond electronic devices such as MISFET devices have been fabricated.

7.2   Experimental Results and Discussion: Surface Smoothing

To study the effect of Ar/Cl$_2$ plasma etching on the diamond surface, various ICP etch conditions such as ICP coil power and etching duration, have been exploited in detail.

7.2.1   Variation of ICP Coil Power

A series of ICP coil powers of 100, 400 and 900 W with a constant ICP platen power of 300 W were employed. The other ICP parameters used were: a chamber gas pressure of 5 mTorr, flow rates of 25 sccm for Ar and 40 sccm for Cl$_2$. The etching duration was kept at 3 minutes for this experiment. Figure 7.2 plots the surface root-mean-squared (RMS) roughness of a etched natural diamond as a function of ICP coil power. The surface RMS roughness of as-received sample was measured to be 1.1 nm for a 5 x 5 μm area using AFM technique.
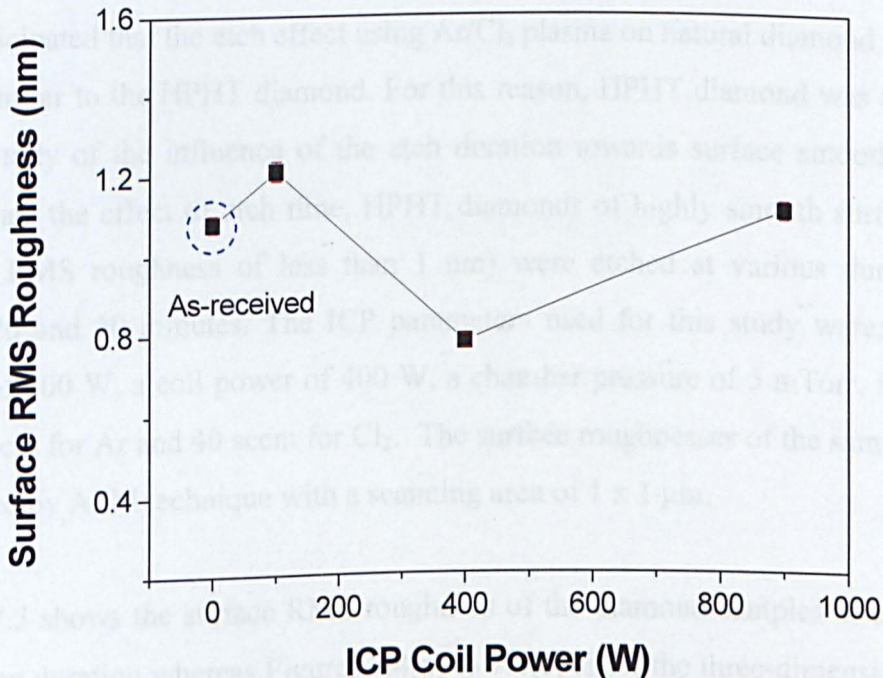

Figure 7.2   **Surface RMS roughness as a function of ICP coil power with etching duration of 3 mins, chamber pressure of 5 mTorr and Ar/Cl$_2$ flow rates of 25/40 sccm.**

It is observed that the surface roughness decreases to a minimum of ~ 0.8 nm when the coil power increases to 400 W. Thus, an ICP coil power of 400 W was selected when studying the effects of etching durations on the surface roughness as reported in the **subsection 7.2.2.**

The etching mechanism of SiC in Ar/Cl$_2$ plasma has been studied by *Jiang et al.* [11] and the following etch process was proposed:

$$SiC + Cl_2 \rightarrow SiCl_x + CCl_x \tag{7.1}$$
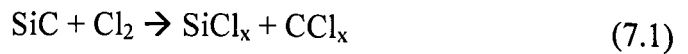
Hence, one could anticipate that the etching mechanism of the diamond with Ar/Cl$_2$ plasma to be:

$$C + Cl_2 \rightarrow CCl_x \tag{7.2}$$
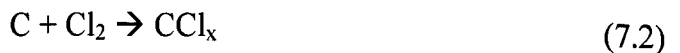
During the process, Ar ions bombard diamond and knock out the carbon atoms from the diamond surface, which enables the chemical reaction of the chlorine ions with the carbon atoms to form the etch products of CCl$_x$. The etch product, CCl$_x$, has been found to be volatile [11] and thus is pumped out from ICP chamber.

7.2.2 Variation of Etch Duration

It is anticipated that the etch effect using Ar/Cl$_2$ plasma on natural diamond should be quite similar to the HPHT diamond. For this reason, HPHT diamond was employed in the study of the influence of the etch duration towards surface smoothness. To investigate the effect of etch time, HPHT diamonds of highly smooth surface (with surface RMS roughness of less than 1 nm) were etched at various durations of 5, 10, 20 and 30 minutes. The ICP parameters used for this study were: a platen power of 300 W, a coil power of 400 W, a chamber pressure of 5 mTorr, flow rates of 25 sccm for Ar and 40 sccm for Cl$_2$. The surface roughnesses of the samples were measured by AFM technique with a scanning area of 1 x 1 μm.

Figure 7.3 shows the surface RMS roughness of the diamond samples as a function of etching duration whereas Figures 7.4(a) to 7.4(e) show the three-dimensional (3-D) AFM images of these samples.

All the as-received samples were measured to have a similar surface roughness of 0.53 ± 0.1 nm. After the first 5 minute etching, there is only a slight reduction in surface roughness i.e. RMS changes from 0.53 to 0.50 nm. When the etching duration increases to 10 minutes, the surface roughness decreases drastically by almost 2.5 times, i.e. from 0.53 to 0.19 nm. However, further increasing of the etch duration to 20 and 30 minutes, does not improve the surface smoothness further. In fact, for longer etching duration, the surface roughness increases a little bit (up to 0.28 nm) and remains almost unchanged.
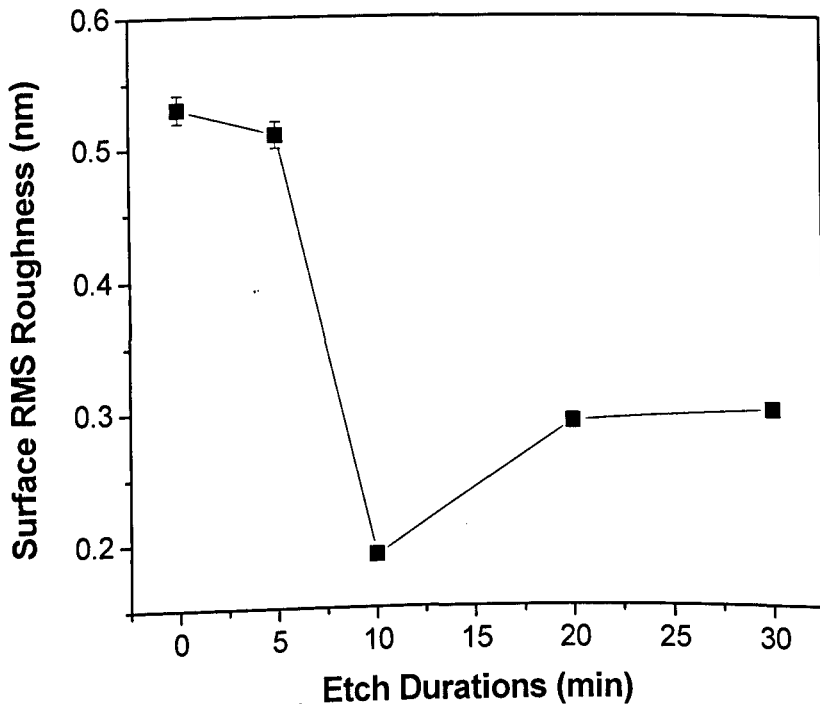
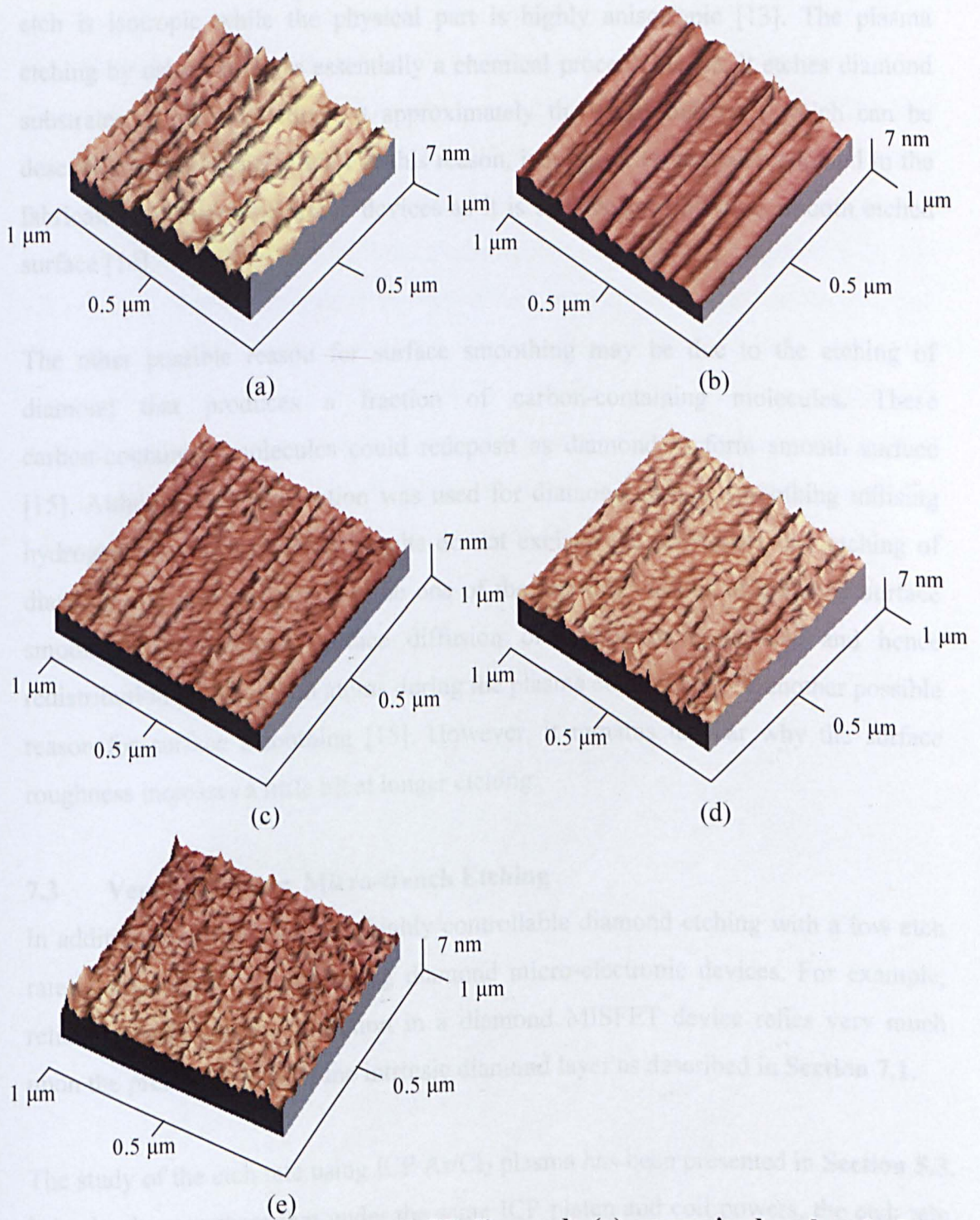**Figure 7.3**   **Surface RMS roughness as a function of etching duration.**

(a)

(b)

(c)

(d)

(e)

Figure 7.4 AFM images of HPHT diamonds (a) as-received and etched by Ar/Cl$_2$ plasma for (b) 5 min, (c) 10 min, (d) 20 min and (e) 30 min at ICP platen and coil powers of 300 and 400 W respectively.

The big reduction of the surface roughness as shown in Figure 7.3 is possibly related to following reasons. Surface smoothing of diamond utilising Ar/Cl$_2$ plasma may

result from the diamond isotropic etching. In dry etching, the chemical part of the etch is isotropic while the physical part is highly anisotropic [13]. The plasma etching by using Ar/Cl$_2$ is essentially a chemical process. Hence, it etches diamond substrates of all orientations at approximately the same etch rate, which can be described as "isotropic" etch. For this reason, isotropic etch has been adopted in the fabrication of micro-electronic devices as it is capable in producing smooth etched surface [14].

The other possible reason for surface smoothing may be due to the etching of diamond that produces a fraction of carbon-containing molecules. These carbon-containing molecules could redeposit as diamond to form smooth surface [15]. Although this explanation was used for diamond surface smoothing utilising hydrogen plasma, the present results do not exclude the possibility that etching of diamond and re-deposition may be one of the possible reasons of diamond surface smoothing. In addition, surface diffusion of carbonaceous species and hence redistribution of the carbon atoms during the plasma etching may be another possible reason for surface smoothing [15]. However, it remains unclear why the surface roughness increases a little bit at longer etching.

7.3   Vertical Shallow Micro-trench Etching

In addition to smooth surface, highly controllable diamond etching with a low etch rate is also crucial in fabricating diamond micro-electronic devices. For example, reliable ohmic contact formation in a diamond MISFET device relies very much upon the precise etching of the intrinsic diamond layer as described in **Section 7.1**.

The study of the etch rate using ICP Ar/Cl$_2$ plasma has been presented in **Section 5.3**. It is clearly seen there that under the same ICP platen and coil powers, the etch rate of Ar/Cl$_2$ plasma is only half of that obtained by Ar/O$_2$ plasma etching. In order to investigate the capability and controllability of diamond etching by Ar/Cl$_2$ plasma, diamond vertical shallow micro-trenches have been fabricated and characterised. The optimised etch parameters and conditions obtained from these studies are used for developing diamond electronic devices.

First of all, diamond micro-trenches with depths of 16 nm and 53 nm were fabricated on the CVD diamond. The sample was cleaned and standard photolithography process (as described in Chapter 3) was performed. By employing a photoresist mask, diamond micro-trenches were fabricated using ICP Ar/Cl_2 plasma etching. The ICP platen and coil powers were set to 300 W and 400 W respectively. The chamber pressure used was 5 mTorr. The durations of 15 and 44 seconds, respectively, were used. The 3-D AFM images of these micro-trenches are shown in Figure 7.5 (a) and 7.5 (b). It is observed that these micro-trenches have a well defined width of 2 μm. The measured RMS roughnesses at the etched surface are 0.9 nm and 0.7 nm for the micro-trenches with depths of 16 nm and 53 nm respectively, which are slightly less than the surface RMS roughness (1.0 nm) measured on the non-etched surface. These results show again the smooth effect of Ar/Cl_2 plasma etching, although the improvement is not so remarkable due to a very short etching duration.
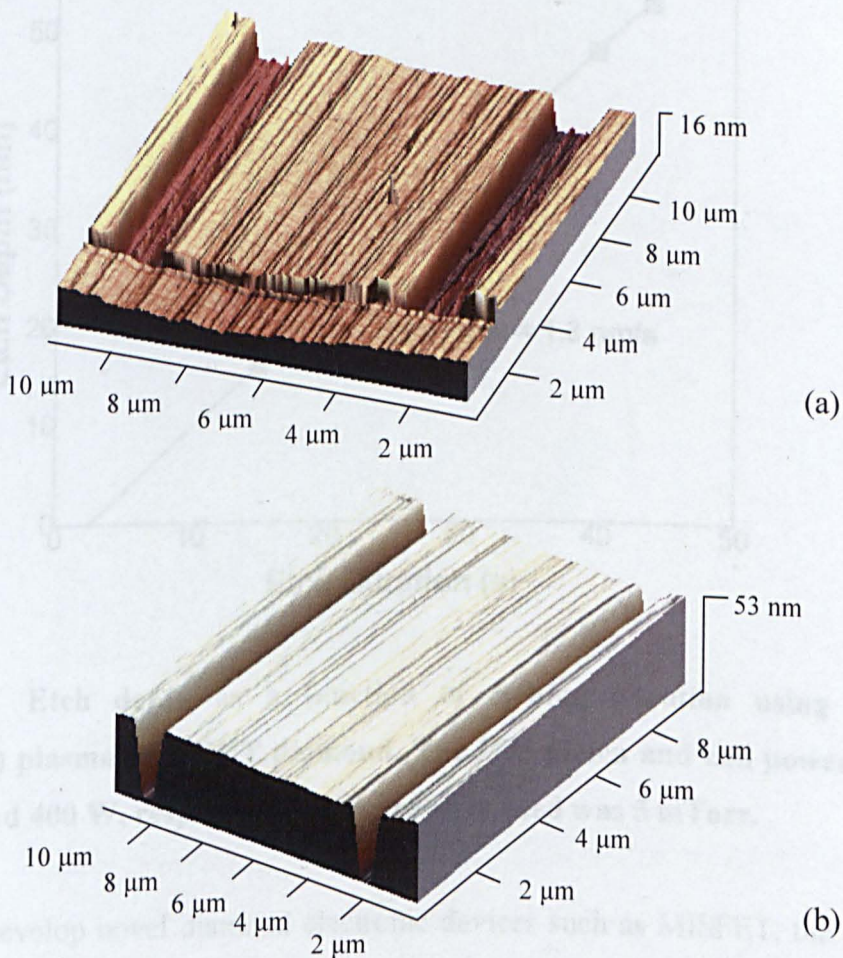

Figure 7.5   **AFM images of CVD diamond micro-trenches with a width of 2 μm and depth of (a) 16 nm and (b) 53 nm.**

Using the same ICP etch conditions, diamond micro-trenches with etch durations of 20 and 40 seconds have also been fabricated. AFM measurements confirmed that the depths of these trenches are 23 nm and 48 nm respectively. From these results, a linear relationship between the etch depth and etch duration is observed as shown in Figure 7.6. The etch rate is calculated to be 1.3 nm/s for various depths. The etch rate can be calculated based on the gradient of the line of etch depth versus etch duration. It can be seen that the etch depths are fitted very well with the linear line. This demonstrates a good etch controllability of using Ar/Cl_2 plasma to fabricate of diamond microstructures. From this figure, it is noticed that the diamond etching starts at 2.5 seconds due to the delay of plasma stabilisation. By knowing this fact, one could calculate the etch duration precisely for a designed etch depth.
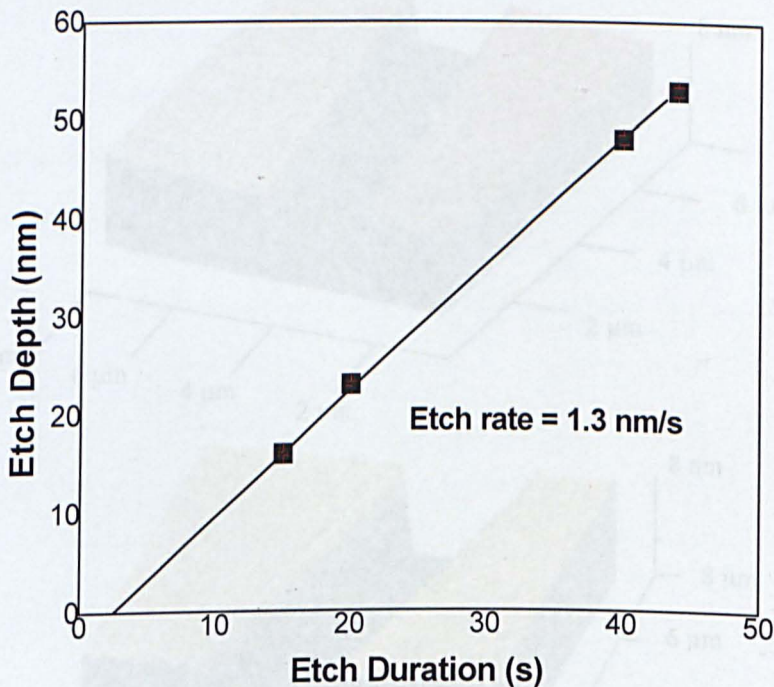

Figure 7.6 **Etch depth as a function of etching duration using Ar/Cl_2 (25/40 sccm) plasma on HPHT diamond. The ICP platen and coil powers were set to 300 and 400 W, respectively. The pressure used was 5 mTorr.**

In order to develop novel diamond electronic devices such as MISFET, the etching capability in fabricating very shallow (< 10 nm) micro-structures such as micro-trenches in diamond is required. To prove the etch controllability and

repeatability of Ar/Cl$_2$ plasma etching, diamond micro-trenches with a depth of 8 nm (Figure 7.7(a)) were fabricated on HPHT diamond by using the above etch recipe. The sample was etched for 9 seconds with an etch rate of 1.3 nm/s. The experiment was repeated for three successive times at different etch runs. It is observed that the etch depth of the second repeated experiment (Figure 7.7(b)) is also measured to be 8 nm for the 9 second etching. These results prove that the Ar/Cl$_2$ plasma etch is very stable and this technique can be employed in diamond shallow etching with good repeatability, particularly for the etch depth of less than 10 nm.
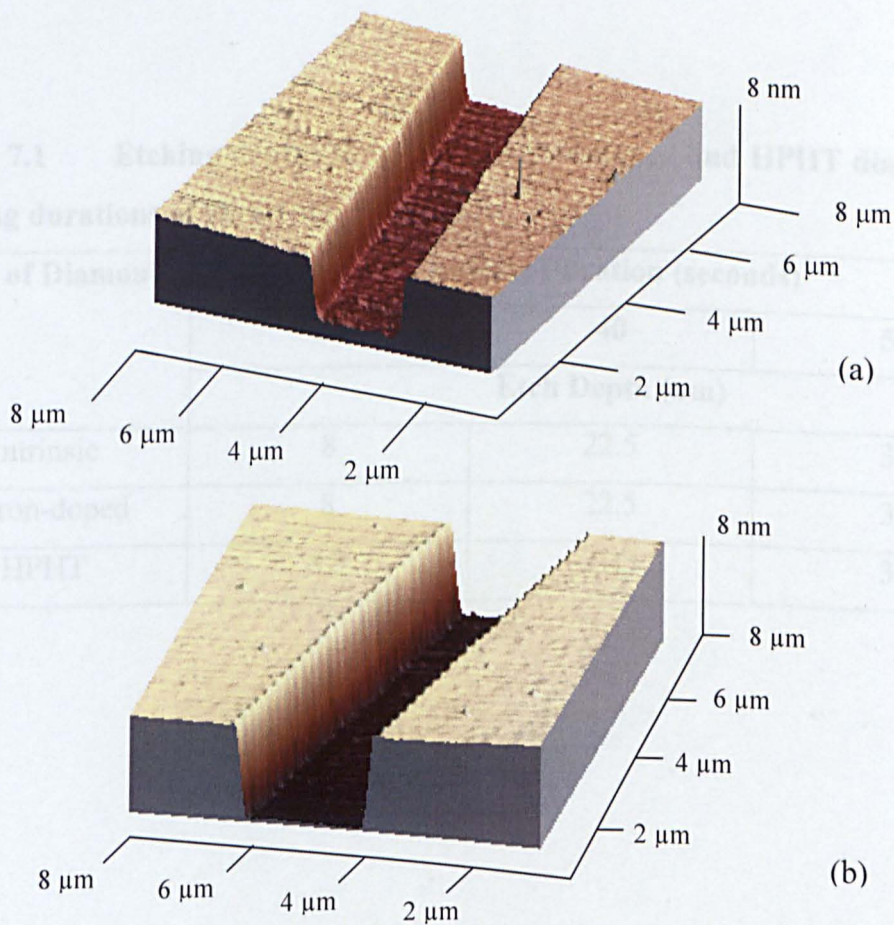

Figure 7.7   Micro-trench of 8 nm depth and 2 μm width on HPHT diamond sample using Ar/Cl$_2$ ICP plasma (a) first trial and (b) second trial.

To further reduce the etch rate, a etching recipe with a platen power of 300 W, a coil power of 100W, a chamber pressure of 5 mTorr, gas flow rates of 25 sccm for Ar and 40 sccm for Cl_2 has been developed. The etching experiment with such a low etch rate was performed on three different groups of diamond samples i.e. intrinsic diamond, boron-doped diamond (doping concentration of 5 x 10^{19} cm^{-3}) and HPHT diamond samples. Micro-trenches with different depths from each group of the diamond samples were fabricated. The etch durations were set to 20, 40 and 50 seconds. The etch depths were measured by using AFM technique and are summarised in Table 7.1. Figure 7.8 shows the 3D AFM images of the micro-trenches fabricated on the intrinsic diamond samples with depths of 8, 22.5 and 30 nm.

Table 7.1   Etching depths of intrinsic, boron-doped and HPHT diamonds at etching durations of 20, 40 and 50 seconds.

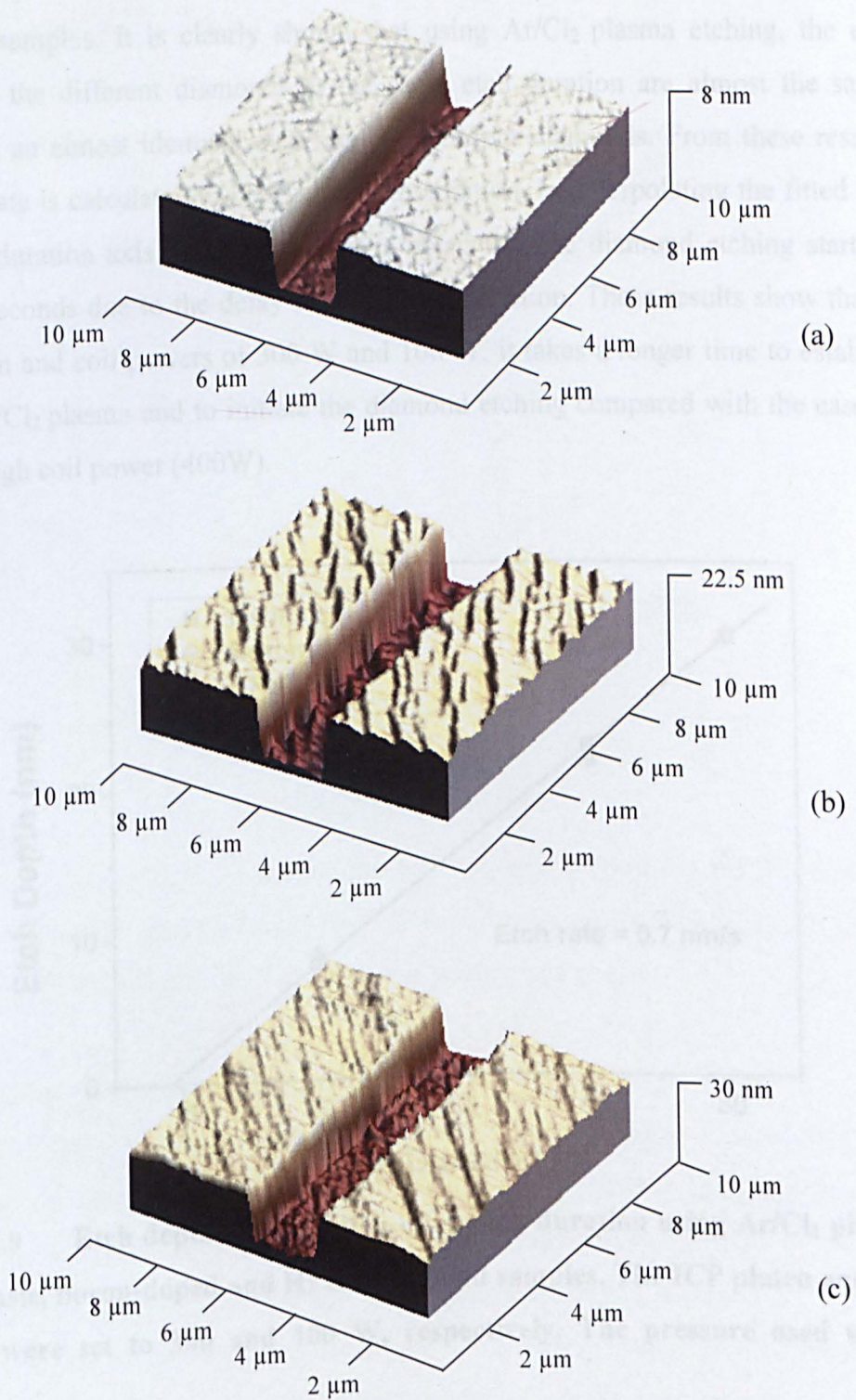| Type of Diamond	Etching Duration (seconds)		
	20	40	50
	Etch Depth (nm)		
Intrinsic	8	22.5	30
Boron-doped	8	22.5	30
HPHT	8.5	21.5	30

Figure 7.8 **AFM images of intrinsic diamond samples etched with Ar/Cl₂ plasma for (a) 20 (b) 40 and (c) 50 seconds. The ICP platen and coil powers were set to 300 and 100 W, respectively. The pressure used was 5 mTorr.**

Figure 7.9 plots the etch depth as a function of etch duration for each group of the diamond samples. It is clearly shown that using Ar/Cl_2 plasma etching, the etch depths of the different diamonds at the same etch duration are almost the same, indicating an almost identical etch rate for different diamonds. From these results, the etch rate is calculated to be 0.7 nm/s. In addition, by interpolating the fitted line with the duration axis in Figure 7.9, it is noted that the diamond etching starts at about 9 seconds due to the delay of plasma stabilisation. These results show that at ICP platen and coil powers of 300 W and 100 W, it takes a longer time to establish stable Ar/Cl_2 plasma and to initiate the diamond etching compared with the case by using a high coil power (400W).
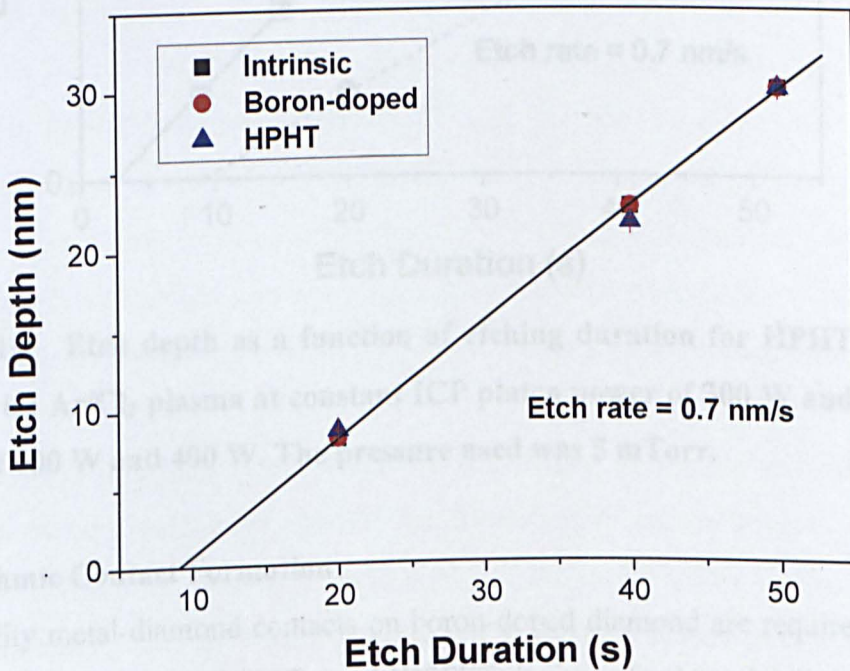

Figure 7.9 **Etch depth as a function of etching duration using Ar/Cl_2 plasma on intrinsic, boron-doped and HPHT diamond samples. The ICP platen and coil powers were set to 300 and 100 W, respectively. The pressure used was 5 mTorr.**

The etch depths of the HPHT diamond samples by using the lower ICP coil power of 100 W are compared with the etch depths on the same diamond samples but etched with a higher coil power of 400 W. This comparison is shown in the Figure 7.10. It is noticed that the etch rate with the lower ICP coil power is almost half of the rate

obtained by using the higher ICP coil power. This shows that the diamond etch rate can be manipulated by adjusting the ICP coil power.
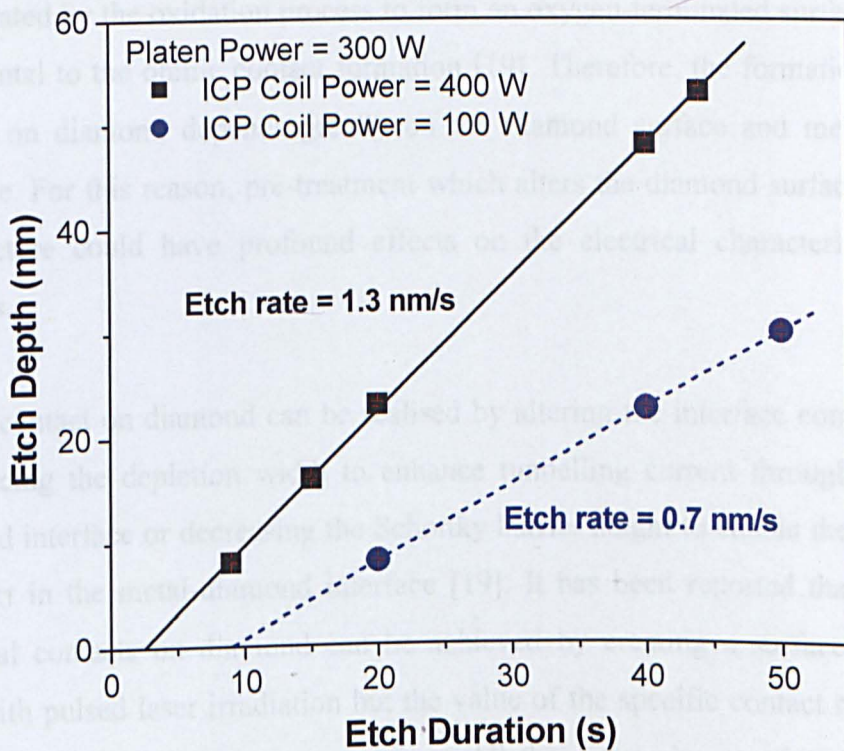

Figure 7.10 **Etch depth as a function of etching duration for HPHT samples treated with Ar/Cl$_2$ plasma at constant ICP platen power of 300 W and ICP coil powers of 100 W and 400 W. The pressure used was 5 mTorr.**

7.4 Ohmic Contact Formation

High-quality metal-diamond contacts on boron-doped diamond are required [16-17] for fabricating diamond MISFET and MOSFET devices. To date, the metal contacts on diamond such as Ti, Au, Ti/Au have been studied and reported by several research groups [16-19]. Ti/Au metal contact has been widely chosen for the ohmic contact formation on diamond as a compound TiC is easily formed at the Ti/diamond interface which facilitates a good ohmic contact [17]. Similar results were also reported on Mo/diamond contact [20]. A very low specific contact resistance of 2.3×10^{-7} $\Omega.cm^2$ has been reported for Al/Si contacts on diamond after annealing at 450 °C [21]. In this experiment, Al was deposited on top of the Si layer. The low contact resistance was attributed to the formation of a SiC layer at the metal-diamond interface which lowers the metal-diamond barrier height to enhance hole tunnelling.

The surface of the boron-doped diamond was reported to be hydrogen-terminated [22]. This hydrogen-terminated surface is highly conductive and thus it is easy to form a good ohmic contact. However, the hydrogen-terminated surface can be easily deteriorated by the oxidation process to form an oxygen-terminated surface, which is detrimental to the ohmic contact formation [19]. Therefore, the formation of ohmic contact on diamond depends greatly on the diamond surface and metal-diamond interface. For this reason, pre-treatment which alters the diamond surface chemistry or structure could have profound effects on the electrical characteristics of the contacts.

Ohmic contact on diamond can be realised by altering the interface conditions such as reducing the depletion width to enhance tunnelling current through the metal-diamond interface or decreasing the Schottky barrier height to enable the free carrier transport in the metal-diamond interface [19]. It has been reported that the ohmic electrical contacts on diamond can be achieved by creating a surface graphitised layer with pulsed laser irradiation but the value of the specific contact resistance on such a graphitised surface was not given. All these experiments show that surface treatment is an indispensable process to achieve ohmic contact on diamonds.

In this section, the effects of the surface treatments by using ICP plasma etching, aqua regia etching, and laser ablation on formation of ohmic contact on highly boron-doped diamonds will be investigated. Prior to the study of the effect of surface treatments, the method of measuring the contact resistance should be fully understood and the test contact patterns should be designed and fabricated.

7.4.1 Specific Contact Resistance: Circular Transmission Line Method (CTLM)

Test contact patterns of either circular or rectangular geometry are commonly used to determine the specific contact resistance of ohmic contact systems in semiconductor devices [23]. However, a mesa structure which confines the current flow between two contacts needs to be fabricated when the rectangular test pattern is employed [23]. Such complication can be avoided by using the circular test pattern approach

(Circular Transmission Line Method (CTLM)) and this method is thus chosen in this work.
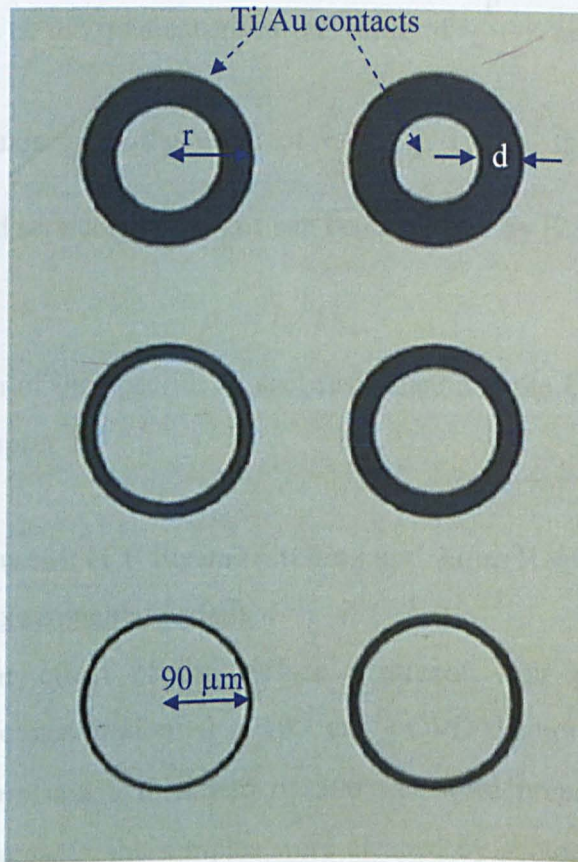

Figure 7.11   An optical image of CTLM Ti/Au contacts fabricated on the boron-doped diamond sample. *r* is the radius of the outer circular contacts and *d* is the separation within the contacts.

A CTLM mask with six circular test contacts has been designed. By using this mask, CTLM Ti/Au contacts have been fabricated on the surface of one boron-doped diamond sample as shown in Figure 7.11. In this pattern, the separations, d, between the circular contacts are 5, 10, 15, 25, 35 and 45 μm, respectively, and r is the radius of the outer circular contact and it is fixed at 90 μm for each outer circular contact. The total resistance, R_T, which is obtained from the gradient of voltage over current or V/I for such a circular contact is expressed by [23]:

$$R_T = \frac{R_s}{2\pi r}[d + 2L_T]$$

(7.3)

where R_s is the sheet resistance of the semiconductor layer and L_T is the transfer length.

By plotting R_T versus d, the gradient gives the value of $\dfrac{R_s}{2\pi r}$ and the interception

with the vertical R_T-axis gives the value of $\dfrac{R_s}{\pi r}[L_T]$. Hence, the specific contact

resistance of metal and semiconductor, ρ_c, can be calculated by [23]:

$$\rho_c = L_T^2 x R_s \qquad (7.4)$$

A complete derivation of the specific contact resistance and the CTLM method has been discussed in **Chapter 2.**

7.4.2 Surface Treatment: ICP Plasma Etching and Aqua Regia Etching

7.4.2.1 Samples and Experimental Details

In order to study the effect of the surface treatment, four (S1 - S4) highly boron-doped (doping concentration ~1 x 10^{20} cm^{-3}) CVD diamond samples with a size of 8 mm x 8 mm and a thickness of 300 μm were prepared. Prior to the fabrication of metal contacts, the samples were cleaned by aceton and followed by methanol in ultrasonic bath for 20 minutes for each solution. The samples were then cleaned with piranha solution (H_2SO_4: H_2O_2 = 4:1) so as to remove any organic contaminant. CTLM Ti/Au patterns were fabricated by using the standard photolithography technique. Prior to metal deposition, the diamond samples were subjected to the different surface treatment as listed in Table 7.2.

Table 7.2   Surface treatment conditions of S1 to S4.

Sample ID	Platen Power (W)	Coil Power (W)	Chamber Pressure (mTorr)	Type of Gas; Flow rate (sccm)	Etching Duration (min)	Aqua Regia (1 min)
S1	300	900	5	Ar; 50	1	No
S2	50	400	5	H$_2$; 50	1	No
S3	No	No	No	No	No	No
S4	No	No	No	No	No	Yes

Sample S1 was ICP etched with argon plasma. The ICP parameters used were: a platen power of 300 W, a coil power of 900 W, a chamber pressure of 5 mTorr, a gas flow rate of 50 sccm with an etching duration of 1 minute. High platen power was chosen in this case to create a damaged surface which includes graphite and amorphous carbon [16]. Sample S2 was surface treated with ICP hydrogen plasma. The ICP parameters used were a platen power of 50 W, a coil power of 400 W, a chamber pressure of 5 mTorr, a gas flow rate of 50 sccm with an etching duration of 1 minute. No surface treatment was performed on Sample S3 which serves as a control sample. Boiling aqua regia (HNO_3: HCl with volume ratio of 3:1) was applied to Sample S4 for 1 minute. A metal layer of Ti (50nm) was then sputtered followed by Au (100 nm) onto the diamond samples. Standard lift-off process was used to fabricate CTLM contact patterns. After pattern fabrication, all the samples were subjected to a rapid thermal annealing (RTA) process in nitrogen ambient at 450 °C for 1 minute.

7.4.2.2 Experimental Results and Discussion

Figure 7.12(a) shows the *I-V* characteristics of the circular contacts with different separations *d* on the control sample S3. Linear *I-V* characteristic is observed, indicating the ohmic contact behaviour of the Ti/Au-diamond interface. For this sample, a low electrical conductive thin hydrocarbon layer may be present on the diamond surface given that this layer can be normally found on the as-grown diamond [24]. From the *I-V* curves, the total resistance, R_T, between the circular contacts can be deduced as explained in **Section 7.4.1.** Figure 7.12(b) plots R_T as a function of *d*. It is evident that the relationship between the total resistance and the separation of the circular contacts is linear. The interception of the fitted straight line with the vertical R_T-axis and the slope of the line are 63.24 Ω and 40849.28 Ωcm^{-1}, respectively. Hence, the sheet resistance (R_s) and the transfer length (L_T) can be calculated by using equation (7.3) and calculated values are 2309.97 Ω and 7.741 x 10^{-4} cm, respectively. Using equation (7.4), the specific contact resistance, ρ_c is estimated to be 1.38 x 10^{-3} $\Omega.cm^2$.
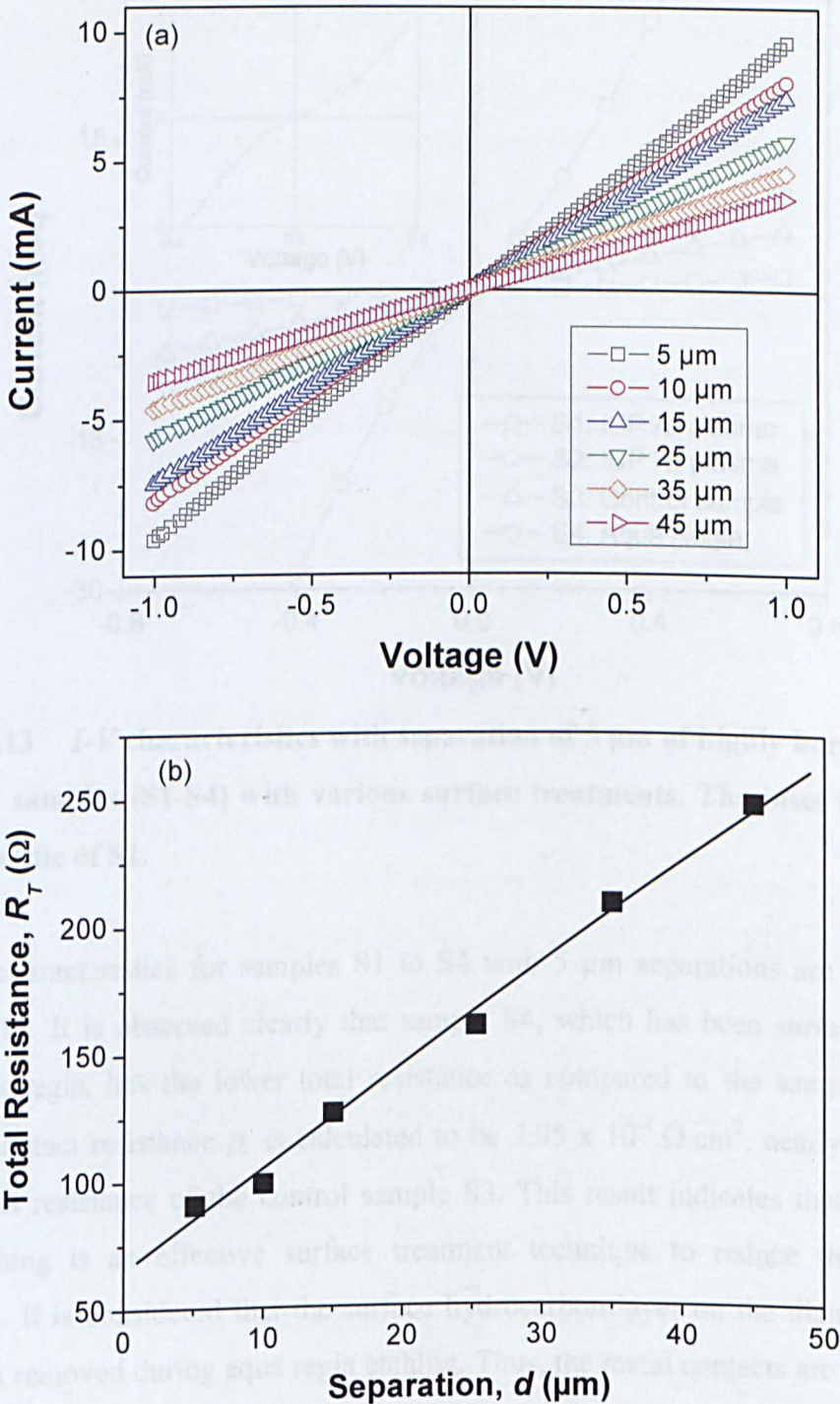
Figure 7.12 **(a) Typical *I-V* characteristics between circular (Ti/Au) boron-doped diamond contacts, and (b) total resistance versus separation between circular diamond contacts of control sample S3.**
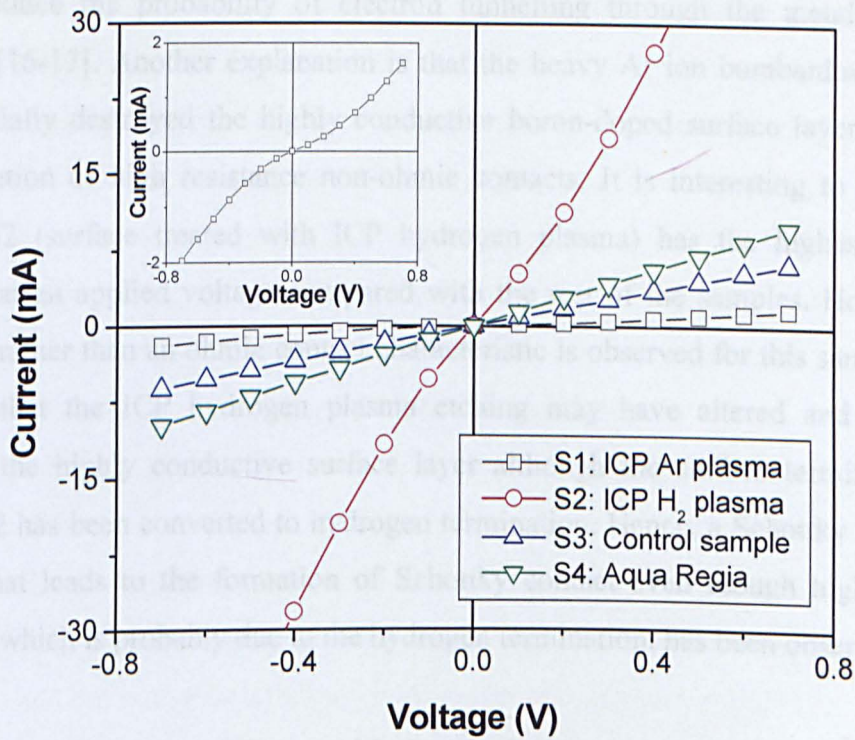
Figure 7.13 *I-V* **characteristics with separation of 5 μm of highly boron-doped diamond samples (S1-S4) with various surface treatments. The inset is the** *I-V* **characteristic of S1.**

The *I-V* characteristics for samples S1 to S4 with 5 μm separations are shown in Figure 7.13. It is observed clearly that sample S4, which has been surface treated with aqua regia, has the lower total resistance as compared to the sample S3. Its specific contact resistance ρ_c is calculated to be 7.95 x 10^{-4} $\Omega.cm^2$, nearly a half of the contact resistance of the control sample S3. This result indicates that the aqua regia etching is an effective surface treatment technique to reduce the contact resistance. It is considered that the surface hydrocarbon layer on the diamond may have been removed during aqua regia etching. Thus, the metal contacts are deposited directly on the high conductive boron-doped diamond layer underneath, resulting in a low contact resistance. It has been reported that the hydrocarbon layer may be removed by the acid cleaning in Ref. 24. Sample S1, which was surface treated with ICP Ar plasma at high platen and coil powers, shows non-ohmic behaviour which is shown more clearly in the inset of Figure 7.13. The non-ohmic behaviour could be due to the surface damage and defects resulting from the high energy Ar ion bombardment. The defects at the diamond surface may widen the depletion width

and/or reduce the probability of electron tunnelling through the metal-diamond junction [16-17]. Another explanation is that the heavy Ar ion bombardments may have partially destroyed the highly conductive boron-doped surface layer, causing the formation of high resistance non-ohmic contacts. It is interesting to note that sample S2 (surface treated with ICP hydrogen plasma) has the highest current intensity at an applied voltage compared with the rest of the samples. However, a Schottky rather than an ohmic contact characteristic is observed for this sample. It is believed that the ICP hydrogen plasma etching may have altered and partially removed the highly conductive surface layer although the surface termination of sample S2 has been converted to hydrogen termination. Hence, a Schottky barrier is created that leads to the formation of Schottky contact even though high current intensity, which is probably due to the hydrogen termination, has been observed.

7.4.3 Surface Treatment: Laser Ablation Technique

7.4.3.1 Samples and Experimental Details

Two highly boron-doped (doping concentration ~ 5×10^{19} cm^{-3}) CVD diamond samples (L1 and L2) with a size of 8 x 8 mm and a thickness of 300 μm were ablated by a 248 nm UV KrF laser. The total ablation area is 1200 μm x 900 μm. The spot size per laser shot is 60 x 60 μm. In this work, the energy density of laser ablation is 6.1 J/cm^2 which was achieved by two laser shots. Under this dosage, the ablated area at diamond surface converts into graphite [25-26] which has a high electrical conductivity. Both samples L1 and L2 were then cleaned with piranha solution (H_2SO_4: H_2O_2 = 4:1) before further processes.

Table 7.3   Surface treatment conditions of L1 and L2.

Sample ID	Platen Power (W)	Coil Power (W)	Chamber Pressure (mTorr)	Type of Gas; Flow rate (sccm)	Etching Duration (min)	Aqua Regia (1 min)
L1	300	900	15	Ar/O$_2$; 15/40	1	Yes
L2	300	900	15	Ar/O$_2$; 15/40	1	No

Sample L1 was cleaned further with boiling aqua regia prior to metal deposition. The CTLM patterns were then fabricated onto the laser ablated and non-ablated areas by standard photolithography method. After photoresist patterning, metal layers of Ti(50nm)/Au(100nm) were deposited and lifted-off to form contact patterns. The sample was then subjected to rapid thermal annealing at 450 °C for 1 minute. In order to remove the highly conductive graphitised layer between the metal contacts, ICP dry etching of Ar/O_2 plasma was carried out. The ICP parameters used were a platen power of 300 W, a coil power of 900W, a chamber pressure of 15 mTorr, flow rates of 15 sccm for Ar and 40 sccm for O_2, and an etching duration of one minute was required in order to remove the laser ablated layer. The actual thickness of the laser ablated layer was determined to be about 0.2 μm, which will be described in the next paragraph. For Sample L2, no aqua regia treatment was performed before metal deposition and the following fabrication processes are identical with Sample L1.

In order to determine the actual thickness of the laser ablated layer, ICP Ar/O_2 plasma was used to etch a test diamond sample which had been ablated with the 248 nm laser under the same laser ablation conditions and duration. The ICP etching conditions are the same as those used for samples L1 and L2. Figure 7.14(a) shows the optical image of the graphitised layer of this test sample after the acetone cleaning prior to plasma etching. The half sample was then masked by photoresist and another half was etched by ICP plasma. Figure 7.14(b) shows that the laser ablated layer has been removed by Ar/O_2 plasma after 1 minute etching. The etch depth was measured to be approximately 0.2 μm using an alpha-stepper, giving an etch rate of 0.2 μm/min. Further ICP etching would induce more defects onto the diamond as illustrated in Figure 7.14(c) and 7.14(d).
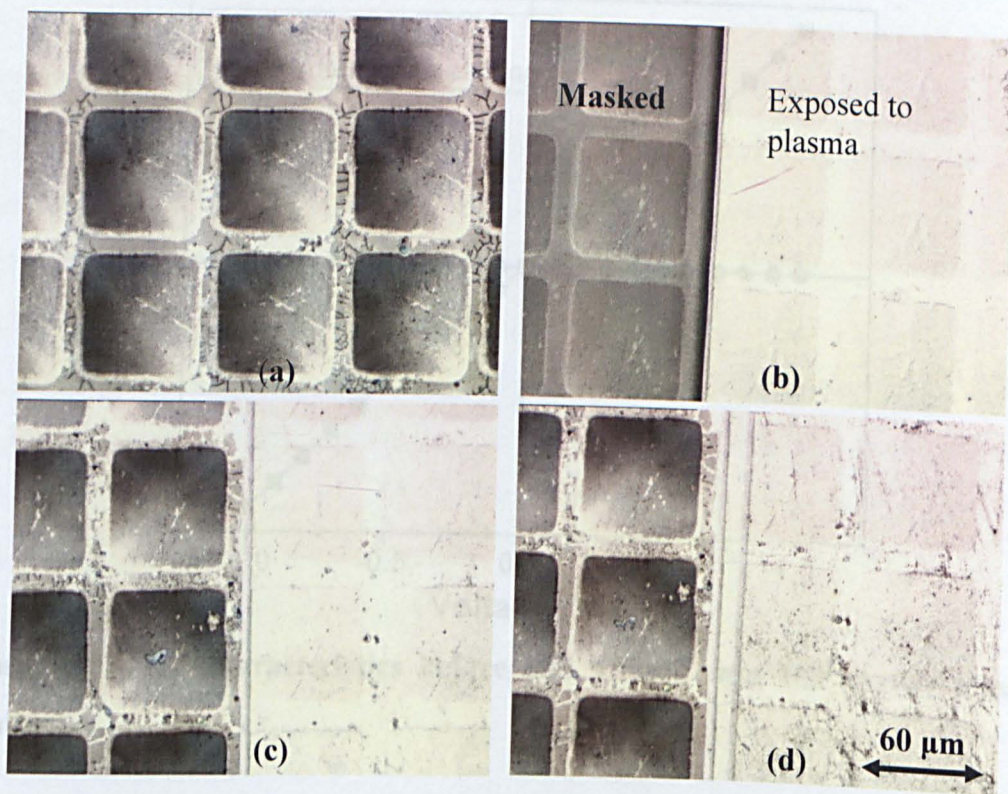
Figure 7.14   Optical images of laser ablated diamond layer (a) prior to ICP etching; and after Ar/O$_2$ plasma etching for (b) 1 min, (c) 2 min and (d) 4 min.

To further confirm the thickness of the graphitised layer, an electrical test was performed. A CTLM pattern was first fabricated directly on top of the laser ablated layer of the above test sample. Then ICP etching with the same etch conditions and duration used for samples L1 and L2 was carried out so as to remove the graphitised layer between the inner and outer circular contacts. Figure 7.15 shows the I-V characteristics of the sample before and after ICP etching using Ar/O$_2$ plasma. Clearly, after the ICP etching, the sample is no longer conductive, confirming that the highly conductive graphitised layer between the contacts has been fully removed. Therefore, it can be concluded that the depth of the laser ablated layer is about 0.2 μm, which is closed to the targeted value. Hence, one-minute Ar/O$_2$ plasma etching used for sample L1 and sample L2 is sufficient to etch away the graphitised layer between the contacts.
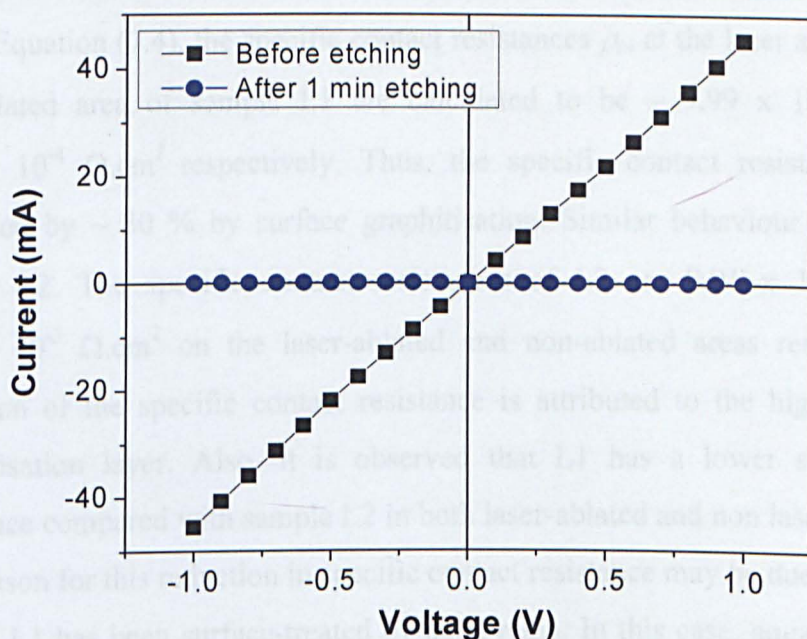
Figure 7.15 *I-V* **characteristics before and after 1 min ICP Ar/O₂ plasma etching.**

7.4.3.2 Experimental Results and Discussion

Figure 7.16 shows the *I-V* curves of sample L1 and L2. These curves show that all the contacts are ohmic. For either sample L1 or L2, the resistance between the contacts made on the laser ablated areas is lower than those between the contacts on non-ablated area.
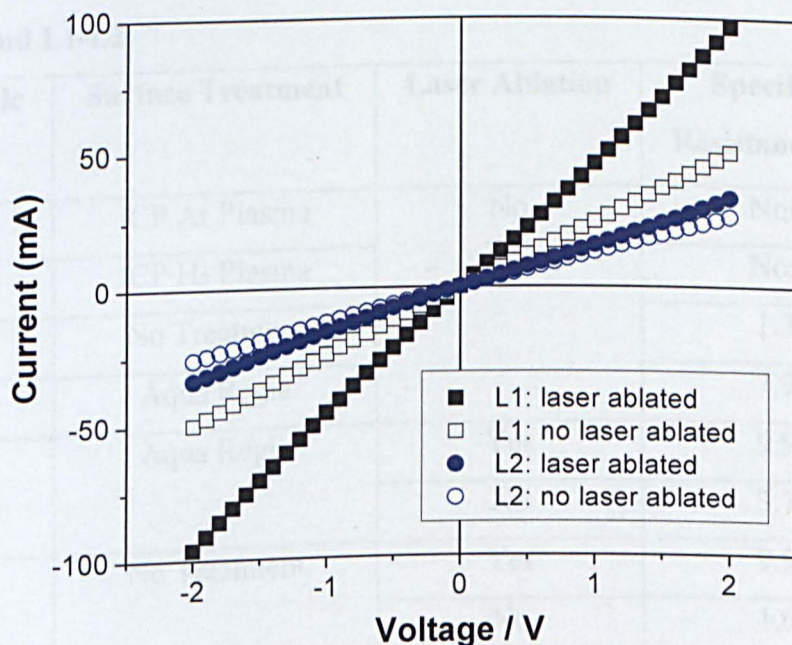

Figure 7.16 *I-V* **characteristics with separation of 5 μm of Sample L1 and L2 on laser-ablated and non-ablated areas.**

Using Equation (7.4), the specific contact resistances ρ_c, at the laser ablated area and non-ablated area of sample L1 are calculated to be $\sim 9.99 \times 10^{-5}$ $\Omega.cm^2$ and 3.78×10^{-4} $\Omega.cm^2$ respectively. Thus, the specific contact resistance has been improved by $\sim 30\%$ by surface graphitisation. Similar behaviour is observed in sample L2. The specific contact resistances of L2 are 9.91×10^{-4} $\Omega.cm^2$ and 1.68×10^{-3} $\Omega.cm^2$ on the laser-ablated and non-ablated areas respectively. The reduction of the specific contact resistance is attributed to the highly conductive graphitisation layer. Also, it is observed that L1 has a lower specific contact resistance compared with sample L2 in both laser-ablated and non laser-ablated areas. The reason for this reduction in specific contact resistance may be due to the fact that sample L1 has been surface-treated by aqua regia. In this case, aqua regia may has successfully removed a thin non-graphite carbon layer or contaminants deposited during the laser shot. A reduction in ohmic contact resistance due to utilisation of aqua regia has also been shown in **Section 7.4.2**. Hence, these results show that aqua regia treatment is an effective method to reduce the contact resistance. Table 7.4 summarises the specific contact resistances of all the diamond samples described in **Sections 7.4.2** and **7.4.3**.

Table 7.4   **Surface treatments and specific contact resistance for samples S1-S4 and L1-L2.**

Sample ID	Surface Treatment	Laser Ablation	Specific Contact Resistance, ρ_c ($\Omega.cm^2$)
S1	ICP Ar Plasma	No	Non Ohmic
S2	ICP H_2 Plasma		Non Ohmic
S3	No Treatment		1.38×10^{-3}
S4	Aqua Regia		7.95×10^{-4}
L1	Aqua Regia	Yes	9.99×10^{-5}
		No	3.78×10^{-4}
L2	No Treatment	Yes	9.91×10^{-4}
		No	1.68×10^{-3}

As a summary, the specific contact resistance, ρ_c, of the highly boron-doped diamond samples have been substantially reduced by surface treatment and laser ablation techniques. Aqua regia surface treatment has been identified to be an effective method in achieving good ohmic contact on highly boron-doped diamond. On the other hand, laser ablation, which creates a highly conductive graphitised layer, also enables the reduction of the specific contact resistance on diamond. A lowest specific contact resistance of 9.99×10^{-5} $\Omega.cm^2$ has been achieved by combining both surface aqua regia treatment and laser ablation. Unfortunately, laser ablation technique is not adopted in the future experiment for field effect transistor fabrication (in **Chapter 8**) due to the limited access of the laser equipment. In addition, the lateral resolution of the ablating laser is currently not small enough to fabricate a practical transistor.

7.4.4 Effect of Ar/Cl₂ Plasma

In order to fabricate diamond MISFET devices, contact windows in intrinsic diamond layer which serves as a gate dielectric should be created so that high quality ohmic contacts can be fabricated on highly boron-doped layer. To achieve this target, Ar/Cl₂ plasma etching is employed to make such contact windows due to its high controllability, and repeatability and smoothing effect as discussed in **Section 7.2 and Section 7.3**. To investigate the influences of Ar/Cl₂ plasma etching on the electrical contact characteristic, Ar/Cl₂ plasma etching was carried out and CTLM patterns were fabricated on a HPHT diamond sample C1 with a highly boron-doped surface layer (doping concentration ~ 1×20^{21} cm^{-3}). During the etch process, half of the sample was Ar/Cl₂ plasma etched whereas the other half was not etched, which was accomplished by masking half of the sample with photoresist during the ICP plasma etching. The ICP etching conditions were: ICP platen power of 300 W, coil power of 400 W, Ar/Cl₂ flow rates of 25/45 sccm and a chamber pressure of 5 mTorr. The etching duration was set to 15 seconds in order to remove a 4 nm-thick boron-doped surface layer. The CTLM patterns were fabricated on both etched and non-etched areas of the sample. The contact metals used were Ti (50 nm) and Au (100 nm). The fabrication process sequence is summarised in Figure 7.17. An optical image of the CTLM patterns formed on sample C1 is presented in Figure 7.18. The specific contact resistance was calculated using Equation (7.4).
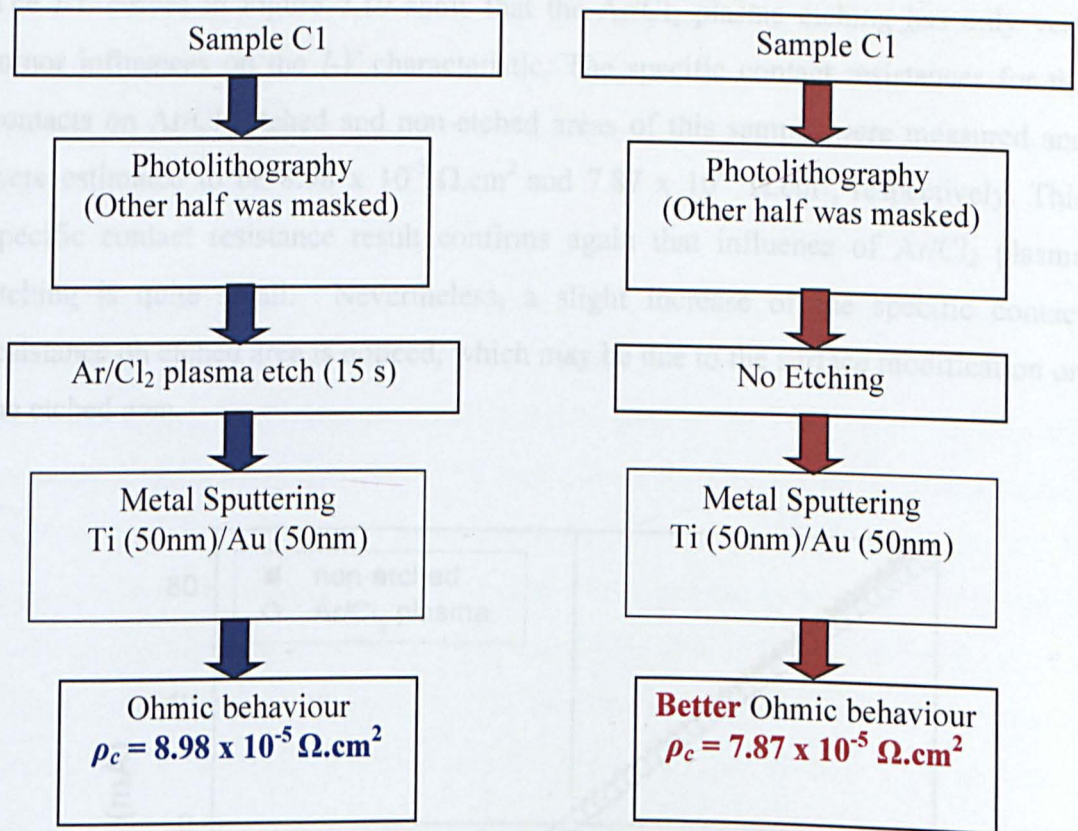
Sample C1	Sample C1
Photolithography (Other half was masked)	Photolithography (Other half was masked)
Ar/Cl$_2$ plasma etch (15 s)	No Etching
Metal Sputtering Ti (50nm)/Au (50nm)	Metal Sputtering Ti (50nm)/Au (50nm)
Ohmic behaviour $\rho_c = 8.98 \times 10^{-5}$ $\Omega.cm^2$	**Better** Ohmic behaviour $\rho_c = 7.87 \times 10^{-5}$ $\Omega.cm^2$

Figure 7.17 Fabrication process sequence of sample C1 to confirm the effect of Ar/Cl$_2$ plasma etch on the specific contact resistance.
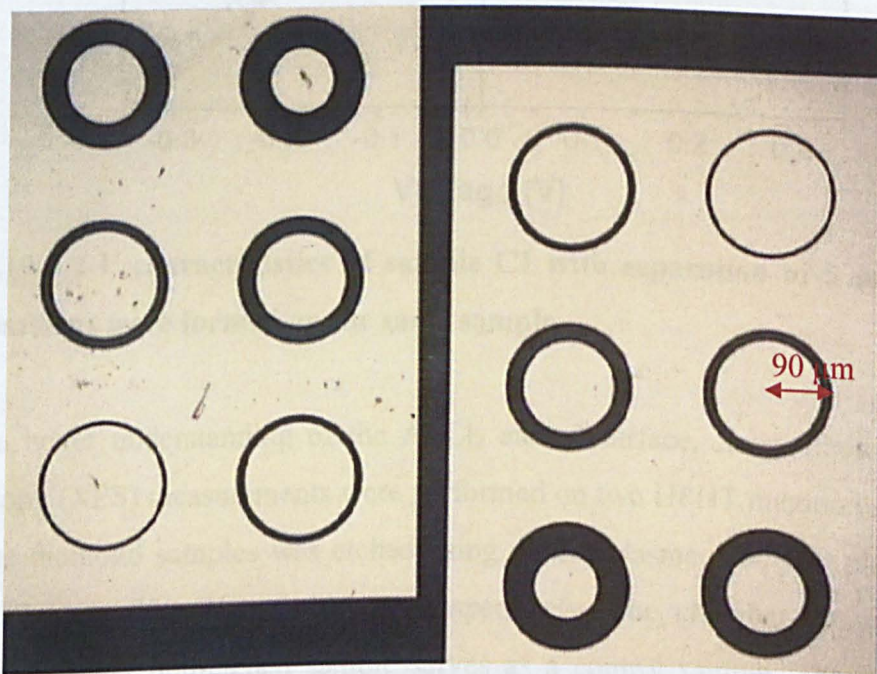
Figure 7.18 Optical images of the CTLM patterns fabricated on the sample C1 where the left CTLM pattern was fabricated by the non-etched processes and the right CTLM pattern was fabricated by Ar/Cl$_2$ plasma etching processes.

The *I-V* curves in Figure 7.19 show that the Ar/Cl_2 plasma etching has only very minor influences on the *I-V* characteristic. The specific contact resistances for the contacts on Ar/Cl_2 etched and non-etched areas of this sample were measured and were estimated to be 8.98×10^{-5} $\Omega.cm^2$ and 7.87×10^{-5} $\Omega.cm^2$, respectively. This specific contact resistance result confirms again that influence of Ar/Cl_2 plasma etching is quite small. Nevertheless, a slight increase of the specific contact resistance on etched area is noticed, which may be due to the surface modification on the etched area.
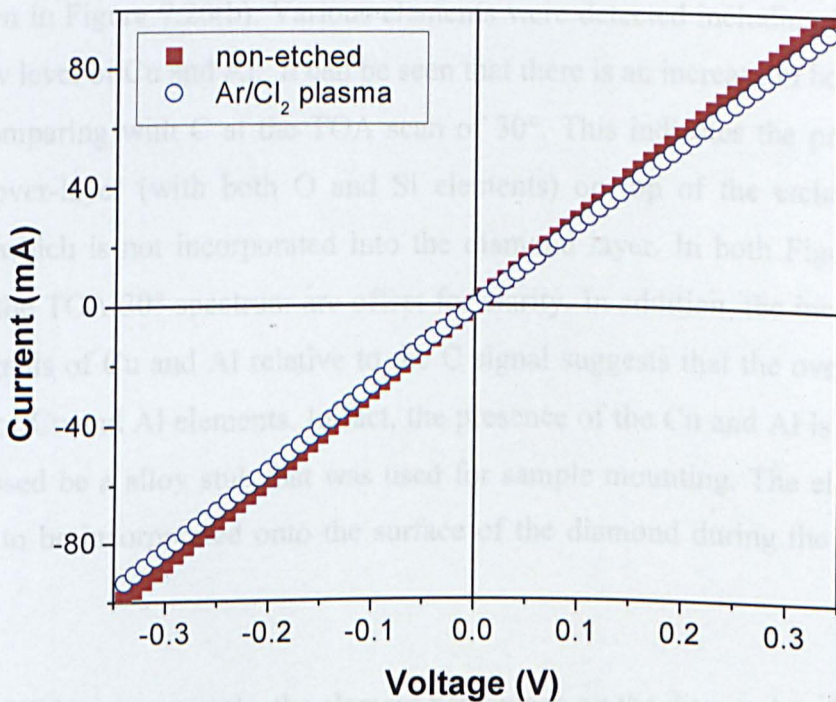
Figure 7.19 *I-V* **characteristics of sample C1 with separation of 5 μm. Both CTLM patterns were formed on the same sample.**

To gain a better understanding of the Ar/Cl_2 etched surface, X-ray Photoelectron Spectroscopy (XPS) measurements were performed on two HPHT diamond samples. One of the diamond samples was etched using Ar/Cl_2 plasma. The ICP platen and coil powers were 300 W and 100 W, respectively. The chamber pressure was 5 mTorr. The other non-etched sample serves as a control sample. The XPS was performed under contract for Element Six Ltd. using Mg Kα x-ray source with a energy of 100 eV. The XPS scan was done with two take-off-angles (TOA) at 30°

and 90° where TOA of 30° results in the half sampling depth as compared to that of 90°. Angle resolved XPS analysis was performed at a particular angle (i.e. 30°) in order to limit the depth of photoelectron detection and hence to increase the surface sensitivity.

Figure 7.20(a) shows the XPS spectrum of the non-etched sample. This spectrum indicates the presence of the elements, C, O and low level of N on the non-etched diamond surface. The increase of the O and N level at the TOA of 30° implies the presence of surface impurity. The XPS results from the Ar/Cl_2 plasma etched surface are shown in Figure 7.20(b). Various elements were detected including C, O, Cl, Si and a low level of Cu and Al. It can be seen that there is an increase in both O and Si levels comparing with C at the TOA scan of 30°. This indicates the presence of a surface over-layer (with both O and Si elements) on top of the etched diamond surface, which is not incorporated into the diamond layer. In both Figures 7.20(a) and (b), the TOA 30° spectrum are offset for clarity. In addition, the increase of the metal signals of Cu and Al relative to the C signal suggests that the over-layer also consists of Cu and Al elements. In fact, the presence of the Cu and Al is most likely to be caused be a alloy stub that was used for sample mounting. The element Cl is believed to be incorporated onto the surface of the diamond during the ICP Ar/Cl_2 etching.

From the XPS measurements, the element percentage on the diamond surfaces can be estimated. These data are summarised in Table 7.5. The percentages of the O level obtained at TOA 90° for both non-etched and Ar/Cl_2 plasma etched surface are about half compared to the TOA scan of 30°. This confirms that oxygen is present as a surface over-layer, which is not bonded to the diamond. The same phenomenon can also be observed in Si level. Both O and Si elements may be originated from the silicone grease that was used to attach the samples during the XPS analysis. The Si element may also be originated from the silicon tray that was used during the ICP Ar/Cl_2 plasma etching. This leads to the possibility that a mixture of silicone or silicate, Cu and Al type of layer is distributed over the chlorinated diamond surface.
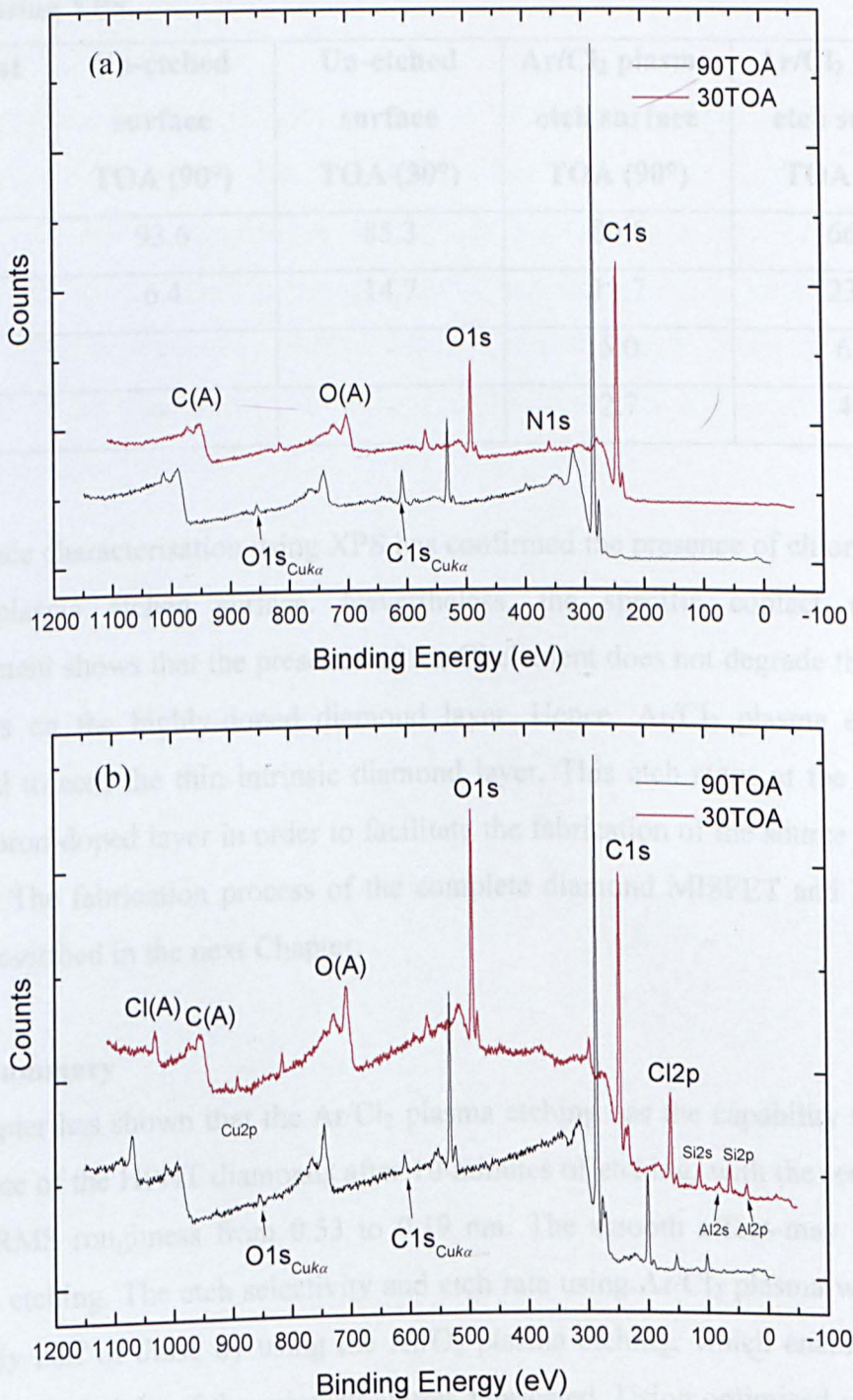
Figure 7.20 **Surface characterisation using XPS on (a) control sample without any surface etch and (b) a sample subjected to Ar/Cl₂ plasma etch.**

Table 7.5   Elemental composition of the un-etched and Ar/Cl₂ plasma etched surface using XPS.

Element	Un-etched surface TOA (90°)	Un-etched surface TOA (30°)	Ar/Cl₂ plasma etch surface TOA (90°)	Ar/Cl₂ plasma etch surface TOA (30°)
C	93.6	85.3	80.6	66.1
O	6.4	14.7	11.7	23.0
Cl	-	-	5.0	6.2
Si	-	-	2.7	4.7

The surface characterisation using XPS has confirmed the presence of chlorine in the Ar/Cl₂ plasma etched surface. Nevertheless, the specific contact resistance measurement shows that the presence of the Cl element does not degrade the contact properties on the highly-doped diamond layer. Hence, Ar/Cl₂ plasma etching is employed to etch the thin intrinsic diamond layer. This etch stops at the very thin highly boron-doped layer in order to facilitate the fabrication of the source and drain contacts. The fabrication process of the complete diamond MISFET and MOSFET will be described in the next Chapter.

7.5   Summary

This chapter has shown that the Ar/Cl₂ plasma etching has the capability to smooth the surface of the HPHT diamonds after 10 minutes of etching, with the reduction of surface RMS roughness from 0.53 to 0.19 nm. The smooth effect may be due to isotropic etching. The etch selectivity and etch rate using Ar/Cl₂ plasma were found to be only half of those by using the Ar/O₂ plasma etching, which enables a good control on the height of the microstructures fabricated. Using optimised conditions, shallow micro-trenches with depths of 16 and 53 nm were fabricated on the CVD diamond. By varying the ICP coil power, the etch rate of diamond can be further reduced to 0.7 nm/s. With such a low etch rate, very shallow diamond micro-trenches with a depth of 8 nm have been fabricated. Excellent etch reproducibility and controllability by using Ar/Cl₂ plasma were demonstrated. These results also confirm

that the etch rates for different types of diamond including intrinsic, boron-doped and HPHT diamonds are almost identical.

Diamond micro-electronic devices such as MISFETs and MOSFETs require good ohmic contact formation. The specific contact resistances, ρ_c of the highly boron-doped diamond samples (i.e. 5 $\times 10^{19}$ cm^{-3}) have been effectively reduced by means of surface treatment using aqua regia and laser ablation technique which creates a highly conductive graphitised layer. A lowest specific contact resistance of 9.99 x 10^{-5} Ω.cm^2 has been achieved by applying both surface treatment and laser ablation technique followed by RTA at 450 °C for 1 minute.

7.6 References

[1] F.C. Champion, *Electronic Properties of Diamond*, Butterworths, London (1963).

[2] J.E. Field, *The properties of Diamond*, Academic, New York (1979).

[3] L.S. Pan, D.R. Kania, *Diamond: Electronic Properties and Applications*, Springer (1994).

[4] J. Isberg, J. Hammersberg, E. Johansson, T. Wilkstrom, D.J. Twitchen, A.J. Whitehead, S.E. Coe, G.A. Scarsbrook, *Science*, **297**, 1670 (2002).

[5] J. Asmussen, D. Reinhard, *Diamond Films Handbook*, CRC Press (2002).

[6] M.H. Nazare, A.J. Neves, *Properties, Growth and Application of Diamond*, INSPEC (2001).

[7] M.A. Prelas, G. Popovici, L.K. Bigelow, *Handbook of Industrial Diamonds and Diamond Films*, Marcel Dekker (1997).

[8] W. Tsai, M. Delfino, D. Hodul, M. Riaziat, L.Y. Ching, G.Reynolds, C.B. Cooper, *IEEE Electron Device Lett.*, **12**, 157 (1991).

[9] G.S. Gildenblat, S.A. Grot, C.W. Hatfield, *Sol. Stat. Elect.*, **36**, 462 (1993).

[10] H.W. Choi, E. Gu, C. Liu, J.M. Girkin, M.D. Dawson, *J. of Appl. Phys.*, **97** (6), 063101 (2005).

[11] L. Jiang, N.O.V. Plank, M.A. Blauw, R. Cheung, E. van der Drift, *J. Phys. D: Appl. Phys.*, **37**, 1809 (2004).

[12] C.H. Jeong, D.W. Kim, J.W. Bae, Y.J. Sung, J.S. Kwak, Y.J. Park, G.Y. Yeom, *Mat. Sci. & Eng. B*, **93**, 60 (2002).

[13] J. Chaffey, M. Austin, I. Switala, K .Grant, *Optoelectronic and Microelectronic Materials and Devices, 2002 Conference on 11-13 Dec. 2002*, 575 (2002).

[14] M. Gad-el-Hak, *MEMS: Design and Fabrication*, CRC Press (2005).

[15] R.E. Rawles, S.F. Komarov, R. Gat, W.G. Morris, J.B. Hudson, M.P. D'Evelyn, *Dia. Rel. Mat.*, **6**, 791 (1997).

[16] T. Tachibana, B.E. Williams, J.T. Glass, *Phys. Rev. B*, **45**, 11968 (1992).

[17] T. Tachibana, B.E. Williams, J.T. Glass, *Phys. Rev. B*, **45**, 11975 (1992).

[18] K. Das, V. Venkatesan, K. Miyata, D.L. Dreifus, J.T. Glass, *Thin Sol. Films*, **212**, 19 (1992).

[19] Y. Chen, M. Ogura, S. Yamasaki, H. Okushi, *Semicond. Sci. Tehnol.*, **20**, 860 (2005).

[20] C.A. Heweet, J.R. Zeidler, *Dia. Rel. Mat.*, **1**, 688 (1992).

[21] M. Werner, C. Johnston, P.R. Chalker, S. Romani and I.M. Buckley-Golder, *J. Appl. Phys.*, **79**, 2535 (1996).

[22] K. Hayashi, S. Yamanaka, H. Watanabe, T. Sekiguchi, H. Okushi, K. Kajimura, *J. Appl. Phys.*, **81**, 744 (1997).

[23] G.S. Marlow, M.B. Das, *Sol. Stat. Elec.*, **25**, 91 (1982).

[24] S.A. Grot., G.S. Gildenblat, C.W. Hatfield, C.R. Wronski, A.R. Badzian, T. Badzian, R. Messier, *IEEE Elect. Dev. Lett.*, **11**, 100 (1990).

[25] R. Walker, S. Prawer, D.N. Jamieson, K.W. Nugent, *Appl. Phys. Lett.*, **71**, 1492 (1997).

[26] S. Gloor, S.M. Pimenov, E.D. Obraztsova, W. Luthy, H.P. Weber, *Dia. Rel. Mat.*, **7**, 607 (1998).

Chapter 8

Diamond Micro-electronic Devices:

Metal Insulator Semiconductor Field Effect Transistor and

Metal Oxide Semiconductor Field Effect Transistor

8.1   Introduction

Due to its unique electrical properties such as high breakdown strength and high hole mobility [1], diamond is an ideal semiconductor material for developing high functional electronic devices for example, diamond field effect transistors. In this chapter, the fabrications and characterisations of two types of diamond-based transistors, metal insulator semiconductor field effect transistor (MISFET) and metal oxide semiconductor field effect transistor (MOSFET), are reported. The insulator used in MISFET was intrinsic diamond whereas SiO_2 was employed as insulator in MOSFET. The basic theory of FET devices is discussed in **Chapter 2**.

8.2   MISFET Devices

With the capability of ICP Ar/Cl_2 plasma of highly controllable etch rate (in nanometre scale) and surface smoothing effect (removing sub-surface damage), as shown in **Section 7.2 and 7.3**, a MISFET device can be fabricated.

8.2.1   Fabrication Process

A photo-mask is required for fabricating diamond MISFET devices. Figure 8.1(a) shows the mask design of a three-terminal (drain, source and gate) MISFET device. The schematic diagram of a MISFET device is shown in Figure 8.1(b). In this device, the channel length is designed to be 17 μm, which should be considered as a long-channel-effect device [2]. The channel length is the length in between the drain and source terminals, as shown in **Chapter 2**. Device with the channel length greater than 2 μm is considered as long channel-effect device [2]. The gate length is designed to be 5 μm. For this device, the gate is designed on top of the intrinsic diamond layer and the drain and source terminals are in contact directly with the highly-boron doped diamond layer.

(a)

(b)
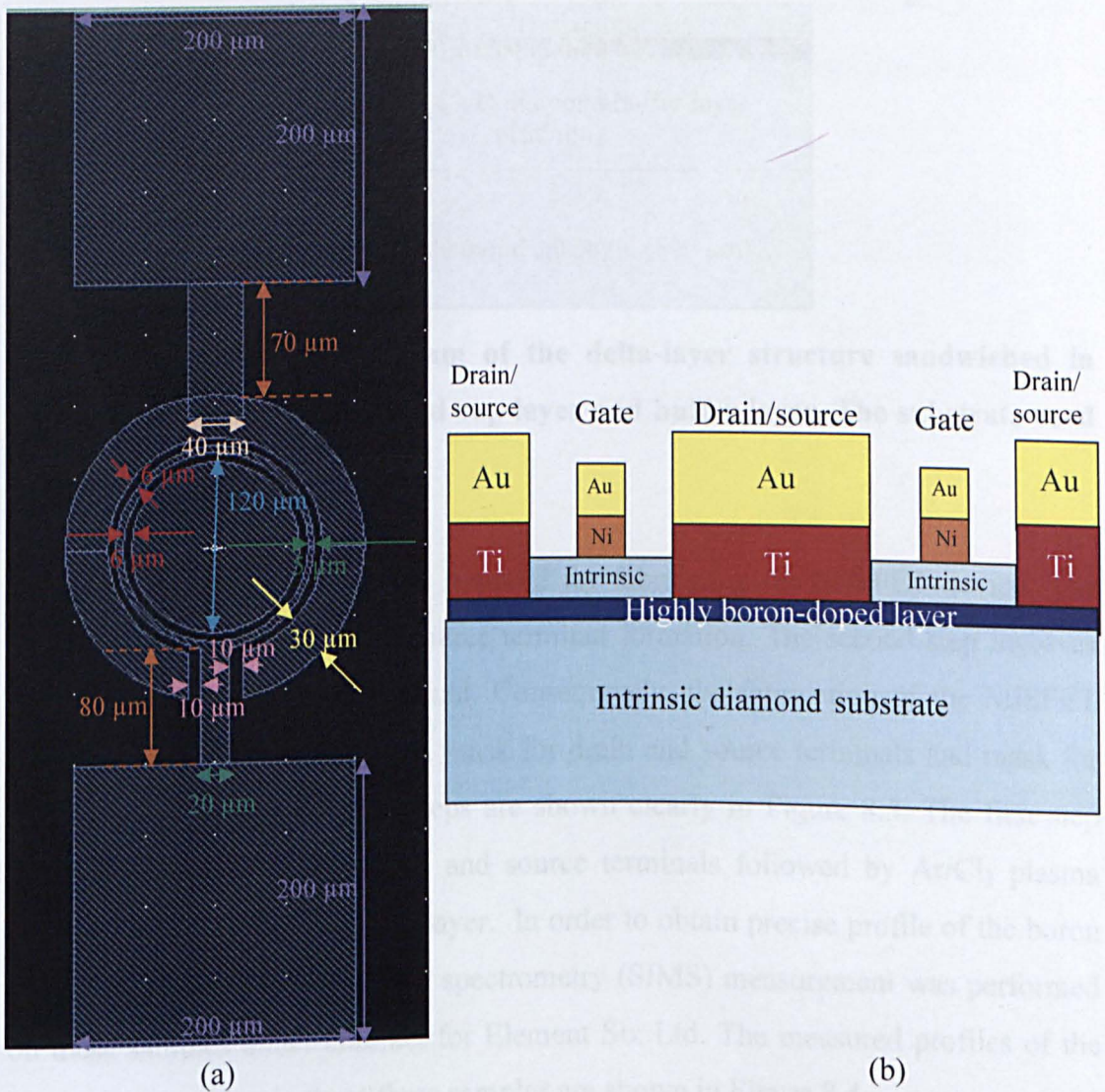
Figure 8.1   (a) A mask design of a MISFET or MOSFET device. The gate length and the channel length are 5 and 17 μm, respectively. (b) The corresponding schematic diagram of the MISFET device.

Three samples with a highly-boron doped delta layer, namely M1, M2 and M3, were used for the MISFET fabrication. In these samples, the highly-doped layer has been sandwiched in between the CVD diamond capping layer and CVD buffer layer as shown in Figure 8.2.
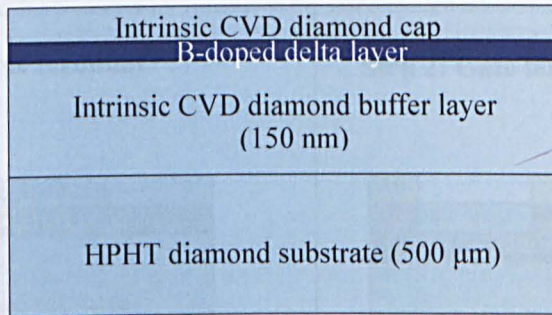
| Intrinsic CVD diamond cap |
| B-doped delta layer |
| Intrinsic CVD diamond buffer layer (150 nm) |
| HPHT diamond substrate (500 μm) |

Figure 8.2 **Schematic diagram of the delta-layer structure sandwiched in between intrinsic CVD diamond cap layer and buffer layer. The substrate used is a HPHT substrate.**

Two photolithographic steps are required for fabricating the MISFET device. The first one is used for drain and source terminal formation. The second step involves the fabrication of the gate terminal. Consequently, the fabrication of the MISFET requires two different masks, i.e. mask for drain and source terminals and mask for gate terminal. The fabrication steps are shown clearly in Figure 8.3. The first step involves patterning of the drain and source terminals followed by Ar/Cl$_2$ plasma etching of the intrinsic diamond layer. In order to obtain precise profile of the boron doped layer, secondary ion mass spectrometry (SIMS) measurement was performed on these samples under contract for Element Six Ltd. The measured profiles of the boron concentration in these three samples are shown in Figure 8.4.

Figure 8.3   Fabrication steps of a MISFET device, involving a two-step photolithography process, drain-source terminal and gate terminal.
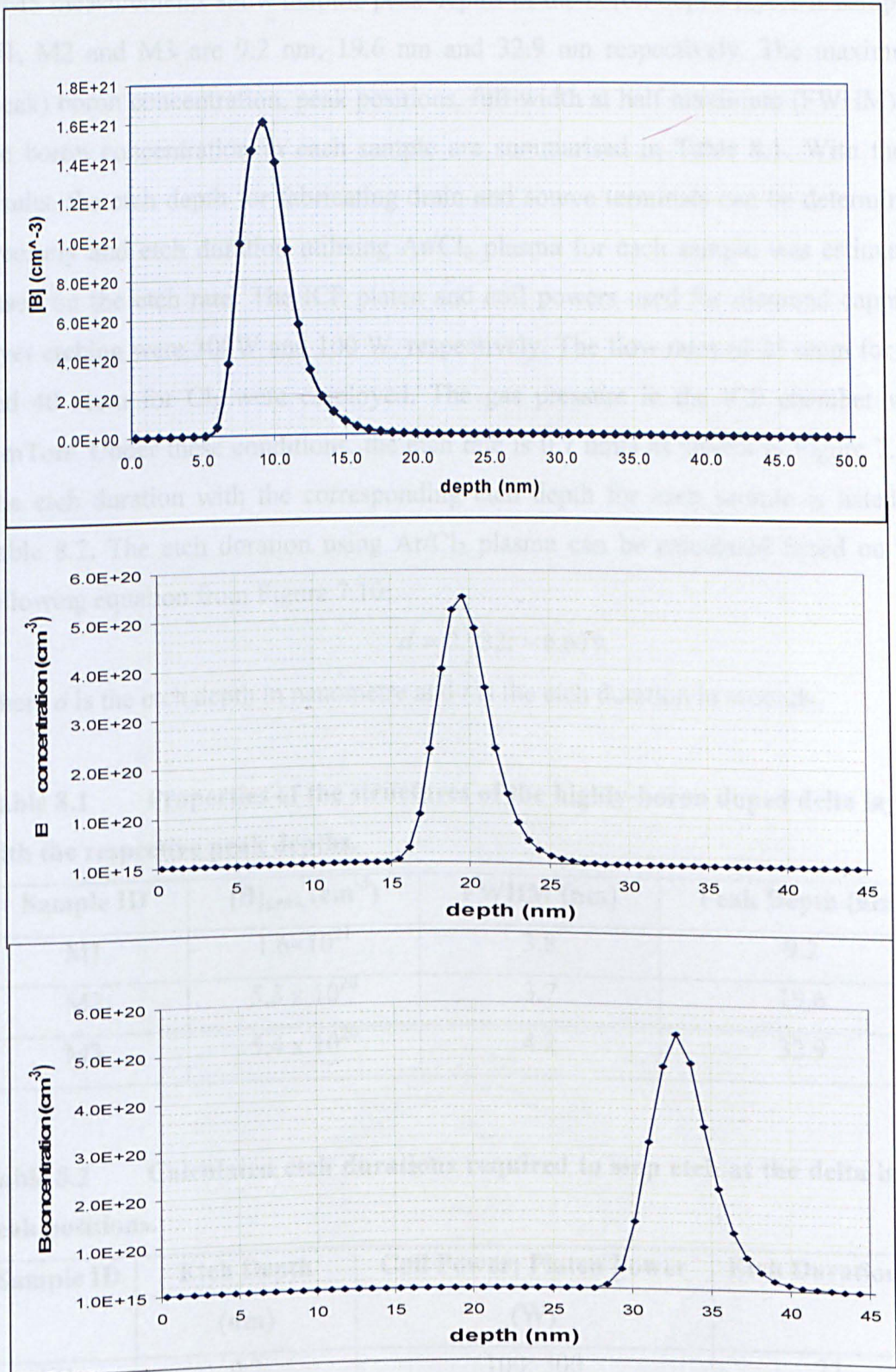
Figure 8.4 Boron concentration profiles for samples, M1, M2 and M3 measured using SIMS.

SIMS measurements show that the peak depths of the boron-doped layers in samples M1, M2 and M3 are 9.2 nm, 19.6 nm and 32.9 nm respectively. The maximum (peak) boron concentration, peak positions, full-width at half maximum (FWHM) of the boron concentration in each sample are summarised in Table 8.1. With these results, the etch depth for fabricating drain and source terminals can be determined precisely and etch duration utilising Ar/Cl$_2$ plasma for each sample was estimated based on the etch rate. The ICP platen and coil powers used for diamond capping layer etching were 300W and 100 W, respectively. The flow rates of 25 sccm for Ar and 40 sccm for Cl$_2$ were employed. The gas pressure in the ICP chamber was 5 mTorr. Under these conditions, the etch rate is 0.7 nm/s as shown in Figure 7.10. The etch duration with the corresponding etch depth for each sample is listed in Table 8.2. The etch duration using Ar/Cl$_2$ plasma can be calculated based on the following equation from Figure 7.10:

$$d = 0.732t - 6.679$$

where d is the etch depth in nanometre and t is the etch duration in seconds.

Table 8.1   Properties of the structures of the highly-boron doped delta layers with the respective peak depths.

Sample ID	[B]$_{peak}$ (cm^{-3})	FWHM (nm)	Peak Depth (nm)
M1	1.6×10^{21}	3.8	9.2
M2	5.5×10^{20}	3.7	19.6
M3	5.4×10^{20}	4.2	32.9

Table 8.2   Calculated etch durations required to stop etch at the delta layer peak positions.

Sample ID	Etch Depth (nm)	Coil Power; Platen Power (W)	Etch Duration(s)
M1	9.2	100; 300	22
M2	19.6	100; 300	36
M3	32.9	100; 300	54

Ti metal with a thickness of 50 nm was then sputtered on the surface of the highly boron doped layer followed by depositing 100nm thick Au metal layer. After the metal lift-off process, the samples were annealed at 450 °C for 1 minute in order to form TiC compound to achieve ohmic contact with low contact resistance [4-5]. The gate fabrication begins with a photolithographic process to form a gate terminal pattern. A Ni layer (10nm) and a Au layer (10nm) were then deposited on top of the intrinsic diamond layer. After the metal lift-off process, the fabrication of depletion mode p-type MISFET devices is completed. Figure 8.5(a) and Figure 8.5(b) show optical images of the fabricated MISFET devices. The three terminals of drain, source and gate are labeled in the figures.
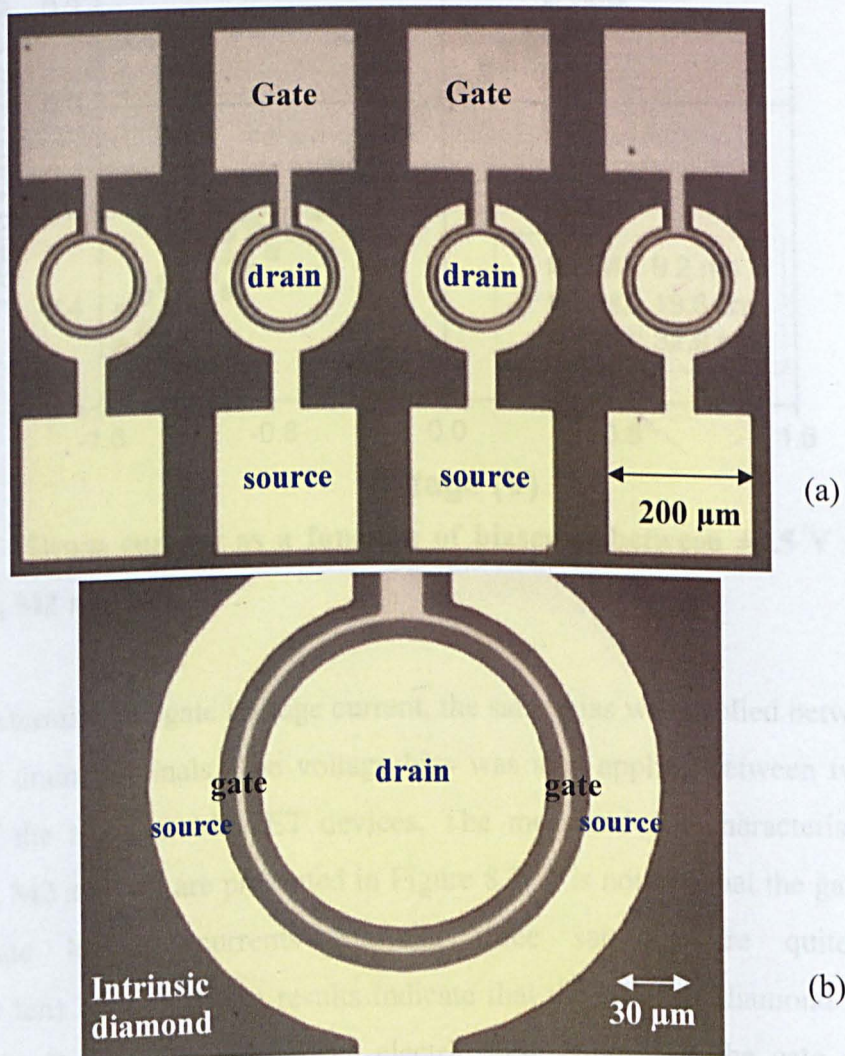
Figure 8.5   **Optical images of (a) four fabricated MISFET devices and (b) magnified image of a single MISFET device.**

8.2.2 Experimental Results and Discussion

The MISFET device was measured using a Parameter Analyser HP5145A. A two-probe measurement was first performed across the source and drain terminals. Figure 8.6 shows the source-drain current for the samples M1, M2 and M3 with the bias of ± 1.5 V. It is observed clearly that all *I-V* curves are linear, indicating ohmic contact behaviour. These results show that the Ar/Cl$_2$ plasma etching is able to stop precisely just at the narrow delta layers, resulting in good ohmic contact formation.
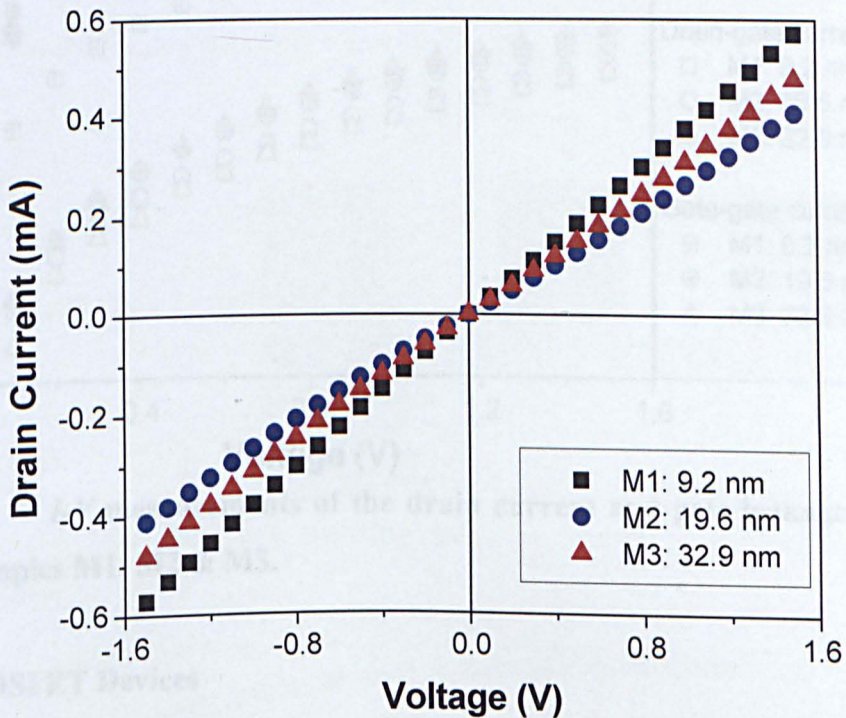
Figure 8.6 **Drain current as a function of biases at between ±1.5 V for the samples M1, M2 and M3.**

In order to determine the gate leakage current, the same bias was applied between the gate and the drain terminals. The voltage bias was also applied between two gate terminals of the adjacent MISFET devices. The measured *I-V* characteristics for samples M1, M2 and M3 are presented in Figure 8.7. It is noticed that the gate-drain and gate-gate leakage currents for the three samples are quite large (up to a few tens of µA). These results indicate that the intrinsic diamond capping layer is leaky. Due to this reason, the electric field control by the gate of these devices is not observed. Clearly, a high quality intrinsic diamond layer is required in order to prevent the severe gate leakage current. Hence, Element Six Ltd is carrying

on the quality improvement of the intrinsic capping layer. As an alternative approach, we have developed diamond metal oxide field effect transistor (MOSFET) devices.

Figure 8.7 *I-V* **measurements of the drain current and gate leakage current for the samples M1, M2 & M3.**

8.3 MOSFET Devices

Instead of the diamond capping layer, dielectrics such as SiO_2 can be chosen as a gate material. This leads to the development of MOSFET devices.

Prior to device fabrication, it is crucial to investigate the minimum SiO_2 thickness that can withstand the large gate bias. To optimise the SiO_2 thickness, three HPHT type Ib diamond substrates with highly boron-doped CVD cap layers were employed. The thickness of the highly doped capping layer is 50 nm with the doping concentration of $\sim 1 \times 10^{21}$ cm^{-3}. A SiO_2 layer was then deposited on the highly boron-doped cap layer of the diamond samples by using plasma enhanced chemical vapour deposition (PECVD) method. The thickness of the SiO_2 layer for each sample is different and is controlled by the deposition duration. By setting the deposition duration at 1, 1.5 and 2 minutes, the SiO_2 layer thicknesses (T_{SiO2}) obtained for the

three samples are 29 nm, 43 nm and 55 nm respectively. The metal contacts were then fabricated on the SiO_2 layer, as shown in Figure 8.8.

8.3.1   Effect of SiO_2 Thickness

Figure 8.9 shows the *I-V* measurements of the three test samples with different SiO_2 layer thicknesses. It is observed that the sample with the thinnest SiO_2 layer (29 nm) has a high leakage current (> 1 mA) even with the bias as low as 1 V. The sample with the thickest SiO_2 layer (55 nm) is able to withstand large bias up to 20 V and at this bias, the leakage current is only a few tens of nA.
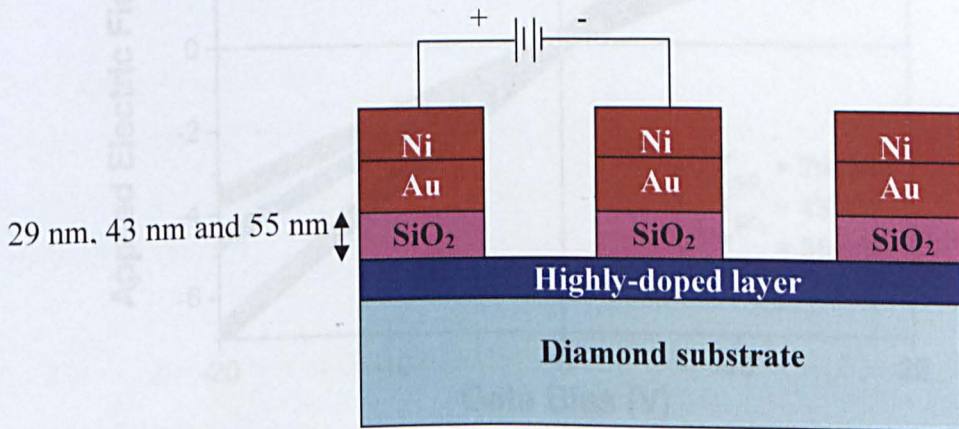
Figure 8.8   A test structure utilising SiO_2 as dielectric to investigate the leakage current.
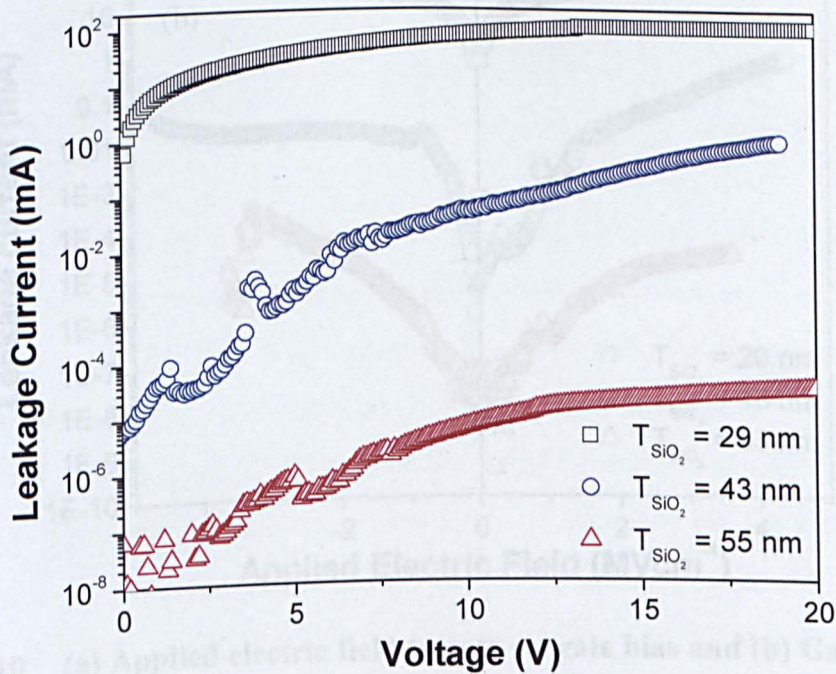
Figure 8.9   *I-V* measurements for SiO_2 thickness of 29, 43 and 55 nm on top of a highly boron-doped diamond of 1×10^{21} cm^{-3}.

The electric field in the SiO₂ layers with different thicknesses can be calculated from Figure 8.9 by dividing the applied bias with respective SiO₂ thickness, assuming the voltage drop across the highly boron-doped layer can be neglected compared to the voltage drop across the SiO₂. The calculated results are shown in Figure 8.10.
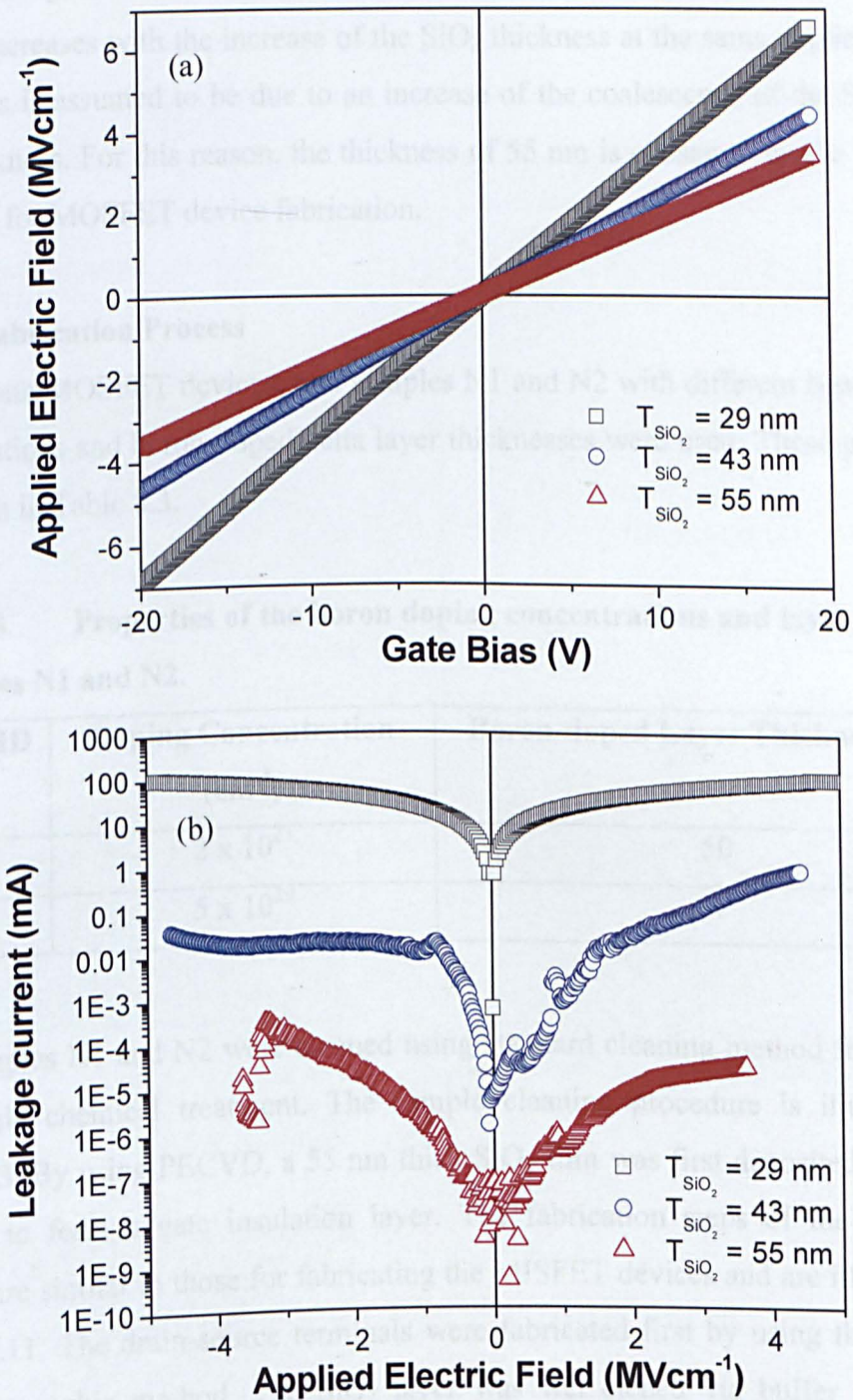
Figure 8.10   (a) Applied electric field to gate vs. gate bias and (b) Gate leakage current vs. applied electric field for samples with SiO₂ thicknesses of 29, 43 and 55 nm.

The electric field at bias of 20 V for SiO_2 with thickness of 29, 43 and 55 nm is calculated to be 6.90, 4.65 and 3.64 $MVcm^{-1}$, respectively. It can be seen that the applied electric field is associated with the SiO_2 thickness. Figure 8.10(a) shows that the applied electric field to the gate decreases with the increase of the SiO_2 thickness at the same gate bias. However, it is noted from Figure 8.10(b) that the leakage current decreases with the increase of the SiO_2 thickness at the same applied electric field. This is assumed to be due to an increase of the coalescence of the SiO_2 layer with thickness. For this reason, the thickness of 55 nm is chosen to be the SiO_2 gate thickness for MOSFET device fabrication.

8.3.2 Fabrication Process

To fabricate MOSFET devices, two samples N1 and N2 with different boron-doping concentrations and boron-doped delta layer thicknesses were used. These parameters are shown in Table 8.3.

Table 8.3 **Properties of the boron doping concentrations and layer thickness of samples N1 and N2.**

Sample ID	Doping Concentration (cm^{-3})	Boron-doped Layer Thickness (nm)
N1	2×10^{21}	50
N2	5×10^{20}	4

Two samples N1 and N2 were cleaned using standard cleaning method followed by aqua reqia chemical treatment. The sample cleaning procedure is illustrated in Chapter 3. By using PECVD, a 55 nm thick SiO_2 film was first deposited onto both samples to form a gate insulation layer. The fabrication steps of the MOSFET devices are similar to those for fabricating the MISFET devices and are illustrated in Figure 8.11. The drain-source terminals were fabricated first by using the standard photolithographic method. The SiO_2 layer was wet etched via buffer oxide etch (BOE) solution ($NH_3(OH):HF = 1:7$) for 1 minute in view of the fact that BOE does not etch diamond at all. After the SiO_2 etch, Ti (50 nm) and Au (100 nm) metal layers were sputtered onto the drain and source pattern area. The samples were then

annealed at 450 °C for 1 minute to form ohmic contacts. The fabrication processes of the gate terminal are identical with the MISFET fabrication steps. It involves Ni (10 nm) and Au (10 nm) metal depositions on top of the SiO_2 layer by using e-beam evaporation method. After the metal lift-off process, the fabrication of the diamond *p*-type depletion mode MOSFET device is completed. Optical images of the MOSFET device (sample N1) are presented in Figure 8.12. Two-probe measurements were performed across the source and drain terminals for both samples N1 and N2 using a Parameter Analyser HP 4155A.
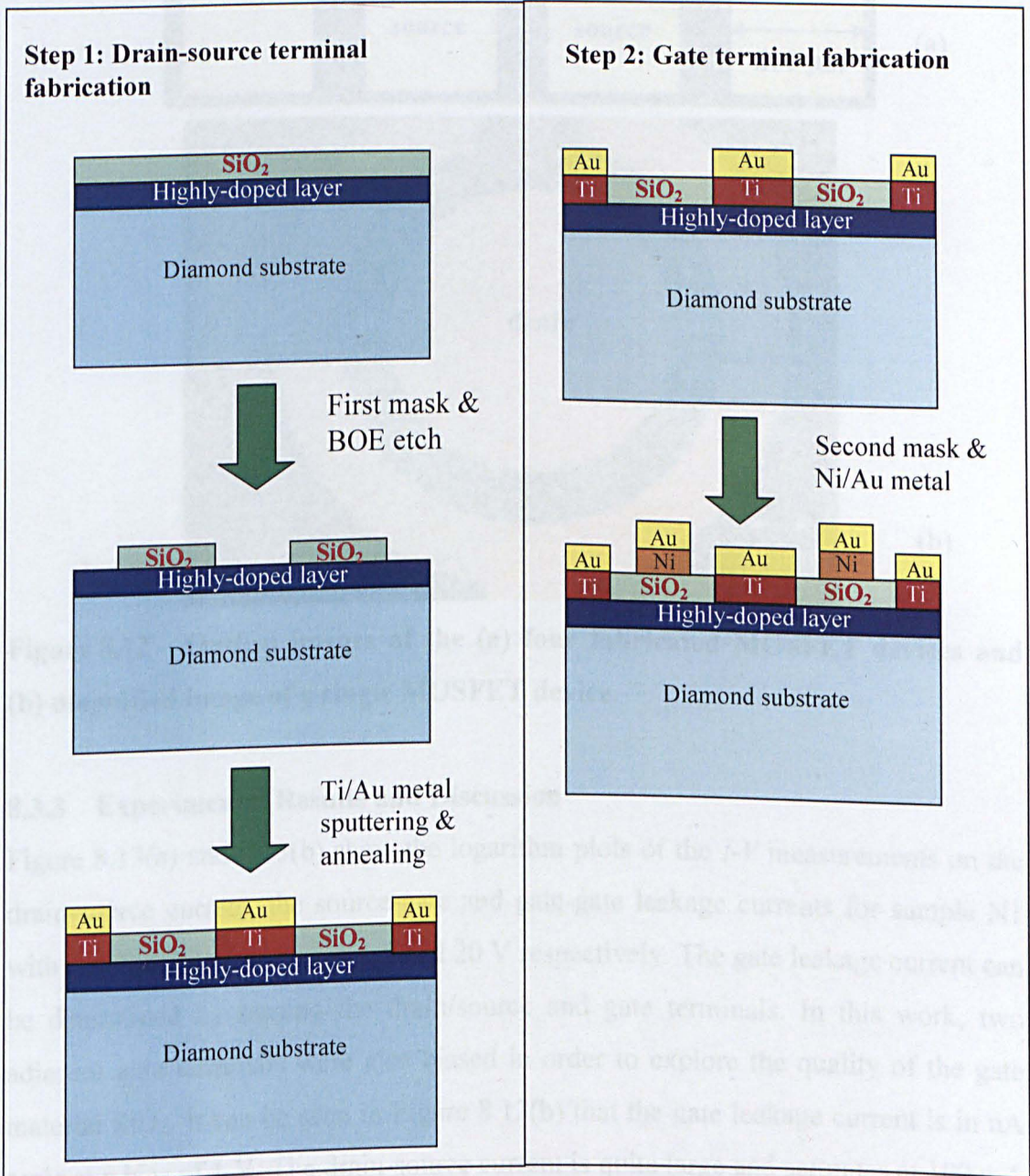
Figure 8.11 Fabrication steps for the MOSFET device. This involves a two-step photolithography process, drain-source terminal and gate terminal.
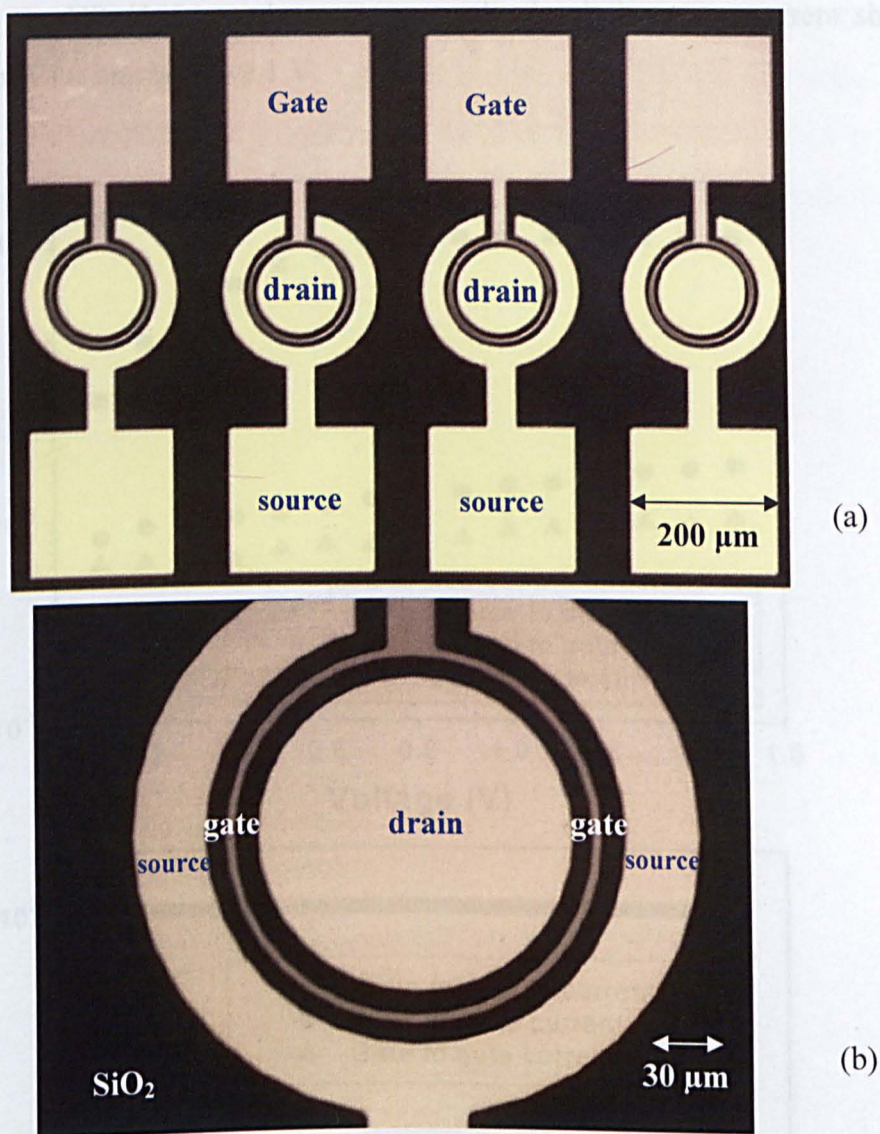
Figure 8.12 **Optical images of the (a) four fabricated MOSFET devices and (b) magnified image of a single MOSFET device.**

8.3.3 Experimental Results and Discussion

Figure 8.13(a) and 8.13(b) show the logarithm plots of the *I-V* measurements on the drain-source current, the source-gate and gate-gate leakage currents for sample N1 with two maximum biases of 1.5 and 20 V respectively. The gate leakage current can be determined by biasing the drain/source and gate terminals. In this work, two adjacent gate terminals were also biased in order to explore the quality of the gate material SiO_2. It can be seen in Figure 8.13(b) that the gate leakage current is in nA scale at a bias of 1 V. The drain-source current is quite large and saturates at 100 mA for a bias of less than 1 V. The current saturation is due to the current limitation set at

100 mA for the HP 4155A analyser. As a result, the drain-source current should exceed 100 mA for biases above 1 V.
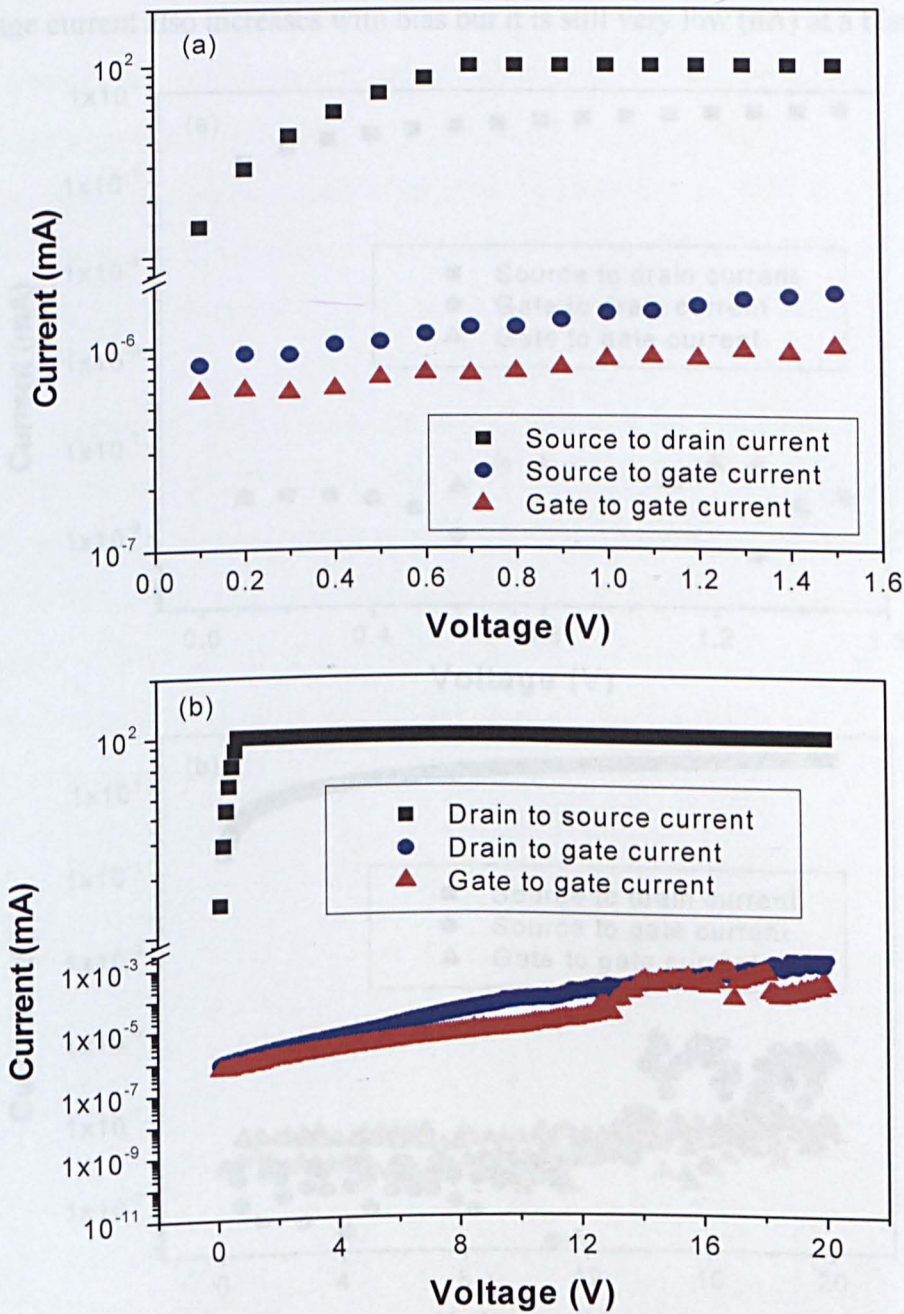
Figure 8.13 *I-V* **measurement on drain-source terminals (without gate bias) and gate leakage current for sample N1 (2 x 10^{21} cm^{-3}) with a maximum bias of (a) 1.5 V and (b) 20 V.**

Figure 8.14(a) and 8.14(b) show the *I-V* measurements for sample N2 with a thinner delta layer (4 nm) and a doping concentration of 5 x 10^{20} cm^{-3}. For a source-drain

bias up to 1.5 V, the source-drain current is about 1 mA. On the other hand, the gate leakage current at the same bias is extremely low, which is in pA scale. The source-drain current increases to above 70 mA when biased at 20 V. The gate leakage current also increases with bias but it is still very low (nA) at a bias of 20 V.
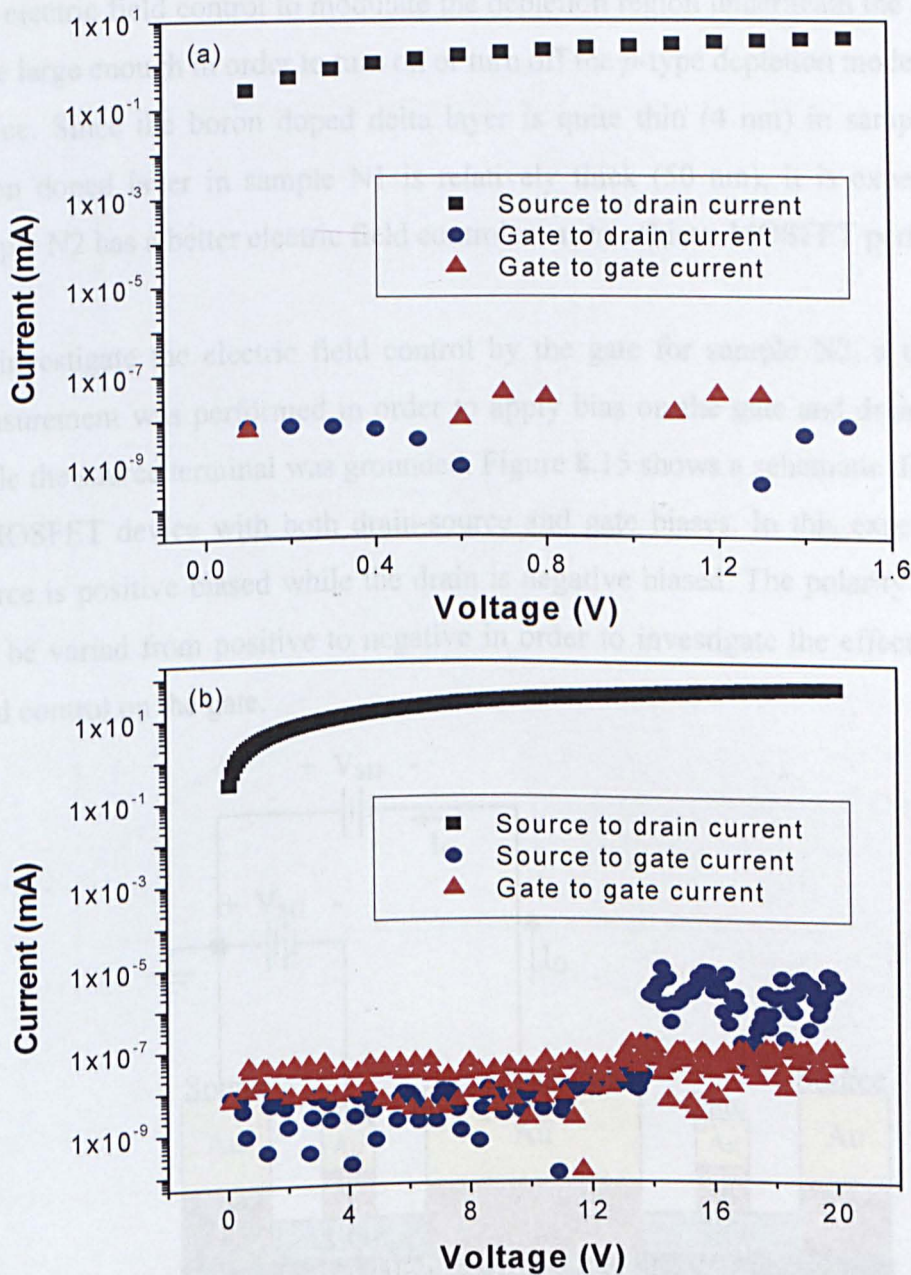
Figure 8.14 *I-V* measurement on drain-source terminals (without gate bias) and gate leakage current for sample N2 (5×10^{20} cm^{-3}) with a maximum bias of (a) 1.5 V and (b) 20 V.

It can be summarised that the MOSFET devices (N1 and N2) have a slightly larger drain-source current and much lower gate leakage currents compared to the MISFET

devices (M1, M2 and M3) as discussed in **Section 8.2**. As discussed before, the large gate leakage current for the MISFET devices is probably due to the low quality of the diamond intrinsic capping layer.

The electric field control to modulate the depletion region underneath the gate needs to be large enough in order to turn on or turn off the *p*-type depletion mode MOSFET device. Since the boron doped delta layer is quite thin (4 nm) in sample N2 and boron doped layer in sample N1 is relatively thick (50 nm), it is expect that the sample N2 has a better electric field control so as to achieve MOSFET performances.

To investigate the electric field control by the gate for sample N2, a three probe measurement was performed in order to apply bias on the gate and drain terminals while the source terminal was grounded. Figure 8.15 shows a schematic diagram of a *p*-MOSFET device with both drain-source and gate biases. In this experiment, the source is positive biased while the drain is negative biased. The polarity of the gate can be varied from positive to negative in order to investigate the effect of electric field control on the gate.
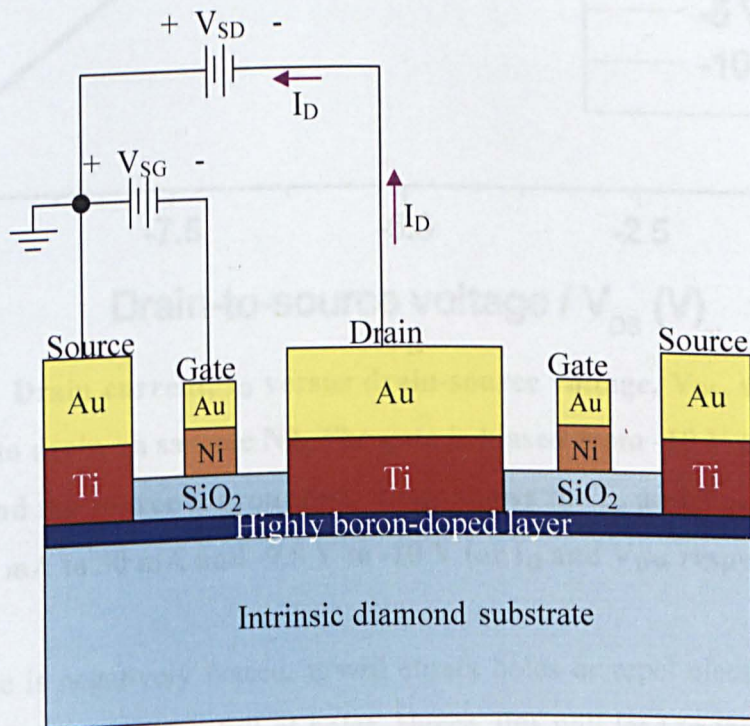
Figure 8.15 Schematic diagram of an electric circuit of a *p*-MOSFET device with drain-source and gate biases.

Figure 8.16 shows the changes of the drain current while both of the gate and drain biases are applied. It can be seen that there is only a minor change in the source-drain current with the application of the gate bias. The source-drain current increases about 0.2 % for every gate bias change of 5 V. This phenomenon can be explained as follows:
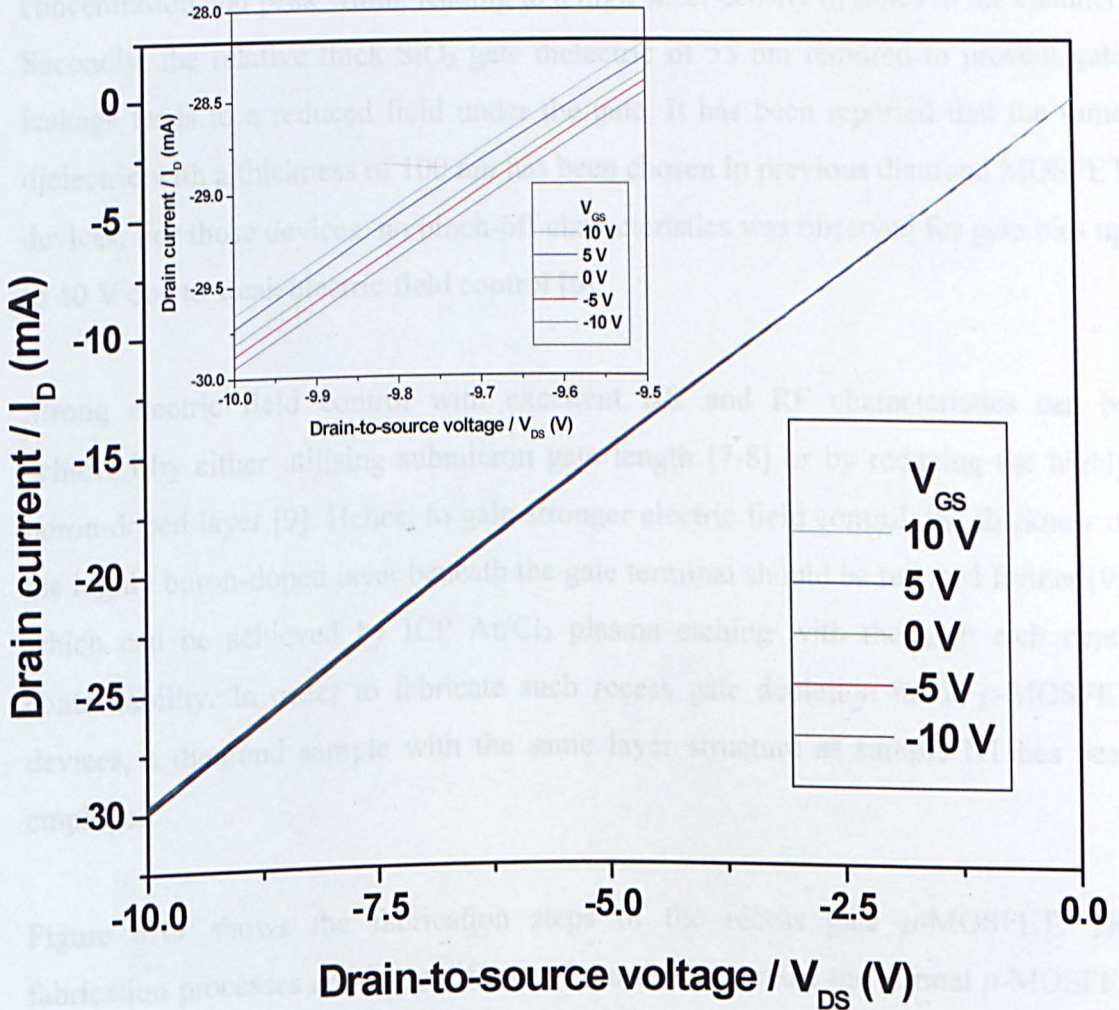
Figure 8.16 **Drain current, I_D versus drain-source voltage, V_{DS}, with negative bias applied to drain on sample N2. The gate is biased from -10 V to 10 V in the step of 5 V and the source is grounded. Inset shows the I_D and V_{DS} on a smaller scale (i.e. -28 mA to 30 mA and -9.5 V to -10 V for I_D and V_{DS}, respectively).**

When the gate is negatively biased, it will attract holes or repel electrons and as a result, the p-doped channel is full of holes. Hence, this will lead to the increment of the source-drain current. On the other hand, positive gate bias will result in the hole

repulsion or electron attraction and thus there are fewer holes in the p-doped channel. Consequently, there is a reduction in source-drain current.

However, no current saturation and pinch-off was observed which can be attributed to two factors. Firstly, the boron-doped delta layers have relatively high peak boron concentration and peak width, leading to a high sheet density of holes in the channel. Secondly, the relative thick SiO_2 gate dielectric of 55 nm required to prevent gate leakage leads to a reduced field under the gate. It has been reported that the same dielectric with a thickness of 100 nm has been chosen in previous diamond MOSFET devices. For those devices, no pinch-off characteristics was observed for gate bias up to 40 V due to weak electric field control [6].

Strong electric field control with excellent DC and RF characteristics can be achieved by either utilising submicron gate length [7-8] or by reducing the highly boron-doped layer [9]. Hence, to gain stronger electric field control, the thickness of the highly boron-doped layer beneath the gate terminal should be reduced further [9], which can be achieved by ICP Ar/Cl_2 plasma etching with the high etch depth controllability. In order to fabricate such recess gate depletion mode p-MOSFET devices, a diamond sample with the same layer structure as sample N1 has been employed.

Figure 8.17 shows the fabrication steps of the recess gate p-MOSFET. The fabrication processes are fairly different from those to make the normal p-MOSFET devices as described in Figure 8.11. The first step of the fabrication involves the deposition and patterning of Ti (50 nm) and Au (100 nm) source and drain contacts by using photolithographic patterning, sputtering and lift-off techniques. The sample was then annealed at 450 °C for 1 minute in order to form ohmic contacts. By employing the Ti/Au contact as an etch mask, Ar/Cl_2 plasma etching was used to remove 48 nm thick highly doped diamond resulting in a reduction of the layer thickness of highly doped diamond from 50 nm to about 2 nm. By this way, it is expected that the field control in the delta layer will be enhanced. Then a SiO_2 layer of 55 nm was deposited on to the diamond sample to serve as gate insulator. By

utilising the same mask again, the SiO_2 on top of the Ti/Au metal contacts was removed. Finally, the Ni (10 nm) and Au (10 nm) layers was deposited using e-beam evaporation and patterned to form gate contacts.
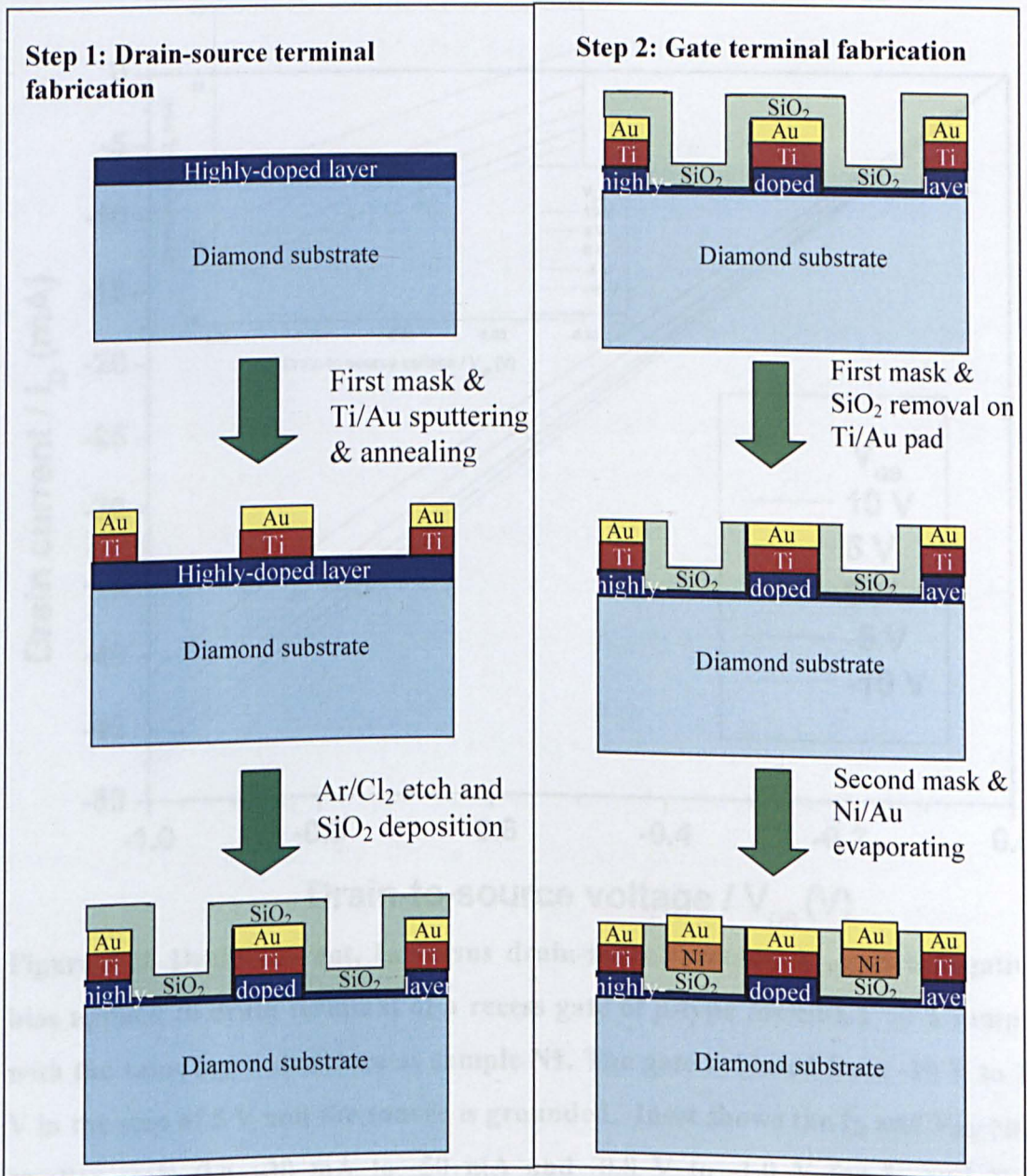

Step 1: Drain-source terminal fabrication

Step 2: Gate terminal fabrication

Figure 8.17 Fabrication steps of a recess gate depletion mode *p*-MOSFET device.

After the completion of the device fabrication, a three-probe measurement was performed. The gate and drain terminals were biased while the source terminal was grounded. Figure 8.18 shows the changes of the source-drain current while both of the gate and drain biases are applied. It can be observed that the modulation in the

source-drain current with the application of the gate bias are relatively large compared to the changes of the p-MOSFET without the recess gate. In this case, the source-drain current increases about 5 % for every gate bias change of 5 V.
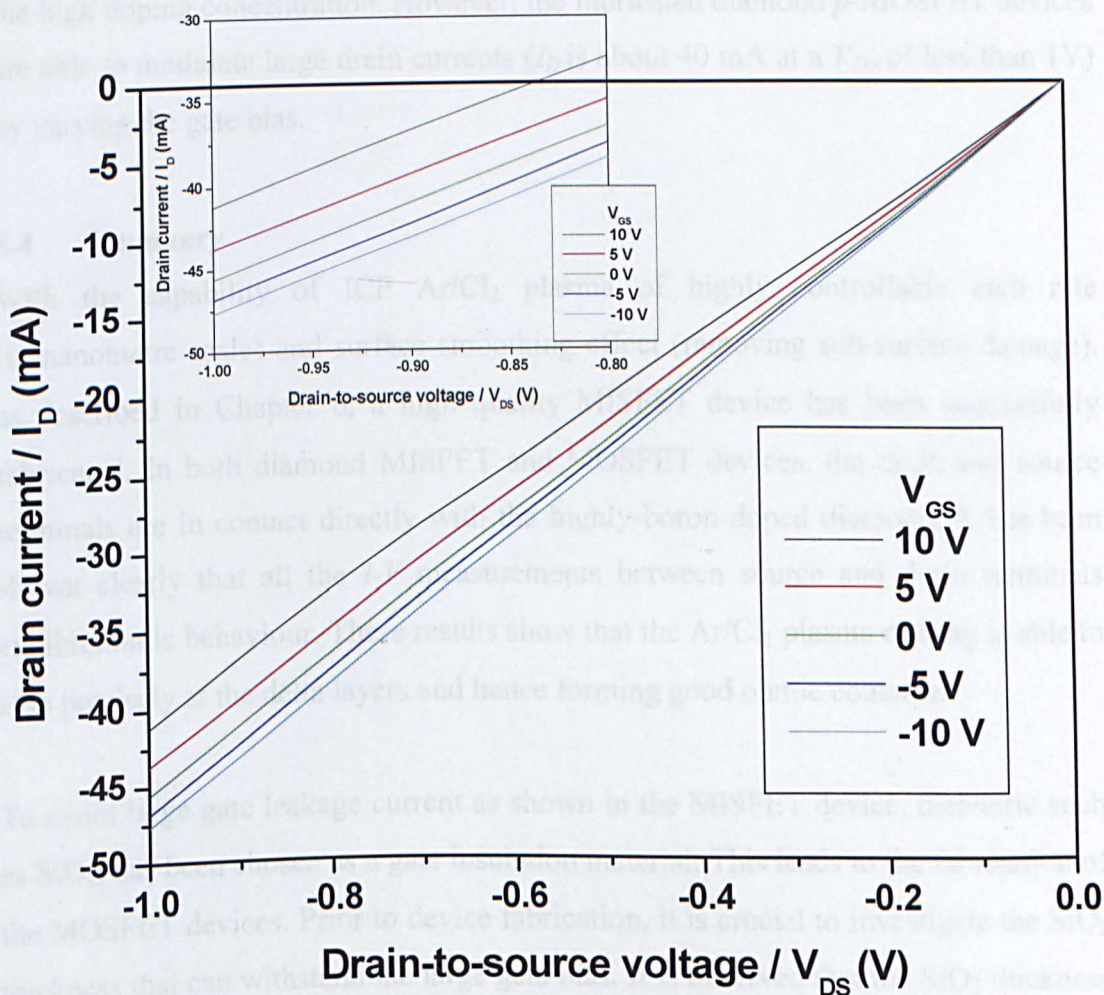
Figure 8.18 Drain current, I_D versus drain-source voltage, V_{DS}, with negative bias applied to drain terminal of a recess gate of p-type MOSFET on a sample with the same layer structure as sample N1. The gate is biased from -10 V to 10 V in the step of 5 V and the source is grounded. Inset shows the I_D and V_{DS} on a smaller scale (i.e. -30 mA to -50 mA and -0.8 V to -1.0 V for I_D and V_{DS}, respectively).

This result shows that the field control of the gate in this recess gate device is much stronger compared to the p-MOSFET without the recess gate. The improvement of the gate electric field control can be attributed to the fact that the thickness of the highly-doped layer beneath the gate terminal has been reduced to 2 nm and hence the

electric field control is stronger. Nonetheless, current saturation or pinch-off of the source-drain current has not been observed although a high gate bias (10V) has been applied. This is probably due to the large thickness of the boron-doped delta layer or the high doping concentration. However, the fabricated diamond p-MOSFET devices are able to modulate large drain currents (I_D is about 40 mA at a V_{DS} of less than 1V) by varying the gate bias.

8.4   Summary

With the capability of ICP Ar/Cl$_2$ plasma of highly controllable etch rate (in nanometre scale) and surface smoothing effect (removing sub-surface damage), as described in Chapter 6, a high quality MISFET device has been successfully fabricated. In both diamond MISFET and MOSFET devices, the drain and source terminals are in contact directly with the highly-boron doped diamond. It has been shown clearly that all the I-V measurements between source and drain terminals exhibit ohmic behaviour. These results show that the Ar/Cl$_2$ plasma etching is able to stop precisely at the delta layers and hence forming good ohmic contacts.

To avoid large gate leakage current as shown in the MISFET device, dielectric such as SiO$_2$, has been chosen as a gate insulation material. This leads to the fabrication of the MOSFET devices. Prior to device fabrication, it is crucial to investigate the SiO$_2$ thickness that can withstand the large gate bias. It is observed that the SiO$_2$ thickness of 55 nm is able to withstand large bias up to 20 V. For this reason, the thickness of 55 nm is chosen to be the SiO$_2$ gate thickness. The fabrication steps for MOSFET devices are very similar to MISFET devices except that the cap layer used in the first case is SiO$_2$. The SiO$_2$ can be etched away by using BOE solution. The electrical measurements show that the MOSFET devices can sustain large gate bias (up to ±20 V due to the limitation of Parameter Analyser) with a large drain current (100 mA) and a very low leakage current. It was found that the fabricated MOSFET devices can not be fully pinched-off. One of the possible reasons for no-pinch off is the relative thick SiO$_2$ gate dielectric of 55 nm required to prevent gate leakage. The other possible reason may be attributed to the high boron doping concentration (2 x 10^{21} cm^{-3}) in the delta layer in association with the relatively thick boron doped

layer of 55 nm. Hence, the thinner delta layer with lower doping concentration should be used in order to obtain stronger electric field control. By fabricating a recess gate of p-MOSFET, which reduces the thickness of the highly doped layer (from 50 nm to 2 nm for a sample with the doping concentration of 2 x 10^{21} cm^{-3}), the gate field control is much enhanced although it is still not strong enough to fully pinch-off the source-drain current.

8.5 References

[1] J. Isberg, J. Hammersberg, E. Johansson, T. Wilkstrom, D.J. Twitchen, A.J. Whitehead, S.E. Coe, G.A. Scarsbrook, *Science*, **297**, 1670 (2002).

[2] D. Neamen, *An Introduction to the Semiconductor Devices*, Mcgraw-Hill (2006).

[3] R.L. Boylestad, L. Nashelsky, *Electronic Devices and Circuit Theory*, Prentice Hall (2006).

[4] T. Tachibana, B.E. Williams, J.T. Glass, *Phys. Rev. B*, **45**, 11968 (1992).

[5] T. Tachibana, B.E. Williams, J.T. Glass, *Phys. Rev. B*, **45**, 11975 (1992).

[6] S.A. Grot, C.W. Hatfield, G.S. Gildenblat, A.R. Badzian, T. Badzian, *Second International Conference of New Diamond Science and Technology*, Washington, DC, 949 (1990).

[7] K. Ueda, M. Kasu, Y. Yamauchi, T. Makimoto, M. Schwitters, D.J. Twitchen, G.A. Scarsbrook, S.E. Coe, *IEEE Elect. Dev. Lett.*, **27**, 570 (2006).

[8] A. Aleksov, A. Denisenko, U. Spitzberg, T. Jenkins, W. Ebert, E.Kohn, *Dia. Rel. Mat.*, **11**, 382 (2002).

[9] S.A. Grot, G.S. Gildenblat, A.R. Badzian, *IEEE Elect. Dev. Lett.*, **13**, 462 (1992).

Chapter 9

Conclusions

9.1 Conclusions of Current Work

In this project, ICP etching of diamond using oxygen-based (Ar/O$_2$) and chlorine-based (Ar/Cl$_2$) plasmas were investigated. I have also studied the effects of ICP platen and coil powers and gas pressures on the diamond etching.

It was demonstrated that Ar/Cl$_2$ plasma etching has the capability to smooth the surface of the HPHT diamonds and the reduction of surface RMS roughness from 0.53 nm to 0.19 nm was achieved. The etch selectivity and diamond etch rate by using Ar/Cl$_2$ plasma is found to be only half of those by using the Ar/O$_2$ plasma, which enables a good control on the etch depth for fabricating diamond microstructures. By varying the ICP coil power, the etch rate of diamond can be further reduced to about 0.7 nm/s. With such a low etch rate, very shallow diamond micro-trenches with a depth of 8 nm have been fabricated. Excellent etch reproducibility and controllability by using Ar/Cl$_2$ plasma were demonstrated. These results also confirmed that the etch rates for different types of diamond including intrinsic, boron-doped and HPHT diamonds are almost the same.

Based on these studies, I have designed and fabricated various diamond micro-optics including diamond micro-spherical positive and negative lenses, special micro-cylindrical and micro-ring lenses, complex micro-lenses and optical gratings. The structural and optical properties of the diamond micro-optics are fully characterised. The characterisations revealed the high optical quality and functionality of the fabricated diamond micro-optics. Working with my colleagues in the Institute of Photonics, I have also explored the applications of the diamond micro-optics, such as to develop micro-lensed micro-VECSEL photonic devices.

By using ICP Ar/Cl$_2$ plasma etching and other processes, I have developed diamond electronic devices such as diamond MISFETs and MOSFETs. To realise such MISFET or MOSFET devices, ohmic contacts with low specific contact resistances

are required. By using aqua regia surface treatment, the specific contact resistance on the highly boron-doped (i.e. 5×10^{19} cm^{-3}) diamond layers was effectively reduced. A lowest specific contact resistance of 9.99×10^{-5} $\Omega.cm^2$ has been achieved by applying both surface treatment and laser ablation techniques followed by contact RTA annealing. With the high controllability (in nanometre scale) and surface smoothing effect (removing sub-surface damage) of ICP Ar/Cl_2 plasma etching, complete diamond MISFET devices have been successfully fabricated. In these devices, the channel length is designed to be 6 μm and the gate sits on top of an intrinsic diamond layer. The drain and source terminals are in contact directly on the highly-boron doped diamond delta layer. All the *I-V* measurements show the drain and source contacts are ohmic, which demonstrates that the Ar/Cl_2 plasma etching is able to stop precisely at the delta layer. However, the diamond structures used for the MISFET device fabrication are the early development samples, and in these it was found that the gate leakage was quite large (in the μA scale). To overcome this problem, I developed the diamond MOSFET devices.

To avoid large gate leakage current, dielectric SiO_2 has been chosen as a gate insulation material. For these MOSFET devices, it is crucial to identify the minimum SiO_2 thickness that can withstand the required gate bias. Our measurements show that a SiO_2 layer with a thickness of 55 nm is able to withstand a bias up to 20 V and such a 55 nm thick SiO_2 layer is chosen for device fabrication. The fabrication steps for diamond MOSFET devices are similar to those of the diamond MISFET devices except that the gate insulation material used in the MOSFET devices is SiO_2. The electrical measurements show that the diamond MOSFET devices can sustain large gate bias (up to ±20 V due to the limitation of Parameter Analyser) with a large drain current (100 mA) and a very low leakage current. It was found that the fabricated MOSFET devices can not be fully pinched-off. One possible reason for no-pinch off is that the boron doping concentration (2×10^{21} cm^{-3}) in the delta layer may be too high. The relatively thick delta layer in the devices may be another possible reason. Hence, thinner delta layer with lower doping concentration should be used in order to achieve stronger electric field control. By fabricating a recess gate *p*-MOSFET, in which the thickness of the highly doped layer (doping concentration of 2×10^{21} cm^{-3})

is reduced from 50 nm to 2 nm, the gate field control is much enhanced although it is still not strong enough to fully pinch-off the source-drain current.

9.2   Future Work

By further optimising the fabrication processes, the quality, functionality and performance of the diamond micro-optics can be improved. It is also possible to develop diamond micro-optics with special parameters such as ultra-shallow and ultra-small micro-lenses for various applications. Furthermore, based on the fabrication processes achieved in this project, novel diamond based optical devices can be fabricated, including diamond waveguides, micro-resonators, photonic crystals and micro-cavities. Such new diamond micro-optics will play crucial role in developing high performance micro-optical systems.

On diamond electronics, current studies showed that surface chemical treatment and laser ablation are critical steps in achieving ohmic contact formation on p-doped diamond. It is expected that the optimisation of the parameters of laser ablation will further reduce the specific contact resistance. And also, surface plasma treatment using other gases, e.g., hydrogen plasma (which is believed to be able to enhance the surface conduction due to the formation of hydrogen terminated surface) are worthy of pursuance. Clearly, for the practical applications of diamond MISFET or MOSFET devices, it is essential to reduce the gate leakage current and also to realise complete channel pinch-off. To achieve these targets, the quality of the intrinsic diamond should be further improved to reduce the gate leakage. Also, the thickness of the highly-doped delta layer should be further minimised so as to achieve the current saturation and pinch-off in the p-channel region of the diamond MOSFET devices.

Appendix A - List of Publications

1) <u>C.L. Lee</u>, H.W. Choi, E. Gu, H. Murphy, M.D. Dawson, *Dia. Rel. Mat.*, **15**, 725 (2006).

2) <u>C.L. Lee</u>, E. Gu, M.D. Dawson, *Dia. Rel. Mat.*, **16**, 944 (2007).

3) <u>C.L. Lee</u>, E. Gu, M.D. Dawson, I. Friel, G.A. Scarsbrook, *Dia. Rel. Mat.*, **17**, 1292 (2008).

4) Nicolas Laurand, <u>C.L. Lee</u>, E. Gu, J.E. Hastie, A.J. Kemp, Stephane Calvez and Martin D. Dawson, *J. Quant. Electron.* (Accepted for publication).

5) N. Laurand, <u>C.L. Lee</u>, E. Gu, J.E. Hastie, S. Calvez, M.D. Dawson, *Opt. Exp.*, **15**, 9341 (2007).

6) S. Giet, <u>C.-L. Lee</u>, S. Calvez, M. D. Dawson, N. Destouches, J.-C. Pommier, and O. Parriaux, *Opt. Exp.*, **15**, 16520 (2007).

7) A.R. Mackintosh, A.J.C. Kuehne, R.A. Pethrick, B. Guilhabert, E. Gu, <u>C.L. Lee</u>, M.D. Dawson, G. Heliotis and D.D.C. Bradley, *J. Phys. D.: Appl. Phys.*, **41**, 094007 (2008).

Appendix B - List of Conferences

1) <u>C.L. Lee</u>, E.Gu, M.D. Dawson, 16th European Conference on Diamond, Diamond-like Materials, Carbon Nanotubes, Nitrides and Silicon Carbide (Diamond 2005), Toulouse, France, September 11th–16th, 2005. (Contributed oral presentation).

2) <u>C.L. Lee</u>, E. Gu, M.D. Dawson, 17th European Conference on Diamond, Diamond-like Materials, Carbon Nanotubes, Nitrides and Silicon Carbide (Diamond 2006), Lisbon, Portugal, September 3rd–8th, 2006. (Contributed oral presentation).

3) <u>C.L. Lee</u>, E. Gu, I. Friel, G. Scarsbrook, 18th European Conference on Diamond, Diamond-like Materials, Carbon Nanotubes, Nitrides and Silicon Carbide (Diamond 2007), Berlin, Germany, September 8th–13th, 2007. (Contributed oral presentation).

Appendix C - Patent Filed

1) Co-inventor on a PCT (Patent Cooperation Treaty) patent (No: PCT/IB2008/050215) entitled "Plasma Etching of Diamond Surfaces", which licensed to Element Six (UK) Ltd.

Appendix D – Calculation of Heights of the Partial Spherical Micro-structures using Turbo C Programme

a) Turbo C Programme

```c
#include <stdio.h>
#include <stdlib.h>

main ()
{
  float h1, h2, h3, h4, r, answer;
  char want_to_continue, newline_char;


  do
  {
  clrscr();
  printf("\n");
  printf("\nPlease enter the height of the cylindrical structure: ");
  scanf("%f", &h1);
  while (h1 <= 0.0)
    {
    printf("\nPlease re-enter the height of the cylindrical structure: ");
    scanf("%f", &h1);
    }

  printf("\nPlease enter the radius of the cylindrical structure: ");
  scanf("%f", &r);
  while (r <= 0.0)
    {
    printf("\Please re-enter the radius of the cylindrical structure: ");
    scanf("%f", &r);
    }
```
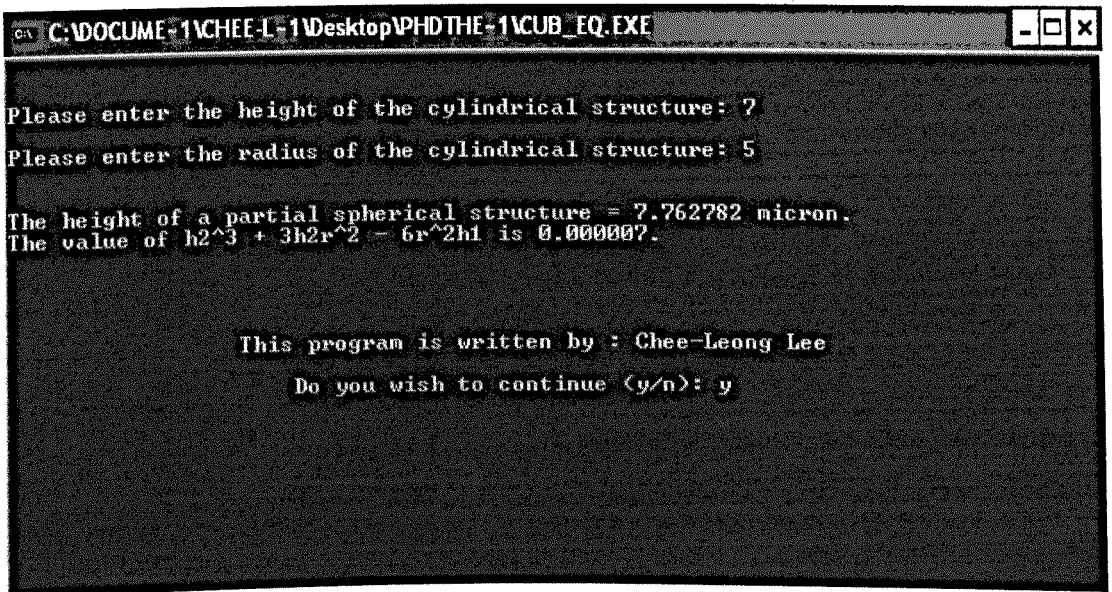
```
h3 = h1 * 2.0;

if (r >= 50)
  h4 = 0.05;
else
if (r >= 25 && r < 50)
  h4 = 0.005;
else
if (r >= 10 && r < 25)
  h4 = 0.001;
else
if (r >= 5 && r < 10)
  h4 = 0.0002;
else
  h4 = 0.00009;

for (h2 = 1.0; h2 <= h3; h2=h2+0.000001)
{
  answer = h2*h2*h2 + 3*h2*r*r - 6*r*r*h1;
  if (answer <= h4 && answer >= -h4)
  { printf("\n");
    printf("\nThe height of a partial spherical structure = %f
micron.",h2);
    printf("\nThe value of h2^3 + 3h2r^2 - 6r^2h1 is %f.",answer);
  }
}
  printf("\n\n\n\n\n%61s","This program is written by : Chee-Leong Lee
");
  printf("\n\n%52s", "Do you wish to continue (y/n): ");
  scanf("%c", &newline_char);
  scanf("%c", &want_to_continue);
```

```
}

while (want_to_continue == 'y' || want_to_continue == 'Y');


return 0;

}
```

b) Example of an Output Screen


```
C:\DOCUME~1\CHEE-L~1\Desktop\PHDTHE~1\CUB_EQ.EXE

Please enter the height of the cylindrical structure: 7
Please enter the radius of the cylindrical structure: 5

The height of a partial spherical structure = 7.762782 micron.
The value of h2^3 + 3h2r^2 - 6r^2h1 is 0.000007.


               This program is written by : Chee-Leong Lee
                  Do you wish to continue (y/n): y
```

Fabrication and characterization of diamond micro-optics

C.L. Lee [a], H.W. Choi [a,1], E. Gu [a,*], M.D. Dawson [a], H. Murphy [b]

[a] Institute of Photonics, University of Strathclyde, 106 Rottenrow, Glasgow, G4 0NW, UK
[b] Element Six Ltd., King's Ride Park, Ascot, Berkshire SL5 8BP, UK

Available online 25 October 2005

Abstract

Owing to its hardness and chemical inertness, most of the previous studies to fabricate structures and devices on diamond have used the conventional Reactive Ion Etching (RIE). Recently, etching of diamond using Inductively Coupled Plasma (ICP) system was reported to have a higher etch rate than using RIE. In this work, ICP etching with Ar/O_2 plasma has been employed to fabricate micro-optics on both natural diamond and high-pressure, high-temperature (HPHT) synthetic diamond. The diamond etch rate has been studied as a function of ICP platen power, coil power and gas pressure. The etch rate is shown to increase with increasing ICP platen and coil powers. Arrays of negative (concave) and positive (convex) diamond microlenses with diameters ranging from 10 to 100 μm were fabricated using hot-embossing and photoresist re-flow methods, respectively, followed by ICP etching. Surface morphology of these diamond micro-lenses was characterized by using both Scanning Electron Microscopy (SEM) and Atomic Force Microscopy (AFM). These measurements show that the natural diamond micro-lenses have root-mean-squared surface roughness of 1.2 nm. The optical properties of the convex diamond microlens arrays, such as focal length and spot size, were characterised by a laser scanning reflection/transmission confocal microscopy technique. The measured optical parameters are close to the calculated values, confirming that the fabricated diamond lenses have a high-quality surface profile.
© 2005 Elsevier B.V. All rights reserved.

Keywords: Natural and synthetic diamonds; Etching; Surface characterization; Optical properties

1. Introduction

Diamond has excellent optical, electrical and thermal properties. It is unmatched in being transparent from the deep ultraviolet to beyond a wavelength of 100 μm making it a particularly attractive material for micro-optics applications. In addition, diamond has high thermal conductivity, 20 W cm^{-1} K^{-1} at room temperature [1,2], making it the best thermal conductor of any material. Thus heat dissipation is much of less concern for diamond-based devices. Diamond can also be coupled into vertical cavity surface-emitting lasers (VCSELs) or other optoelectronic devices for heat dissipation.

One of the most difficult aspects of diamond processing for purposes such as the above is the etching of diamond for isolation or alteration of the surface. Due to its hardness and chemical inertness, most of the previous studies to fabricate structures and devices on diamond have used the dry etching

techniques. To date, the most successful approaches to etching diamond are based on either Reactive Ion Etching (RIE) [3], Inductively Coupled Plasma (ICP) [4–7], or Electron-Cyclotron Resonance etching (ECR) [8].

In this work, we report on the fabrication and characterizations of micro-optics on both natural diamond and high pressure, high temperature (HPHT) synthetic diamonds by using ICP etching. The etch rates have been studied and optimized as a function of the ICP coil power, platen power and gas pressure. Based on this study, two different types of micro-lens arrays, namely, positive and negative micro-lens arrays have been fabricated. Negative micro-lenses can produce divergent beams from a collimated source and hence the combination of both positive and negative micro-lenses will enable complete micro-optical systems to be fabricated [6,9].

2. Experimental

2.1. Etching rate study

An STS Multiplex ICP etcher was used to etch diamond samples using Ar and O_2 gas mixture. In order to optimize the

* Corresponding author. Tel.: +44 141 5485736; fax: +44 141 5521575.
  E-mail address: erdan.gu@strath.ac.uk (E. Gu).
[1] Current address: Department of Electrical and Electronic Engineering, University of Hong Kong, Pokfulam Road, Hong Kong.
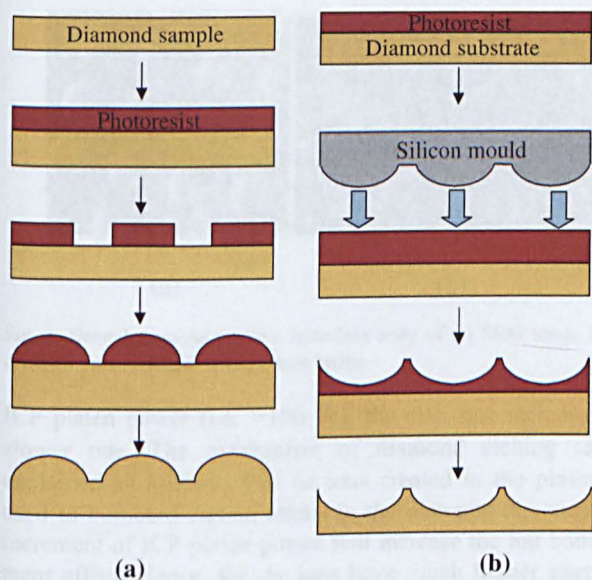
Fig. 1. (a) Process sequence of positive micro-lens fabrication. (b) Process sequence of negative micro-lens fabrication.

etch rates, the ICP platen power was changed progressively from 0 to 300 W and the ICP coil power was varied from 100 to 800 W. The total pressure was changed from 5 to 30 mTorr. The sample holder was helium-cooled. The diamond temperature was maintained to 30 °C throughout the experiments. The flow rates of Ar and O_2 gases were fixed to 15 and 40 sccm, respectively.

2.2. Fabrication of positive micro-lenses

For spherical positive micro-lens array fabrication, photoresist–reflow and ICP etching techniques were adopted, as shown in Fig. 1(a). Shipley SPR220 photoresist was first spin-coated onto the substrates. Cylindrical pillars of photoresist, with diameters ranging from 10 to 100 μm were then fabricated using standard photolithography methods. After the formation of the photoresist pillars, the sample was then placed onto a hotplate at 125 °C for 5 min. The cylindrical pillars melted and formed good spherical structures due to the surface tension. The substrate was then etched using Ar/O_2 plasma at 5 mTorr to transfer the resist pattern onto the diamond substrate.

2.3. Fabrication of negative micro-lenses

In order to fabricate negative micro-lenses, a silicon substrate with spherical micro-lenses of approximately 10 μm height was fabricated by the resist–reflow method to be employed as a mould. A hot-embossing technique was then used to transfer the pattern from the silicon mould onto the HPHT synthetic diamond substrate, as shown in Fig. 1(b). The diamond substrate coated with SPR 220 photoresist was first baked on a 130 °C hotplate for 5 min. The silicon micro-lens mould was then pressed against the photoresist layer on the diamond substrates and the assembly was placed on a hotplate, set to 115 °C, to soften photoresist. Afterwards, the diamond substrate and silicon mould were separated by using tweezers.

Diamond negative micro-lenses were formed by ICP etching using Ar/O_2 plasma. The flow rates of Ar and O_2 were set to 15 and 40 sccm, respectively. The ICP platen and coil powers were set to 50 and 400 W, respectively.

Finally, a Scanning Electron Microscope (SEM) and an Atomic Force Microscope (AFM) were used to study the diamond surface morphology, the etching depth, and the surface roughness for both positive and negative lenses. The optical properties of the micro-lenses, such as focal length, were measured by a laser scanning confocal microscope [5].

3. Results and discussion

3.1. Etching rate investigations

It is observed from Fig. 2(a) that the diamond etch rate initially increases rapidly at low ICP platen power. Similar results have been reported that the increasing the ICP platen power will increase the etch rate significantly [4]. At higher

(a)

(b)
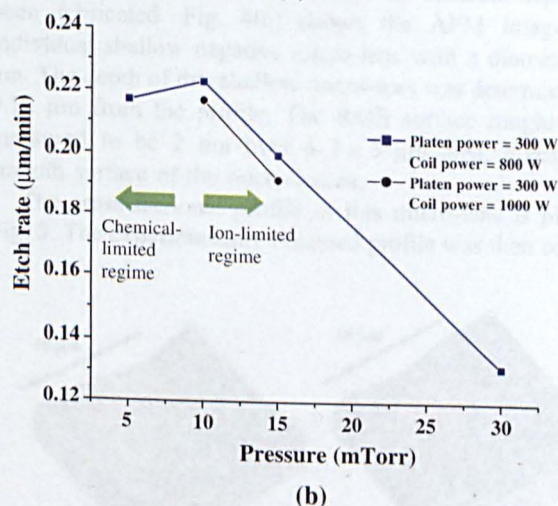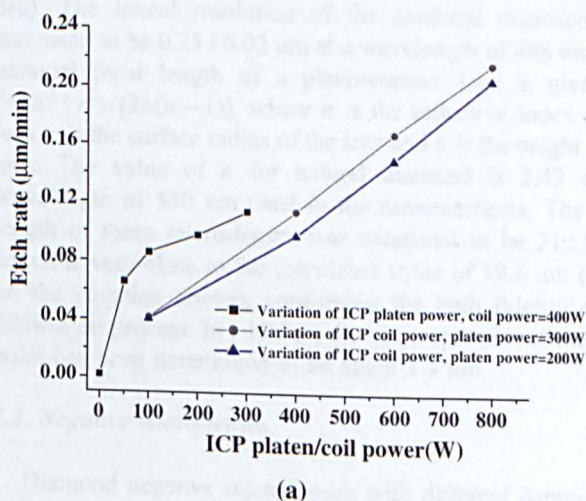
Fig. 2. (a) Etch rate of HPHT synthetic single-crystal diamond versus ICP platen powers (with constant ICP coil power of 400 W) and ICP coil powers (with constant ICP platen power of 200 and 300 W). The gas pressure was set as 5 mTorr. (b) Etch rate versus gas pressure (with constant ICP platen power of 300 W and constant ICP coil powers of 800 and 1000 W).

20 μm

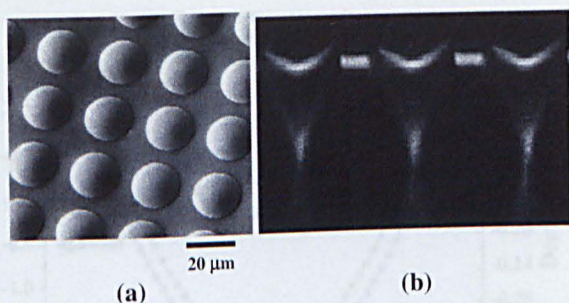(a)   (b)

Fig. 3. Natural diamond positive microlens array of (a) SEM image and (b) confocal reflection/transmission scan image.

ICP platen power (i.e. >100 W), the etch rate increases at a slower rate. The mechanism of diamond etching can be explained as follows. The Ar ions created in the plasma are used to bombard carbon atoms in the diamond structure. The increment of ICP platen power will increase the ion bombardment effect. Hence, the Ar ions have much higher energy to remove carbon atoms. Consequently, the etch rate increases. The carbon atoms removed will then interacted with oxygen ions to form CO_2 or CO gases. However, upon reaching certain ICP platen power, the increase of etch rate becomes slower owing to the limitation of the Ar ion density. In other words, the number of carbon atoms being bombarded away will be still the same no matter how high the Ar ion energy is if the total number of Ar ions remains un-changed.

To further investigate the etch rate characteristics, the coil power was varied from 100 to 800 W. Two different platen powers (i.e. 200 and 300 W) have been used at different coil powers. It is shown in Fig. 2(a) that the etch rate increases with the increment of coil power. An increase in coil power will lead to an increase in ion density. Hence, when the coil power is increased, more ions are created in the plasma and consequently more carbon atoms are bombarded away. This will lead to an increase in the etch rate.

It is also observed in Fig. 2(a) that under the same coil power, the etching with higher platen power (300 W) has a higher etch rate compared to the etching at lower platen power (200 W). It is known that the ion energy increases with the platen power for ICP etching. Thus higher etch rate is achieved by using higher platen power. In this case, the etch rate is determined by the ion energy rather than the ion density since the same coil power has been used.

Fig. 2(b) shows that an optimum pressure (i.e. 10 mTorr) is needed to achieve the highest etch rate of 0.22 ± 0.01 μm/min. The etch rate increases with the increment of the pressure from 5 to 10 mTorr. In this case, more reactive species, such as O, will be generated. Hence, more volatile products (i.e. CO and CO_2) can be formed and removed from the surface of the diamond. Consequently, there is an increase in the etch rate. Therefore, we are in a *chemical-limited regime* when the pressure is less than 10 mTorr. However, the enhanced ion–ion and ion–electron recombination, which occur at higher gas pressure (i.e. >10 mTorr), can induce less Ar ions [10]. As a result, as the pressure goes higher than 10 mTorr, there is a decrease in Ar ion density. Although there is enough of the reactive species to form etch products, the decrease of Ar ion

density could result in the reduction of etch rate in this pressure range. Therefore, an *ion-limited regime* may be established when the pressure is higher than 10 mTorr.

3.2. Positive micro-lenses

Positive micro-lenses in natural diamond with diameters ranging from 10 to 100 μm have been fabricated. Fig. 3(a) shows an SEM image of a representative micro-lens array with a lens diameter of 18 μm. The profiles of the lenses were compared to the theoretical curvature of a circle using a chi-squared fitting algorithm. By fitting the observed lens surface profile, it was confirmed that the micro-lenses produced are very close to spherical in shape. The AFM measurements show that these diamond micro-lenses have a RMS roughness value of 1.2 nm for a 1×1 μm area, indicating the high surface quality of these micro-lenses.

The focal length and beam spot size of these micro-lenses have been measured using the reflection/transmission laser scanning confocal microscopy technique [5], as shown in Fig. 3(b). The lateral resolution of the confocal microscope is estimated to be 0.25 ± 0.02 μm at a wavelength of 488 nm. The paraxial focal length of a plano-convex lens is given by $f = (h^2 + r^2)/[2h(n-1)]$, where n is the reflective index of the lens, r is the surface radius of the lens and h is the height of the lens. The value of n for natural diamond is 2.42 at the wavelength of 530 nm used in the measurements. The focal length of these micro-lenses was measured to be 21 ± 1 μm, which is very close to the calculated value of 19.6 μm (based on the equation above), confirming the high fidelity of the fabrication process. In addition, the beam spot size at the focal point has been determined to be about 1.4 μm.

3.3. Negative micro-lenses

Diamond negative micro-lenses with different depths have been fabricated. Fig. 4(a) shows the AFM image of an individual shallow negative micro-lens with a diameter of 50 μm. The depth of this shallow micro-lens was determined to be 0.18 μm from the profile. The RMS surface roughness was measured to be 2 nm over a 3×3 μm area, revealing the smooth surface of the micro-lenses.

The cross-sectional profile of this micro-lens is plotted in Fig. 5. The experimentally obtained profile was then compared

50 μm   55 μm
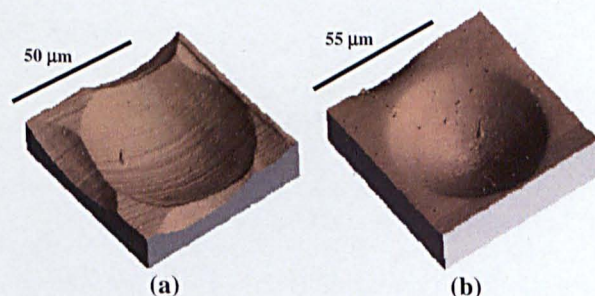
(a)   (b)

Fig. 4. AFM Images of (a) shallow and (b) deep negative micro-lenses in HPHT synthetic diamond.
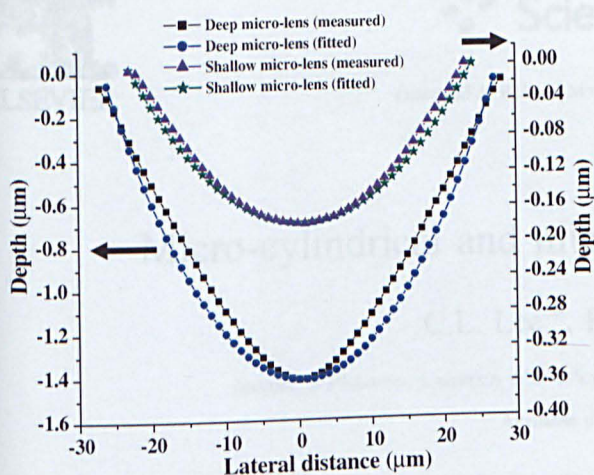
Fig. 5. Measured and fitted surface profiles for both of the deep and shallow negative micro-lenses shown in Fig. 4.

to the theoretical curvature of a circle. It can be seen that the deviation from the theoretical profile is small, indicating the profile of the micro-lenses is very close to a spherical shape.

An AFM three-dimensional scan of a representative deep micro-lens with a diameter of 55 μm is illustrated in Fig. 4(b). Evaluation of the profiles of the micro-lenses was undertaken by comparing the experimental profiles with the theoretical curvature of a circle, as shown in Fig. 4. It reveals again that there is only a small deviation from a perfect spherical surface. However, the RMS roughness of the lens surface is rather high, i.e. 15 nm for a 3×3 μm area. This is due to the intrinsic defects in the HPHT diamond. These intrinsic defects made the etching non-uniform and consequently, the surface to become rough especially after long time ICP etching. It is expected that the surface quality of the micro-lenses will be greatly improved by using high quality diamonds.

4. Conclusion

The ICP etching of natural and synthetic diamonds with Ar/O_2 plasma has been studied. A maximum etch rate of 0.22 ± 0.01 μm/min has been achieved. It is found that ICP platen and coil powers affect the etch rate significantly for the current

configuration of the etching system. Based on this study, positive and negative diamond micro-lens arrays have been successfully fabricated using novel processing techniques. The micro-lenses have diameters ranging from 10 to 100 μm. The positive micro-lenses were fabricated using photoresist re-flow technique. Meanwhile, the negative micro-lenses were fabricated using a hot-embossing technique. The RMS roughness for positive micro-lenses was measured to be 1.2 nm for a 1×1 μm area. The focal length and the beam spot size were determined using laser scanning reflection/transmission confocal microscopy technique. Also, diamond negative micro-lenses with different depths were fabricated and characterized. These negative micro-lenses are very close to spherical in shape. The combination of both positive and negative micro-lenses will enable complete diamond micro-optical systems to be fabricated.

References

[1] M.H. Nazare, A.J. Neves (Eds.), Properties, Growth and Applications of Diamond, INSPEC Inc., 2000.
[2] L.S. Pan, D.R. Kania (Eds.), Diamond: Electronic Properties and Application, Springer, 1994.
[3] G.M.R. Sirineni, H.A. Naseem, Diamond Relat. Mater. 6 (1997) 952.
[4] D.S. Hwang, T. Saito, N. Fujimori, Diamond Relat. Mater. 13 (2004) 2207.
[5] E. Gu, H.W. Choi, C. Liu, C. Griffin, J.M. Girkin, I.M. Watson, M.D. Dawson, Appl. Phys. Lett. 84 (2004) 2754.
[6] H.W. Choi, E. Gu, C. Liu, C. Griffin, J.M. Girkin, I.M. Watson, M.D. Dawson, J. Vac. Sci. Technol., B 23 (2005) 130.
[7] M. Karlsson, K. Hjort, F. Nikolajeff, Opt. Lett. 26 (2001) 1752.
[8] S.J. Pearton, A. Katz, F. Ren, J.R. Lothian, Electron. Lett. 28 (1992) 822.
[9] E. Woerner, C. Wild, W. Mueller-Sebert, P. Koidl, Diamond Relat. Mater. 10 (2001) 557.
[10] L. Jiang, N.O.V. Plank, J. Phys. D: Appl. Phys. 37 (2004) 1809.

Micro-cylindrical and micro-ring lenses in CVD diamond

C.L. Lee *, E. Gu, M.D. Dawson

Institute of Photonics, University of Strathclyde, 106 Rottenrow, Glasgow G4 0NW, United Kingdom

Available online 15 December 2006

Abstract

Micro-cylindrical and micro-ring lenses have been fabricated on chemical vapour deposition (CVD) diamond using photo-resist reflow and inductively-coupled plasma dry etching. The surface morphology of these micro-lenses was characterized using atomic force microscopy, revealing that they have a root-mean-squared surface roughness of less than 3 nm and a cross-sectional profile close to spherical in shape. The optical properties of the micro-lenses were characterized by a laser scanning transmission/reflection confocal microscope. The measured optical parameters are very close to the calculated values, indicating high structural and surface quality of the micro-lenses. The characteristics of these micro-lenses suggest that the approach used is suitable for fabricating complex diamond micro-optics with various functionalities.
© 2006 Elsevier B.V. All rights reserved.

Keywords: Synthetic diamond; Etching; Surface characterization; Optical properties

1. Introduction

Diamond, long known for its unusual combination of physical characteristics, is now emerging as an important material for the development of micro-optical devices. Its optical transmission bandwidth is extremely wide, spanning the deep-ultraviolet to the far infrared spectral region. It possesses a very high thermal conductivity, offering combined heat-spreading and optical functionality when integrated with optical sources such as light-emitting diodes (LED's) and lasers. Furthermore, it has a high refractive index for the confinement and guiding of light, and which, for example, can preserve optical functionality for biomedical applications even in vitro. The fabrication of simple diamond micro-optics such as convex and concave spherical micro-lenses was reported recently [1,2]. Other applications in areas including beam-shaping, optical filters, micro-cavities, and micro-ring resonators, urgently require the development of other more complex forms of micro-structured diamond optical elements. Cylindrical lenses, for example, can be applied to focus collimated light along one axis or to circularize the beam from a laser diode by arranging two cylindrical lenses perpendicularly to each other [3]. Fu et al. have shown that the integration of a SiO_2 micro-cylindrical lens with a laser diode can lead to the improvement of fibre coupling efficiency [4,5]. It has

also been reported that the astigmatism in a diode laser collimator can be corrected by placing a concave micro-cylindrical lens in front of the collimator [4]. Furthermore, micro-light emitters and micro-resonators in ring format have recently attracted much attention [6–9]. Applications of such concepts in areas including deep-ultraviolet LED's [10] and ultraviolet laser diodes (where the refractive index of diamond is a close match to that of gallium nitride), diamond single-photon sources [11] biomedical sensors and in-vitro imaging systems would all benefit from the availability of novel optical microstructures formed in diamond. For these reasons, we concentrate here on demonstrating the fabrication of micro-ring and micro-cylindrical lens structures. We utilize chemical vapour deposition (CVD) polycrystalline diamond with high optical quality. Our results should be equally applicable to natural single-crystal diamond.

2. Experimental

2.1. Fabrication

Due to its hardness and chemical inertness, processing of diamond presents a considerable technical challenge. Several different techniques have been adopted to fabricate diamond microstructures, for example laser micromachining [12], ion beam milling [13] and inductively coupled plasma (ICP) etching [14–16]. In this work, the ICP technique with Ar/O_2 plasma is used for fabricating the diamond lenses due to its high

* Corresponding author. Tel.: +44 141 548 5736; fax: +44 141 552 1575.
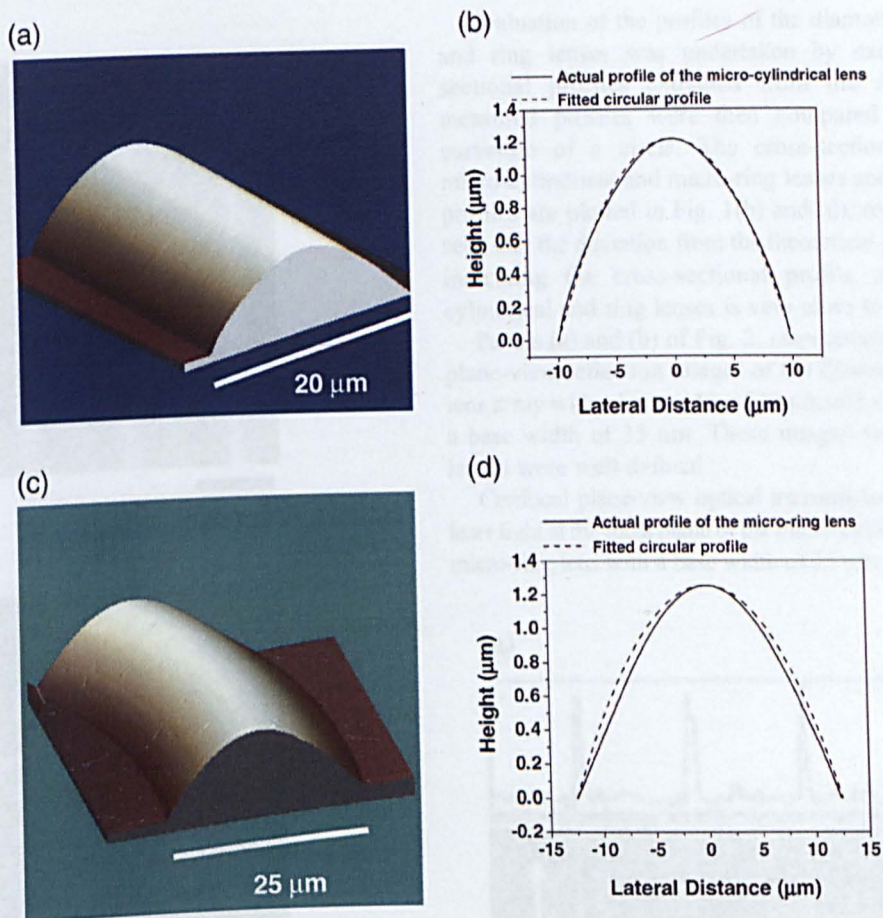 E-mail address: chee.leong.lee@strath.ac.uk (C.L. Lee).

Fig. 1. (a) and (c) AFM images, respectively, of a typical CVD diamond micro-cylindrical lens of 20 μm base width and a section of a micro-ring lens with diameter of 180 μm and ring width of 25 μm; (b) and (d) measured and fitted surface profiles for a micro-cylindrical lens and a micro-ring lens, respectively.

controllability and repeatability. The fabrication of micro-cylindrical and ring lenses was undertaken on a 10 mm × 10 mm CVD diamond substrate with a thickness of 300 μm. The surface quality of the CVD diamond was evaluated with AFM prior to lens fabrication. The measured RMS (root-mean-square) roughness is 3 nm for a 5 μm × 5 μm scanned area. No visible defect was observed on the diamond surface under an optical microscope and both sides of the CVD diamonds have the same optical quality. Micro-cylindrical and micro-ring pillars were first fabricated in photo-resist using a standard photolithography and resist reflow method [17]. A 7 μm thick layer of Shipley SPR220 photo-resist was spin-coated onto the diamond substrate. After mask patterning, the substrate was placed on a hotplate at 125 °C for 2 min to allow the photo-resist to re-flow. Due to the surface tension, both the micro-cylindrical and micro-ring lens structures were successfully formed in the photo-resist. These lens structures were then transferred onto the diamond substrate by ICP etching using the Ar/O$_2$ plasma. The ICP etch parameters employed were, after a series of optimization steps, chosen to be: a platen power of 40 W (−140 V bias), a coil power of 400 W, a chamber pressure of 5 mTorr, and flow rates of 15 sccm (standard cubic centimeter per minute) for Ar and 40 sccm for O$_2$, respectively. Under the above conditions, an etch rate of 0.04 μm/min was achieved. The total etch time was 30 min. During etching, the substrates

were mounted on a silicon wafer with vacuum grease to enhance the heat-spreading in order to avoid photo-resist burning. By this technique, arrays of micro-cylindrical lenses of (base) width as small as 20 μm have been fabricated. The diamond micro-ring lenses fabricated have an outer diameter of 180 μm. The widths (outer minus inner radii) of the micro-ring lenses range from 5 μm to 45 μm.

2.2. Micro-lens characterization

The surface profile and quality of the micro-lenses fabricated were evaluated by atomic force microscopy (AFM). Laser scanning reflection/transmission confocal microscopy, which we demonstrated previously in a related context, [2,15,18] was used to characterize in detail the optical properties of these diamond micro-lenses. The experimental setup of the confocal microscope has been reported elsewhere [15]. This technique allows the collection of both reflected and transmitted light sectional images simultaneously. The transmitted-light sections are here obtained using a beam-expanded and pre-collimated 532 nm solid-state laser beam focused through the micro-lenses. The reflected-light sections are taken under reflection by 488 nm laser light. Whereas the plane-view transmission sections reveal the optical properties of the lenses such as focal length, the plane-view reflection sections locate the position of

(a)

20 μm

(b)

35 μm
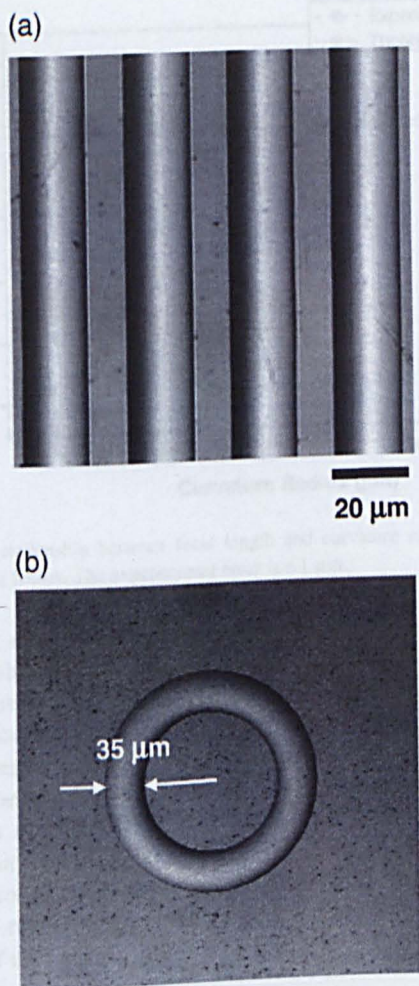
Fig. 2. Confocal plane-view reflection image of the CVD diamond micro-cylindrical lenses with a lens width of 20 μm (a) and micro-ring lens with ring width of 35 μm (b).

the lens and provide information on structural topography. During the measurements, X–Z, Y–Z and X–Y optical sections were collected, to fully reveal the characteristics of these diamond micro-lenses. Here, Z is the perpendicular distance from the lens and X and Y are the orthogonal co-ordinates for a section plane at a given value of Z from the lens.

3. Results and discussion

A three-dimensional AFM image of a portion of a representative diamond micro-cylindrical lens is shown in Fig. 1(a). The base width of the lenses was measured to be 20 μm. Fig. 1(c) shows a section of a diamond micro-ring lens with a base width of 25 μm. Both micro-cylindrical and ring lenses fabricated have the same height of 1.2 μm. The AFM measurements show that the surface RMS (root-mean-square) roughness values of both diamond micro-cylindrical and ring lenses are less than 3 nm for a scanned area of 5 μm × 5 μm. This is in the same value range as for the un-etched diamond surface. This confirms that the etched diamond surfaces are smooth with a low level of surface light scattering, as required for optical applications.

Evaluation of the profiles of the diamond micro-cylindrical and ring lenses was undertaken by examining the cross-sectional profiles extracted from the AFM images. The measured profiles were then compared to the theoretical curvature of a circle. The cross-sectional profiles of the micro-cylindrical and micro-ring lenses and their fitted circular profiles are plotted in Fig. 1(b) and (d), respectively. It can be seen that the deviation from the theoretical profile is very small, indicating the cross-sectional profile of the both micro-cylindrical and ring lenses is very close to spherical in shape.

Panels (a) and (b) of Fig. 2, respectively, show the confocal plane-view reflection images of the diamond micro-cylindrical lens array with a lens width of 20 μm and a micro-ring lens with a base width of 35 μm. These images show that both micro-lenses were well defined.

Confocal plane-view optical transmission sections of 532 nm laser light at the focal plane of the micro-cylindrical lens array and a micro-ring lens with a base width of 35 μm are shown in Fig. 3(a)

(a)

(b)
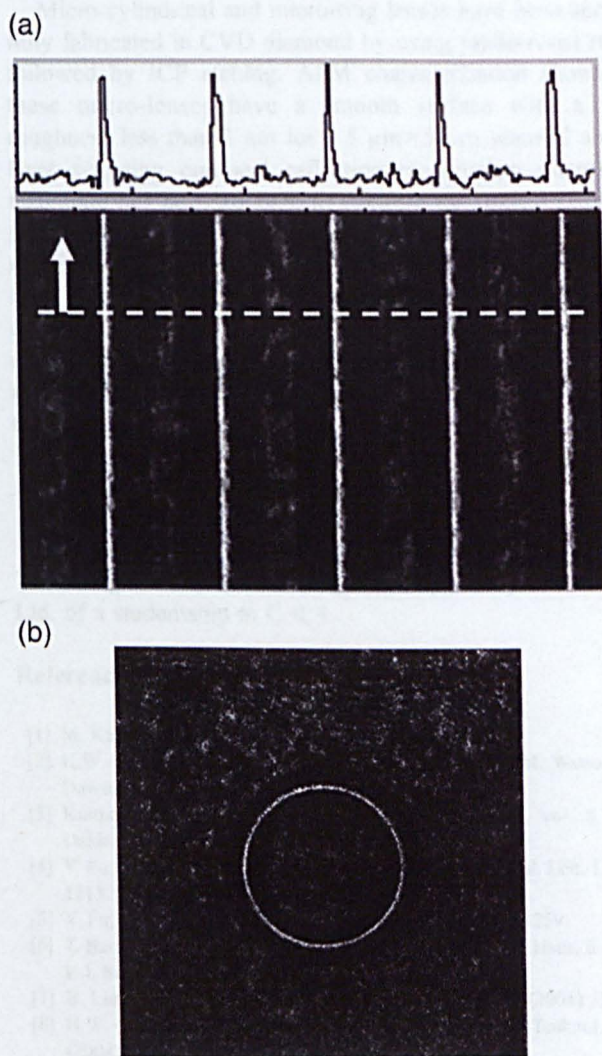
Fig. 3. Confocal plane-view transmission sections at the focal plane of the diamond micro-cylindrical lenses (a) and a micro-ring lens (b). Inset top in (a) is the light intensity at the focal plane, whose position is indicated by the dashed line.
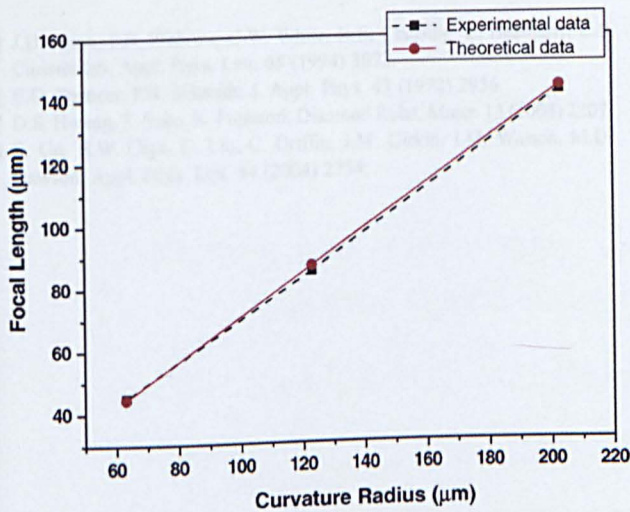
Fig. 4. Relationship between focal length and curvature radius of diamond micro-ring lenses. The experimental error is ±1 μm.

and (b), respectively. The sharp focal lines and a focal ring are clearly observed in these images. The trace at the top of Fig. 3(a) is an intensity scan at the focal plane in the case of the micro-cylindrical lenses. The results show that the light intensity of the focal lines of the micro-cylindrical lenses is quite uniform not only along the lens but also from lens to lens. The focal ring is also uniform as shown in Fig. 3(b), indicating the high structural uniformity and high optical quality of the diamond micro-ring lens.

In cross-section, both the micro-cylindrical and ring lenses can be regarded as plano-convex lenses. The paraxial focal length f of a plano-convex lens is given by [15]

$$f = \frac{R}{(n-1)}, R = \frac{(h^2 + r^2)}{2h} \tag{1}$$

Where n is the reflective index of the lens, R is the radius of curvature, r and h are the surface half-width and the height of the lens, respectively. The value of n for diamond is 2.42 at the wavelength of 532 nm used in the confocal microscopy measurement. The distance between the focal plane and the lens is defined as the focal length of the lens. The focal length of the micro-cylindrical lens with a lens width of 20 μm was measured, using the confocal microscope, to be 26±1 μm, which is very close to the calculated value of 25.6 μm, indicating the high fidelity of the diamond etch process. Focal lengths for the micro-rings were measured in the same way using the confocal microscope. The measured (calculated) values for the micro-ring lenses with ring widths of 25 μm, 35 μm and 45 μm are 45±1 μm (44.5 μm), 85±1 μm (86.7 μm) and 142±1 μm (143.0 μm) respectively. Fig. 4 shows the relationship between the focal length and curvature radius of the micro-ring lenses. It can be seen that the experimental data fitted very well with the theoretical curve based on Eq. (1).

At the focal point of a spherical lens, the diffraction-limited spot size d is theoretically given as [19]

$$d = \frac{2.44 f \lambda}{D} \tag{2}$$

Where λ is the wavelength of the beam, f is the focal length and D is the diameter of the lens. In the cases of cylindrical and ring lenses, D should be the lens width. The measured spot sizes for the micro-cylindrical lens of 20 μm lens width and the micro-ring lens of 35 μm ring width are 1.75 μm and 3.36 μm respectively. They are very close to the theoretical values calculated for both of the micro-cylindrical and ring lenses, based on Eq. (2), with spot sizes of 1.66 μm and 3.22 μm, respectively. The f-ratio, defined as f/D and therefore closely related to the beam spot size, serves as one of the important lens parameters. For a given lens diameter (width), the diffraction-limited spot size can be reduced by decreasing the focal length of the lens. The lens with a short focal length can be fabricated by decreasing its curvature radius as shown by Eq. (1). However, spherical astigmatism of the lens becomes prominent with decreasing of the curvature radius of the lens.

4. Conclusion

Micro-cylindrical and micro-ring lenses have been successfully fabricated in CVD diamond by using photo-resist reflow followed by ICP etching. AFM characterization shows that these micro-lenses have a smooth surface with a RMS roughness less than 3 nm for a 5 μm × 5 μm scanned area. A laser scanning confocal reflection/transmission microscopy technique has been adopted to evaluate the optical properties of the diamond micro-lenses. Confocal microscopy measurements show that both micro-cylindrical and ring lenses exhibit high optical quality and functionality. With a smooth surface and high uniformity, these special diamond micro-lenses offer a range of applications, especially when integrated with photonic and optoelectronic devices to achieve required light manipulation and directionality.

References

[1] M. Karlsson, F. Nikolajeff, Opt. Express 11 (2003) 502.
[2] H.W. Choi, E. Gu, C. Liu, C. Griffin, J.M. Girkin, I.M. Watson, M.D. Dawson, J. Vac. Sci. Technol., B 23 (2005) 130.
[3] Kuttner, Laser Beam Scanning, Optical Engineering, vol. 8, Marcel Dekker, New York, 1985.
[4] Y. Fu, B.N.K. Ann, O.N. Shing, IEEE Photonics Technol. Lett. 12 (2000) 1213.
[5] Y. Fu, B.N.K. Ann, J. Vac. Sci. Technol., B 19 (2001) 1259.
[6] T. Barwicz, M.A. Popovic, P.T. Rakich, M.R. Watt, H.A. Haus, E.P. Ippen, H.I. Smith, Opt. Express 12 (2004) 1437.
[7] B. Liu, A. Shakouri, J.E. Bowers, Appl. Phys. Lett. 79 (2001) 3561.
[8] H.W. Choi, C.W. Jeon, M.D. Dawson, IEEE Photonics Technol. Lett. 16 (2004) 33.
[9] H.W. Choi, P.R. Edwards, R.W. Martin, M.D. Dawson, Appl. Phys. Lett. 83 (2003) 4483.
[10] V. Adivarahan, S. Wu, W.H. Sun, V. Mandavilli, M.S. Shatalov, G. Simin, J.W. Yang, H.P. Maruska, M.A. Khan, Appl. Phys. Lett. 85 (2004) 1838.
[11] B. Lounis, M. Orrit, Rep. Prog. Phys. 68 (2005) 1129.

[12] J.D. Hunn, S.P. Withrow, C.W. White, R.E. Clausing, L. Heatherly, C.P. Christensen, Appl. Phys. Lett. 65 (1994) 3072.
[13] E.G. Spencer, P.H. Schmidt, J. Appl. Phys. 43 (1972) 2956.
[14] D.S. Hwang, T. Saito, N. Fujimori, Diamond Relat. Mater. 13 (2004) 2207.
[15] E. Gu, H.W. Choi, C. Liu, C. Griffin, J.M. Girkin, I.M. Watson, M.D. Dawson, Appl. Phys. Lett. 84 (2004) 2754.

[16] M. Karlsson, K. Hjort, F. Nikolajeff, Opt. Lett. 26 (2001) 1752.
[17] Z.D. Popovic, R.A. Sprague, G.A.N. Connell, Appl. Opt. 27 (1988) 1281.
[18] C.J.R. Sheppard, D.M. Shotton, Confocal Laser Scanning Microscopy, BIOS Scientific, 1997.
[19] S.H. Park, H. Jeon, Y.J. Sung, G.Y. Yeom, Appl. Opt. 40 (2001) 3698.

ELSEVIER

Etching and micro-optics fabrication in diamond using chlorine-based inductively-coupled plasma

C.L. Lee [a,*], E. Gu [a], M.D. Dawson [a], I. Friel [b], G.A. Scarsbrook [b]

[a] Institute of Photonics, University of Strathclyde, Glasgow, G4 0NW, United Kingdom
[b] Element Six Ltd, King's Ride Park, Ascot, Berkshire SL5 8BP, United Kingdom

Abstract

The effect of Inductively-Coupled Plasma (ICP) etching on diamond using chlorine-based plasma has been investigated. The diamond materials studied include type IIa natural diamond, High Pressure and High Temperature (HPHT) diamond and Chemical Vapour Deposition (CVD) diamond. It was found that argon and chlorine (Ar/Cl$_2$) ICP plasma etching can improve the smoothness of the diamond surface. By using this method, a minimum root-mean-squared (rms) surface roughness of 0.19 nm has been achieved. To demonstrate optimized Ar/Cl$_2$ plasma etching, diamond spherical micro-lenses and micro-trenches were fabricated. Compared to argon and oxygen (Ar/O$_2$) plasma etching, Ar/Cl$_2$ plasma etching has a low selectivity with respect to the photo-resist mask, which enables an accurate control over the dimensions of the microstructures fabricated. The surface quality and profiles of these micro-lenses and micro-trenches were characterized by atomic force microscopy (AFM) and were shown to be better than those fabricated by Ar/O$_2$ ICP plasma.
© 2008 Elsevier B.V. All rights reserved.

Keywords: ICP etch; Chlorine-based plasma; Micro-optics; Surface smoothing

1. Introduction

Diamond is an ideal material for optical applications due to its unique properties such as wide optical transmission bandwidth, high thermal conductivity and large refractive index. Additionally, with a very high breakdown voltage and high carrier mobility, [1] diamond is also a promising semiconductor material for high power electronic and optoelectronic devices. However, the processing of diamond remains a substantial technical challenge, as it is the hardest of all known materials and is extremely chemically inert. To date, the most successful approaches to etching diamond are based on dry etching techniques such as Reactive Ion Etching (RIE), [2] Inductively Coupled Plasma (ICP), [3–6] Electron-Cyclotron Resonance etching (ECR) [7] or focused-ion beam milling [8]. The fabrication of high quality of micro-lenses on natural diamond using ICP Ar/O$_2$ plasma was reported recently by Lee et al. [4] and Choi et al. [5] To further develop and improve the fabrication of diamond microstructures so as to achieve high structural quality such as high surface smoothness and a better control on the microstructure dimensions, diamond ICP etching using different gas plasmas such as Ar/Cl$_2$ have

been explored. Although Ar/Cl$_2$ plasma has been employed to etch several hard materials such as Gallium Nitride (GaN) [9], Silicon Carbide (SiC) [10] and sapphire [11], to the best of our knowledge, diamond Ar/Cl$_2$ plasma etching has not been previously reported.

In this work, the effect of ICP etching with Ar/Cl$_2$ gas mixture on diamond was investigated. The diamond materials studied include natural type IIa diamond, High Pressure and High Temperature (HPHT) diamond and Chemical Vapour Deposition (CVD) diamond. Our work shows that Ar/Cl$_2$ plasma etching is capable of surface smoothing on HPHT diamond. Using optimized etching conditions of argon and chlorine (Ar/Cl$_2$) plasma, microstructures such as micro-lenses and micro-trenches were successfully fabricated on the natural diamond and CVD diamond respectively. Good control of the etching depth has been demonstrated, which is especially critical for fabricating shallower diamond microstructures.

2. Experimental

2.1. Chlorine-based (Ar/Cl$_2$) plasma etching

In order to fully understand the effect of Ar/Cl$_2$ plasma etching including etch rate, etch selectivity (defined as the ratio of the

---

* Corresponding author.
  E-mail address: chee.leong.lee@strath.ac.uk (C.L. Lee).

diamond etch rate to the etch rate of photoresist) and surface root-mean-squared (rms) roughness of etched diamond, a series of ICP coil powers (100 W, 400 W and 900 W) with constant ICP platen power of 300 W was employed. The other ICP parameters used were: a chamber pressure of 5 mTorr, flow rates of 25 sccm for Ar and 40 sccm for Cl_2. The etching duration is 3 min.

The effect of Ar/Cl_2 plasma on surface smoothing of diamond substrate is also investigated. Four different HPHT diamond samples have been etched for different durations (5, 10, 20 and 30 min). The ICP parameter used for this study were: a platen power of 300 W, a coil power of 400 W, a chamber pressure of 5 mTorr, flow rates of 25 sccm for Ar and 40 sccm for Cl_2.

2.2. Micro-lens and micro-structure fabrication

To demonstrate optimized Ar/Cl_2 plasma etching, diamond spherical micro-lenses and micro-trenches were fabricated. Spherical micro-lenses were fabricated by using photoresist reflow method [2,4,5,12]. Photoresist reflow method is a technique to form spherical microlenses. The basic principle requires exposing and developing photoresist to leave small pedestals. Once the pedestals have been formed, the photoresist temperature is raised above its glass transition temperature (T_g) [12]. Above this temperature, the photoresist becomes liquid, flows and the final form taken is determined by the surface adhesive forces, surface tension, and the internal modulus of the photoresist [12]. To form micro-spherical lens in our work, a 7 μm thick layer of Shipley SPR220 photoresist was first spin-coated onto the diamond substrate which is a circular natural type IIa diamond of 4 mm diameter. After mask patterning, the photoresist pillars were formed. The substrate was then placed on a hotplate at 125 °C for 2 min to allow the photoresist pillars to re-flow. Due to the surface tension, spherical lens structures were formed. These lens structures were then transferred onto the diamond substrate by ICP etching using Ar/Cl_2 plasma. The ICP parameters used were: a platen power of 100 W, a coil power of 400 W, a chamber pressure of 5 mTorr, flow rates of 25 sccm for Ar and 40 sccm for Cl_2, with an etching duration of 25 min. A low platen power of 100 W was used here so as to avoid resist burning during long time etching. The resulting surface profiles of the micro-lenses were evaluated by atomic force microscopy (AFM).

Micro-trenches with different depths were fabricated by ICP etching on a 7 mm × 7 mm polycrystalline CVD diamond. The ICP parameter used were: a platen power of 300 W, a coil power of 400 W, a chamber pressure of 5 mTorr, flow rates of 25 sccm for Ar and 40 sccm for Cl_2. Under these conditions, the etch rate was measured to be 1.0 nm/s.

3. Results and discussion

3.1. Chlorine-based (Ar/Cl_2) plasma etching

The diamond etch rate and etch selectivity of Ar/Cl_2 plasma as a function of the ICP coil power are plotted in Fig. 1(a). It is observed that the etch selectivity remains almost constant, regardless of the ICP coil powers being applied. The etch rate, on the other hand, increases with the ICP coil power. It is well known that the ion density increases with the ICP coil power.

Thus at a high coil power, more chlorine radicals are generated, resulting in a high etch rate. The etch results shown in Fig. 1(a) also imply that the etch rate of photoresist increases with the ICP coil power owing to the fact that the etch selectivity remains almost constant. Similar behaviour has also been observed in Ar/O_2 plasma etching [5].

The surface rms roughness of as-received natural diamond sample was measured to be 1.1 nm for a 5 μm × 5 μm area. For the short duration of Ar/Cl_2 plasma etching (3 min), the rms roughness of the etched diamond does not vary greatly with the ICP coil power as shown in Fig. 1(b), indicating the impact of the ICP coil power towards the surface rms roughness is not significant.

To investigate the capability of Ar/Cl_2 plasma etching in surface smoothing of the diamond substrates, four HPHT diamonds were etched and measured by AFM. Fig. 2(a) and (b) shows the three dimensional (3-D) AFM images of the sample for 1 μm × 1 μm area before and after ICP etch using Ar/Cl_2 plasma for 10 min. It is observed that Ar/Cl_2 plasma is able to smooth the surface of the diamond substrate after 10 min of etching. The results on surface rms roughness for all the above samples were summarized in Fig. 2(c). It can be seen that the there is a significant reduction in surface rms roughness from 0.53 nm to 0.19 nm after the HPHT diamond has been etched for 10 min. Extending the etch duration to 20 or 30 min does not improve the
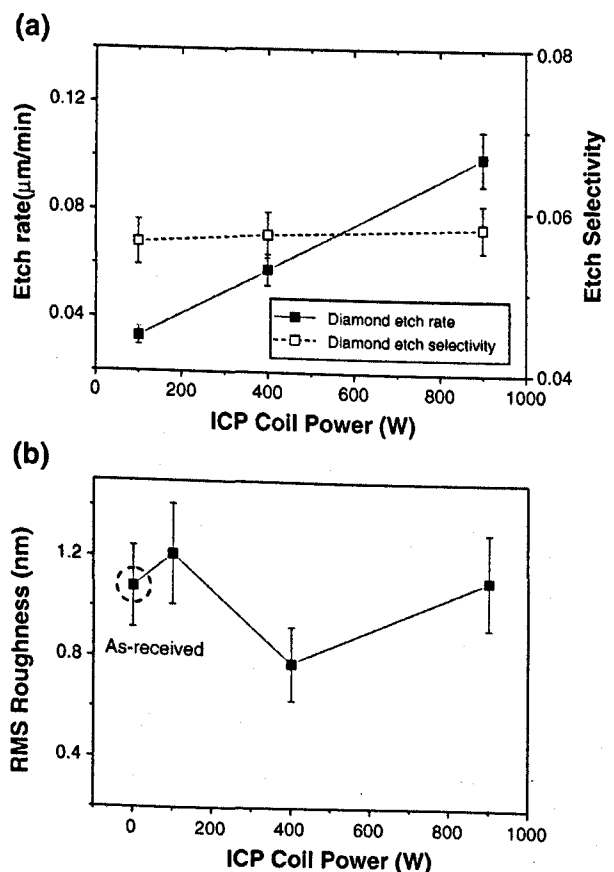

Fig. 1. (a) Etch rate and selectivity of natural diamond as a function of ICP coil power with the ICP platen power of 300 W, and (b) corresponding surface rms roughness for a 5 μm × 5 μm area.
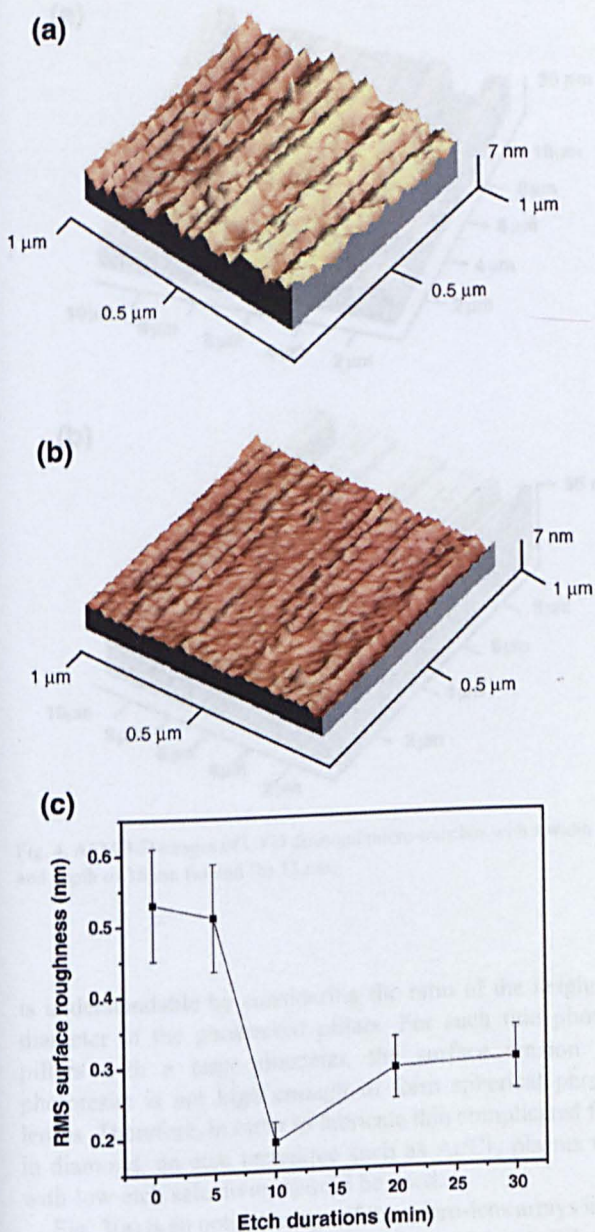
(a)

(b)

(c)

Fig. 2. (a) AFM images of an as-received HPHT diamond, and (b) the HPHT diamond etched by Ar/Cl₂ plasma for 10 min at an ICP platen and coil powers of 300 W and 400 W, respectively. (c) Surface rms roughness versus etch durations for a 1 μm x 1 μm area after etched with ICP Ar/Cl₂ plasma.

surface smoothness further. The surface smoothing effect is possibly due to the diamond isotropic etching.

Under the same conditions, the etch selectivities on natural diamond using Ar/Cl₂ and Ar/O₂ plasmas are 0.057 and 0.098 respectively. The etch selectivity on HPHT diamond using Ar/Cl₂ plasma with the same ICP parameters has been determined as 0.055 which is very close to that on natural diamond. These results show that under the same etch conditions, the etch selectivity on natural diamond using Ar/Cl₂ plasma is almost half of that by using Ar/O₂ plasma etching. Hence, with the same thickness of photoresist mask, the height/depth of the microstructures fabricated in diamond such as micro-lenses using Ar/Cl₂ plasma

etching is only half of those fabricated by using Ar/O₂ plasma. The low etch rate and etch selectivity will enable a good control on the etch depth of the microstructure fabricated.

To fabricate the shallower features in diamond, either a thin photoresist mask or etching with low etch selectivity should be adopted. Furthermore, for the fabrication of some shallow structures, only the technique with low etch selectivity is suitable. For example, in the case of micro-lens fabrication, thin photoresist pillars with large diameters (>50 μm) are not able to form good micro-lens patterns by the reflow method, which
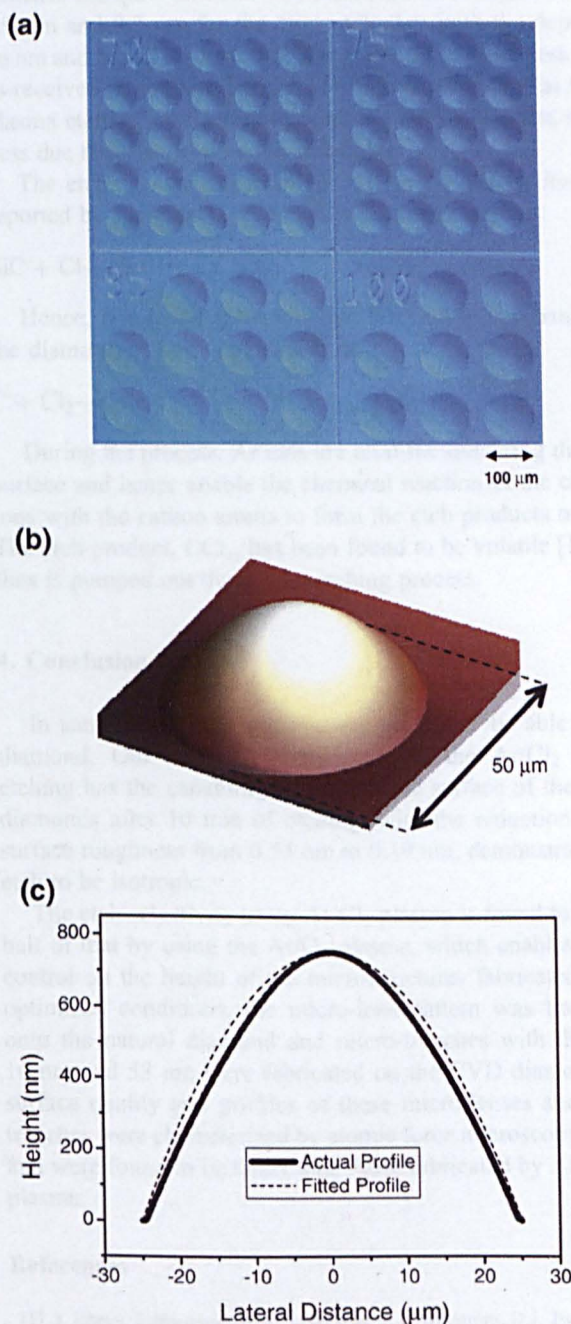
(a)

(b)

(c)

Fig. 3. (a) Optical image of arrays of natural diamond micro-lenses with different diameters, and (b) AFM 3-D image of a natural diamond micro-lens with a diameter of 50 μm, (c) Measured and fitted surface profiles of the micro-lens shown in (b).
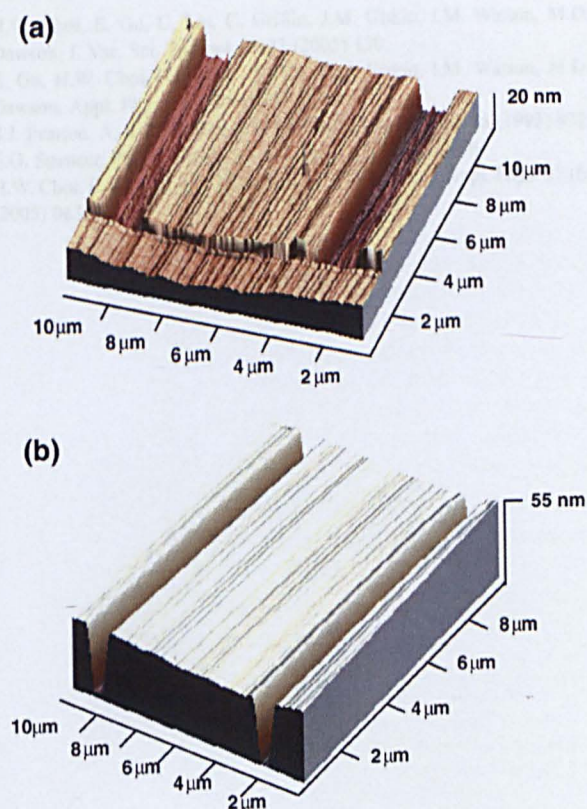
Fig. 4. AFM 3-D images of CVD diamond micro-trenches with a width of 2 μm and depth of 16 nm (a) and (b) 53 nm.

is understandable by considering the ratio of the height to the diameter of the photoresist pillars. For such thin photoresist pillars with a large diameter, the surface tension of the photoresist is not high enough to form spherical photoresist lenses. Therefore, in order to fabricate thin complicated features in diamond, an etch technique such as Ar/Cl$_2$ plasma etching with low etch selectivity should be used.

Fig. 3(a) is an optical image of the micro-lens arrays in a type IIa natural diamond, which were fabricated by Ar/Cl$_2$ plasma etching. A three-dimensional AFM image of a representative diamond micro-lens is shown in Fig. 3(b). The surface diameter and height of this lens were measured to be 50 μm and 0.75 μm respectively. The AFM measurements show that the surface rms roughness of the diamond micro-lenses is less than 1.0 nm for a scanned area of 5 μm × 5 μm. These results confirm that the diamond lenses etched by Ar/Cl$_2$ plasma are smooth and have a better quality than the diamond micro-lenses fabricated by using Ar/O$_2$ plasma etching, which has the surface rms roughness of less than 3 nm for a scanned area of 5 μm × 5 μm [4]. The profile of the diamond micro-lenses was reviewed by examining the cross-sectional scan of the AFM images. The measured cross-sectional profile of a diamond micro-lens and the fitted spherical profile are plotted in Fig. 3(c). It can be seen that the difference between two profiles is very small, indicating the cross-sectional profile of the micro-lens is very close to spherical in shape.

Again, using Ar/Cl$_2$ plasma etching, diamond micro-trenches with different depths (i.e. 16 nm and 53 nm) were successfully fabricated on the polycrystalline CVD diamond. 3-D AFM images of these micro-trenches are shown in Fig. 4(a) and (b). It is observed that these micro-trenches have a well defined width of 2 μm. In addition, the trench depth is consistent with that estimated from the etch rate (i.e. 1.0 nm/s), demonstrating a good etch controllability of the Ar/Cl$_2$ plasma in the fabrication of shallow diamond microstructures. The AFM measurements show that the etched bottom surfaces of the micro-trenches are quite smooth. The measured rms roughnesses are 0.9 nm and 0.7 nm for the micro-trenches with the depths of 16 nm and 53 nm respectively. The surface rms roughness of the as-received sample was 1.0 nm. The rms results show that Ar/Cl$_2$ plasma etching would slightly improve the surface rms roughness due to the short duration of etching.

The etching mechanism of SiC in Ar/Cl$_2$ plasma has been reported by Jiang et. al. [10] and is shown as follows:

$$SiC + Cl_2 \rightarrow SiCl + CCl_x \qquad (1)$$

Hence, one could anticipate that the etching mechanism of the diamond in Ar/Cl$_2$ plasma to be:

$$C + Cl_2 \rightarrow CCl_x \qquad (2)$$

During the process, Ar ions are used for sputtering diamond surface and hence enable the chemical reaction of the chlorine ions with the carbon atoms to form the etch products of CCl$_x$. The etch product, CCl$_x$, has been found to be volatile [10] and thus is pumped out during the etching process.

4. Conclusion

In summary, Ar/Cl$_2$ plasma was proven to be able to etch diamond. Our work demonstrates that the Ar/Cl$_2$ plasma etching has the capability to smooth the surface of the HPHT diamonds after 10 min of etching, with the reduction of rms surface roughness from 0.53 nm to 0.19 nm, demonstrating the etch to be isotropic.

The etch selectivity using Ar/Cl$_2$ plasma is found to be only half of that by using the Ar/O$_2$ plasma, which enables a good control on the height of the microstructures fabricated. Using optimized conditions, the micro-lens pattern was transferred onto the natural diamond and micro-trenches with depths of 16 nm and 53 nm were fabricated on the CVD diamond. The surface quality and profiles of these micro-lenses and micro-trenches were characterized by atomic force microscopy (AFM) and were found to be better than those fabricated by Ar/O$_2$ ICP plasma.

References

[1] J. Isberg, J. Hammersberg, E. Johansson, T. Wikström, D.J. Twichen, A.J. Whitehead, S.E. Coe, G.A. Scarsbrook, Science 297 (2002) 1670.
[2] C.L. Lee, H.W. Choi, E. Gu, H. Murphy, M.D. Dawson, Diamond Relat. Mater. 15 (2006) 725.
[3] M. Karlsson, K. Hjort, F. Nikolajeff, Opt. Lett. 26 (2001) 1752.
[4] C.L. Lee, E. Gu, M.D. Dawson, Diamond Relat. Mater. 16 (2007) 944.

[5] H.W. Choi, E. Gu, C. Liu, C. Griffin, J.M. Girkin, I.M. Watson, M.D. Dawson, J. Vac. Sci. Technol., B 23 (2005) 130.
[6] E. Gu, H.W. Choi, C. Liu, C. Griffin, J.M. Girkin, I.M. Watson, M.D. Dawson, Appl. Phys. Lett. 84 (2004) 2754.
[7] S.J. Pearton, A. Katz, F. Ren, J.R. Lothian, Electron. Lett. 28 (1992) 822.
[8] E.G. Spencer, P.H. Schmidt, J. Appl. Phys. 43 (1972) 2956.
[9] H.W. Choi, E. Gu, C. Liu, J.M. Girkin, M.D. Dawson, J. Appl. Phys. 97 (6) (2005) 063101.
[10] L. Jiang, N.O.V. Plank, M.A. Blauw, R. Cheung, E. van der Drift, J. Phys., D, Appl. Phys. 37 (2004) 1809.
[11] C.H. Jeong, D.W. Kim, J.W. Bae, Y.J. Sung, J.S. Kwak, Y.J. Park, G.Y. Yeom, Mater. Sci. Eng., B, Solid-State Mater. Adv. Technol. B93 (1-3) (2002) 60.
[12] Dan Daly, Microlens Arrays, Taylor & Francis, 2001.

Microlensed microchip VECSEL

Nicolas Laurand*, C. L. Lee, E. Gu, J.E. Hastie, Stephane Calvez and Martin D. Dawson

Institute of Photonics, University of Strathclyde, 106 Rottenrow, G4 0NW Glasgow
Corresponding author: Nicolas.laurand@strath.ac.uk

Abstract: We report a 1.055-µm microchip VECSEL array which uses a microlens-patterned diamond both as a heatspreader and as an array of concave output mirrors. This configuration, which is suitable for laser array operation, is here exploited to perform a systematic study of a set of microchip lasers with the same semiconductor structure but different cavity properties. The transverse mode selection of individual VECSELs is found to depend on the mode-matching conditions and on the microlens aperture size. Mode-matched single-device emission in the fundamental mode ($M^2 \sim 1.1$) with pump-limited output power of 70 mW is demonstrated.

References and links

1. J.E. Hastie, J.M. Hopkins, S. Calvez, C.W. Jeon, D. Burns, R. Abram, E. Riis, A.I. Ferguson, M.D. Dawson, "0.5-W single transverse-mode operation of an 850-nm diode-pumped surface-emitting semiconductor laser," IEEE Photonic. Technol. Lett. 15 (2003) 894-896.
2. J.E. Hastie, J.M. Hopkins, C.W. Jeon, S. Calvez, D. Burns, M.D. Dawson, R. Abram, E. Riis, A.I. Ferguson, W.J. Alford, T.D. Raymond, A.A. Allerman, "Microchip vertical external cavity surface emitting lasers," Electron. Lett. 39 (2003) 1324-1326.
3. S.A. Smith, J.M. Hopkins, J.E. Hastie, D. Burns, S. Calvez, M.D. Dawson, T. Jouhti, J. Kontinnen, M. Pessa, "Diamond-microchip GaInNAs vertical external-cavity surface-emitting laser operating CW at 1315 nm," Electron. Lett. 40 (2004) 935-937.
4. A.J. Kemp, A.J. Maclean, J.E. Hastie, S.A. Smith, J.M. Hopkins, S. Calvez, G.J. Valentine, M.D. Dawson, D. Burns, "Thermal lensing, thermal management and transverse mode control in microchip VECSELs," Appl. Phys. B-Laser O. 83 (2006) 189-194.
5. R.I. Aldaz, M.W. Wiemer, D.A.B. Miller, J.S. Harris, "Monolithically-integrated long vertical cavity surface emitting laser incorporating a concave micromirror on a glass substrate," Opt. Express 12 (2004) 3967-3971.
6. K.S. Kim, Y.H. Lee, B.Y. Jung, C.K. Hwangbo, "Single mode operation of a curved-mirror vertical-emitting laser with an active distributed Bragg reflector," Jpn. J. Appl. Phys. 2 41 (2002) L827-L829.
7. A.M. Sarangan, G.M. Peake, "Enhancement of lateral mode discrimination in broad-area VCSELs using curved Bragg mirrors," J. Lightwave Technol. 22 (2004) 543-549.
8. G.A. Keeler, D.K. Serkland, K.M. Geib, G.M. Peake, A. Mar, "Single transverse mode operation of electrically pumped vertical-external-cavity surface-emitting lasers with micromirrors," IEEE Photonic. Technol. Lett. 17 (2005) 522-524.
9. H.W. Choi, E. Gu, C. Liu, C. Griffin, J.M. Girkin, I.M. Watson, M.D. Dawson, "Fabrication of natural diamond microlenses by plasma etching," J. Vac. Sci. Technol. B 23 (2005) 130-132.
10. K.F. Riley, S.J. Hobson, S.J. Bence, *Mathematical methods for physics and engineering* (Cambridge University Press, 2006).

---

1. Introduction

Vertical-External Cavity Surface Emitting Lasers (VECSELs) have attracted a lot of attention lately because of attractive attributes including high-power, circularly-symmetric output beams and versatility in operating wavelength. The main element constituting a VECSEL is the semiconductor active structure: it is made by a quantum well gain region grown on top of a distributed Bragg reflector (DBR). The laser cavity is usually completed by an external mirror, or mirrors, separated from the semiconductor chip by an air-gap. Heat removal from the gain region is important in these devices in order to maximize the output power. One way

to do this efficiently is to capillary-bond a transparent high-thermal conductivity crystal as heatspreader on to the VECSEL surface [1]. As well as facilitating power-scaling and broad wavelength coverage, this configuration has enabled a quasi-monolithic VECSEL format, the so-called microchip VECSEL (μ-VECSEL) [2, 3]. In this particular case, the heatspreader is directly mirror-coated on its outer surface, creating a plane-plane cavity. The μ-VECSEL is therefore an integrated version of the VECSEL with potential for volume production.

One drawback of the μ-VECSEL is that the laser cavity is mainly stabilized by a thermal lens appearing in the gain region when it is being pumped [4]. As the power is ramped up, the thermal lens effect increases and the fundamental mode spot size in the active region decreases. This means that mode-matching the pump to the fundamental laser mode is possible for one given power only and the output beam quality tends to degrade (due to the appearance of higher transverse modes) as the power is varied. To overcome this problem and ensure stable fundamental mode operation, a microchip laser having a plano-concave cavity is preferable [5-8], because the mode size is then mainly determined by the physical characteristics of the cold cavity.

In this paper we demonstrate the operation and investigate the properties of an array of micro-lensed μ-VECSELs whose plano-concave cavities are obtained by micro-patterning a diamond heatspreader. This array geometry, also suited for laser array operation, is here used to perform a parametric study of the influence of the cavity properties on the performance of micro-lensed μ-VECSELs. Section 2 of the present paper details the design and realization of the devices. In section 3 we report the experimental study of a single μ-VECSEL, i.e. when only one element in an array is probed at one time. Finally, Section 4 is devoted to the analysis of the experimental results. Attention is paid to the mode-matching conditions and aperture losses in the selection of the lasing modes.

2. Device design and fabrication

The 1055-nm-emitting micro-lensed μ-VECSELs under study are constituted of a semiconductor part liquid-capillarity bonded to a single-crystal diamond heatspreader, whose outer surface has been shaped into an array of spherical micro-lenses (μ-lenses) and subsequently mirror-coated. The semiconductor structure includes 10 InGaAs strain-compensated QWs (one per antinode) grown on top of a 30.5-pair AlAs/$Al_{0.2}Ga_{0.8}As$ DBR. The micro-lenses are fabricated using the 'resist-reflow' technique followed by a inductively coupled plasma etching using Ar/O_2 [9]. The lenses obtained are accurately spherical with a rms roughness less than 3 nm [9]. A SiO_2/TiO_2 coating with nominal peak reflectivity of 95% at 1.055 μm, anti-reflection at 808 nm, was deposited onto the diamond outer surface in order to create the concave output couplers. A schematic of an individual plano-concave μ-VECSEL cavity is shown in Fig. 1. Fig. 2 shows a picture of the final μ-VECSEL array, where different μ-lenses (acting as concave micromirrors), having a diameter d ranging from 10 to 100 μm, are distributed over different sections of the array. The other devices parameters (as shown in Fig. 1) are $t \sim 250$ μm, $h \sim 0.75$ μm and the micro-lens radius of curvature R is given by $R = (d^2 + 4h^2)/(8h)$.
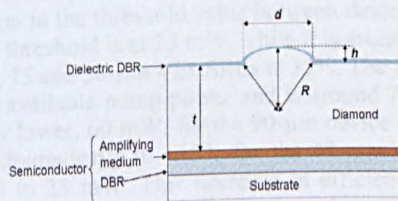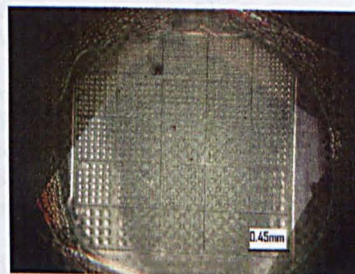

Fig. 1. Schematic of an individual μ-VECSEL.

Fig. 2. Picture of the μ-VECSEL array.

3. Single μ-VECSEL experiment

In this section, we study the characteristics of individual μ-VECSELs having different lens diameters. A schematic of the experimental set-up is shown in Fig. 3. The μ-VECSEL array is directly mounted on a copper holder held at 10°C. The holder is fixed on a XYZ translation stage for alignment. The device is pumped, through the heatspreader, with polarization-coupled 810-nm diode lasers. The pump beam, with up to 210 mW of average power, is delivered using a 15-mm focal length lens (NA~ 0.25), yielding pump spot size in the 13-30-μm range. As can be seen in Fig. 3, the μ-VECSEL signal is separated from the pump by the use of a dichroic mirror followed by a high-pass filter.
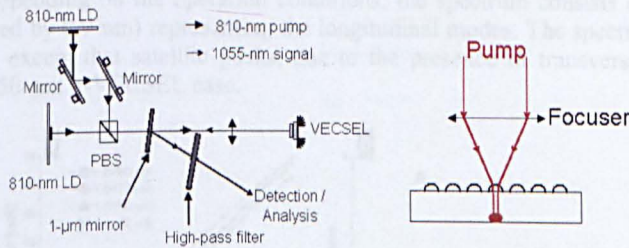
Fig. 3. Left: Experimental set-up. Right: schematic of the single μ-VECSEL probing.

The equivalent plane-plane μ-VECSEL is characterized first by probing a region with no lenses (such a region can be seen at the bottom centre of Fig. 2). Figs. 4 (a) and 4 (b) show the results. A 25-mW threshold and a pump limited output power of 60 mW are found. As expected [4], the M^2 varies with the power indicating that the mode-matching condition changes with the power. At 50 mW output power the M^2 is 1.9.
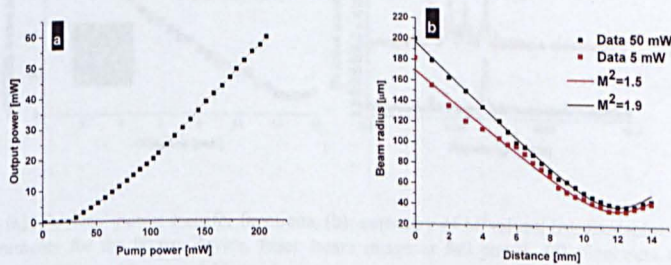

Fig. 4. Plane-plane μ VECSEL (a): Output power transfer function (b): M2 measurements.

Micro-lensed μ-VECSELs with lens diameter d of 90, 75, 50 and 42 μm, respectively, were then measured. For each device the output power transfer function, the spectrum and the M^2 of the output beam were recorded. The results are summarized in Fig. 5. There is no large variation in the threshold value between devices. We can nevertheless observe that the 90-μm device threshold is at 25 mW, while it is around 15 mW for the others. The slope efficiency of the 90, 75 and 50-μm VECSELs is 35%. The maximum output power for all devices is limited by the available pump power and is around 70 mW for both the 50 and 75-μm devices. It is slightly lower, 60 mW, for the 90-μm device due to its higher threshold. The slope efficiency drops dramatically to ~15% for the 42-μm VECSEL and consequently the output power is limited to 25 mW. This decrease in efficiency can be attributed to both an increase in the mode-mismatch and in the aperture losses (see next section). We can further note that μ-VECSELs with lower lens diameters (down to 10 μm) did not lase. These achieved power levels are consistent with previous micro-cavity laser reports [2, 3, 5]. The absence of roll-over and the low device thermal resistance, measured to be 140 K/mW, demonstrate the

effective heat sinking provided by the diamond heatspreader and suggest that single emitter operation with output powers greater than 100 mW would be achievable. A detailed report and analysis of the latter effects will be presented elsewhere.

An example of M^2 measurements for the 90-μm μ-VECSEL is shown in Fig 5 (c), while results for all devices are plotted in Fig. 5 (b). The μ-VECSELs operate in the TEM_{00} mode with $M^2 < 1.3$ for lens diameters above 75 μm ($M^2 \sim 1.1$ for the 90-μm device). The 50-μm μ-VECSEL has a device $M^2 \sim 2.8$. The 42-μm has a lower M^2 of 1.6. This can also be explained by the increasing aperture losses filtering out the highest order modes. Unlike the plane-plane case, M^2 values are found not to vary significantly with the power.

In Fig. 5 (d), spectra for the 90, 50 and 42-μm μ-VECSELs at their respective full powers are plotted. Depending on the operation conditions, the spectrum consists of one or several peaks (separated by 0.9 nm) representing the longitudinal modes. The spectrum is similar for other devices, except that satellite peaks, due to the presence of transverse modes [6], are present in the 50-μm μ-VECSEL case.
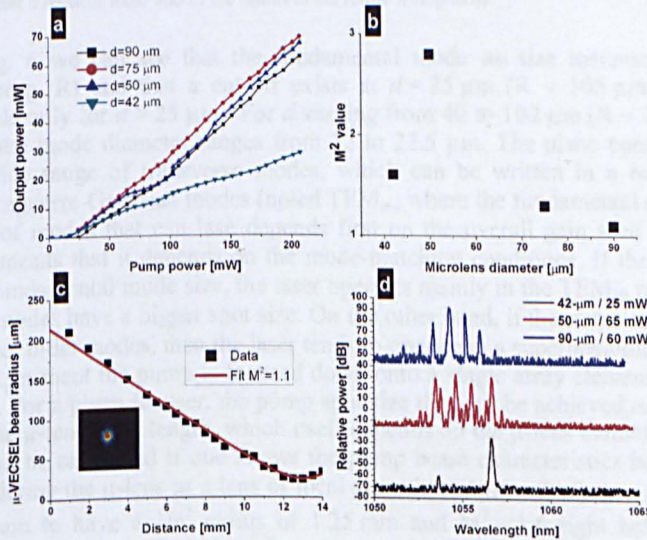

Fig. 5. (a): Devices' power transfer functions, (b): summary of M^2values, (c): Examples of M^2 measurements for the 90 μm device. Inset: beam image at full power, (d): Spectrum at full power of the 90-μm, 50-μm and 42-μm devices.

These results show that plano-concave cavities can be a solution to ensure stable single-transverse mode lasing in μ-VECSELs at power levels of several tens of mW.

4. Micro-lensed μ-chip analysis

The previous results concerning the mode selection and evolution with d can be explained as the combination of two phenomena: the variation of the mode-matching condition and the aperture losses. Given the micro-lensed μ-VECSEL parameters, the fundamental mode size in the gain region, i.e. at the semiconductor plane, can be inferred by:

$$\omega_0 = \left[\frac{t\lambda}{n\pi} \sqrt{nR-1} \right]^{\frac{1}{2}} \tag{1}$$

In Eq. (1), λ is the wavelength in vacuum, n is the heatspreader refractive index (and for diamond at $\lambda \sim 1$ μm, $n \sim 2.42$) and R is the radius of curvature of the micro-lens.
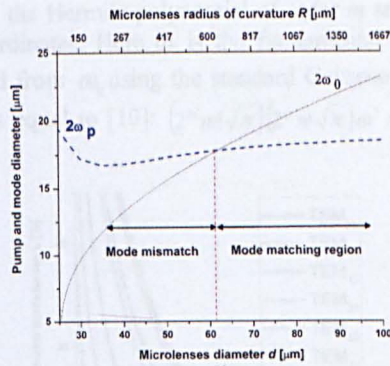
Fig. 6. Fundamental mode ($2\omega_0$) and pump ($2\omega_p$) diameter evolution as a function of the lens diameter d (bottom axis) and of the radius of curvature R (top axis).

From Fig. 6 we can see that the fundamental mode ω_0 size increases with the lens diameter d (resp. R) and that a cut-off exists at $d = 25$ μm (R ~ 105 μm). The cavity is therefore stable only for $d > 25$ μm. For d varying from 40 to 100 μm (R ~ 267 to 1667 μm) the fundamental mode diameter ranges from 12 to 22.5 μm. The plano-concave cold cavity supports a wide range of transverse modes, which can be written in a basis of Hermite-Gaussian or Laguerre-Gaussian modes (noted TEM_{mn} where the fundamental mode is TEM_{00}). The number of modes that can lase depends first on the overall gain seen by the different modes. This means that it depends on the mode-matching conditions. If the pump spot size matches the fundamental mode size, the laser operates mainly in the TEM_{00} mode because the higher order modes have a bigger spot size. On the other hand, if the pump spot is big enough to excite higher order modes, then the laser tends to operate in a superposition of modes.

In our experiment the pump is focused down onto a single array element through the top of the device. For a given focuser, the pump spot size that can be achieved on the gain region depends on the μ-lens focal length, which itself depends on the μ-lens diameter. The expected pump spot can be calculated if one knows the pump beam characteristics before the focuser and by considering the μ-lens as a lens of focal given by: $f(d) = R(d)/(n-1)$. We measured the pump beam to have a $1/e^2$ radius of 1.25 mm and $M^2 \sim 1.6$ right before the focuser. Results of the pump spot calculations for a 15-mm focal length focusing lens are shown in Fig. 6 along with the fundamental spot size. A minimum pump spot size smaller than the fundamental mode size indicates that mode-matching is possible by simply changing the position of the focus with respect to the μ-VECSEL. We can see that in our case, mode-matching is possible for devices with μ-lens diameter above ~65 μm (i.e. R > 705 μm). Below this value the pump spot is wider than the fundamental mode, which favors the excitation of higher transverse modes. This effect explains why the M^2 shoots up to almost 3 for $d = 50$ μm, while it is below 1.3 for d equal or above 75 μm (see previous section). However, another factor is responsible for the improvement of the M^2 recorded at $d = 42$ μm.

Due to its finite transverse size, the concave mirror (i.e. the μ-lenses) also acts as an aperture and introduces a certain amount of loss for the transverse modes. To illustrate this point, we plot in Fig. 7, for a few Hermite-Gaussian modes, the losses L due to the reflection on the concave mirror. This was done by taking the overlap integral of the mode power over a circular aperture and dividing it by the total power carried by the mode.

$$L = \frac{\displaystyle\iint_{aperture} \left[H_m\left(\frac{\sqrt{2}x}{\omega}\right)\right]^2 \left[H_n\left(\frac{\sqrt{2}y}{\omega}\right)\right]^2 \exp\left(-2\frac{x^2-y^2}{\omega^2}\right)dxdy}{\displaystyle\iint_{-\infty}^{+\infty} \left[H_m\left(\frac{\sqrt{2}x}{\omega}\right)\right]^2 \left[H_n\left(\frac{\sqrt{2}y}{\omega}\right)\right]^2 \exp\left(-2\frac{x^2-y^2}{\omega^2}\right)dxdy} \tag{2}$$

In Eq. (2), H_m and H_n are the Hermite polynomial of order m and n respectively, x and y are the spatial Cartesian coordinates. Here, ω is the fundamental mode radius at the aperture plane and can be deduced from ω_0 using the standard Gaussian propagation formulas. The denominator of Eq. (2) is equal to [10]: $\left(2^m\, m!\sqrt{\pi}\right)\left(2^n\, n!\sqrt{\pi}\right)\omega^2/2$. The results are shown in Fig. 7.
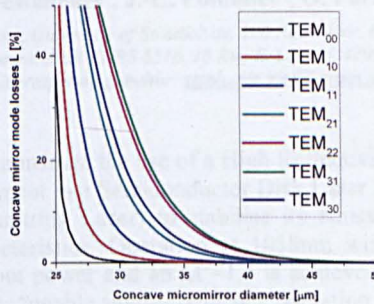
Fig. 7. Aperture losses of a few Hermite-Gaussian modes reflecting on concave micro-mirrors.

The losses increase for decreasing mirror diameter, i.e. aperture. Losses are higher for higher order modes because of their bigger size. The aperture of the concave mirror therefore acts as a filter for the higher order modes. This feature can be interesting in order to reduce the number of μ-VECSEL transverse modes when the condition of mode-matching is not fulfilled. It explains the improvement in the M^2 and the cleaner optical spectrum (see Fig. 5 (d)) at $d = 42$ μm (when compared to $d = 50$ μm) even though the mode-mismatch is worse for this device. However, TEM$_{00}$ losses need to be kept at a minimum and consequently the μ-lenses aperture needs to be wide enough to accommodate the fundamental mode. Please note that Fig. 7 represents the losses incurred by the mode for one reflection. However, the lasing modes experience many round-trips in the cavity and the aperture effect is exacerbated. In consequence, such μ-VECSELs with μ-lens diameter below 30 μm are too lossy to reach lasing threshold.

The combination of the two phenomena discussed above is believed to be the cause for the dramatic decrease in the slope efficiency at low d recorded in section 3.

5. Conclusion

In this paper, we have reported the demonstration of monolithic micro-lensed μ-VECSELs. The devices were fabricated by micro-patterning a diamond heatspreader in a μ-lens array format. The heatspreader was then high-reflection coated and capillary-bonded to a semiconductor DBR-active region structure to create the μ-VECSEL array. We have studied the importance of mode-matching the pump beam and of the μ-lens aperture in the selection of the lasing modes. Mode-matched μ-lensed μ-VECSELs were found to address the main issue of plane-plane μ-VECSELs, by ensuring stable fundamental mode emission. Pump limited output power up to 70 mW and slope efficiency of 35% were reported. Higher pump power should readily enable these devices to reach powers above 100 mW. Increasing the micro-lens radius of curvature in order to increase the mode size in the active region should allow the use of higher power pump laser. This, in conjunction with the mode diameter increase, should yield microchip devices emitting several hundreds of mW in the fundamental mode.

Acknowledgements

Stabilization of a Semiconductor Disk Laser using an intra-cavity High Reflectivity Grating

S. Giet[*,1], C.-L. Lee[1], S. Calvez[1], M.D. Dawson[1],
N. Destouches[2], J.-C. Pommier[2], O. Parriaux[2]

[1] Institute of Photonics, University of Strathclyde, 106 Rottenrow, Glasgow G4 0NW, UK
[2] Laboratoire Hubert Curien,UMR CNRS 5516, 18 Rue B. Lauras, 42000 Saint-Etienne, FRANCE
*Corresponding author: stephanie.giet@strath.ac.uk

Abstract: We demonstrate the use of a High Reflectivity Grating (HRG) as an intra-cavity element in a Semiconductor Disk Laser (or Vertical External Cavity Surface Emitting Laser) to stabilise its emission wavelength and polarization characteristics. Operation at 1058nm with up to 645mW of pump-limited output power and an M^2~1.4 is achieved. We also show that this scheme permits tunable single-frequency operation.

©2007 Optical Society of America

OCIS codes: (140.5960) Semiconductor lasers; (140.3425) Laser stabilization.

References and links

1. A.C. Tropper, and S. Hoogland, "Extended cavity surface-emitting semiconductor lasers," Prog. Quantum Electron. **30**, 1-43 (2006).
2. M.A. Holm, D. Burns, A.I. Ferguson and M.D. Dawson, "Actively Stabilised, Single-Frequency, Vertical External Cavity AlGaAs Laser," IEEE Photon. Techn. Lett. **11**, 1551-1553 (1999).
3. J. Chilla, S. Butterworth, A. Zeitschel, J. Charles, A. Caprara, M. Reed, and L. Spinelli, "High power optically pumped semiconductor lasers," Proc. SPIE **5332**, 143-150 (2004).
4. J.-Y. Kim, S. Cho, S.-J. Lim, J. Yoo, G.B. Kim, K.-S. Kim, J. Lee, S.-M. Lee, T. Kim and Y. Park, "Efficient blue lasers based on gain structure optimizing of vertical-external cavity surface emitting laser with second harmonic generation," J. Appl. Phys. **101**, 033103 (2007).
5. L. Fan, M. Fallahi, J.T. Murray, R. Bedford, Y. Kaneda, A.R. Zakharian, J. Hader, J.V. Moloney, W. Stolz and S.W. Koch, "Tunable high-power high-brightness linearly polarized vertical external-cavity surface-emitting lasers," Appl. Phys. Lett. **88**, 021105 (2006)
6. H. Lindberg, M. Strasser, and A. Larsson, "Improved Spectral Properties of an Optically Pumped Semiconductor Disk Laser Using a Thin Diamond Heat Spreader as an Intracavity Filter," IEEE Photon. Technol. Lett. **17**, 1363-1365 (2005).
7. P. Zorabedian, "Tunable External-cavity semiconductors lasers," in *Tunable laser handbook*, F.J. Duarte ed. (Academic, 1995), 349-442.
8. A.Q. Liu and X.M. Zhang, "A review of MEMS external-cavity tunable lasers," J. Micromech. Microeng. **17**, R1-R13 (2007).
9. O.M. Efimov, L.B. Glebov, L.N. Glebova, K.C. Richardson and V.I. Smirnov, "High efficiency Bragg gratings in photothermorefrative glass," Appl. Opt. **38**, 619-627 (1999).
10. N.Destouches, A.V. Tishchenko, J.C. Pommier, S. Reynaud, O. Parriaux, "99% efficiency measured in the -1st order of a resonant grating," Opt. Express **13** (9), 3230-3235 (2005).
11. N.Destouches,J.-C. Pommier, O. Parriaux, T. Clausnitzer, N. Lyndin, S. Tonchev, "Narrow band resonant grating of 100% reflection under normal incidence," Opt. Express **14**, 12613-12622 (2006).
12. S. Giet, H.D. Sun, S. Calvez, Dawson, S. Suomalainen, A. Harkonen, M. Guina, O. Okhnotnikov, and M. Pessa, "Spectral narrowing and locking of a vertical external-cavity surface-emitting laser using an intra-cavity volume Bragg grating," IEEE Photon. Technol. Lett. **18**, 1786-1788 (2006).
13. K.S. Kim, J.R. Yoo, S.M. Lee, S.J. Lim, J.Y. Lim, J.H. Lee, S.H. Cho, T. Kim, Y.J. Park, "Highly efficient InGaAs QW vertical external cavity surface emitting lasers emitting at 1060 nm," J. Cryst Growth **287**, 629-632 (2006).
14. G.A. Golubenko, A.S. Svakhin, V.A. Sychugov, A.V. Tishchenko, "Total reflection of light from the corrugated surface of a dielectric waveguide," Sov. J. Quantum Electron., **15**, 886-887 (1985)
15. F. van Loon, A.J. Kemp, A.J. Maclean, S. Calvez, J.-M. Hopkins, J.E. Hastie, M.D. Dawson and D. Burns, "Intracavity diamond heatspreaders in lasers: effect of birefringence," Opt. Express **14**, 9250-9260 (2006)
16. I.A. Avrutsky, V. A. Sychugov "Reflection of a beam of finite size from a corrugated waveguide," J. Mod. Opt. **36**, 1527-1539 (1989)

17. A. Maclean, A.J. Kemp, S. Calvez, J.-Y. Kim, T. Kim, M.D. Dawson and D. Burns, "Continuous tuning and efficient intra-cavity generation in a semiconductor disk laser with intra-cavity heatspreader," accepted for publication in IEEE J. Quantum Electron.

1. Introduction

Semiconductor Disk Lasers (SDLs), also known as Vertical External-Cavity Surface-Emitting Lasers (VECSELs), are attractive diode-pumped semiconductor lasers which combine remarkable wavelength versatility with the operational flexibility afforded by an open-access cavity configuration [1]. Watt-power-level demonstrators, of fundamental emission ranging from 640nm to 2.4μm and frequency-doubled operation in the visible and ultra-violet, show the potential of these sources for applications such as laser projection displays, reprographics and printing, spectroscopy and telecommunications [1-6].

Emission with stable linear polarization and single spatial and longitudinal mode outputs is crucial to many of these applications and has thus motivated investigations on stabilization techniques. To-date, high-power (>100mW), narrow-linewidth operation of semiconductor disk lasers has mainly been obtained by using intra-cavity birefringent filters [2-5] or by exploiting the Fabry-Perot characteristics of a thin intracavity heatspreader [6]. An alternative but very attractive approach is to exploit intra-cavity grating-based techniques, as they readily offer large tunability with high spectral purity [7] and are better suited for use in compact geometries in particular when using micro-electro-mechanical integration [8]. However, because of the inherent low gain of SDLs, the implementation of such techniques has only been made possible by the recent emergence of two types of gratings with peak reflectivity greater than 99%: volume Bragg gratings [9] and high-reflectivity gratings (HRGs) [10-11]. The former kind of grating has been shown to allow high-power narrow-linewidth operation of SDLs [12] but lacked the linear polarization output.

In this letter, we report in full the characteristics of a 1060nm SDL which incorporates an HRG as an intra-cavity element. High-power, tunable, narrow-linewidth and polarization stable laser operation is achieved.

2. Semiconductor structure

The SDL epistructure, grown by Molecular Organic Vapour Phase Epitaxy, comprises a 30.5-pair AlAs/Al$_{0.2}$Ga$_{0.8}$As Distributed Bragg Reflector, an active region with ten strain-compensated InGaAs quantum wells (QWs) distributed over ten antinodes of the standing wave pattern, an AlGaAs confinement window and a 10nm GaAs cap to prevent oxidation [13]. A temperature-dependent backscattered photoluminescence (PL) study showed the maximum PL intensity is achieved for a temperature of 60°C suggesting an in-built offset of -4nm at 20°C between the quantum-well gain peak and cavity resonance. Thermal management of this semiconductor structure is obtained by liquid-capillarity bonding a 500-μm-thick, plane-plane, type-IIa natural diamond heatspreader to the epi-surface and subsequently mounting this composite in a brass-mount. The assembly temperature is kept constant using recirculating water at 10°C.

3. High Reflectivity Grating

The HRG used here is a resonant grating which exploits the proximity of a corrugation and a surface wave to achieve a high degree of polarization, incident angle and wavelength selectivity [10-11;14]. Its high reflectivity and very sharp wavelength selectivity result from the excitation of a TE-guided mode of the multilayer mirror as in [11]. However, this effect is designed here to occur under oblique incidence rather than surface normal illumination.

The HRG was designed to exhibit high-reflectivity at 1058nm for a ~7° angle of incidence. It was fabricated by first etching an 18nm-deep 518.6nm-period grating into a silica mirror substrate and subsequently depositing successively a SiO$_2$/Ta$_2$O$_5$ guide and multilayer mirror by ion plating technology which replicates the surface morphology [11] as shown in the inset of Fig. 1(a). The grating was obtained by exposing a 300nm-thick positive resist to

an interference pattern created by a 442 nm-emitting HeCd laser and subsequently transferring this pattern into the substrate by reactive ion etching (RIE). This fabrication sequence was chosen to minimize the loss by guided mode leakage [10].

Polarization-resolved transmission spectral characteristics of the HRG were measured using as a source the amplified spontaneous emission of an Yb-doped singlemode fibre collimated into a 4mm-diameter beam and on the detection side an optical spectrum analyzer with 0.06nm resolution. Fig. 1(a) shows the results when the component is illuminated at 7.64° of incidence. As expected, the characteristics show a broadband reflection of about 91% with ripples due to the uncoated, polished back surface of the 6mm-thick silica substrate. The TE-polarized reflection presents the desired additional narrow peak (<1nm halfwidth) of reflectivity>99%. The latter feature is expected to ensure both wavelength and polarization selectivity once the grating is inserted in the laser cavity. Temperature assessments indicate that the wavelength corresponding to the peak reflectivity varies at a rate of 0.06nm/K. Angular characterization (see Fig. 1b) shows that the HRG peak shifts at ~5nm/degree for angles greater than 6.5° and disappears for low angles of incidence (absent at 0°).
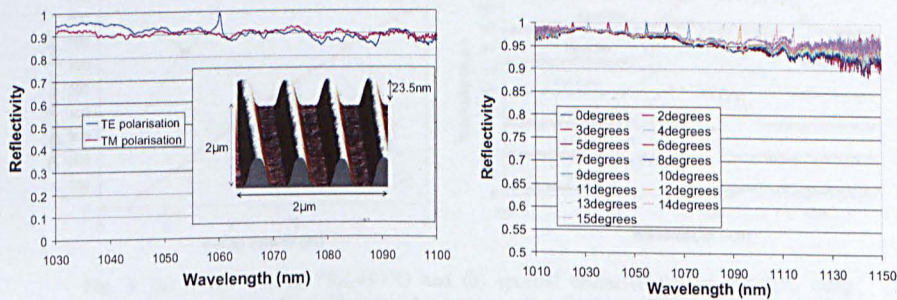
Fig. 1. (a) HRG reflectivity curves for 7.64° incidence angle. Inset: Atomic Force Microscope image of part of the HRG top surface (b) Angular dependence of the HRG TE- reflectivity.

4. Laser Operation

4.1 Cavity Setup

A four-mirror laser cavity was setup (see Fig. 2) with the HRG positioned at one of the folds of the cavity with the etched grooves oriented vertically (i.e. out of the plane of the figure). The curved mirror of radius of curvature R= -100mm was positioned ~57mm away from the semiconductor chip and ~304mm away from the HRG. The planar HR mirror was placed 37mm away from the HRG. Cold-cavity calculations using Winlase™ show that, for a 7° angle of incidence, the vertical and horizontal laser mode sizes at the HRG are respectively 177µm and 209µm and are close to the mode matching condition at the semiconductor wafer for the ~80µm-diameter pump spot size obtained by relaying up to 9.8W of the output of a 100µm-core fibre-coupled 808nm-diode array using a 14mm/8mm collimator/focuser.
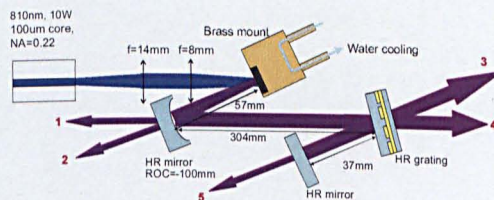
Fig. 2. Plan schematic of the laser cavity setup

4.2 Operation using conventional output coupling mirrors

The laser performance was initially assessed using the cavity of Fig. 2 but with conventional plane output coupling mirrors instead of the HRG. The output power measured at the output 4 of the laser under maximum pumping conditions (P_p=9.8W) is optimum for a mirror of 97% reflectivity as shown in Fig. 3(a). The recorded power transfer (Fig. 3a) indicates a threshold of 0.865W, a maximum output power of 824mW and a slope efficiency of 9.2%. It should be noted that the output 3 of the laser shows power performance similar to output 4 and that the maximum power achieved is mainly limited by the evolution of the slope efficiency with output coupling. As illustrated in Fig. 3(b), this gain-controlled operation is characterized by a multi-peaked spectrum with a peak-to-peak separation of 0.4nm corresponding to the diamond etalon and shows a thermally-induced redshift of 0.42nm/W. The laser emission was found to be circularly polarized, a state attributed to undesirable birefringence of the heatspreader [15].
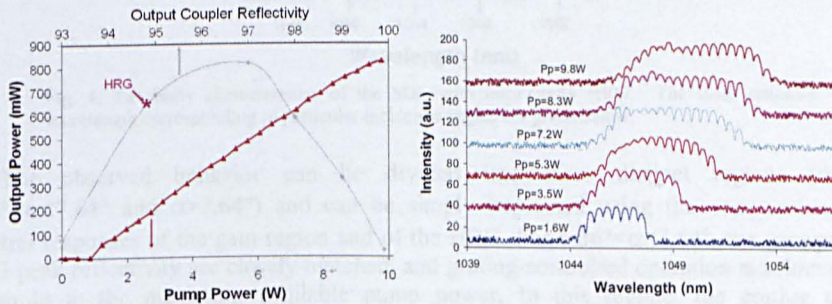
Fig. 3. (a) Power transfer (R_{OC}=97%) and (b) spectral characteristics of the SDL using conventional output couplers. The pink star corresponds to the best laser results obtained when using the HRG intra-cavity (see next section).

4.3 Operation with the high reflectivity grating

To evaluate the impact of the HRG on the laser performance, we recorded the laser spectral and power characteristics for a variety of angles of incidence (5.98 to 9°) on the HRG, rotating the flat HR end-mirror appropriately for feedback. Fig. 4 summarizes the main tuning characteristics of the laser: threshold, maximum output power and the minimum pump power required to have the source to operate at the grating peak wavelength.
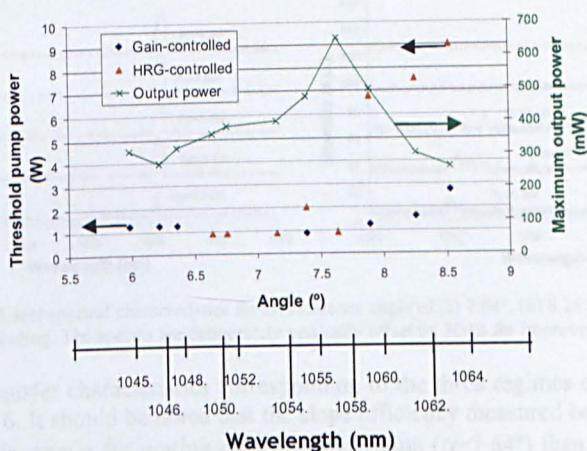
Fig. 4. Tunability characteristics of the SDL with intra-cavity HRG. The laser emission wavelength corresponding to particular incidence angles are given below.

The observed behavior can be divided into three distinct regions ($\alpha \leq 6.36°$, $6.36° < \alpha < 7.64°$ and $\alpha > 7.64°$) and can be simply explained using the convolution of the spectral responses of the gain region and of the HRG. For $6.36° < \alpha < 7.64°$, the gain peak and HRG peak reflectivity are closely matched, and grating-controlled operation is achieved from threshold to the maximum available pump power. In this regime, the grating sets the wavelength (see Fig. 5(a)) and polarization of the laser. Emission with up to 645mW of output power (see Fig. 6) at output 4 (see Fig. 2), an $M^2 \sim 1.4$ (measured for 500mW of output) and a linear polarization (13:1 polarization ratio) aligned with the grooves of the grating ($\pm 2°$) is demonstrated in this configuration. For $\alpha \leq 6.36°$, grating-controlled operation is not possible, an observation consistent with the disappearance of the HRG narrowband reflection feature for low angle of incidence, further enhanced by the relatively small beam size at the grating plane used here [16]. For $\alpha > 7.64°$, the grating peak wavelength redshifts away from the wavelength corresponding to the maximum gain of the active region (~1054nm under maximum pump power), the maximum output power decreases and the minimum pump power required to reach the grating-controlled regime (see represented by triangles in Fig. 3) increases sharply. From the above, the combined wavelength tuning span achieved in grating-controlled tunable operation ($\alpha > 6.36°$) is 15nm with an upper limit of 1064nm (see Fig. 4). Though only discrete tuning at the wavelengths corresponding to the diamond etalon modes was achieved here, continuous tuning should be possible provided an anti-reflection coated wedged diamond is used instead of the plane-plane heatspreader [17].

However, there are subtleties in the laser behavior (see Fig. 4, 5(b) and 6) which originates from the fact that HRG base reflectivity is not quite low enough to prevent gain-controlled operation in all conditions. In particular, the latter regime of operation is achieved for $\alpha \leq 6.36°$ i.e. when the HRG narrow reflection peak is absent. Similarly, for $\alpha > 7.64°$, and as shown in Fig. 5b, there is a transition from the gain-controlled to the grating-controlled regime which reflects the change in the maximum net gain as the pump is increased i.e. as the semiconductor-chip gain broadens and shifts towards longer wavelengths.
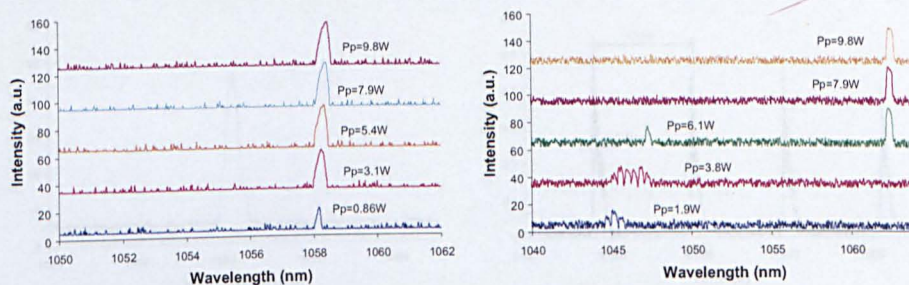
Fig. 5. Laser spectral characteristics for an incidence angle of (a) 7.64°, (b) 8.26° and 10°C water cooling. The spectra are deliberately vertically offset by 30dB for improved visibility

The power transfer characteristics corresponding to the three regimes described above are provided in Fig. 6. It should be noted that the slope efficiency measured between 1 to 4 Watts of pump power is greater for grating-controlled operation (α=7.64°) than for gain-controlled operation (α=6.36 and 8.26°). This is consistent with the over output coupling occurring when the laser operates on the HRG base reflectivity (see Section 4.1). To evaluate the effective reflectivity of the HRG at its peak wavelength, we measured the output powers of the 5 numbered output beams (see Fig. 2) whilst the laser was operated in grating-controlled mode (α=7.64°). The obtained values (P_1=1.13mW, P_2=0.89mW, P_3=116mW, P_4=102mW and P_5=1.22mW, respectively) confirmed the reflectivity of the HR mirrors to be of 99.9% and revealed that the peak reflectivity of the HRG was of 94.8%. The discrepancy between the latter figure and the maximal reflectivity measured with the transmission experiment (see Fig. 1) is believed to be due to the influence of beam aperturing effects occurring for small (<200μm-diameter) beams [16]. With this evaluation, it can be observed from Fig. 3(a) that spectral narrowing does not significantly affect the laser performance.
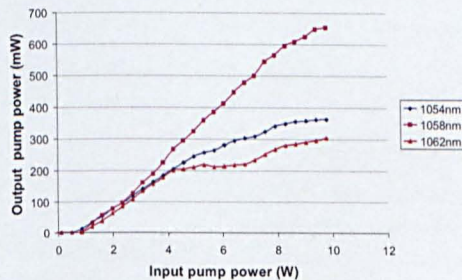

Fig. 6. Laser power transfers recorded for 3 angles of incidence representative of the three respective regimes of operation.

To investigate further the quality of the spectral output in the grating-controlled regime, we performed a detailed spectral analysis of the laser output where the incident angle on the grating is of 7.89° i.e. the laser emits at 1060.24nm. For 200mW of output power, the scan obtained with a commercial scanning Fabry-Perot interferometer with a 1GHz free spectral range shows (see Fig. 7(b)) a measured linewidth of ~90MHz with no feature appearing at the 375 MHz inter longitudinal mode spacing of our 398mm-long cavity, establishing that the laser emission is single longitudinal mode.
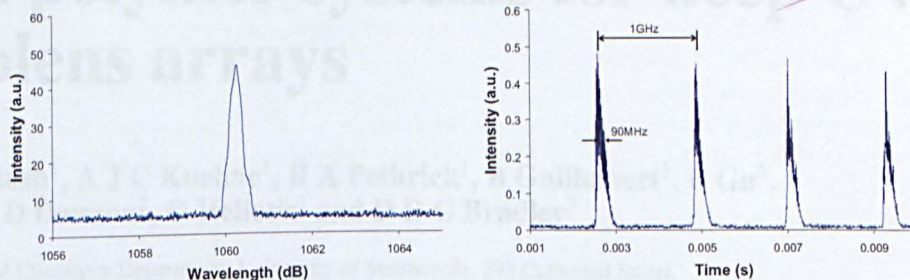
Fig. 7. Spectral analysis of grating-controlled regime with α=7.89° and 200mW output power using (a) an optical spectrum analyzer and (b) a commercial Fabry-Perot interferometer.

5. Conclusion

We have explored the use of a high reflectivity grating (HRG) as an intra-cavity element in a semiconductor disk laser to obtain high-power narrow linewidth operation with stable linear polarization. In particular, it has been established that when the grating peak reflectivity is close to the gain maximum, grating-controlled operation with output power up to 645mW and $M^2 \sim 1.4$ was achievable using this technique. Finally, we also showed that the scheme was suitable to realize single-frequency tunable operation by demonstrating singlemode emission at 1060nm with 200mW output power and tunability over 15nm by simultaneously rotating the HRG and an end mirror.

Acknowledgements

Novel polymer systems for deep UV microlens arrays

A R Mackintosh[1], A J C Kuehne[1], R A Pethrick[1], B Guilhabert[2], E Gu[2],
C L Lee[2], M D Dawson[2], G Heliotis[3] and D D C Bradley[3]

[1] Pure and Applied Chemistry Department, University of Strathclyde, 295 Cathedral Street,
Glasgow G1 1XL, UK
[2] Institute of Photonics, University of Strathclyde, 106 Rottenrow, Glasgow G4 0NW, UK
[3] Experimental Solid State Physics Group, Blackett Laboratory, Imperial College London,
Prince Consort Road, London SW7 2AZ, UK

E-mail: Allan.mackintosh@strath.ac.uk

Abstract

We report for the first time a UV curable polymer with effective optical transmission below
300 nm. Through careful control of kinetics, various viscosities can be generated to optimize
the film forming properties via spin coating. The transmission of the monomers and films is
investigated over a spectral range which spans the 240–370 nm output of ultraviolet AlInGaN
light-emitting diodes. The refractive index of the polymer has been measured by ellipsometry
to give a value of 1.57 at 280 nm. Using standard lithography techniques with reactive ion
etching, arrays of microlenses have been fabricated in this polymer with diameters of 30 μm
and below and are characterized by atomic force microscopy and confocal microscopy.

(Some figures in this article are in colour only in the electronic version)

1. Introduction

High-performance, deep ultraviolet (UV) light-emitting diodes (LEDs) based on AlInGaN alloys with emission in the region 233–290 nm have recently been reported [1–4]. The creation of micropixellated LED arrays with emissions in the deep UV leads to new possibilities in terms of device applications and challenges in terms of microelectronic fabrication technology [5–8]. Deep UV-LEDs emitting below 300 nm can be used for photocuring of polymers used in UV photolithography, photo-activation of shape-memory actuators and in microscale reactors and devices for biosynthesis and microanalysis. The fabricated devices are delicate and are conventionally protected by encapsulation in a tin can with sapphire windows. For the microarrays to achieve their full potential it is desirable to be able to form microoptical components on the elements of these arrays. The processing requires that the material used should have characteristics which are compatible with the operation of the device and easily processed. Conventionally inorganic vapour phase deposited materials which are etched to give an appropriate structure have been used; however polymeric materials, if they have appropriate characteristics, could be an attractive alternative. The fabricated micro-array will have optical elements which need to be protected from solvent or mechanical damage. The light produced from multiquantum well (MQW) devices is highly divergent ($\sim$75°) and it is desirable to shape the beam through the construction of a lens on top of the device. The lens should be constructed from a material which has little or preferably no absorption in the region of operation of the device. Materials such as quartz, sapphire and diamond have the required transmission characteristics, but are expensive and not easily used to form the required integrated optical elements [9]. The alternative approach is to use a polymeric based material. Polyethylene and polvinylidene fluoride have the required UV transmission characteristics but are not easily deposited on the microarrays. Acrylic based polymers are widely used in electronic applications and can be spin coated; however these materials lack transparency below 300 nm.

The simplest approach to solving this problem would be to use a photolithographic material which can be cured by microarrays to create the required optical elements. The deposited polymer materials can be used simultaneously as an optical element and encapsulate the device [8]. The monolithic integration of optical elements via the device being used to

carry out the lithographic steps leads to a simple fabrication process.

The challenge to materials is to create a photolithographic system which in its processed state has high UV transmission characteristics at ~240 nm. Conventionally, photolithography has been based on the use of the novolac epoxy system (e.g. SU-8 or Norland NOA63). These materials have the required processing characteristics but have significant limitations in relation to their UV transmission characteristics. The challenge addressed in this paper is the development of a system which in its processed state has the desired UV transmission characteristics.

This paper presents for the first time a selection of photopolymerizable monomers and photocrosslinkable polymer materials that can be cured by UV activated photoacid generators (PAG) and are in the processed state transparent to the deep UV. These materials are easily shaped via standard lithographic processes [10] and can be self aligned with the microLED devices [12].

2. Basic photolithographic material

Ideally the polymer created photolithographically should have a minimum absorption of UV radiation. Amorphous polyethylene has the required optical characteristics but does not have the desired processability. A monomer system which has a high aliphatic content yet retains the ability to be photoprocessed is 1,4-cyclohexanedimethanol diglycidyl ether (CHDG), which is a mixture of cis/trans isomers, figure 1(a).
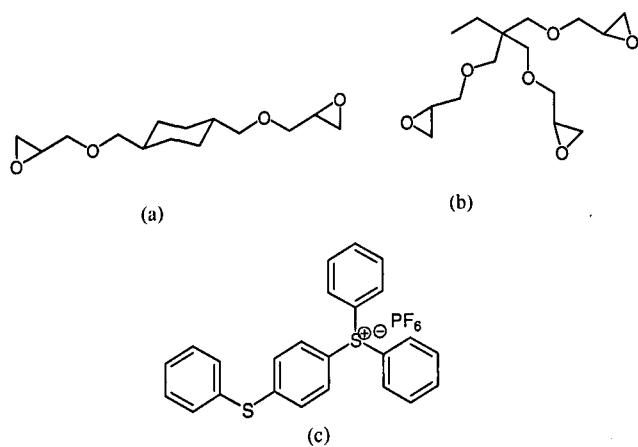

Figure 1. Chemical structures of the monomers: 1,4-cyclohexandimethanol diglycidyl ether (CHDG) (a) and trimethylolpropane triglycidyl ether (TMTG) (b) and triarylsulfonium hexafluorophosphate salt (PAG) (c).

To improve the thermal stability of the matrix we also incorporate trimethylolpropane triglycidyl ether (TMTG), which having a higher functionality will aid network formation but still retain the simple aliphatic polymer backbone, figure 1(b). Similar to the commercially available photoresist SU-8, conversion of the monomer to a stable thin film is achieved via cationic polymerization using sulfonium salts as photoinitiator. The photoinitiator used was a (50/50) mixture of triarylsulfonium hexafluorophosphate salt in propylene glycol, figure 1(c). The propylene glycol acts as a stabilizer for the photoacid. Neither 1,4-cyclohexanedimethanol diglycidyl ether nor trimethylolpropane tiglycidyl ether has previously been used for photolithography. All the chemicals used were obtained from the Aldrich chemical company.

Photoinitiated cationic photopolymerization involves opening of the epoxy (oxirane) ring with the creation of an aliphatic ether backbone and ultimately the formation of a cross-linked polymer network [13–25]. During the photopolymerization process, the (PAG) will undergo a series of transformation reactions, figure 2, ultimately leading to the generation of free acid which initiates the polymerization process [24].

2.1. UV absorption characteristics of monomers and PAG

In order to assess the spectral characteristics of the monomers and the PAG the absorption spectra were measured using a Varian Cary 300 UV-Vis spectrometer. Dilute solutions in acetonitrile and cyclohexane were created and measurements were made using quartz cuvettes with a pathlength of 10 mm, figure 3. It should be noted that polar solvents may evoke a hypso- or a bathochromic shift on the absorption spectra of the molecules under investigation. However, unpolar cyclohexane was chosen as the solvent for CHDG and TMTG. More polar acetonitrile was chosen to dissolve the PAG since it will also be in a polar environment, when admixed with the CHDG/TMTG photoresist. This way sound absorption coefficients of CHDG, TMTG and the PAG could be calculated. The PAG has a significantly higher absorption at the frequencies used for photolithography, ~240–300 nm, than the monomer systems. The kinetics of the photoinitiated polymerization process have been studied using photodifferential scanning calorimetry (PDSC) and are described elsewhere [25].

The strong absorption occurring below 350 nm reflects the absorption of the conjugated aromatic entities and is associated with π–π^* transitions within the PAG molecule. For photoactivation to occur the system must be illuminated in the region of this absorption band. For the polymerization to be efficient, it is important that the monomer is transparent
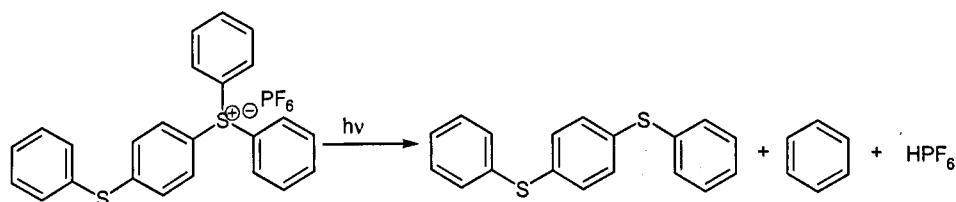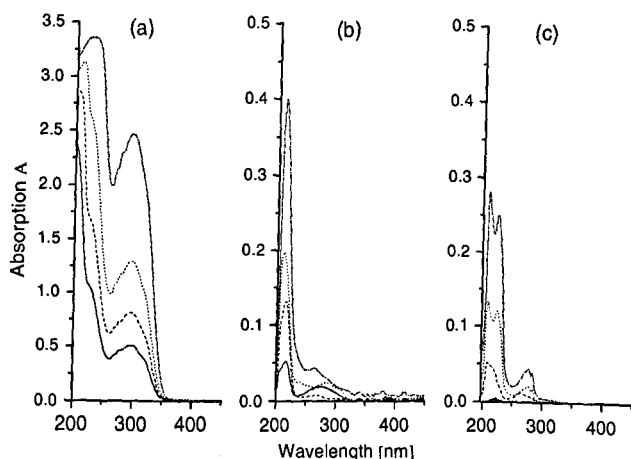

Figure 2. The photolytic degradation of triarylsulfonium hexafluorophosphate. The spectral characteristics change after photoinitiation with a shift in the absorption to shorter wavelengths.

J. Phys. D: Appl. Phys. **41** (2008) 094007

A R Mackintosh *et al*

Figure 3. UV Absorption of PAG, CHDG, TMTG at different concentrations, pathlength 10 mm. (*a*) TA-PF6 in acetonitrile: (solid line): 0.003 wt% (0.38×10^{-4} mol L^{-1}), (dashed line): 0.005 wt% (0.63×10^{-4} mol L^{-1}), (dotted line): 0.008 wt% (1.00×10^{-4} mol L^{-1}), (dotted–dashed line): 0.01 wt% (1.25×10^{-4} mol L^{-1}), (*b*) CHDG in cyclohexane: (solid line): 0.0001 mol L^{-1}, (dashed line): 0.001 mol L^{-1}, (dotted line): 0.01 mol L^{-1}, (dotted–dashed line): 0.02 mol L^{-1}, (*c*) TMTG in cyclohexane: (solid line): 0.0001 mol L^{-1}, (dashed line): 0.001 mol L^{-1}, (dotted line): 0.01 mol L^{-1}, (dotted–dashed line): 0.02 mol L^{-1}.

Table 1. Molar absorption coefficients (mol^{-1} L cm^{-1}) for the PAG, CHDG and TMTG at three wavelengths.

Wavelength (nm)	PAG (TA-PF$_6$)	CHDG	TMTG
260	8476 ± 64	2.090 ± 0.141	1.264 ± 0.238
290	10831 ± 87	1.583 ± 0.249	0.511 ± 0.076
368	67 ± 29	0.434 ± 0.065	0 ± 0

at the wavelength used for activation of the PAG. Plots of the logarithm of the absorption coefficient versus concentration were shown to be linear and to conform to the Beer Lambert law:

$$\log\left(\frac{I_t}{I_0}\right) = -\varepsilon \cdot c \cdot l, \qquad (1)$$

where I_0 is the initial intensity and I_t is the transmitted intensity, ε is the molar extinction coefficient, c is the concentration and l is the path length. Values of the molar extinction coefficients are presented in table 1. The values of ε are a factor of $\sim10^3$ greater for the PAG compared with those for the monomers. The differences in the spectral characteristics of the CHDG and TMTG reflect the effects of the differences in the dielectric permittivity of the liquids on the ease of spectroscopic transition.

2.2. Determination of optical and viscosity parameters

The absorption characteristics of a mixture of 1 wt% of PAG in CHDG were investigated as a function of exposure time, figure 4. The films were exposed to 368 nm UV irradiation from a broad area UV lamp of 6 mW cm^{-2}. The decrease in the peak intensity at $\sim$320 nm over time is indicative of the photobleaching of the system due to the consumption of the PAG.
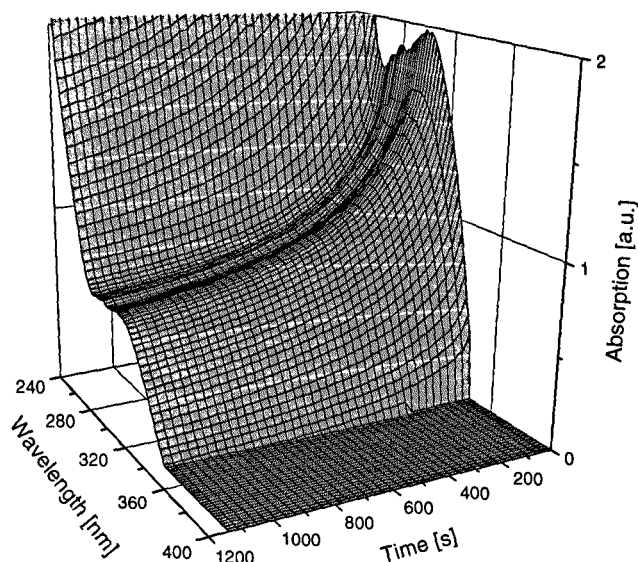

Figure 4. Changes in the absorption coefficient with exposure time for a 1 wt% of PAG in CHDG exposed at 25 °C.
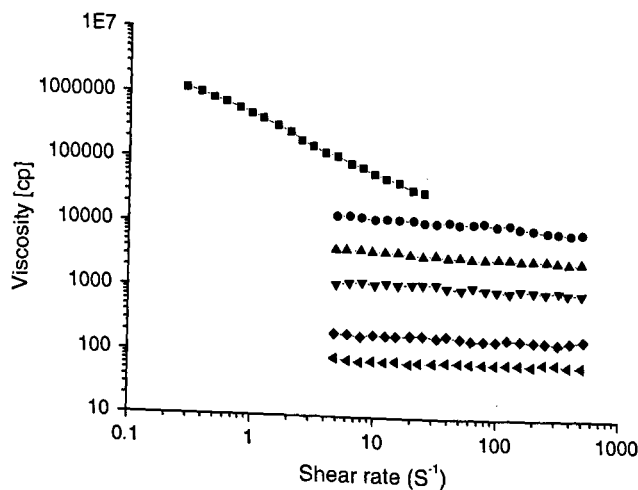

Figure 5. Viscosity against shear rate of the monomers, blends and a prepolymer at 25 °C (key: 100% prepol (■), 75% prepol/25% TMTG (●), 50% prepol/50% TMTG (▲), 25% prepol/75% TMTG (▼), monomer TMTG (♦), monomer CHDG (◄)).

In order to be able to use these systems to create thin films it is essential that the resin should have the correct viscosity characteristics [26]. In order to achieve control of the physical properties of the thin films formed during photolithography it is desirable to be able to adjust the proportions of the di and tri functional monomers in the resin. Changing the proportions of these components will not only alter the physical properties of the final films but will also influence their spinning characteristics through changes in the viscosity of the resin. The viscosities of the resins were measured using a CSL-2 TA rheometer, using a 4 cm parallel plate configuration and a 200 μm gap. The measurements were performed at 40 °C. The simple monomers and their mixtures exhibit viscosities which are independent of shear rate, figure 5, the values of the viscosity changing with the composition of the resin blend. In addition to the pure monomer components a polymerized form of CHDG was synthesized, which exhibits

Table 2. Glass transition temperatures of the CHDG/TMTGE blends.

Blend composition	CHDG 100%	CHDG/TMTG 60/40%	CHDG/TMTG 40/60%	CHDG/TMTG 20/80%	TMTG 100%
T_g	$30.2 \pm 2\,°C$	$34.2 \pm 2\,°C$	$35.3 \pm 2\,°C$	$40.7 \pm 2\,°C$	$48.6 \pm 2\,°C$

a distinctly shear dependent characteristic. This material has a higher molecular mass than that of the monomers and exhibits shear thinning. The higher molar mass significantly enhances the viscosity of the resin and assists in achieving the desired spinning characteristics when thicker film profiles are required. The variation of the viscosity of the blends of the monomer reflects the effects of change in the chemical structure on the intermolecular forces.

The blending of CHDG with TMTG will alter the topography of the network which is formed on photocuring and this will in turn change a number of physical properties of the films formed. The initial viscosities of the monomers are low and insufficient to give good film forming properties [26]. To increase the viscosity the CHDG can be prepolymerized to produce a viscous prepolymer which also has enhanced wetting characteristics. The prepolymer has the required viscosity characteristics for it to produce uniform films of controlled thickness. The prepolymerization of CHDG was achieved by mixing 0.18 wt% of TAS-PF6 into the monomer with continuous stirring and irradiation using a 368 nm UV source operating at $6\,mW\,cm^{-2}$. When the reaction mixture reaches ~43 °C, UV irradiation and stirring is stopped and the prepolymerized material is rapidly cooled to room temperature. Heating the reaction mixture to ~43 °C is necessary to increase the solubility of the TAS-PF6 in the monomer. The resulting photoresist is a viscous, transparent material that is stable for several months when stored in a cool dark environment.

2.3. Determination of physical properties

The nature of the blends of the monomers will influence the topography of the network which is formed on photocure and this in turn will influence the physical characteristics of the films formed. Thin films of blends of the monomers were prepared using a constant dose of $2000\,mJ\,cm^{-2}$ from a broad area near-UV source of 368 nm wavelength and were subjected to dynamic mechanical thermal analysis (DMTA) using a Polymer Laboratories Ltd Mk III DMTA. Rectangular samples of 10 mm × 5 mm and of approximately $200\,\mu m$ thickness were clamped using a single cantilever configuration and a knife-edge clamping arrangement. The clamping torque used was 40 N, and the temperature was scanned between −80 and +120 °C. The samples were re-clamped at low temperatures to minimize slippage. The measurements were performed at a frequency of 1 Hz. The main feature observed is the glass–rubber transition (T_g) and its position was determined as the peak tan δ curve and they are listed in table 2.

2.4. Transmission characteristics of thin films

To determine the transmission characteristics of the polymerized films of a thickness comparable to that of

encapsulants used in LED devices, photoresist was prepared as follows. The photoresist system was prepared by adding 0.5 wt% of PAG to the CHDG/TMTG monomer blend. The photoresist was spin casted onto a 2 inch quartz or sapphire wafer and cured at 328 nm with $6\,mW\,cm^{-2}$ for 10 min to produce a thin film of $\sim 23\,\mu m$ thickness. The absorption spectra were measured on a Varian Cary 300 UV-Vis spectrometer and the transmission characteristics are presented in figure 6. The films formed showed good transparency at 230 nm (35%) and 270 nm (45%). Above 350 nm, almost full transparency to light (>98%) is achieved. The deposition procedure will not necessarily have completely cured the films and better characteristics are achieved if post cure is carried out by heating the films at 120 or 140 °C. The post-cure process removes residual epoxy moieties and this increases the transmission characteristics, respectively, at 230–250 nm and 250–350 nm. Increasing the temperature up to 180 °C induces the decomposition of the PAG, leads to the formation of an acid function and reduces the transparency of the film. The negative effects of the thermal dissociation process on the transmission characteristics of the films create an upper limit for the post-cure process. For comparison, a commercially available epoxy-based polymer resist (Norland NOA 63) deposited at the same thickness was examined, figure 6. The photoresist formulations based on the CHDG/TMTG photoresist demonstrate superior transmission characteristics to the commercial resist in the deep UV.

In terms of device fabrication and design it is desirable to have the refractive index of the films available at the wavelength of operation. Ellipsometry measurements were performed on a 8 μm film coated onto a fused silica substrate. The refractive index range changes from a value of 1.58 at 256 nm to a value of 1.53 at 370 nm. The commercial polymer (Norland NOA63) has a refractive index of 1.56 at 370 nm [10]. The full refractive index dispersion is included in figure 6.

2.5. Processing characteristics

The first stage in processing for most photoresist applications is the deposition of a thin film by spin coating. A series of experiments using a variety of substrates indicated that a satisfactory uniform film can be deposited using a spinning speed of 3600 rpm and a spin time of 1 min. Increasing the spinning speed from 3600 rpm to 7200 rpm decreases the film thickness from 18 μm to 10 μm, respectively, when spinning for 1 min. Increasing the spin time might also lead to thinner film thicknesses. The perfection of the surface of the films was examined using atomic force microscopy (AFM). The Digital Instruments multimode Nanoscope IIIa was used in the tapping mode and revealed that the root mean square (rms) roughness was of the order of 10.2 nm over an area of 5 μm × 5 μm for a spin-coated film of thickness 23 μm on polished sapphire.

(a)

(b)

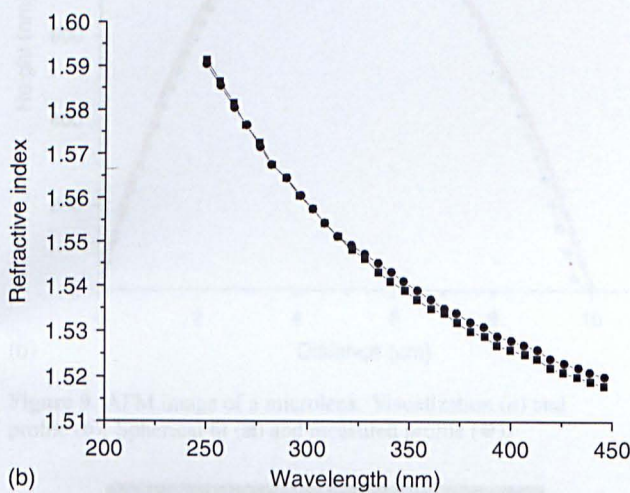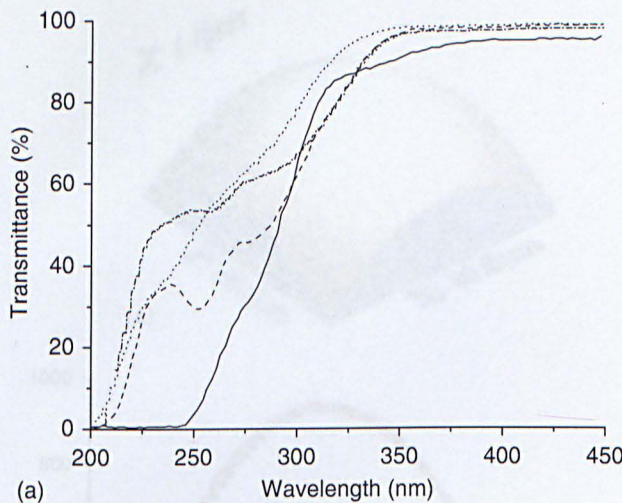**Figure 6.** (*a*) Transmission spectra of deposited photoresist films with a thickness of ~20 μm (key: Norland NOA63 (solid line), the CHDG/TMTG photoresist—without post baking (dashed line), with 10 min post baking at 120 °C (dotted line) and 140 °C (dotted–dashed line)). (*b*) Refractive index variation with wavelength (key: CHDG/THTG, with post bake, 120 °C (●) and with post bake 140 °C (■)).

3. Device fabrication—lens structures located on top of the microLED elements

Polymer microlenses were fabricated in this material using photoresist reflow and reactive ion etching (RIE) techniques [11, 12]. This fabrication process involves two main steps: first a sacrificial mask in photoresist is formed using photolithography and thermal reflow which is then followed by RIE. The double-polished sapphire substrate used for coating by the polymer film in this experiment is transparent to light down to ~200 nm. The polymer was coated at the desired thickness by controlling the spinning speed and hardened using a portable UV light source (4 W) for 2 h. The resist layer was then baked at 120 or 140 °C using the procedure described above. This latter process was carried out to increase the deep UV light transmission characteristics of the polymer film. A layer of resist was then coated and patterned into discs on the polymer of 30 μm diameter and below using photolithographic techniques; the centre-to-centre spacing of
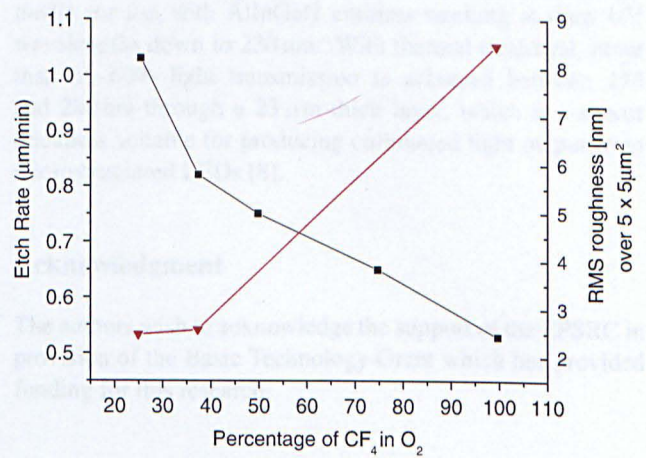

Figure 7. Variation of the etch rate (–■–) and the resulting surface roughness (–▼–) as a function of CF_4/O_2 concentration.
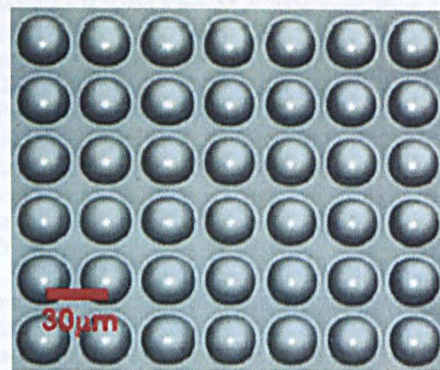

Figure 8. Optical microscopy image of a 30 μm spherical lens array.

these discs was 45 μm. After development, the patterned photoresist was melted on a hot plate at 115 °C for 2 min, during which the resist discs melted into spherical lenslets by minimizing the surface energy. The patterned mask was then transferred into the underlying UV-transparent polymer by RIE etching. The plasma chemistry for RIE etching used a combination of O_2 and CF_4 gases which etches away both photoresist and polymer material effectively [14]. Figure 7 shows the variation in the etch rate and surface roughness with various CF_4/O_2 combinations. Using this O_2 and CF_4 gas chemistry (40/20 sccm) and a dc bias of 415 V, etch rates of the resist and the UV polymer of 0.7 μm min^{-1} and 0.5 μm min^{-1}, respectively, were achieved.

3.1. Examination of the fabricated lenses

The quality of the lenses produced was assessed using a Dektak stylus profiler, atomic force microscope (AFM) and optical and confocal microscopy. Figure 8 shows an optical microscopic image of an array of polymer microlenses and microstripes after RIE etching.

Figure 9 shows an AFM image of the microlens and indicates that it has a 30 μm diameter and a radius of curvature of 13.3 μm with a surface roughness of 7 nm over an area of 1 μm × 1 μm. Using confocal microscopy it is possible to assess the optical performance of the microlens, figure 10. In
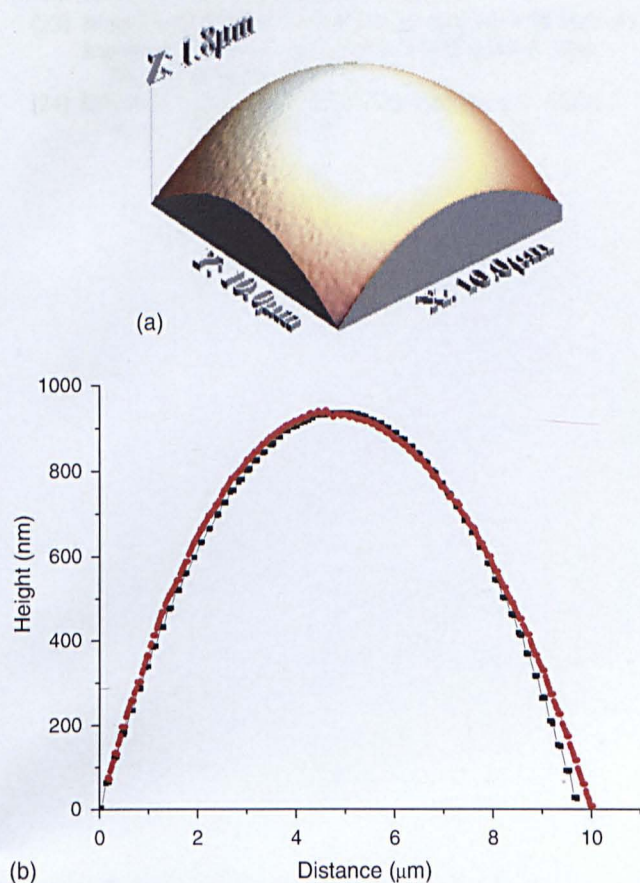
(a)

(b)

Figure 9. AFM image of a microlens. Visualization (*a*) and profile (*b*). Spherical fit (■) and measured profile (●).
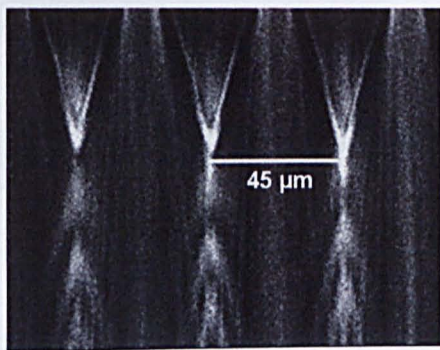

Figure 10. Confocal image of the focusing of the lens.

this technique, a pre-collimated green laser beam is focused by the lens and a series of transverse optical sections at progressive distances from the lens follows the focusing of the beam. The focal length in this case was determined to be 46 μm. This is in close agreement with the value of 44.9 μm calculated for a spherical lens in the manner described previously [10, 11].

4. Summary and conclusions

In summary, the photoresist developed in this project has demonstrated UV-transparent characteristics which make it suitable for use as an encapsulant and device fabrication

media for use with AlInGaN emitters working at deep UV wavelengths down to 230 nm. With thermal treatment, more than 55–60% light transmission is achieved between 250 and 280 nm through a 23 μm thick layer, which is a spacer thickness suitable for producing collimated light output from microstructured LEDs [8].

Acknowledgment

References

[1] Adivarahan V, Sun W H, Chitnis A, Shatalov M, Wu S, Maruska H P and Khan M A 2004 *Appl. Phys. Lett.* **85** 2175
[2] Zhang J P, Hu X, Bilenko Yu, Deng J, Lunev A, Shur M S, Gaska R, Shatalov M, Yang J W and Khan M A 2004 *Appl. Phys. Lett.* **85** 5532
[3] Fischer A J, Allerman A A, Crawford M H, Bogart K H A, Lee S R, Kaplar R J, Chow W W, Kurtz S R, Fullmer K W and Figiel J J 2004 *Appl. Phys. Lett.* **84** 3394
[4] Hirayama H, Yatabe T, Noguchi N, Ohashi T and Kamata N 2007 *Appl. Phys. Lett.* **91** 071901-1
[5] Wu S, Chhajed S, Yan L, Sun W H, Shatalov M, Adivarahan V and Asif Khan M 2006 *Japan. J. Appl. Phys., Part 2* **45** L352
[6] Jeon C W, Choi H W, Gu E and Dawson M D 2004 *IEEE Photon. Technol. Lett.* **16** 2421
[7] Zhang H X, Gu E, Jeon C W, Gong Z, Dawson M D, Neil M A A and French P M W 2006 *IEEE Photon. Technol. Lett.* **18** 1681
[8] Jeon C W, Gu E and Dawson M D 2005 *Appl. Phys. Lett.* **86** 221105
[9] Lee C L, Choi H W, Gu E, Dawson M D and Murphy H 2005 *Diamond Relat. Mater.* **15** 725
[10] Jeon C W, Gu E, Liu C, Girkin J M and Dawson M D 2005 *IEEE Photon. Technol. Lett.* **17** 1887
[11] Choi H W, Liu C, Gu E, McConnell G, Girkin J M, Watson I M and Dawson M D 2004 *Appl. Phys. Lett.* **84** 2253–5
[12] Gu E, Zhang H X, Sun H D, Dawson M D, Mackintosh A R, Kuehne A J C, Pethrick R A, Belton C and Bradley D D C 2007 *Appl. Phys. Lett.* **90** 031116
[13] Chandra R, Thapliyal B P, Babita S and Soni R K 1992 *Polym. Int.* **29** 185–90
[14] Chandra R and Soni R K 1993 *Polym. Int.* **31** 239–45
[15] Sipani V, Kirsch A and Scanton A B 2004 *J. Polym. Sci., Part A: Polym. Chem.* **42** 4409–16
[16] Scott T F, Cook W D and Forsythe J S 2002 *Polymer* **43** 5839–45
[17] Nelson E W, Jacobs J L, Scanton A B, Anseth K S and Bowman C N 1995 *Polymer* **36** 4651–6
[18] Crivello J V and Lam L H W 1996 *J. Polym. Sci., Part A: Polym. Chem.* **34** 3231–53
[19] Lecamp L, Youssef B, Bunel C and Lebaudy P 1997 *Polymer* **38** 6089–96
[20] Corcione C E, Grevco A and Maffezzoli A 2004 *J. Appl. Polym. Sci.* **92** 3484–91
[21] Decker V C and Moussa K 1990 *J. Polym. Sci., Part A: Polym. Chem.* **28** 3429–43
[22] Cook W D 1993 *J. Polym. Sci., Part A: Polym. Chem.* **31** 1053–67

[23] Bulut U and Crivello J V 2005 *Macromolecules* **38** 3584–95
     Esposito Corcione C, Grevco A and Maffezzoli A 2005
     Polymer **46** 8018–27
[24] Crivello J V and Lam L W H 1979 *J. Polym. Sci., Part A:
     Polym. Chem.* **17** 977–99

[25] Troge A, Mackintosh A R, Kuehne A J K, Hayward D
     and Pethrick R A 2007 *Thermo Chem. Acta*
     submitted
[26] Pethrick R A and Rankin K E 1999 *J. Mater. Sci.* **10**
     141–4